


2016

The theory of eddy current nondestructive evaluation by using the volume integral equation method

Tao Wu

Iowa State University

Follow this and additional works at: <https://lib.dr.iastate.edu/etd>

 Part of the [Electrical and Electronics Commons](#), and the [Electromagnetics and Photonics Commons](#)

Recommended Citation

Wu, Tao, "The theory of eddy current nondestructive evaluation by using the volume integral equation method" (2016). *Graduate Theses and Dissertations*. 16058.
<https://lib.dr.iastate.edu/etd/16058>

This Dissertation is brought to you for free and open access by the Iowa State University Capstones, Theses and Dissertations at Iowa State University Digital Repository. It has been accepted for inclusion in Graduate Theses and Dissertations by an authorized administrator of Iowa State University Digital Repository. For more information, please contact digirep@iastate.edu.

**The theory of eddy current nondestructive evaluation by using the volume
integral equation method**

by

Tao Wu

A dissertation submitted to the graduate faculty
in partial fulfillment of the requirements for the degree of
DOCTOR OF PHILOSOPHY

Major: Electrical Engineering

Program of Study Committee:

John R. Bowler, Major Professor

Jiming Song

Nicola Bowler

Nathan Neihart

Mani Mina

Iowa State University

Ames, Iowa

2016

Copyright © Tao Wu, 2016. All rights reserved.

DEDICATION

To my wife Yuhan Tang,

Without whose supports and patience, I would not have been able to complete this work,

And to my parents, Qifu Wu and Shuilian Fang,

Who brought me up and had sacrificed a lot to get me a good education.

TABLE OF CONTENTS

LIST OF TABLES	viii
LIST OF FIGURES	ix
ACKNOWLEDGEMENTS	xviii
ABSTRACT	xix
CHAPTER 1. INTRODUCTION	1
1.1 Eddy-current Nondestructive Evaluation	2
1.2 Statement of the Problem	4
1.3 Thesis Organization	7
CHAPTER 2. LITERATURE REVIEW	9
2.1 Modeling of Probe Field and Interaction with Flawless Structures	10
2.2 Modeling of Probe-Flaw Interaction	11
2.2.1 Analytical and Semi-analytical Methods of Structures with Simplifying Crack	12
2.2.2 Numerical Methods	12
2.3 Modeling of the Ferromagnetic Conductors	15
CHAPTER 3. VOLUME INTEGRAL EQUATION AND FORMULATIONS 17	
3.1 Electromagnetic Fundamentals	17
3.1.1 Understanding of Skin Depth δ	19
3.2 Dyadic Green's Function	20
3.2.1 Dyadic Green Functions with Electric Source	21
3.2.2 Dyadic Green Functions with Magnetic Source	23

3.3	Volume Integral Equation for a Layered Medium with a Flaw	24
3.3.1	Volume Integral Equation for Eddy-current Application in the Quasi-static Limit	27
3.3.2	Matrix Approximation of Volume Integral Equations	29
3.4	Dyadic Green's Kernels of a Layered Medium	32
3.4.1	Dyadic Green's Kernels in the Cartesian Coordinate System	36
3.4.2	Dyadic Green's Kernels in the Cylindrical Coordinate System	38
CHAPTER 4. INCIDENT FIELD EVALUATION FOR PLANAR AND CYLINDRICAL STRUCTURES		39
4.1	Incident Field in Planar Layered Structure	40
4.1.1	The Fields for a Coil in Free-space	40
4.1.2	The Fields for a Coil above an Infinite Half-space Conductor	44
4.1.3	The Fields for a Coil above an Infinite Conductor Slab	47
4.2	Incident Field in Cylindrical Layered Structure	51
4.2.1	Incident Field in Free-space	53
4.2.2	Incident Field in the Conductive Region for a Borehole	55
4.2.3	Incident Field in a Tube	57
CHAPTER 5. COIL IMPEDANCE CHANGES DUE TO CRACKS IN FERROMAGNETIC PLANAR STRUCTURES		60
5.1	Green's Function for an Unbounded Domain	60
5.2	Dyadic Green's Function for a Ferromagnetic Half-space Conductor	61
5.3	Dyadic Green's Function for a Ferromagnetic Conductive Slab	68
5.4	Singularity of \mathcal{G}_{ee} , \mathcal{G}_{mm} in an Unbounded Domain	71
5.4.1	Cuboidal Exclusion Region	73
5.4.2	Spherical Exclusion Region	75
5.4.3	Integral Evaluation in Regular Region	77
5.5	Singularity of \mathcal{G}_{em} , \mathcal{G}_{me}	78
5.6	Singularity Treatment Verification by Calculation of RCS of a Dielectric Sphere	79

5.7	Modeling Verification for Non-ferromagnetic Material	81
5.7.1	Experiment 1: Conductor Plate with a Rectangular Crack	81
5.7.2	Experiment 2: Conductor Plate with a Semi-elliptical Crack	83
5.7.3	Experiment 3: Conductor Plate with a Through-thickness Crack	86
CHAPTER 6. EXPERIMENTAL VALIDATION AND RESULTS OF FER-		
ROMAGNETIC SPECIMEN 90		
6.1	Eddy-current Impedance Measurement System	91
6.2	Measurement of Conductivity and Permeability	94
6.3	Experiment Data for a Ferromagnetic Steel Specimen with a Semi-elliptical Notch	96
6.3.1	13 mm Thick Slab Specimen	96
6.3.2	3 mm Thin Slab Specimen	112
6.4	Liftoff Effect on Probability of Detection	118
6.5	The Comparison of the Impedance Variation between Ferromagnetic and Non-	
	ferromagnetic Steel	122
CHAPTER 7. ARBITRARY ORIENTATION INDUCTION COIL IN-		
TERACTING WITH CYLINDRICAL STRUCTURES 125		
7.1	Abstract	125
7.2	Introduction	125
7.3	Field Analysis	127
7.3.1	Scalar Decomposition of the Field	127
7.3.2	Field of a Circular Current Filament	128
7.3.3	Coordinate Transform	130
7.3.4	Circular Filament with an Azimuthal Tilt	134
7.3.5	Circular Filament with a Polar Tilt	135
7.3.6	Rotary Filament	136
7.4	Free Space Coil Field	136
7.5	Coil Impedance Change and Experiment	138
7.5.1	Model Predicted Results	139

7.5.2	Experimental Results	144
7.5.3	Conclusion	145
CHAPTER 8. ARBITRARY ORIENTATION INDUCTION COIL IN-		
TERACTING WITH PLANAR STRUCTURES		
8.1	Abstract	147
8.2	Introduction	147
8.3	Circular Filament Field and Source Function Evaluation	149
8.3.1	Scalar Decomposition of the Fields	149
8.3.2	Field of a Tilted Circular Filament Loop	149
8.3.3	Source Coefficient Evaluation	152
8.4	Coil Field Analysis	154
8.4.1	Coil Field in the Free-space	154
8.4.2	Induced Eddy Current in the Conductive Half-space	155
8.5	Impedance Variation	156
8.6	Conclusion	158
APPENDIX A. REFLECTION AND TRANSMISSION COEFFICIENT FOR		
PLANARLY AND CYLINDRICALLY LAYERED MEDIUM		
A.1	Reflection and Transmission in a Cartesian Coordinate System	159
A.1.1	Half Space Coefficients	159
A.1.2	Slab with a Source Above It	161
A.1.3	Slab with an Internal Source	163
A.2	Reflection and Transmission in a Cylindrical Coordinate System	164
A.2.1	Borehole with an Internal Source	166
A.2.2	Borehole with an External Source	170
A.2.3	Tube with an Internal Source	172
A.2.4	Tube with a Source between inner and outer surface	174
A.2.5	Tube with an External Source	175

APPENDIX B. BOBBIN COIL CO-AXIAL WITH BOREHOLE AND TUBE	
STRUCTURES	177
APPENDIX C. USEFUL MATHEMATICAL FORMULATIONS	180
C.1 Fourier and Bessel Transforms	180
C.2 Identities	180
C.2.1 Differential Operators	181
C.2.2 Integral Identities	182
C.3 Bessel Function	182
BIBLIOGRAPHY	194

LIST OF TABLES

Table 4.1	Coil and borehole parameters	56
Table 5.1	Coil and crack parameters for Team Workshop Problem 15	81
Table 5.2	Coil and crack parameters for experiment 2	83
Table 5.3	Coil and crack parameters for experiment 3	86
Table 6.1	Probe coil 1, 13 mm specimen and notch parameters	99
Table 6.2	Probe coil 1, 3 mm specimen and notch parameters	113
Table 7.1	Coil and inconel steam generator tube parameters for experiment . . .	142
Table 7.2	Coil and inconel steam generator tube parameters for theoretical calcu- lation	144
Table 8.1	Coil and specimen parameters	156

LIST OF FIGURES

Figure 1.1	An circular air-cored coil with alternating current excited scans above planar conductor plate	3
Figure 1.2	Eddy current probe coil of different situation involved in modeling	5
Figure 3.1	Planarly multilayered medium with flaws in layer j	24
Figure 4.1	Horizontal circular filament loop in the unbounded space	40
Figure 4.2	Horizontal coil in the unbounded space	41
Figure 4.3	The electromagnetic fields of a coil in the free space	43
Figure 4.4	Horizontal coil above half-space conductive metal	44
Figure 4.6	Horizontal coil above conductive slab	47
Figure 4.5	The electromagnetic fields of TEM Problem 15	48
Figure 4.7	The electromagnetic fields of TEM Problem 15, the slab thickness is 6 mm	52
Figure 4.8	A rotary coil locates in free space	53
Figure 4.9	The $ E_\phi $ field at the borehole interface	57
Figure 5.1	Half Space with Point Source in Region 2	62
Figure 5.2	Slab with Embedded Point Source in Region 2	68
Figure 5.3	RCS results comparison between VIE method and Mie-series with 32 cells	79
Figure 5.4	RCS results comparison between VIE method and Mie-series with 280 cells	80
Figure 5.5	RCS results comparison between VIE method and Mie-series with 912 cells	80

Figure 5.6	The mesh of the crack region of TEM Problem 15	81
Figure 5.7	Comparison between experimental and theoretical result of resistance changes of TEM Problem 15 at 900 Hz	82
Figure 5.8	Comparison between experimental and theoretical result of reactance changes of TEM Problem 15 at 900 Hz	82
Figure 5.9	The mesh of the crack region of experiment 2	83
Figure 5.10	Comparison between experimental and theoretical result of resistance changes of experiment 2 at 1027 Hz	84
Figure 5.11	Comparison between experimental and theoretical result of reactance changes of experiment 2 at 1027 Hz	84
Figure 5.12	Comparison between experimental and theoretical result of resistance changes of experiment 2 at 2081 Hz	85
Figure 5.13	Comparison between experimental and theoretical result of reactance changes of experiment 2 at 2081 Hz	85
Figure 5.14	Comparison between model prediction and experiment of resistance changes at 0.631 kHz	87
Figure 5.15	Comparison between model prediction and experiment of resistance changes at 0.631 kHz	87
Figure 5.16	Comparison between model prediction and experiment of resistance changes at 2.5 kHz	88
Figure 5.17	Comparison between model prediction and experiment of resistance changes at 2.5 kHz	88
Figure 5.18	Comparison between model prediction and experiment of resistance changes at 10 kHz	89
Figure 5.19	Comparison between model prediction and experiment of resistance changes at 10 kHz	89
Figure 6.1	Impedance add-on circuit structure	91

Figure 6.2	Eddy-current impedance measurement system which includes power supply, lock-in amplifier and impedance add-on module	92
Figure 6.3	Experimental bench used to measure the coil impedance change due to the narrow notch in the 440SS steel slab	93
Figure 6.4	Eddy-current probe structure	93
Figure 6.5	ACPD test bench for measuring specimen conductivity and permeability	95
Figure 6.6	The variation of specimen conductivity and permeability in terms of position	95
Figure 6.7	Thick 440SS steel slab specimen with semi-elliptical notch	96
Figure 6.8	8 mm notch (middle one) in 13mm thick specimen with the EDM cutting tool	96
Figure 6.9	The resistance change of a circular coil above a flawles 440SS slab as a function of frequency	97
Figure 6.10	The reactance change of a circular coil above a flawles 440SS slab as a function of frequency	97
Figure 6.11	Along the notch scan diagram	98
Figure 6.12	Comparison between model prediction and experimental data of resistance variation at 3 kHz	99
Figure 6.13	Comparison between model prediction and experimental data of reactance variation at 3 kHz	100
Figure 6.14	Comparison between model prediction and experimental data of impedance variation in impedance plane at 3 kHz	100
Figure 6.15	Comparison between model prediction and experimental data of resistance variation at 4 kHz	101
Figure 6.16	Comparison between model prediction and experimental data of reactance variation at 4 kHz	101
Figure 6.17	Comparison between model prediction and experimental data of impedance variation in impedance plane at 4 kHz	102

Figure 6.18	Comparison between model prediction and experimental data of resistance variation at 5 kHz	102
Figure 6.19	Comparison between model prediction and experimental data of reactance variation at 5 kHz	103
Figure 6.20	Comparison between model prediction and experimental data of impedance variation in impedance plane at 5 kHz	103
Figure 6.21	Across the notch scan diagram	104
Figure 6.22	Comparison between model prediction and experimental data of resistance variation at 3 kHz	105
Figure 6.23	Comparison between model prediction and experimental data of reactance variation at 3 kHz	105
Figure 6.24	Comparison between model prediction and experimental data of impedance variation in impedance plane at 3 kHz	106
Figure 6.25	Comparison between model prediction and experimental data of resistance variation at 4 kHz	106
Figure 6.26	Comparison between model prediction and experimental data of reactance variation at 4 kHz	107
Figure 6.27	Comparison between model prediction and experimental data of impedance variation in impedance plane at 4 kHz	107
Figure 6.28	Comparison between model prediction and experimental data of resistance variation at 5 kHz	108
Figure 6.29	Comparison between model prediction and experimental data of reactance variation at 5 kHz	108
Figure 6.30	Comparison between model prediction and experimental data of impedance variation in impedance plane at 5 kHz	109
Figure 6.31	Comparison between model prediction and experimental data of resistance variation at 7 kHz	109
Figure 6.32	Comparison between model prediction and experimental data of reactance variation at 7 kHz	110

Figure 6.33	Comparison between model prediction and experimental data of impedance variation in impedance plane at 7 kHz	110
Figure 6.34	Impedance real part variation contour of 13mm specimen at 10kHz with semi-elliptical notch based on experiment	111
Figure 6.35	Impedance imaginary part variation contour of 13mm specimen at 10kHz with semi-elliptical notch based on experiment	111
Figure 6.36	Thin 440SS steel slab specimen with semi-elliptical notch	112
Figure 6.37	6 mm notch in 3mm thick specimen with the EDM cutting tool	112
Figure 6.38	Comparison between model prediction and experiment data of resistance variation at 10 kHz	114
Figure 6.39	Comparison between model prediction and experiment data of reactance variation at 10 kHz	114
Figure 6.40	Comparison between model prediction and experiment of resistance changes at 10 kHz for across-the-notch scan	115
Figure 6.41	Comparison between model prediction and experiment of reactance changes at 10 kHz for across-the-notch scan	115
Figure 6.42	Comparison between model prediction and experiment of resistance changes at 10 kHz for both scans	116
Figure 6.43	Comparison between model prediction and experiment of resistance changes at 10 kHz for both scans	116
Figure 6.44	Impedance real part variation contour of 3mm specimen at 10kHz with semi-elliptical notch	117
Figure 6.45	Impedance imaginary part variation contour of 3mm specimen at 10kHz with semi-elliptical notch	118
Figure 6.46	The real part of impedance variation contour in terms of different liftoff based on experiment	119
Figure 6.47	The imaginary part of impedance variation contour in terms of different liftoff based on experiment	120
Figure 6.48	The POD curve as a function of liftoff	121

Figure 6.49 The simulated 2-D resistance variance due to the semi-elliptical notch of ferromagnetic steel 122

Figure 6.50 The simulated 2-D resistance variance due to the semi-elliptical notch of non-ferromagnetic steel 123

Figure 6.51 The simulated 2-D reactance variance due to the semi-elliptical notch of ferromagnetic steel 123

Figure 6.52 The simulated 2-D reactance variance due to the semi-elliptical notch of non-ferromagnetic steel 124

Figure 7.1 A circular induction coil of arbitrary orientation inside a conductive tube 127

Figure 7.2 Circular filament centered at the point Q in the plane $x_0 = x'_0$ having radius ρ_0 . The azimuthal rotation angle is ϕ and θ is the polar tilt angle. 128

Figure 7.3 Triangle used to relate addition theorem variables using the cosine rule. 130

Figure 7.4 Circular filament centered at point Q. The filament surface S_0 intersects with $y = 0$ plane at the line AB 131

Figure 7.5 Plan view of the xy -plane intersected by the circular filament centered at Q. 132

Figure 7.6 Integration over the surface S_0 bounded by the circular filament is divided at the line AB into two parts. The linear function $Y_0(z_0)$, shown in the diagram, defines the perpendicular distance of this line from the plane $y_0 = 0$. In carrying out the intergration over z'_0 one needs to set the limits at the filament and at the line AB depending on the value of y'_0 133

Figure 7.7 The cross-section view of a circular coil at $y = 0$ plane with polar tilt angle θ is shown in dashed outline. The coil is centered at point P and one filament loop of the coil is also shown to illustrate the filament superposition 137

Figure 7.8 The effect of tilted angle ϕ on normalized resistance changes for a circular coil with different ϕ inside a tube 139

Figure 7.9 The effect of tilted angle ϕ on normalized reactance changes for a circular coil inside a tube 139

Figure 7.10 The effect of tilted angle θ on normalized resistance changes for a circular coil with different θ inside a tube 140

Figure 7.11 The effect of tilted angle θ on normalized reactance changes for a circular coil with different θ inside a tube 140

Figure 7.12 Comparison between coaxial bobbin coil and polar tilt coil with $\theta = 90^\circ$ and $x_1 = 0$ of normalized resistance changes for a coil inside a tube of different frequency 141

Figure 7.13 Comparison between coaxial bobbin coil and polar tilt coil with $\theta = 90^\circ$ and $x_1 = 0$ of normalized reactance changes for a coil inside a tube of different frequency 142

Figure 7.14 The $|\mathbf{E}|$ distribution at the tube inner interface. a is the tube inner radius. The induced current can be obtained by multiplying conductivity of the conductor. 143

Figure 7.15 Comparison between experimental and theoretical result of normalized resistance changes for a coil inside a tube of different frequency 145

Figure 7.16 Comparison between experimental and theoretical result of normalized reactance changes for a coil inside a tube of different frequency 145

Figure 8.1 An air-cored circular coil located above conductive plate. The coil axis (dash line) has a polar tilted angle θ relative to z axis 148

Figure 8.2 Circular filament centered at the point Q in the plane $z_0 = z'_0$ having radius ρ_0 . The axis of the circular loop coincides with z_0 axis 150

Figure 8.3 A circular filament loop with titled angle θ in the free-space. The cross-section view shows the $y = 0$ plane. 150

Figure 8.4 The triangle DEF used to relate addition theorem variables 152

Figure 8.5	Circular filament centered at point Q . the filament surface S_0 intersects with $y = 0$ plane at the line AB , which split the S_0 into two parts. The triangles ΔRTS shows how Graf's addition theorem is applied on it . . .	153
Figure 8.6	The plane view of a tilted circular filament loop. The triangles ΔRTS and ΔRTU are used to transform the global source coordinates to local coordinates by Graf's addition theorem	153
Figure 8.7	The cross-section view of a tilted circular coil is shown in dashed outline. The coil is centered at point P and one filament loop of the coil is also shown to illustrate the filament superposition	154
Figure 8.8	Amplitude Contour of eddy currents induced on the surface of a conductive half-space by a circular coil with different titled angle	155
Figure 8.9	The comparison of resistance variation between tilted coil with titled angle $\theta = 0^\circ$ and horizontal coil formulation due to the existence of half-space conductor	157
Figure 8.10	The comparison of reactance variation between tilted coil with titled angle $\theta = 0^\circ$ and horizontal coil formulation due to the existence of half-space conductor	158
Figure A.1	Half-space medium with source in region 1	159
Figure A.2	Infinite large slab with source in region 1	161
Figure A.3	Slab with Embedded Source in Region 2	163
Figure A.4	Borehole structure with the source in region 1. The radius of hole is a	166
Figure A.5	Borehole structure with the source in region 2. The radius of hole is a	170
Figure A.6	Tube structure with the source in region 1	172
Figure A.7	Tube with source in region 2	174
Figure A.8	Tube with source in region 3	175
Figure B.1	A eddy current coil located inside coaxial with borehole, the number 1,2,3,4 indicates different region	177

Figure B.2 A eddy current coil located inside coaxial with Tube, the number 1,2,3,4,5
indicates different region 178

Figure B.3 A eddy current coil located outside coaxial with Tube, the number
1,2,3,4,5 indicates different region 179

ACKNOWLEDGEMENTS

I would like to take this opportunity to express my thanks to those who helped me with various aspects of conducting research and the writing of this thesis.

First and foremost, I would like to thank Dr. John Bowler for his guidance, support and patience throughout my research and study. His insights and words of encouragement have often inspired me and renewed my hopes when encountering difficulties in my research. From him, I learned a lot not only the knowledge of eddy current NDE but the general methodology of how to solve a problem in the research. Besides, his EE588 course is so enlightening that it opens the secret door of the eddy current NDE area for me. I am truly honored to have completed my doctorate degree study under his guide.

I would like to thank my committee members for their suggestions and helps to this work: Dr. Nicola Bowler, Dr. Jiming Song, Dr. Nathan Neihart and Dr. Mani Mina. Besides, I would like to thank Dr. Jiming Song for his four great courses about electromagnetic fields, which are very instructive and help me to gain valuable insights and better understanding on this area. I would like to thank Dr. Nathan Neihart, the instructor of EE514, who taught us a lot about RF circuit design, simulation and test.

I would additionally like to say thanks to my colleagues, Yuan Ji and Dr. Yi Lu, for their help in my study and research at Iowa State University. My humble thanks goes to all my friends, Dr. Kun Chen, Dr. Zhiwei Liu, Praveen Gurralla, Yang Bao, Liang Zhang and many more, for their helps and encourage.

Last but not least, I would like to thank family. To my grandmother Meilan Wang, parents Qifu Wu and Shuilian Fang, and sister Chunmei Wu, I am extremely thankful for their love and support.

ABSTRACT

Since 1950s sodium cooled fast reactors (SFR) have been developed and have been approaching their commercialization as nuclear power plants through the development of experimental and prototype reactors. High-performance steels such as 9Cr-1Mo, oxide dispersion strengthened (ODS) have been used for metallic parts such as heat exchanger tubes and fuel cladding in fast reactors. They are favored because of their high temperature creep and fatigue resistance properties. Periodical nondestructive in-service inspection (ISI) of those metallic parts is essential since any damage in the parts can lead to malfunction or even destructive accidents. However, most of the numerical and theoretical models are developed for non-magnetic materials. In this dissertation, theoretical and computational approaches are proposed to solve eddy current problems for both ferromagnetic and non-ferromagnetic conductors.

By applying the volume equivalence theorem, the effects of a flaw in the conductor are represented by an equivalent electric current dipole density and a magnetic dipole density. Volume integral equations are then derived for multi-layered structures. The general dyadic Green's kernels dedicated to a layered geometry are derived here based on a decomposition of the electromagnetic field into a transverse electric scalar potential and a transverse magnetic scalar potential. The dyadic Green's kernels for either planar-layered or cylindrical-layered structures can be derived from the corresponding scalar kernels.

The dedicated dyadic Green's kernels for a conductive half-space and slab are derived and discussed. Naturally, the method of moments (MoM) is used to obtain the numerical approximation of the integral equations. The incident field, also known as the unperturbed field, plays an important role in the method of moments and is determined in Chapter 4, 7 and Chapter 8. For better accuracy and calculation efficiency, a simple analytical method for evaluating the hyper-singular element is provided for the matrix component calculation and validated by calculating the radar cross-section (RCS) of dielectric sphere.

Experiments are carried out to obtain the impedance variation of a circular coil probe due to narrow notches in a ferromagnetic steel slabs (440 stainless steel) for comparison with theoretical and computational models. Good agreement has been achieved. The model validation of the non-ferromagnetic conductor has also done by comparing model predictions with existing benchmark experimental data. This numerical model can be used to refine the eddy current probe design and predict the probe signal due to cracks in ferromagnetic metallic parts.

A particular challenge of eddy current inspection in a fast reactor is that the coil position cannot be guided by optical aids due to the presence of liquid sodium during the periods when inspection is possible. However, electromagnetic sensing can be used. in the dissertation, we proposed a novel theoretical electromagnetic model of an eddy current probe with arbitrary orientation with respect to a tube or a plate. The experiment is also carried out and compared with theoretical prediction showing excellent agreement. The theoretical results are also useful in wobble noise analysis and the numerical method for fast evaluation of incident field term of integral equation method.

CHAPTER 1. INTRODUCTION

Nondestructive evaluation (NDE) is an interdisciplinary field of study which concentrates on the process of inspecting, testing and evaluating structures, materials, components or assemblies for fatigue, flaws or differences in characteristics without impairing the future usefulness of the part or system. Because NDE can provide valuable information about objects under detection, which help us to control and monitor their quality and safety status, and does not damage them, it is a highly valuable technique that is widely used in manufacturing, fabrication and in-service inspection as a stand-by system to control manufacturing processes to ensure product integrity and reliability and to ensure the usefulness and safety of the products in use.

NDE includes a wide range of categories used in science and industry. The method category names often refer to the type of penetrating medium or the equipment used to perform the test. Current NDE methods include acoustic emission, electromagnetic, guided wave, ground penetrating radar, laser, liquid penetrant, radiographic, ultrasonic, vibration, therm-graphic and visual methods.

Electromagnetic (EM) NDE methods is an important category and involves the application of electromagnetic energy to evaluate the condition of objects under test by analyzing the interaction process between the EM fields and materials. EM NDE generally comprises several different subsidiary methods or techniques based on different classification standards. It includes magnetic flux leakage, eddy current, radio frequency (RF), microwave wave and terahertz radiation. The working frequency of magnetic flux leakage method is usually near 0 Hz. As the frequency increases from DC, the fundamental physical process gradually changes. From 100 Hz to 10 MHz, the displacement current component of Maxwell's equations is negligible and the field is usually refer to as a quasi-static field [1]. At these frequencies, the Maxwell's equations reduce to diffusion equations. As the frequency increase further, the field propa-

gates in the form of waves and has the property to transmit a long distance, which is widely used as an antenna in the wireless communication [2]. Below 20 MHz, we have AC/DC field measurement method, magnetic flux leakage method, remote field method based on EM fields measurement and alternating current potential drop (ACPD) method [3]. From the application perspective, the eddy current method is usually for the inspection of metallic conductors, while RF, microwave and Terahertz methods are mostly used in weak-conductive materials such as multi-layer dielectric slabs, laminated composites [4] and the EM imaging field [5]. Of these several EM sub-methods, the eddy-current method is the most widely used in both economic field inspection and academic research.

1.1 Eddy-current Nondestructive Evaluation

The eddy current method involves the use of time-varying magnetic field which will induce the eddy current in the conductor. Hence, in general, eddy current tests are applicable to materials with significant electrical conductivity, such as metals, alloys and composites with conducting layers or fibers. It can also used to measure the thickness of non-conductive layers on the surface of metallic materials by using the liftoff effect [1].

Although a comprehensive understanding of the underlying physical process should be gained through Maxwell's equations, the technique basis can also be understood qualitatively. When a coil excited by an alternating current is placed in close proximity to a homogeneous conductive specimen without a flaw, Fig. 1.1, the primary field, set up by the eddy current coil, induces eddy currents within the conductive specimen. In conformity with Lenz's law, the secondary field generated by these eddy currents will oppose the change of the primary field and consequently the terminal impedance of the coil changes. For a specific coil, the impedance change is affected by the probe size and liftoff, the conductivity and permeability of material and frequency. If a discontinuity, crack or flaw exists in the test specimen, the eddy current will redistribute and the inductance and resistance of the eddy current coil will be correspondingly changed.

For a non-ferromagnetic specimen, the inductance of coil is always decreased due to the opposing nature of the primary and secondary fields. However, for a ferromagnetic specimen,

the inductance of coil can increase due to the higher permeability of the material. At the same time, the coil resistance will also increase because of both the hysteresis and eddy current losses [1, 6].

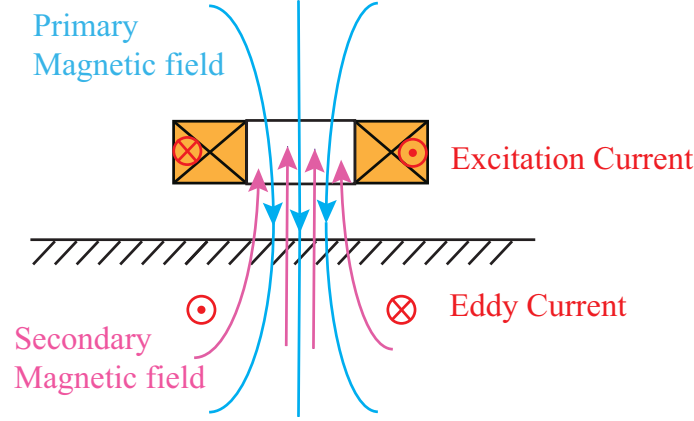


Figure 1.1: An circular air-cored coil with alternating current excited scans above planar conductor plate

There are several different eddy current testing techniques. They are the single frequency eddy current, the multi-frequency eddy current, pulsed eddy current, remote field eddy current, SQUID-based eddy current [7], eddy current probe array techniques beginning with the conventional and moving to the recent developments [8].

From the modeling point of view, there are two general problems, the forward problem and the inverse problem. The crack size, shape and specimen properties of the forward problem are usually known. One subset of the forward modeling problem is to obtain the probe field distribution and impedance change with or without the existence of unflawed specimen by analytical or numerical method. A classic study of circular air-cored coil over a planar-layered conductor with the coil axis perpendicular with the conductor plane and encircling co-axially with a cylindrical-layered cylinder is given in an analytical formulation by Dodd and Deeds [9]. The impedance variation of eddy current coil, ΔZ due to the presence of the flawless structure is given by

$$\Delta Z = Z - Z_0 = \Delta R + j\Delta X \quad (1.1)$$

where Z_0 is the coil impedance in the free space, Fig. 1.2a, and Z is the coil impedance in the presence of the flawless structure, Fig. 1.2b.

Another subset of the forward modeling problem is the probe-defect interaction, Fig 1.2c, which aim at getting a better understanding and insight of probe-defect interactions in order to optimize the probe design and even the whole eddy-current measurement system design to obtain the best parameter settings. The impedance variation of eddy current coil, ΔZ_c , due to the presence of the crack is given by

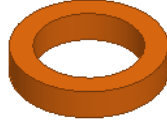
$$\Delta Z_c = Z_c - Z = \Delta R_c + j\Delta X_c \quad (1.2)$$

where Z_c is the coil impedance with the existence of crack structure, Fig. 1.2c.

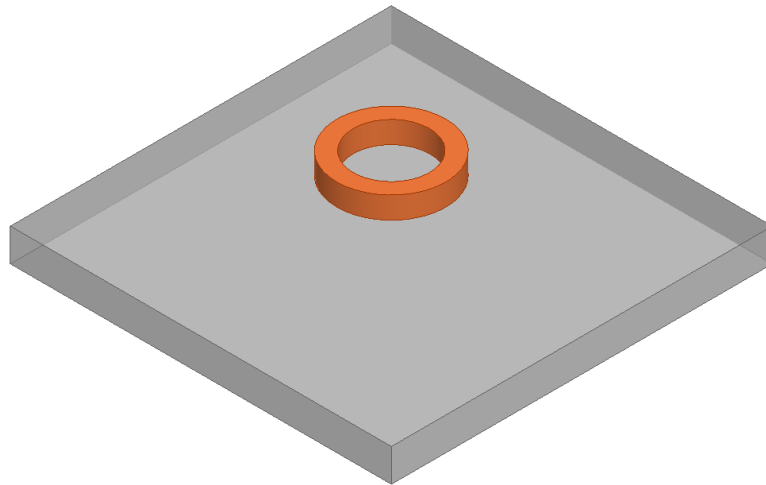
The inversion problem of eddy current nondestructive evaluation, which is aimed to determine the size, shape and/or material properties of a flaw or other features of conductor structures from a set of observations on EMF, is another big topic in the eddy current modeling [10]. Generally speaking, the inversion problem is a far more complex problem compared with forward modeling. A more detailed summary about inversion problem can be found in [10, 11].

1.2 Statement of the Problem

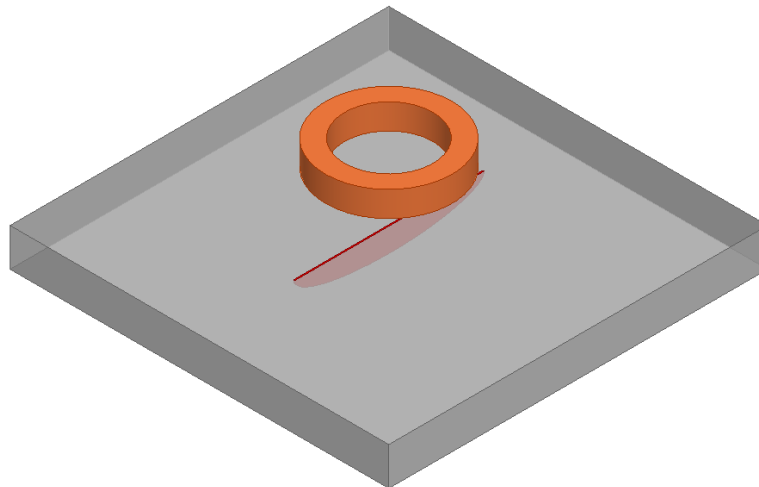
Compared with most existing thermal reactors, fast neutron reactors can extract more energy from nuclear fuel, reduce the total radiotoxicity of nuclear waste, and dramatically reduce the waste's lifetime to several hundreds of years [12]. High-performance steels such as 9Cr-1Mo, oxide dispersion strengthened (ODS) find extensive applications to fabricate metallic parts such as heat exchanger tubes of fast reactor in view of its favorable high temperature creep and fatigue resistance properties. Periodical nondestructive in-service inspection (ISI) of those metallic parts is essential since any damage in the parts can lead to malfunction or even destructive accidents. The magnetic flux leakage (MFL) technique is being explored as it can detect both shallow surface and deep sub-surface defects in the SFR heat exchanger tubes [13]. However it's usually limited to the ferromagnetic material and the metallic parts in the reactor are mainly non-ferromagnetic. In addition, it is challenging due to the physical constraints of placing the magnetizing coils and sensing circuit with the existence of high temperature conductive coolant.



(a) An circular air-cored coil in free space with impedance $Z_0 = jX_0$



(b) An circular air-cored coil above a flawless conductive slab with impedance $Z = R + jX$



(c) An circular air-cored coil with alternating current excited scans above crack with impedance $Z_c = R_c + jX_c$

Figure 1.2: Eddy current probe coil of different situation involved in modeling

Eddy-current method are widely used for inspections of steam generator tubes in power plants due to its high accuracy, easy use and ability to detect defects both inside and outside the tube wall. However, the eddy-current inspection in SFR is more challenging due to the resulting weak probe signal of cracks, the presence of liquid conductive coolant, high temperature (250 °C).

In order to refine inspection methods and gain an insight into the eddy current probe responses due to flaws, a number of theoretical and computational models include analytical methods, semi-analytical methods and numerical methods have been developed. Although semi-analytical solutions are accessible for certain structures with ideal cracks by applying some idealized approximations, such as TREE method [14, 15] and thin-skin approximation at high frequency [16, 17], it is expedient to seek numerical approximations of the probe signals and electromagnetic fields since numerical methods are more flexible to handle general probe-flaw interaction problem. Finite element methods (FEM) tend to be more general but expensive in computational resources due to requirement of discretization of the whole domain of interest. In contrast, integral equation method has attracted more and more attention due to the fact that it only needs discretization of the flaw region in many important cases which means much fewer unknowns are needed and much faster calculations are possible.

Integral equation models of planar and cylindrical structures with flaws has been developed via the volume and boundary element method [18, 19, 20, 21, 22]. However, to the best of our knowledge, most of these models are developed for non-magnetic metals or few details are provided about the key steps in the theory such as dealing with hyper-singularity [23, 21]. So an eddy-current inspection system with better sensitivity of small signal due to small localized defects is demanded. In addition, the demand for an effective 3-D numerical electromagnetic model, which is valid for arbitrary volumetric flaws, ferromagnetic conductors and non-ferromagnetic conductors is increasing. All the equations involved in the numerical 3-D model, such as integral equations, incident field. etc, are also needed to extend to cover ferromagnetic materials.

Another challenge of eddy current inspection that we have addressed is that in a fast reactor environment, the coil position cannot be guided by sonar and optical aids but electromagnetic sensing can be used. In this thesis, we proposed a novel theoretical electromagnetic model of an

eddy current probe used as a position sensor with respect to a tube and plate. This method can also be used to analyze the signal noise caused by unwanted probe tilt encountered in practical eddy current testing.

1.3 Thesis Organization

The dissertation is organized as follows: Chapter 1 mainly introduces the nondestructive evaluation background including fundamental concepts in the eddy-current nondestructive evaluation. In addition, the problems that this thesis concentrates on are also described. Chapter 2 presents the literature review on eddy-current NDE problems and modeling, especially the numerical modeling for probe-flaw interaction problem and the ferromagnetic conductor. Chapter 3 shows the general volume integral equation method formulation for layered-medium, which is valid for both Cartesian coordinate system and cylindrical coordinate system. Then the dyadic kernels for specific coordinate system are described and presented in terms of scalar Green's kernels. Chapter 4 presents the incident fields formulation based on analytical methods. The expressions are presented separately in Cartesian coordinate system and cylindrical coordinate system. Chapter 5 shows the implementation of a volume scheme using the moment method for half-space model and conductive slab model, which are valid for both ferromagnetic and non-ferromagnetic metals. The explicit dyadic Green's kernel formulation is discussed and presented. It also provides simple analytical expressions to deal with the hyper-singularity involved in integral element term evaluation, which avoids the singularity exclusion procedure. We implemented the analytical expressions for singularity in the radar cross-section (RCS) calculation of dielectric sphere in the free space and compared with results obtained based on Mie-series method. Finally, the comparison with existing benchmark experiments are provided and excellent agreement is achieved. Chapter 6 discusses the experimental validation and results of 440 stainless ferromagnetic steel with dedicated designed notch. The comparison between model prediction and test results are presented. Chapter 7 focus on the modeling of the circular air-cored coil with arbitrary orientation with the exist of cylindrical structure. The potential application is the position sensor and analysis of the liftoff and tilt noise due to probe liftoff variation and probe tilt during scan. Chapter 8 focus on the modeling of the circular

air-cored coil with arbitrary orientation with the exist of planar structure, such as half-space conductor, thin conductive slab, etc.

Appendix A presents the reflection and transmission coefficients derivation in both Cartesian coordinate system and cylindrical coordinate system for conductive and ferromagnetic materials. Appendix B shows the impedance changes calculation for the scenario where the probe coil is coaxial with the borehole, tube and rod. Appendix C concludes frequently used mathematical identities and transforms.

CHAPTER 2. LITERATURE REVIEW

The development of eddy current techniques for detecting flaws or cracks in metallic structures has been a topic of research for many years and have found widespread applications in the field of NDE [11]. Similar to other problems in electromagnetics, such as EM scattering problem, eddy current NDE problems can also be solved by a number of methods which includes analytical and semi-analytical methods, approximation methods and numerical methods. Except for a few of special configurations, analytical solutions usually can only be found for unflawed canonical geometries, which are widely used in calculation of the incident field for the probe-flaw interaction modeling [24, 25, 26, 27, 9]. Although semi-analytical solutions are achievable for certain structures with ideal cracks by applying some simplifying approximations, such as TREE method [14, 15] and thin-skin approximation at high frequency [16, 17], it is expedient to seek numerical approximations of the probe signals and electromagnetic fields since numerical methods are more flexible to handle general probe-flaw interaction problem. Finite element methods (FEM) tend to be more general but expensive in computational resources due to requirement of discretization of the whole domain of interest. In contrast, integral equation methods have attracted more and more attention due to the fact that we only need discretization of the flaw region which means much fewer unknowns and faster calculations. It is more efficient because that the dyadic Green's kernels $\mathcal{G}(\mathbf{r}, \mathbf{r}')$ in integral equations automatically account for the boundary conditions at the interfaces of a part.

A brief literature review of forward eddy current NDE problems is presented in this chapter. It mainly covers two important modeling categories, namely the probe field and interaction with flawless structures and the probe-defect interaction. Finally a survey of EC modeling in ferromagnetic material is summarized.

2.1 Modeling of Probe Field and Interaction with Flawless Structures

The analysis of air-cored circular induction coil fields and their interaction with conductive plates and circular rods or the corresponding planar and cylindrical layered systems are studied to serve as the basis for the theory of induced current and its sensor applications. An important motivation for the analysis is to produce formula that are widely available for fast and accurate calculations and which can be easily embedded in codes that predict results for a variety of configurations. At an early stage in these developments, analytical formula were found for the field and impedance of a circular coil whose axis is normal to the surface of a planar plate and a coil coaxial with a circularly cylindrical conductor by Dodd and Deed [9]. The same method was later extended to planar multi-layered structure [28, 29] and cylindrical multi-layered structures [30].

Following these early results, expression have been derived for the field of a circular air-cored coil of rectangular cross section with its axis parallel to the surface of a homogeneous conducting half space by Burke [31]. And the closed-form expression results were also compared with the thin-skin approximation results. The effect of an eddy current bobbin coil probe with its axis parallel to that of a tube has been analyzed by Theodoulidis [32]. Later, the impedance and fields of a rotary coil whose axis is perpendicular to that of a borehole was derived [33]. This work shows the rotary coil might provide more accurate information about crack in the circumferential direction of the borehole compared with conventional bobbin coil. A closed-form expression for an arbitrary tilted coil above a plate was provided for better understanding the noise due to the unexpected tilt of probe in the inspection [34]. Recently a solution for the case of a circular coil whose axis is arbitrary with respect to the axis of a tube or hole has also been derived in terms of spherical coordinate system [24].

The TREE method was widely applied in EC modeling problems to simplify the problem by applying artificial boundary conditions [35, 36]. Using this method, the formulation of the calculation of eddy currents in a cylindrical conductive rod of finite length due to a coaxial circular coil was derived by Bowler [37]. Then the same idea was applied to layered rod [38] and finite length hole [39]. Later the analytical solution in series form for the electromagnetic

field of a cylindrical eddy current probe coil near the open end of a borehole in a conductor was provided accounting for edge effects by using TREE method [40].

The theory of the circular coil interaction with right-angled conductive wedge was proposed by Theodoulidis [15]. By using the TREE method, an alternative solution was provided [41]. This work can give a better understanding of the edge fields and forms the basis for further solutions of edge-related problems containing corner cracks. Later, a closed-form expression for the impedance of a tangential eddy-current coil in the presence of an infinite arbitrary angle conducting wedge was derived [42]. The results of three specific angles, namely quarter-space, 225 degrees and semi-infinite conducting sheet, were presented. Evaluation of the probe field of some complicated air-cored probe, say rectangular-shaped probe [43, 44], elliptical-shaped probe [45, 46], curved rectangular spiral coil [47] and so on, have also been reported. Apart from the air-cored coil, the analytical models of a ferrite-cored coil used as an eddy current probe were also developed [48, 49, 50].

The numerical methods, mainly finite difference, the finite element method (FEM), method of moments and hybrid, are also adopted to evaluate EC solutions [51, 52, 53]. The advantage of the numerical methods are the flexibility to handle any structure regardless of geometrical shape, material inhomogeneity and shape of coil. Finite difference method was the only available numerical method at the early stage of development of numerical methods. Later, FEM and moment method are now the most widely used methods. However FEM is usually expensive in computational resources due to requirement of discretization of the whole domain of interest and moment method requires Greens' functions, which usually are not available for complex structures.

2.2 Modeling of Probe-Flaw Interaction

The probe-flaw interaction problem is much more difficult particularly when it aims to treat arbitrary flaws and cracks. Except for certain simple structures with ideal cracks [54], analytical solutions are not usually accessible. In order to meet the demand of solving the general probe-flaw interaction problem, numerical methods are used. A brief review of analytical method and numerical methods for eddy current probe-flaw modeling are presented in this section.

2.2.1 Analytical and Semi-analytical Methods of Structures with Simplifying Crack

The close-form solution for the crack problem is only available in some cases, such as an infinite long cylinder containing a radial surface crack [54]. However, semi-analytical solutions are accessible for more general structures with ideal cracks by applying some idealized approximations, such as the TREE method, the thin-skin approximation at high frequency and the thick-skin approximation.

By using the TREE method, the interaction between a long coil and a long slot with a rectangular cross section in a conductive plane and was studied by Theodoulidis and Bowler [15]. Similarly, the solution for a rectangular cross-section circular coil above a conductive plate with a coaxial hole was provided [55]. With the thin-skin approximation, namely the assumption that the skin-depth is much smaller than the length and depth of the flaw, the solution of a normal coil over a surface-breaking crack in the conductor was presented by Bowler and Harfield [56, 16, 17]. In the thick-skin approximation, the surface-breaking crack or EDM notches was modeled by a thin ellipsoidal void located at the specimen surface or modeled by using the hydrodynamic flow analogy [11].

2.2.2 Numerical Methods

In recent years, a remarkable expansion of the applications of numerical methods to EC NDE has occurred due to its flexibility to manipulate many complicated structures and flaws rather than the canonical structures that can be dealt with using analytical solution. Two of the most popular numerical approaches today used in the EC NDE field are the FEM and the method of moments (MoM). For example, a computational model of ferrite-cored probe by using MoM based on volume integral equations was proposed by Bowler [57]. In this model, the EM field and impedance of probe is obtained by finding the magnetization of the ferrite core in the presence of homogeneous or even anisotropic layered specimen. The MoM is used to approximate the integral equations and conjugate gradient method is adopted to solve the matrix equations. Due to the requirement of very fine mesh, which means more unknowns, when the skin-depth is very small in the conductor, the finite difference method (FDM) is now

rarely used in the eddy current modeling. In this dissertation, we will focus on the discuss of the FEM and MoM.

2.2.2.1 Finite Element Method

FEM is a numerical technique for solving boundary-value problems for partial differential equations. In the early 1960s, FEM was first used by engineers to approximate solutions of problems in stress analysis, fluid flow and other areas. Compared with MoM, it's subject to less fundamental limitations and is available in several computer tools provided with a versatile graphical user interface (GUI) and comprehensive user manuals [58]. The first attempt to use FEM to solve the eddy current problem date back to 1970s [59]. In the 1980s, intense studies and research was conduced many researchers [60, 61]. The finite element analysis of 3-D eddy current was presented by O.Biro [52]. This work reviews various magnetic and electric potential formulations of eddy current problems and necessary gauging conditions are used to ensure the uniqueness of the solution. A coupled FEM-BEM solution for solving a EC problem was presented by Fetzer [62]. This work shows that representation of the surrounding air with boundary elements could greatly reduce the computational effort.

Similar to FDM, FEM also tends to consume too much computational resource due to a large number of elements needed to discretize the whole solution domain. In order to increase the efficiency of solving the large matrix equations generated by FEM, an efficient technique was proposed by Nakata et al [63].

2.2.2.2 Method of Moments

Method of moments was first introduced into electromagnetic field computations to solve antenna and scattering problems [64]. Like the pulse response used in signal and system analysis, the Green's functions have to be derived first for a specific source and object structure. Although limited to a particular geometry, the advantage of such models is that their computational cost is low and accuracy relatively easy to control. This is because the kernels involved in the method embody the interface conditions of the part geometry, only the flaw region is rendered in discrete form and this region is usually very small, Consequently only a few unknowns

are needed to compute the source density via the moment method which results in very fast calculations [65]. The disadvantage of the approach, at present, is that it can only be used for canonical structures for which it is relatively simple to obtain the analytical expression of the Green's function. However, from modeling point of view, many practical EC NDE problems can be represented as simple structure models, such as planar-layered structure, whose Green's function is available. Furthermore, even if the structure is complicated, the Green's function can also be obtained via numerical method saved as value table.

In tackling the problem using an MoM, the formulation could be expressed as either a surface or volume integral and its corresponding methods are the boundary element method (BEM) and the volume boundary element method (VEM).

BEM was proposed to solve a 2-D eddy current problem by Rucker et al [66]. Later, surface integral equations were developed for EM fields on the surface of a 3-D flaw in a conducting medium for EC NDE application by Beissner [67]. By using BEM, a matrix equation for tangential current density and magnetic field vectors on the flaw surface was obtained. The eddy current field on the 3-D rectangular slot was calculated and presented. The eddy current interaction with an general ideal crack having a negligible opening and acting as a barrier to electric current was studied via the boundary integral formulation by Bowler [68]. Based on this rapid numerical procedure, a inverse problem for reconstructing the flaw shape and size might be possible. The impedance boundary condition was adopted to do the eddy current analysis by Ishibashi [69]. In order to increase the efficiency, the fast multipole method was introduced to BEM in 2-D EC problem by Song [70].

VEM is also an efficient way to deal with a surface-breaking crack problem [71] but also the problem of an embedded flaw in the conductor [72]. The volume integral method has been used in geophysics applications by Weidelt [73] and was applied to EC problem by Dunbar [74, 75]. The correlation between the model prediction and experiment was of poor quality due to numerical problem encountered in evaluation of unperturbed field and singularities. These problems were then overcome by McKirdy [76] by calculating the singular integral more accurately and using Hankel transform to get the incident field. The conjugate gradient method was incorporated to solve the matrix equation based on VIE by Bowler [57]. The volume integral

equation method was also adopted to analyze 3-D nonlinear eddy current problems in induction heating [77]. A new discretization schemes based on non-uniform B-splines was proposed for solving EC problem via VIE by Dular [78]. Recently, the eddy current calculations on a right-angled corner cracks was solved efficiently by using VEM and an approximate Greens function for a conductive quarter-space by Bowler [14]. Also, the eddy current probe due to cracks in fastener holes was studied by using both BEM and VEM [19].

Green's function is a key part for the MoM and many derivation of Green's functions were done for specific structures. The Green's function of the half-space conductor was derived by Bowler [79] and the corresponding time domain dyadic version was also provided in 1999 [80]. These Green's functions were also used in the implementation of MoM for half-space conductor [22] and the numerical implementation details were studied [81]. Later, the Green's function for a plate was sought by Bowler [82] and that due to alternative current was also provided [83]. The Green's kernel for a long tube was derived by Barlow [84]. In order to increase the efficiency of evaluation of Green's function, an efficient method to calculate dyadic Green's function of an eddy current field in a conducting plate was proposed by Xing [85].

2.3 Modeling of the Ferromagnetic Conductors

Modeling of flaws in ferromagnetic conductors has been developed by using FEM or integral equation methods. For example, the overlapping FEM was implemented for EC problem of ferromagnetic media to take into account of skin effect [86]. This section will mainly present a review related to the integral equation method.

Integral equation models of planar and cylindrical structures with flaws has been developed using the volume and boundary element method [18, 19, 20, 21, 22]. However, to the best of our knowledge, most of these models are developed for non-magnetic metals. The reasons might be the high burden of the calculation of the dyadic Green's kernels and the challenge of experiments. It is, however, of general interest to develop a model which can account for effects of both permeability changes and conductivity changes.

The theory of circular eddy current probe interactions with long surface cracks in ferromagnetic steel was developed by Harfield and Bowler [87, 88]. In this work, the thin-skin

approximation was used and the crack was assumed to be infinite long. EM fields on the crack faces were described in terms of a potential which satisfies a 2-D Laplace equation. A numerical model based on a nonlinear integral equation for EC problem was proposed to simulate the EM field in ferromagnetic steel parts by Ioan [23]. The edge element and vectorial volume elements were involved in the discretization. However, few details are provided about the key steps such as dealing with hyper-singularity.

A VIE formulation for ferromagnetic tube structures with volumetric defects was developed by Skarlatos et al [21]. According to the volume equivalence theorem [89], flaws was represented in effect as equivalent electric and magnetic dipole distributions that depends on the total field in the flaw region. The dyadic Green's functions of multi-layered cylindrical structures were also presented by using the derivation by Chew [90]. Some numerical implementation issues such as the precondition of matrix equation were also discussed. But few details are provided about dealing with hyper-singularity. The comparison between theoretical results and experimental results were presented and discussed. The agreement between theoretical prediction and test data was not good and part of the reason might be that it's difficult to get good experiment data due to local variations of the magnetic permeability in the region of the flaw and the effect of heating or mechanical tension during manufacture.

CHAPTER 3. VOLUME INTEGRAL EQUATION AND FORMULATIONS

3.1 Electromagnetic Fundamentals

The well-known Maxwells equations in differential form are expressed as follow

$$\nabla \times \mathbf{E}(\mathbf{r}, t) = -\frac{\partial \mathbf{B}(\mathbf{r}, t)}{\partial t} - \mathbf{M}(\mathbf{r}, t) \quad (3.1)$$

$$\nabla \times \mathbf{H}(\mathbf{r}, t) = \frac{\partial \mathbf{D}(\mathbf{r}, t)}{\partial t} + \mathbf{J}(\mathbf{r}, t) \quad (3.2)$$

$$\nabla \cdot \mathbf{B}(\mathbf{r}, t) = \rho_m(\mathbf{r}, t) \quad (3.3)$$

$$\nabla \cdot \mathbf{D}(\mathbf{r}, t) = \rho_e(\mathbf{r}, t) \quad (3.4)$$

All these quantities here are assumed to be time-varying, and each is a function of the space coordinates and time. \mathbf{E} , \mathbf{H} are the electrical and magnetic field intensity. \mathbf{D} and \mathbf{B} are the electrical and magnetic flux density. ρ_e and ρ_m are the electric and magnetic charge density. \mathbf{J} and \mathbf{M} are the electric and magnetic current density. Maxwell's equations are the fundamentals of modern wireless communication, RF/Microwave components and circuit design [91]. Unlike the integral-form Maxwells equations which are valid everywhere, the differential Maxwells equations describe field behavior at a point in a continuous medium [92]. As the frequency is relative low (usually less than 10MHz) in eddy-current applications, the displacement current is very small so that it can be ignored and this approximation is called quasi-static approximation.

We analyze the time-harmonic fields and can, if needed, determine the transient field using the Fourier transform, (3.5) . By using the Fourier Transform, the time-varying Maxwell's equations can be written as the followings in the frequency domain [92]

$$\mathbf{F}(\mathbf{r}, t) = \frac{1}{2\pi} \int_{-\infty}^{\infty} \tilde{\mathbf{F}}(\mathbf{r}, \omega) e^{-i\omega t} d\omega \quad (3.5)$$

$$\nabla \times \mathbf{E}(\mathbf{r}, \omega) = i\omega\mathbf{B}(\mathbf{r}, \omega) - \mathbf{M}(\mathbf{r}, \omega) \quad (3.6)$$

$$\nabla \times \mathbf{H}(\mathbf{r}, \omega) = -i\omega\mathbf{D}(\mathbf{r}, \omega) + \mathbf{J}(\mathbf{r}, \omega) \quad (3.7)$$

$$\nabla \cdot \mathbf{D}(\mathbf{r}, \omega) = \rho_e(\mathbf{r}, \omega) \quad (3.8)$$

$$\nabla \cdot \mathbf{B}(\mathbf{r}, \omega) = \rho_m(\mathbf{r}, \omega) \quad (3.9)$$

A medium usually has a significant effect on EM fields and affects it through three phenomena, namely electric polarization, magnetization and electric conduction. In order to include these effects for linear materials, the constitutive relations are introduced shown as follow

$$\mathbf{D} = \bar{\epsilon}\mathbf{E} \quad (3.10)$$

$$\mathbf{B} = \bar{\mu}\mathbf{H} \quad (3.11)$$

$$\mathbf{J} = \bar{\sigma}\mathbf{E} \quad (3.12)$$

where $\bar{\epsilon}$, $\bar{\mu}$ and $\bar{\sigma}$ are expressed in tensor form. If the medium is isotropic, the material properties will be expressed in scalar form. Based on whether the medium is dispersive and/or inhomogeneous, materials properties can be functions of frequency and position.

The differential form of Maxwell's equations are valid at any point in a continuous medium but not at the interfaces between different media. The remedy to it is to get the boundary conditions which describes the relations between the fields on the two sides of an interface based on integral form Maxwell's equations.

$$[\mathbf{B}_n] = \rho_{ms} \quad (3.13)$$

$$[\mathbf{D}_n] = \rho_{es} \quad (3.14)$$

$$[\mathbf{H}_t] = \mathbf{J}_s \quad (3.15)$$

$$[\mathbf{E}_t] = \mathbf{M}_s \quad (3.16)$$

Note that the notation $[\cdot]$ stands for the jump of the quantity at the interface. The subscript n means the surface normal component and t means the surface tangential component. ρ_{ms} , ρ_{es} , \mathbf{J}_s and \mathbf{M}_s are the surface magnetic charge density, electric charge density, surface current

density and magnetic current density. For eddy-current case, the conductivity of conductor are finite, the \mathbf{J}_s vanishes. Up to now, ρ_{ms} and \mathbf{M}_s are not found so they can also be set as zero.

Based on the Maxwell's equations and mathematical manipulations, we can derive some important theorems that reveal certain important properties of electromagnetic fields. The uniqueness theorem, which establishes the conditions for a unique solution of Maxwell's equations, and the reciprocity theorem, which establishes a relation between two solutions due to two different sources, are the most important two theorems. Since these two theorems and some other theorems such as equivalence theorem, image theory are thoroughly discussed in many literature and books [89, 90, 92, 93, 94, 95, 96, 97], we will not discuss these in this dissertation.

3.1.1 Understanding of Skin Depth δ

We know the plane wave with a constant amplitude A can be expressed in the form $Ae^{i\mathbf{k}\cdot\mathbf{r}}$. \mathbf{k} is the wave number with magnitude k . In the highly conductive medium, we have

$$k \approx \sqrt{i\omega\mu_0\sigma_0} = i(\alpha - i\beta) \quad (3.17)$$

where α accounts for the attenuation and β accounts for the phase changing. μ_0 is the permeability of medium and σ_0 is medium conductivity. Then we have

$$\alpha = \beta = \sqrt{\pi f\mu_0\sigma_0} \quad (3.18)$$

The skin depth is defined as

$$\delta = \frac{1}{\alpha} = \frac{1}{\sqrt{\pi f\mu_0\sigma_0}} \quad (3.19)$$

If the wave is propagating in z direction, we obtain

$$e^{i\mathbf{k}\cdot\mathbf{r}} = e^{-\alpha z} e^{i\beta z} = e^{-\frac{1}{\delta}z} e^{i\frac{1}{\delta}z} \quad (3.20)$$

In the MoM calculation for the free space or good dielectric case, 10-12 unknowns per wavelength are usually enough for reasonable accuracy. However, for eddy current problem, we prefer to use the metric based on skin depth δ due to the high attenuation in lossy conductor.

In lossless medium problem, the phase shift is 2π per wavelength. In the conductive region, the phase shift is 1 rad per δ . Hence we can estimate about 2 unknowns for one rad or δ .

$$\frac{10 \sim 12}{2\pi} \approx 2 \quad (3.21)$$

which implies 2 unknowns per skin depth is usually enough for eddy-current numerical calculation.

3.2 Dyadic Green's Function

Before we introduce the concept of dyadic green functions, we would like to review Maxwell's equations in a dyadic form first[96]. The medium under consideration is assumed to be linear, isotropic and homogeneous media with the permeability μ , conductivity σ and permittivity ϵ .

A vector function or a vector quantity in coordinate system is defined as

$$\mathbf{F} = \sum_{i=1}^3 F_i \hat{x}_i \quad (3.22)$$

where $\hat{x}_i, i = 1, 2, 3$ denotes the unit normal vectors of specific coordinate system, such as $\hat{x}, \hat{y}, \hat{z}$ of Cartesian coordinate system and $\hat{\rho}, \hat{\phi}, \hat{z}$ of cylindrical coordinate system. F_i is the corresponding components in the coordinate system. From now on, the summation index always runs from 1 to 3 unless specified otherwise. The number 3 above the summation symbol can be eliminated like

$$\mathbf{F} = \sum_{i=1} F_i \hat{x}_i \quad (3.23)$$

Now we consider three distinct vector functions denoted as

$$\mathbf{F}_j = \sum_i F_{ij} \hat{x}_i, j = 1, 2, 3 \quad (3.24)$$

Then a dyadic function or a dyad, denoted by $\bar{\mathbf{F}}$, can be expressed as

$$\bar{\mathbf{F}} = \sum_j \mathbf{F}_j \hat{x}_j = \sum_i \sum_j F_{ij} \hat{x}_i \hat{x}_j = \begin{bmatrix} F_{11} & F_{12} & F_{13} \\ F_{21} & F_{22} & F_{23} \\ F_{31} & F_{32} & F_{33} \end{bmatrix} \quad (3.25)$$

by juxtaposing three vectors. Note that the order of \mathbf{F}_j and \hat{x}_j must be kept. \mathbf{F}_j are the vector components of dyadic $\bar{\mathbf{F}}$. The order of $\hat{x}_i \hat{x}_j$ are usually not commutative except for the case with $i = j$.

3.2.1 Dyadic Green Functions with Electric Source

We assume there are three sets of harmonically fields with same frequency and in the same environment which are produced by three distinct electric current distributions \mathbf{J}_j with $j = 1, 2, 3$.

$$\nabla \times \mathbf{E}_j = i\omega\mu\mathbf{H}_j \quad (3.26)$$

$$\nabla \times \mathbf{H}_j = \mathbf{J}_j - i\omega\varepsilon\mathbf{E}_j \quad (3.27)$$

$$\nabla \cdot \mathbf{D}_j = \rho_{e,j} \quad (3.28)$$

$$\nabla \cdot \mathbf{B}_j = 0 \quad (3.29)$$

We put all three sets of Maxwell's equations together and replace the quantities by dyadic form. Then all equations are transferred into dyadic forms as follow

$$\nabla \times \bar{\mathbf{E}} = i\omega\mu\bar{\mathbf{H}} \quad (3.30)$$

$$\nabla \times \bar{\mathbf{H}} = \bar{\mathbf{J}} - i\omega\varepsilon\bar{\mathbf{E}} \quad (3.31)$$

$$\nabla \cdot \bar{\mathbf{D}} = \rho_e \quad (3.32)$$

$$\nabla \cdot \bar{\mathbf{B}} = 0 \quad (3.33)$$

Similarly, we get the continuous condition in dyadic form as follow

$$\nabla \cdot \bar{\mathbf{J}} = i\omega\rho_e \quad (3.34)$$

Let us now consider three current distributions with amplitude c_j

$$\mathbf{J}_j = c_j\delta(\mathbf{r} - \mathbf{r}')\hat{x}_j \quad (3.35)$$

which satisfies $\iiint \mathbf{J}_j dv = c_j\hat{x}_j$. Here we normalize the current moment by applying $i\omega\mu c_j = 1$.

$$i\omega\mu\bar{\mathbf{J}} = \mathcal{I}\delta(\mathbf{r} - \mathbf{r}') \quad (3.36)$$

By using continuous equation and dyadic identity $\nabla \cdot (\mathcal{I}f) = \nabla f$, we obtain

$$\rho_e = \frac{1}{i\omega}\nabla \cdot \bar{\mathbf{J}} = \frac{-1}{\omega^2\mu}\nabla \cdot (\mathcal{I}\delta(\mathbf{r} - \mathbf{r}')) = \frac{-1}{\omega^2\mu}\nabla\delta(\mathbf{r} - \mathbf{r}') \quad (3.37)$$

where \mathcal{I} is unit dyad. Here we define the dyadic Green's kernels by doing the following replacement [96]

$$\bar{\mathbf{E}} = \mathcal{G}_{ee} \quad (3.38)$$

$$i\omega\mu\bar{\mathbf{H}} = \mathcal{G}_{me} \quad (3.39)$$

where \mathcal{G}_{ee} and \mathcal{G}_{me} are the dyadic Green's functions. The first letter of subscript stands for the field quantities and the second one indicates the source kind. For example, \mathcal{G}_{ee} indicates the electric field due to electric source. The dyadic Maxwell's equations are rewritten as

$$\nabla \times \mathcal{G}_{ee} = \mathcal{G}_{me} \quad (3.40)$$

$$\nabla \times \mathcal{G}_{me} = \mathcal{I}\delta(\mathbf{r} - \mathbf{r}') + k^2\mathcal{G}_{ee} \quad (3.41)$$

$$\nabla \cdot \mathcal{G}_{ee} = \frac{-1}{k^2}\nabla\delta(\mathbf{r} - \mathbf{r}') \quad (3.42)$$

$$\nabla \cdot \mathcal{G}_{me} = 0 \quad (3.43)$$

Eliminating the \mathcal{G}_{me} , we get

$$\nabla \times \nabla \times \mathcal{G}_{ee}(\mathbf{r}, \mathbf{r}') - k^2\mathcal{G}_{ee}(\mathbf{r}, \mathbf{r}') = \mathcal{I}\delta(\mathbf{r} - \mathbf{r}') \quad (3.44)$$

Similarly, we have

$$\nabla \times \nabla \times \mathcal{G}_{me} - k^2\mathcal{G}_{me} = \nabla\delta(\mathbf{r} - \mathbf{r}') \times \mathcal{I} \quad (3.45)$$

by eliminating the \mathcal{G}_{ee} , where $k^2 = \omega^2\mu\varepsilon$. For quasi-static case $k^2 = i\omega\mu\sigma$, which is widely used in eddy-current nondestructive evaluation area. Note that we can also get \mathcal{G}_{me} by using

$$\nabla \times \mathcal{G}_{ee} = \mathcal{G}_{me} \quad (3.46)$$

For unbounded domain, we get

$$\mathcal{G}_{ee} = \left(\mathcal{I} + \frac{1}{k^2}\nabla\nabla \right) G_0(\mathbf{r} - \mathbf{r}') \quad (3.47)$$

$$\mathcal{G}_{me} = \nabla \times \mathcal{G}_{ee} = \nabla G_0 \times \mathcal{I} \quad (3.48)$$

where G_0 is the free space Green's function which satisfies

$$(\nabla^2 + k^2)G_0 = -\delta(\mathbf{r} - \mathbf{r}') \quad (3.49)$$

Note that the identity $\nabla \times \nabla \mathbf{F} = 0$ is applied in the derivation.

3.2.2 Dyadic Green Functions with Magnetic Source

Similarly, we assume there are three sets of harmonically fields with same frequency and in the same environment which are produced by three distinct magnetic current distributions \mathbf{M}_j with $j = 1, 2, 3$. we get the dyadic form Maxwell's equation as

$$\nabla \times \bar{\mathbf{E}} = i\omega\mu\bar{\mathbf{H}} - \bar{\mathbf{M}} \quad (3.50)$$

$$\nabla \times \bar{\mathbf{H}} = -i\omega\varepsilon\bar{\mathbf{E}} \quad (3.51)$$

$$\nabla \cdot \bar{\mathbf{D}} = 0 \quad (3.52)$$

$$\nabla \cdot \bar{\mathbf{B}} = \rho_m \quad (3.53)$$

and the continuous condition in dyadic form as

$$\nabla \cdot \bar{\mathbf{M}} = i\omega\rho_m. \quad (3.54)$$

Let us now consider three current distributions $\mathbf{M}_j = c_j\delta(\mathbf{r} - \mathbf{r}')\hat{x}_j$ with amplitude c_j . We normalize the current moment with $i\omega\varepsilon c_j = 1$. Then we have

$$\bar{\mathbf{M}} = \frac{\mathcal{I}\delta(\mathbf{r} - \mathbf{r}')}{i\omega\varepsilon} \quad (3.55)$$

$$\rho_m = \frac{1}{i\omega}\nabla \cdot \bar{\mathbf{M}} = \frac{-1}{\omega^2\varepsilon}\nabla \cdot (\mathcal{I}\delta(\mathbf{r} - \mathbf{r}')) = \frac{-\mu}{k^2}\nabla\delta(\mathbf{r} - \mathbf{r}') \quad (3.56)$$

By applying replacement with

$$-i\omega\varepsilon\bar{\mathbf{E}} = \mathcal{G}_{em} \quad (3.57)$$

$$\bar{\mathbf{H}} = \mathcal{G}_{mm} \quad (3.58)$$

we obtain

$$\nabla \times \mathcal{G}_{em} = k^2\mathcal{G}_{mm} + \mathcal{I}\delta(\mathbf{r} - \mathbf{r}') \quad (3.59)$$

$$\nabla \times \mathcal{G}_{mm} = \mathcal{G}_{em} \quad (3.60)$$

$$\nabla \cdot \mathcal{G}_{em} = 0 \quad (3.61)$$

$$\nabla \cdot \mathcal{G}_{mm} = \frac{-1}{k^2}\nabla\delta(\mathbf{r} - \mathbf{r}') \quad (3.62)$$

where \mathcal{G}_{em} and \mathcal{G}_{mm} are the dyadic Green's functions due to magnetic source. By eliminating the \mathcal{G}_{em} or \mathcal{G}_{mm} , we have

$$\nabla \times \nabla \times \mathcal{G}_{mm}(\mathbf{r}, \mathbf{r}') - k^2 \mathcal{G}_{mm}(\mathbf{r}, \mathbf{r}') = \mathcal{I} \delta(\mathbf{r} - \mathbf{r}') \quad (3.63)$$

$$\nabla \times \nabla \times \mathcal{G}_{em} - k^2 \mathcal{G}_{em} = \nabla \delta(\mathbf{r} - \mathbf{r}') \times \mathcal{I} \quad (3.64)$$

We also can get \mathcal{G}_{em} by $\nabla \times \mathcal{G}_{mm} = \mathcal{G}_{em}$

For unbounded domain, we have

$$\mathcal{G}_{mm} = \left(\mathcal{I} + \frac{1}{k^2} \nabla \nabla \right) G_0(\mathbf{r} - \mathbf{r}') \quad (3.65)$$

$$\mathcal{G}_{em} = \nabla G_0 \times \mathcal{I} \quad (3.66)$$

3.3 Volume Integral Equation for a Layered Medium with a Flaw

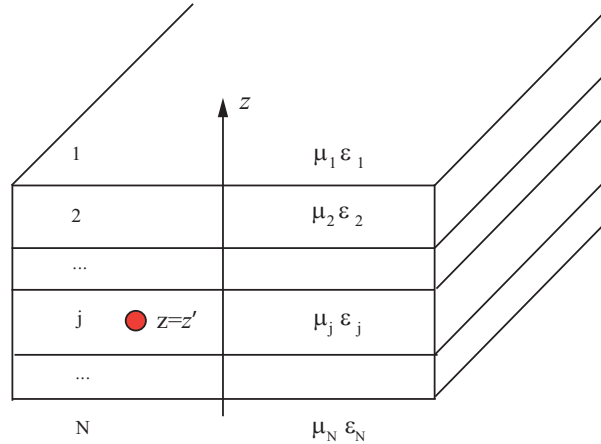


Figure 3.1: Planarly multilayered medium with flaws in layer j

We consider a planarly layered medium consisting of finite number linear, isotropic and homogeneous layers Fig. 3.1. μ_i and ϵ_i are the magnetic permeability and permittivity of the layer i medium. An external source (for example eddy-current coil in EC NDE) carrying a time-harmonic current varying as the real part of $Ie^{-i\omega t}$ is used to detect the flaw in layer j . The flaw is finite support and fully contained in layer j with local $\mu(\mathbf{r})$ and $\epsilon(\mathbf{r})$ variation. In accordance with the volume equivalent theorem [89], one defines equivalent electric and

magnetic dipole densities as equivalent magnetic current source and electric current source as follows.

$$\mathbf{M} = -i\omega[\mu(\mathbf{r}) - \mu_j]\mathbf{H} \quad (3.67)$$

$$\mathbf{J} = -i\omega[\varepsilon(\mathbf{r}) - \varepsilon_j]\mathbf{E} \quad (3.68)$$

where μ_j and ε_j are the host permeability and permittivity of the layer j medium where flaw lies in. Based on classical scattering theory, the total field can be separated into two parts, namely the incident field caused by out-impressed sources without flaw and the scattering field caused by the equivalent \mathbf{M} and/or \mathbf{J} due to flaw as

$$\mathbf{E} = \mathbf{E}^0 + \mathbf{E}^s \quad (3.69)$$

$$\mathbf{H} = \mathbf{H}^0 + \mathbf{H}^s \quad (3.70)$$

where the subscript ⁰ denotes the incident field and the subscript ^s denotes the scattering field or perturbed field. The scattered fields will satisfy the following equations in the layer i

$$\nabla \times \mathbf{E}^s = i\omega\mu_i\mathbf{H}^s - \mathbf{M} \quad (3.71)$$

$$\nabla \times \mathbf{H}^s = -i\omega\varepsilon_i\mathbf{E}^s + \mathbf{J} \quad (3.72)$$

Both are only non-zero in the flaw region. By taking a curl on the above equations, we have in the layer i

$$\nabla \times \nabla \times \mathbf{E}^s - k_i^2\mathbf{E}^s = i\omega\mu_i\mathbf{J} - \nabla \times \mathbf{M} \quad (3.73)$$

$$\nabla \times \nabla \times \mathbf{H}^s - k_i^2\mathbf{H}^s = i\omega\varepsilon_i\mathbf{M} + \nabla \times \mathbf{J} \quad (3.74)$$

where $k_i^2 = \omega^2\mu_i\varepsilon_i$. By applying Green's second theorem to the (3.73), (3.74) and imposing boundary conditions of electric and magnetic fields at the interfaces and radiation condition at infinity [96, 21], the total electric field and magnetic field can be expressed as volume integral equations in terms of dyadic Green's functions

$$\begin{aligned} \mathbf{E}^s &= i\omega\mu_j \int_{V_f} \mathcal{G}_{ee}^{ij}(\mathbf{r}, \mathbf{r}') \cdot \mathbf{J}(\mathbf{r}') dv' - \frac{\varepsilon_j}{\varepsilon_i} \int_{V_f} \mathcal{G}_{em}^{ij}(\mathbf{r}, \mathbf{r}') \cdot \mathbf{M}(\mathbf{r}') dv' \\ &= \omega^2\mu_j \int_{V_f} \mathcal{G}_{ee}^{ij}(\mathbf{r}, \mathbf{r}') \cdot [\varepsilon(\mathbf{r}) - \varepsilon_j]\mathbf{E}_j(\mathbf{r}') dv' + i\omega \frac{\varepsilon_j}{\varepsilon_i} \int_{V_f} \mathcal{G}_{em}^{ij}(\mathbf{r}, \mathbf{r}') \cdot [\mu(\mathbf{r}) - \mu_j]\mathbf{H}_j(\mathbf{r}') dv' \end{aligned} \quad (3.75)$$

$$\begin{aligned}
\mathbf{H}^s &= i\omega\varepsilon_j \int_{V_f} \mathcal{G}_{mm}^{ij}(\mathbf{r}, \mathbf{r}') \cdot \mathbf{M}(\mathbf{r}') dv' + \frac{\mu_j}{\mu_i} \int_{V_f} \mathcal{G}_{me}^{ij}(\mathbf{r}, \mathbf{r}') \cdot \mathbf{J}(\mathbf{r}') dv' \\
&= \omega^2\varepsilon_j \int_{V_f} \mathcal{G}_{mm}^{ij}(\mathbf{r}, \mathbf{r}') \cdot [\mu(\mathbf{r}') - \mu_j] \mathbf{H}_j(\mathbf{r}') dv' - i\omega \frac{\mu_j}{\mu_i} \int_{V_f} \mathcal{G}_{me}^{ij}(\mathbf{r}, \mathbf{r}') \cdot [\varepsilon(\mathbf{r}') - \varepsilon_j] \mathbf{E}_j(\mathbf{r}') dv'
\end{aligned} \tag{3.76}$$

The superscript ij of \mathcal{G} indicates the field in layer i due to a source in layer j . V_f denotes the flaw region where the integration is performed. Note that the following reciprocity relationships of dyadic Green's functions [96] are used in the derivation.

$$\frac{1}{\mu_i} \mathcal{G}_{ee}^{ij}(\mathbf{r}, \mathbf{r}') = \frac{1}{\mu_j} [\mathcal{G}_{ee}^{ji}(\mathbf{r}', \mathbf{r})]^T \tag{3.77}$$

$$\frac{1}{\varepsilon_i} \mathcal{G}_{mm}^{ij}(\mathbf{r}, \mathbf{r}') = \frac{1}{\varepsilon_j} [\mathcal{G}_{mm}^{ji}(\mathbf{r}', \mathbf{r})]^T \tag{3.78}$$

where the superscript T denotes the transpose of matrix.

The dyadic kernels satisfy

$$\nabla \times \mathcal{G}_{ee}^{ij} = \mathcal{G}_{me}^{ij} \tag{3.79}$$

$$\nabla \times \mathcal{G}_{me}^{ij} = k_i^2 \mathcal{G}_{ee}^{ij} + \delta_{ij} \mathcal{I} \delta(\mathbf{r} - \mathbf{r}') \tag{3.80}$$

for the electric current source.

$$\nabla \times \mathcal{G}_{mm}^{ij} = \mathcal{G}_{em}^{ij} \tag{3.81}$$

$$\nabla \times \mathcal{G}_{em}^{ij} = k_i^2 \mathcal{G}_{mm}^{ij} + \delta_{ij} \mathcal{I} \delta(\mathbf{r} - \mathbf{r}') \tag{3.82}$$

for the magnetic current source.

$$\nabla \times \nabla \times \mathcal{G}_{ee}^{ij}(\mathbf{r}, \mathbf{r}') - k_i^2 \mathcal{G}_{ee}^{ij}(\mathbf{r}, \mathbf{r}') = \delta_{ij} \mathcal{I} \delta(\mathbf{r} - \mathbf{r}') \tag{3.83}$$

$$\nabla \times \nabla \times \mathcal{G}_{me}^{ij} - k_i^2 \mathcal{G}_{me}^{ij} = \delta_{ij} \nabla \delta(\mathbf{r} - \mathbf{r}') \times \mathcal{I} \tag{3.84}$$

$\delta_{ij} = 1$ only when $i = j$, otherwise it's vanished.

In order to apply the MoM, we always set the observation point and source point in the same layer, here is the flaw region V_f . Then $i = j$ will be applied. For simplicity, we will drop the layer index.

$$\begin{aligned}
\mathbf{E}^s &= i\omega\mu_h \int_{V_f} \mathcal{G}_{ee}(\mathbf{r}, \mathbf{r}') \cdot \mathbf{J}(\mathbf{r}') dv' - \int_{V_f} \mathcal{G}_{em}(\mathbf{r}, \mathbf{r}') \cdot \mathbf{M}(\mathbf{r}') dv' \\
&= \omega^2\mu_h \int_{V_f} \mathcal{G}_{ee}(\mathbf{r}, \mathbf{r}') \cdot [\varepsilon(\mathbf{r}') - \varepsilon_h] \mathbf{E}(\mathbf{r}') dv' + i\omega \int_{V_f} \mathcal{G}_{em}(\mathbf{r}, \mathbf{r}') \cdot [\mu(\mathbf{r}') - \mu_h] \mathbf{H}(\mathbf{r}') dv'
\end{aligned} \tag{3.85}$$

$$\begin{aligned}
\mathbf{H}^s &= i\omega\epsilon_h \int_{V_f} \mathcal{G}_{mm}(\mathbf{r}, \mathbf{r}') \cdot \mathbf{M}(\mathbf{r}') dv' + \int_{V_f} \mathcal{G}_{me}(\mathbf{r}, \mathbf{r}') \cdot \mathbf{J}(\mathbf{r}') dv' \\
&= \omega^2\epsilon_h \int_{V_f} \mathcal{G}_{mm}(\mathbf{r}, \mathbf{r}') \cdot [\mu(\mathbf{r}') - \mu_h] \mathbf{H}(\mathbf{r}') dv' - i\omega \int_{V_f} \mathcal{G}_{me}(\mathbf{r}, \mathbf{r}') \cdot [\epsilon(\mathbf{r}') - \epsilon_h] \mathbf{E}(\mathbf{r}') dv'
\end{aligned} \tag{3.86}$$

where μ_h and ϵ_h are the permeability and permittivity of the flaw host layer j . Note that both Eq.(3.85) and Eq.(3.86) are coupled by Maxwell's equations. Hence it's possible to express the electric field in terms of magnetic field so as to reduce the unknown and decouple the integral equations. By using Maxwell's equation within flaw region, we know the electric field and magnetic field will satisfy the following relationship

$$\nabla \times \mathbf{E} = i\omega\mu(\mathbf{r})\mathbf{H} \tag{3.87}$$

Then we can rewrite Eq 3.67 and 3.68

$$\mathbf{M} = -\frac{\mu(\mathbf{r}) - \mu_h}{\mu(\mathbf{r})} \nabla \times \mathbf{E} = \frac{\mu(\mathbf{r}) - \mu_h}{i\omega\mu(\mathbf{r})} \nabla \times \frac{\mathbf{J}}{\epsilon(\mathbf{r}) - \epsilon_h} \tag{3.88}$$

$$\mathbf{J} = -i\omega[\epsilon(\mathbf{r}) - \epsilon_h]\mathbf{E} \tag{3.89}$$

Then the coupled integral equations become decoupled shown as follow

$$\mathbf{E}^s = \omega^2\mu_h \int_{V_f} \mathcal{G}_{ee}(\mathbf{r}, \mathbf{r}') \cdot [\epsilon(\mathbf{r}') - \epsilon_h] \mathbf{E}(\mathbf{r}') dv' + \int_{V_f} \frac{\mu(\mathbf{r}') - \mu_h}{\mu(\mathbf{r}')} \mathcal{G}_{em}(\mathbf{r}, \mathbf{r}') \cdot \nabla' \times \mathbf{E}(\mathbf{r}') dv' \tag{3.90}$$

By using integration by parts

$$\int_V \mathbf{A} \cdot \nabla \times \mathcal{B} dv = \int_V \mathcal{B}^T \cdot \nabla \times \mathbf{A} dv = \int_V \nabla \times \mathbf{A} \cdot \mathcal{B} dv \tag{3.91}$$

where \mathcal{B} is a dyad. The $\nabla' \times$ in the second term can be moved to the dyadic kernel. Then the basis function of \mathbf{E} doesn't need to be high order. Besides, the required unknowns can be half due to that two coupled integral equations reduce to one. The similar idea has been implemented for free space via surface integral equations [98].

3.3.1 Volume Integral Equation for Eddy-current Application in the Quasi-static Limit

For the eddy current application, the working frequency is usually relatively low (usually < 10 MHz), the displacement current is always negligible compared with the conductive current.

Hence the quasi-static approximation is applied by using $-i\omega\varepsilon \Rightarrow \sigma$. Then we rewrite the equivalent source as

$$\mathbf{M} = [\mu(\mathbf{r}) - \mu_h]\mathbf{H} \quad (3.92)$$

$$\mathbf{P} = [\sigma(\mathbf{r}) - \sigma_h]\mathbf{E}$$

μ_h and σ_h are the host permeability and conductivity of the layer j medium where flaw lies in. The Faraday's law, Ampere law and vector wave equations are modified as

$$\nabla \times \mathbf{E}(\mathbf{r}) = i\omega [\mu_h \mathbf{H}(\mathbf{r}) + \mathbf{M}(\mathbf{r})] \quad (3.93)$$

$$\nabla \times \mathbf{H}(\mathbf{r}) = \sigma_h \mathbf{E}(\mathbf{r}) + \mathbf{P}(\mathbf{r}) \quad (3.94)$$

$$\nabla \times \nabla \times \mathbf{E} - k_h^2 \mathbf{E} = i\omega [\mu_h \mathbf{P} + \nabla \times \mathbf{M}] \quad (3.95)$$

$$\nabla \times \nabla \times \mathbf{H} - k_h^2 \mathbf{H} = \nabla \times \mathbf{P} + i\omega \sigma_h \mathbf{M} \quad (3.96)$$

Meanwhile, the volume integral equations become

$$\mathbf{E} = \mathbf{E}^0 + i\omega \mu_h \int_{V_f} \mathcal{G}_{ee}(\mathbf{r}, \mathbf{r}') \cdot \mathbf{P}(\mathbf{r}') dv' + i\omega \int_{V_f} \mathcal{G}_{em}(\mathbf{r}, \mathbf{r}') \cdot \mathbf{M}(\mathbf{r}') dv' \quad (3.97)$$

$$\mathbf{H} = \mathbf{H}^0 + \int_{V_f} \mathcal{G}_{me}(\mathbf{r}, \mathbf{r}') \cdot \mathbf{P}(\mathbf{r}') dv' + i\omega \sigma_h \int_{V_f} \mathcal{G}_{mm}(\mathbf{r}, \mathbf{r}') \cdot \mathbf{M}(\mathbf{r}') dv' \quad (3.98)$$

In order to apply MoM, the above integral equations can be transformed into an equation only in terms of the electric current density \mathbf{P} and magnetic density \mathbf{M} directly by defining the coefficients

$$v_E(\mathbf{r}) = \frac{\sigma(\mathbf{r}) - \sigma_h}{\sigma_h} \quad (3.99)$$

$$v_H(\mathbf{r}) = \frac{\mu(\mathbf{r}) - \mu_h}{\mu_h} \quad (3.100)$$

and multiplying them individually to Eq. (3.97) and (3.98). Then we obtain

$$\mathbf{P} = \mathbf{P}^0 + k_h^2 v_E(\mathbf{r}) \int_{V_f} \mathcal{G}_{ee}(\mathbf{r}, \mathbf{r}') \cdot \mathbf{P}(\mathbf{r}') dv' + k_h^2 \frac{v_E(\mathbf{r})}{\mu_h} \int_{V_f} \mathcal{G}_{em}(\mathbf{r}, \mathbf{r}') \cdot \mathbf{M}(\mathbf{r}') dv' \quad (3.101)$$

$$\mathbf{M} = \mathbf{M}^0 + \mu_h v_H(\mathbf{r}) \int_{V_f} \mathcal{G}_{me}(\mathbf{r}, \mathbf{r}') \cdot \mathbf{P}(\mathbf{r}') dv' + k_h^2 v_H(\mathbf{r}) \int_{V_f} \mathcal{G}_{mm}(\mathbf{r}, \mathbf{r}') \cdot \mathbf{M}(\mathbf{r}') dv' \quad (3.102)$$

We can find both integral equations are coupled. Once getting electric current dipole density \mathbf{P} and magnetization vector \mathbf{M} , the impedance change of the eddy current coil probe due to the flaw can be given by

$$\Delta Z = -\frac{1}{I^2} \int_{V_f} [\mathbf{E}^0 \cdot \mathbf{P} + i\omega \mathbf{H}^0 \cdot \mathbf{M}] dv \quad (3.103)$$

based on reciprocity relationship [89] [11].

3.3.2 Matrix Approximation of Volume Integral Equations

An operator in an infinite-dimensional space is difficult to compute. Hence we always need to reduce an operator into an approximate, finite-dimensional matrix operator by finding its matrix representation[93]. Given an operator equation

$$\mathbb{L}f = g \quad (3.104)$$

where f and g are functions, we can choose a set of linearly independent vectors or functions denoted as $\{b_n(\mathbf{r}), n = 1, 2, 3, \dots, N\}$ to as the basis functions. Then we can approximate $f(\mathbf{r})$

$$f(\mathbf{r}) \approx \sum_{n=1}^N f_n b_n(\mathbf{r}) \quad (3.105)$$

$D_N = \text{span}\{b_n(\mathbf{r}), n = 1, 2, 3, \dots, N\}$ is a space that approximates the original domain space $D(\mathbb{L})$ of operator \mathbb{L} . If \mathbb{L} is a differential operator, then f is nonunique unless BCs are specified. Substituting Eq. (3.105) into Eq. (3.104) and multiply the testing/weighting function $\{t_m(\mathbf{r}), m = 1, 2, 3, \dots, N\}$, then integrate to obtain

$$\sum_{n=1}^N f_n \langle t_m, \mathbb{L}b_n \rangle = \langle t_m, g \rangle, \quad m = 1, 2, 3, \dots, N \quad (3.106)$$

In order for Eq. (3.104) to have a solution, g must be in the range space $R(\mathbb{L})$. If $R_N = \text{span}\{t_m(\mathbf{r}), m = 1, 2, 3, \dots, N\}$ is a good approximation to $R(\mathbb{L})$. Then Eq. (3.106) is a good approximation equation of Eq. (3.104). Then we obtain the matrix equation

$$[\mathbf{L}] \cdot \mathbf{f} = \mathbf{g} \quad (3.107)$$

where

$$[\mathbf{L}]_{mn} = L_{mn} = \langle t_m, Lb_n \rangle \quad (3.108)$$

$$[\mathbf{f}]_n = f_n \quad (3.109)$$

$$[\mathbf{g}]_n = \langle t_n, g \rangle = g_n \quad (3.110)$$

In this dissertation, Moment method is used to obtain the numerically approximation of the source densities and a pulse-basis point-matching scheme is adopted based on the trade-off between coding-simplicity and accuracy [99, 100]. The point matching is applied at the center point of each element cell. We assume the whole problem domain can be meshed into total N brick cells. In a specific cell g , The basis function can be defined as $\tilde{P}_g(\mathbf{r}) = 1$ only if $\mathbf{r} \in V_g$ and $\tilde{P}_g(\mathbf{r}) = 0$ for elsewhere. Then electric dipole and magnetic dipole densities can be approximated as

$$\mathbf{P}(\mathbf{r}) \simeq \sum_{g=1}^N \mathbf{P}_g(\mathbf{r}) \tilde{P}_g \quad (3.111)$$

$$\mathbf{M}(\mathbf{r}) \simeq \sum_{g=1}^N \mathbf{M}_g(\mathbf{r}) \tilde{P}_g \quad (3.112)$$

Substituting these two equations into (3.101), (3.102) and do the point-matching at the center point of each cell, we have the matrix equation

$$\begin{bmatrix} \mathbf{I} - \mathbf{A}^{ee} & \mathbf{A}^{em} \\ \mathbf{A}^{me} & \mathbf{I} - \mathbf{A}^{mm} \end{bmatrix} \cdot \begin{bmatrix} \bar{P} \\ \bar{M} \end{bmatrix} = \begin{bmatrix} \bar{P}^0 \\ \bar{M}^0 \end{bmatrix} \quad (3.113)$$

where \mathbf{I} is the unit matrix with the size $3N \times 3N$. A specific matrix dyadic element of row q and column g is evaluated by

$$[\mathbf{A}^{ee}]_{qg} = k_h^2 v_E(\mathbf{r}_q) \int_{V_g} \mathcal{G}_{ee}(\mathbf{r}_q, \mathbf{r}') dv' \quad (3.114)$$

$$[\mathbf{A}^{em}]_{qg} = -k_h^2 \frac{v_E(\mathbf{r}_q)}{\mu_h} \int_{V_g} \mathcal{G}_{em}(\mathbf{r}_q, \mathbf{r}') dv' \quad (3.115)$$

$$[\mathbf{A}^{me}]_{qg} = -\mu_h v_H(\mathbf{r}_q) \int_{V_g} \mathcal{G}_{me}(\mathbf{r}_q, \mathbf{r}') dv' \quad (3.116)$$

$$[\mathbf{A}^{mm}]_{qg} = k_h^2 v_H(\mathbf{r}_q) \int_{V_g} \mathcal{G}_{mm}(\mathbf{r}_q, \mathbf{r}') dv' \quad (3.117)$$

where $q, g \in \{1, 2, \dots, N\}$. \bar{P} , \bar{M} are the column vectors of unknowns. \bar{P}^0 , \bar{M}^0 are the column vectors determined by incident fields in the flawless material. Once the \bar{P} and \bar{M} have been calculated, the impedance changes of the excitation coil probe due to the flaw, ΔZ_c , can be determined from the relationship

$$I^2 \Delta Z_c \approx -\Delta v (\bar{E}^0 \cdot \bar{P} + i\omega \bar{H}^0 \cdot \bar{M}) \quad (3.118)$$

where Δv is the element volume and the cells are assumed the same size.

Note that since the conductivity is usual much larger than permeability. it might cause the magnitudes of \mathbf{A}^{em} , \mathbf{A}^{me} differ by several orders and then produce stiff matrix. The precondition process might be needed in order to equilibrate the system and make sure the matrix well-condition[21, 101]. For example, the following VIEs

$$\mathbf{E}^0 = \mathbf{E} - i\omega\mu_h \int_{V_f} \mathcal{G}_{ee}(\mathbf{r}, \mathbf{r}') \cdot \mathbf{P}(\mathbf{r}') dv' - i\omega \int_{V_f} \mathcal{G}_{em}(\mathbf{r}, \mathbf{r}') \cdot \mathbf{M}(\mathbf{r}') dv' \quad (3.119)$$

$$\mathbf{H}^0 = - \int_{V_f} \mathcal{G}_{me}(\mathbf{r}, \mathbf{r}') \cdot \mathbf{P}(\mathbf{r}') dv' + \mathbf{H} - i\omega\sigma_h \int_{V_f} \mathcal{G}_{mm}(\mathbf{r}, \mathbf{r}') \cdot \mathbf{M}(\mathbf{r}') dv' \quad (3.120)$$

can be modified as

$$\mathbf{E}^0 = \mathbf{E} - k^2 v_E \int_{V_f} \mathcal{G}_{ee}(\mathbf{r}, \mathbf{r}') \cdot \mathbf{E}(\mathbf{r}') dv' - i\omega (\mu(\mathbf{r}) - \mu_h) \frac{1}{Z_c} \int_{V_f} \mathcal{G}_{em}(\mathbf{r}, \mathbf{r}') \cdot Z_c \mathbf{H}(\mathbf{r}') dv' \quad (3.121)$$

$$Z_c \mathbf{H}^0 = - (\sigma(\mathbf{r}) - \sigma_h) Z_c \int_{V_f} \mathcal{G}_{me}(\mathbf{r}, \mathbf{r}') \cdot \mathbf{E}(\mathbf{r}') dv' + Z_c \mathbf{H} - k^2 v_H \int_{V_f} \mathcal{G}_{mm}(\mathbf{r}, \mathbf{r}') \cdot Z_c \mathbf{H}(\mathbf{r}') dv' \quad (3.122)$$

Then the matrix form are

$$\begin{bmatrix} \mathbf{I} - \mathbf{A}^{ee} & \frac{1}{Z_c} \mathbf{A}^{em} \\ Z_c \mathbf{A}^{me} & \mathbf{I} - \mathbf{A}^{mm} \end{bmatrix} \cdot \begin{bmatrix} \bar{E} \\ Z_c \bar{H} \end{bmatrix} = \begin{bmatrix} \bar{E}^0 \\ Z_c \bar{H}^0 \end{bmatrix} \quad (3.123)$$

where $Z_c = \sqrt{\mu_h/\varepsilon_h} \approx \sqrt{-i\omega\mu_h/\sigma_h}$

$$[\mathbf{A}^{ee}]_{qq} = k_h^2 v_E(\mathbf{r}_q) \int_{V_g} \mathcal{G}_{ee}(\mathbf{r}_q, \mathbf{r}') dv' \quad (3.124)$$

$$[\mathbf{A}^{em}]_{qq} = -i\omega [\mu(\mathbf{r}_q) - \mu_h] \int_{V_g} \mathcal{G}_{em}(\mathbf{r}_q, \mathbf{r}') dv' \quad (3.125)$$

$$[\mathbf{A}^{me}]_{qq} = - [\sigma(\mathbf{r}_q) - \sigma_h] \int_{V_g} \mathcal{G}_{me}(\mathbf{r}_q, \mathbf{r}') dv' \quad (3.126)$$

$$[\mathbf{A}^{mm}]_{qq} = k_h^2 v_H(\mathbf{r}_q) \int_{V_g} \mathcal{G}_{mm}(\mathbf{r}_q, \mathbf{r}') dv' \quad (3.127)$$

3.4 Dyadic Green's Kernels of a Layered Medium

A derivation of the dyadic kernels dedicated to a layered geometry is based on a decomposition of the electromagnetic field into transverse electric (TE) scalar potential, ψ_1 , and transverse magnetic (TM) scalar potential, ψ_2 , with respect to the z -direction. Since we are dealing with a linear system, we can do the derivation simply by considering the TE and TM potentials that arise from one type of source at a time.

Assuming only electric dipole density \mathbf{P} exists, the magnetic field has zero divergence and can therefore be written in terms of TE and TM potentials

$$\mathbf{H} = \nabla \times \nabla \times (\hat{z}\psi_1) + k_h^2 \nabla \times (\hat{z}\psi_2) \quad (3.128)$$

where $k_h^2 = i\omega\mu_h\sigma_h$. Substituting (3.128) into (3.96) then taking the $\hat{z} \cdot$ and $\hat{z} \cdot \nabla \times$ operation to it separately gives

$$(\nabla^2 + k_h^2) \nabla_t^2 \begin{bmatrix} \psi_1 \\ \psi_2 \end{bmatrix} = \begin{bmatrix} \hat{z} \cdot \nabla \times \mathbf{P} \\ \frac{1}{k_h^2} \hat{z} \cdot \nabla \times \nabla \times \mathbf{P} \end{bmatrix} \quad (3.129)$$

The electric field with the presence of the dipole density \mathbf{P} can be found by taking the curl of (3.128) and applying (3.94), (3.129) and written in the following form that ensures $\nabla \cdot \mathbf{E} = -\nabla \cdot \mathbf{P} / \sigma_h$ required by (3.95).

$$\mathbf{E} = i\omega\mu_h [\nabla \times (\hat{z}\psi_1) + \nabla \times \nabla \times (\hat{z}\psi_2)] - \frac{1}{\sigma_h} \left(\hat{z}\hat{z} + \frac{\nabla_t \nabla_t}{\nabla_t^2} \right) \cdot \mathbf{P} \quad (3.130)$$

Note that this electric representation is even valid in the source region [19].

For the case with only magnetic dipole density \mathbf{M} , a similar procedure can be carried out.

We have

$$(\nabla^2 + k_h^2) \nabla_t^2 \begin{bmatrix} \psi_1 \\ \psi_2 \end{bmatrix} = \frac{1}{\mu_h} \begin{bmatrix} \hat{z} \cdot \nabla \times \nabla \times \mathbf{M} \\ \hat{z} \cdot \nabla \times \mathbf{M} \end{bmatrix} \quad (3.131)$$

The magnetic field in the presence of magnetic density \mathbf{M} can be expressed as

$$\mathbf{H} = [\nabla \times \nabla \times (\hat{z}\psi_1) + k_h^2 \nabla \times (\hat{z}\psi_2)] - \frac{1}{\mu_h} \left(\hat{z}\hat{z} + \frac{\nabla_t \nabla_t}{\nabla_t^2} \right) \cdot \mathbf{M} \quad (3.132)$$

which ensures $\nabla \cdot \mathbf{H} = -\nabla \cdot \mathbf{M}/\mu_h$ required by (3.96). Now the TE and TM potentials for a general case with both sources satisfy

$$(\nabla^2 + k_h^2)\nabla_t^2 \begin{bmatrix} \psi_1 \\ \psi_2 \end{bmatrix} = \begin{bmatrix} \hat{z} \cdot \nabla \times \left(\mathbf{P} + \frac{1}{\mu_h} \nabla \times \mathbf{M} \right) \\ \hat{z} \cdot \nabla \times \left(\frac{1}{k_h^2} \nabla \times \mathbf{P} + \frac{1}{\mu_h} \mathbf{M} \right) \end{bmatrix} \quad (3.133)$$

which are obtained by combining two sets of results of one type of source. This binary system of equations is used to define a set of scalar Green's functions and thereby provide a route leading to a formal solution for the TE and TM potentials. However, rather than evaluating the potentials, we use the scalar Green's function to derive dyadic kernels for the hyper-singular volume integral equations with the goal of finding a numerical approximation of the source densities.

In order to construct the required dyadic kernels, we first define a set of scalar Green's functions satisfying

$$(\nabla^2 + k_h^2) \begin{bmatrix} G_0 + G_{11}^\Gamma & G_{12}^\Gamma \\ G_{21}^\Gamma & G_0 + G_{22}^\Gamma \end{bmatrix} = - \begin{bmatrix} 1 & 0 \\ 0 & 1 \end{bmatrix} \delta(\mathbf{r} - \mathbf{r}') \quad (3.134)$$

where G_0 is the free-space scalar Green's function. The superscript of G_{ij}^Γ denotes the fields associated with field migration from the boundary. The subscripts of G_{ij}^Γ denote the modal character of the field and the source respectively. A TE term is denoted by subscript 1 and a TM term by 2. G_{12}^Γ represents the TE field due to a TM source. The off-diagonal terms G_{12}^Γ and G_{21}^Γ account for the coupling between both modes due to the reflection at the interfaces. In the planarly layered isotropic medium, TE and TM modes are decoupled and both G_{12}^Γ and G_{21}^Γ components are zeros.

The corresponding point-source potentials can be defined as

$$(\nabla^2 + k_h^2)\nabla_t^2 \begin{bmatrix} U_0 + U_{11} & U_{12} \\ U_{21} & U_0 + U_{22} \end{bmatrix} = - \begin{bmatrix} 1 & 0 \\ 0 & 1 \end{bmatrix} \delta(\mathbf{r} - \mathbf{r}') \quad (3.135)$$

with the following relationship

$$G_0(\mathbf{r}, \mathbf{r}') = -\nabla_t^2 U_0 \quad (3.136)$$

$$G_{ij}^\Gamma(\mathbf{r}, \mathbf{r}') = -\nabla_t^2 U_{ij} \quad (3.137)$$

Now using the principle of superposition and the fact that the ψ_1 and ψ_2 can be represented by an integral operator of the point source potentials U acting on the corresponding scalar sources, we write

$$\begin{bmatrix} \psi_1 \\ \psi_2 \end{bmatrix} = \int_{V_f} \begin{bmatrix} U_0 + U_{11} & U_{12} \\ U_{21} & U_0 + U_{22} \end{bmatrix} \cdot \begin{bmatrix} \hat{z} \cdot \nabla' \times \left(\mathbf{P} + \frac{1}{\mu_h} \nabla' \times \mathbf{M} \right) \\ \hat{z} \cdot \nabla' \times \left(\frac{1}{k_h^2} \nabla' \times \mathbf{P} + \frac{1}{\mu_h} \mathbf{M} \right) \end{bmatrix} dv' \quad (3.138)$$

Applying integration by parts [93] to the above equation, the potential due to an electric source can be written as

$$\psi_{1p} = \int_{V_f} \left[\nabla' \times [(U_0 + U_{11})\hat{z}] + \frac{1}{k_h^2} \nabla' \times \nabla' \times [U_{12}\hat{z}] \right] \cdot \mathbf{P}(\mathbf{r}') dv' \quad (3.139)$$

$$\psi_{2p} = \int_{V_f} \left[\nabla' \times [U_{21}\hat{z}] + \frac{1}{k_h^2} \nabla' \times \nabla' \times [(U_0 + U_{22})\hat{z}] \right] \cdot \mathbf{P}(\mathbf{r}') dv' \quad (3.140)$$

and due to magnetic source as

$$\psi_{1m} = \frac{1}{\mu_h} \int_{V_f} [\nabla' \times \nabla' \times [(U_0 + U_{11})\hat{z}] + \nabla' \times U_{12}\hat{z}] \cdot \mathbf{M}(\mathbf{r}') dv' \quad (3.141)$$

$$\psi_{2m} = \frac{1}{\mu_h} \int_{V_f} [\nabla' \times \nabla' \times (U_{21}\hat{z}) + \nabla' \times [(U_0 + U_{22})\hat{z}]] \cdot \mathbf{M}(\mathbf{r}') dv' \quad (3.142)$$

By substituting (3.139) and (3.140) into (3.130) and comparing with the first integral of (3.97) on the right side, we can obtain the dyadic kernel \mathcal{G}_{ee} of the form

$$\mathcal{G}_{ee} = \mathcal{G}_{ee}^0 + \mathcal{G}_{ee}^\Gamma \quad (3.143)$$

with

$$\begin{aligned} \mathcal{G}_{ee}^0(\mathbf{r}, \mathbf{r}') &= -\frac{1}{k_h^2} \left(\hat{z}\hat{z} + \frac{\nabla_t \nabla_t}{\nabla_t^2} \right) \delta(\mathbf{r} - \mathbf{r}') \\ &\quad + (\nabla \times \hat{z})(\nabla' \times \hat{z})U_0(\mathbf{r}, \mathbf{r}') \\ &\quad + \frac{1}{k_h^2} [\nabla \times (\nabla \times \hat{z})][\nabla' \times (\nabla' \times \hat{z})]U_0(\mathbf{r}, \mathbf{r}') \end{aligned} \quad (3.144)$$

$$\begin{aligned} \mathcal{G}_{ee}^\Gamma(\mathbf{r}, \mathbf{r}') &= (\nabla \times \hat{z})(\nabla' \times \hat{z})U_{11}(\mathbf{r}, \mathbf{r}') \\ &\quad + \frac{1}{k_h^2} (\nabla \times \hat{z}) [\nabla' \times (\nabla' \times \hat{z})] U_{12}(\mathbf{r}, \mathbf{r}') \\ &\quad + [\nabla \times (\nabla \times \hat{z})] (\nabla' \times \hat{z})U_{21}(\mathbf{r}, \mathbf{r}') \\ &\quad + \frac{1}{k_h^2} [\nabla \times (\nabla \times \hat{z})] [\nabla' \times (\nabla' \times \hat{z})] U_{22}(\mathbf{r}, \mathbf{r}') \end{aligned} \quad (3.145)$$

where the dyadic kernel is decomposed into singular term \mathcal{G}_{ee}^0 denoted by a superscript zero and regular term \mathcal{G}_{ee}^Γ denoted by a superscript Γ that account for the interaction of the unbounded solution with boundaries. After some transformations used in [94, 19], (3.144) reduces to

$$\mathcal{G}_{ee}^0(\mathbf{r}, \mathbf{r}') = \left(\mathcal{I} + \frac{1}{k_h^2} \nabla \nabla \right) G_0(\mathbf{r}, \mathbf{r}') \quad (3.146)$$

which is the unbounded domain dyadic kernel [94]. Similarly, by substituting (3.141) and (3.142) into (3.132) and comparing with the second integral of (3.98) on the right side, we can obtain the dyadic kernel \mathcal{G}_{mm} of the form

$$\mathcal{G}_{mm} = \mathcal{G}_{mm}^0 + \mathcal{G}_{mm}^\Gamma \quad (3.147)$$

with

$$\begin{aligned} \mathcal{G}_{mm}^\Gamma(\mathbf{r}, \mathbf{r}') &= \frac{1}{k_h^2} (\nabla \times \nabla \times \hat{z}) (\nabla' \times \nabla' \times \hat{z}) U_{11}(\mathbf{r}, \mathbf{r}') \\ &+ \frac{1}{k_h^2} (\nabla \times \nabla \times \hat{z}) (\nabla' \times \hat{z}) U_{12}(\mathbf{r}, \mathbf{r}') \\ &+ (\nabla \times \hat{z}) (\nabla' \times \nabla' \times \hat{z}) U_{21}(\mathbf{r}, \mathbf{r}') \\ &+ (\nabla \times \hat{z}) (\nabla' \times \hat{z}) U_{22}(\mathbf{r}, \mathbf{r}') \end{aligned} \quad (3.148)$$

and $\mathcal{G}_{mm}^0 = \mathcal{G}_{ee}^0$.

To determine the kernel $\mathcal{G}_{me}(\mathbf{r}, \mathbf{r}')$ and $\mathcal{G}_{em}(\mathbf{r}, \mathbf{r}')$, one can apply the curl operator $\nabla \times$ upon \mathcal{G}_{ee} and \mathcal{G}_{mm} as defined in (3.43) and (3.62). Alternatively, $\mathcal{G}_{em}(\mathbf{r}, \mathbf{r}')$ can be gotten by substituting (3.141) and (3.142) into (3.130) and comparing with the second integral of (3.97) as

$$\begin{aligned} \mathcal{G}_{em}^\Gamma(\mathbf{r}, \mathbf{r}') &= (\nabla \times \hat{z}) (\nabla' \times \nabla' \times \hat{z}) U_{11}(\mathbf{r}, \mathbf{r}') \\ &+ (\nabla \times \hat{z}) (\nabla' \times \hat{z}) U_{12}(\mathbf{r}, \mathbf{r}') \\ &+ (\nabla \times \nabla \times \hat{z}) (\nabla' \times \nabla' \times \hat{z}) U_{21}(\mathbf{r}, \mathbf{r}') \\ &+ (\nabla \times \nabla \times \hat{z}) (\nabla' \times \hat{z}) U_{22}(\mathbf{r}, \mathbf{r}') \end{aligned} \quad (3.149)$$

$$\mathcal{G}_{em}^0(\mathbf{r}, \mathbf{r}') = \nabla G_0(\mathbf{r}, \mathbf{r}') \times \mathcal{I} \quad (3.150)$$

Similarly $\mathcal{G}_{me}(\mathbf{r}, \mathbf{r}')$ can be gotten

$$\begin{aligned}\mathcal{G}_{me}^{\Gamma}(\mathbf{r}, \mathbf{r}') &= (\nabla \times \nabla \times \hat{z})(\nabla' \times \hat{z})U_{11}(\mathbf{r}, \mathbf{r}') \\ &+ \frac{1}{k_h^2}(\nabla \times \nabla \times \hat{z})[\nabla' \times (\nabla' \times \hat{z})]U_{12}(\mathbf{r}, \mathbf{r}') \\ &+ k_h^2(\nabla \times \hat{z})(\nabla' \times \hat{z})U_{21}(\mathbf{r}, \mathbf{r}') \\ &+ (\nabla \times \hat{z})[\nabla' \times (\nabla' \times \hat{z})]U_{22}(\mathbf{r}, \mathbf{r}')\end{aligned}\quad (3.151)$$

$$\mathcal{G}_{me}^0(\mathbf{r}, \mathbf{r}') = \nabla G_0(\mathbf{r}, \mathbf{r}') \times \mathcal{I} \quad (3.152)$$

Note that the dyadic kernel expressions in terms of scalar kernels are valid not only the planarly layered structure but also the cylindrical layered structure [19]. Now the derivation of dyadic kernels are completed and once the scalar kernels are obtained, the dyadic kernel can be easily achieved by substituting into corresponding expressions.

3.4.1 Dyadic Green's Kernels in the Cartesian Coordinate System

The dyadic Green function of unbounded domain in Cartesian coordinate system can be explicitly expressed as follow in a matrix form

$$\mathcal{G}_0(\mathbf{r}, \mathbf{r}') = \frac{1}{k_h^2} \begin{bmatrix} (k_h^2 + \frac{\partial^2}{\partial x^2}) & \frac{\partial^2}{\partial x \partial y} & \frac{\partial^2}{\partial x \partial z} \\ \frac{\partial^2}{\partial y \partial x} & (k_h^2 + \frac{\partial^2}{\partial y^2}) & \frac{\partial^2}{\partial y \partial z} \\ \frac{\partial^2}{\partial z \partial x} & \frac{\partial^2}{\partial z \partial y} & (k_h^2 + \frac{\partial^2}{\partial z^2}) \end{bmatrix} G_0(\mathbf{r}, \mathbf{r}') \quad (3.153)$$

The dyadic kernels account for the interaction of the unbounded solution with boundaries can be expressed in matrix forms in terms of scalar Greens' kernels as follows

$$\begin{aligned}\mathcal{G}_{ee}^{\Gamma} &= (\nabla \times \hat{z})(\nabla' \times \hat{z})U_{11} + \frac{1}{k_h^2}[\nabla \times (\nabla \times \hat{z})][\nabla' \times (\nabla' \times \hat{z})]U_{22} \\ &= \begin{bmatrix} \left(\frac{\partial}{\partial y} \frac{\partial}{\partial y'} U_{11} + \frac{1}{k_h^2} \frac{\partial^4}{\partial x' \partial z' \partial x \partial z} U_{22} \right) & \left(-\frac{\partial}{\partial y} \frac{\partial}{\partial x'} U_{11} + \frac{1}{k_h^2} \frac{\partial^4}{\partial y' \partial z' \partial x \partial z} U_{22} \right) & -\frac{1}{k_h^2} \nabla_t'^2 \frac{\partial^2}{\partial x \partial z} U_{22} \\ \left(-\frac{\partial}{\partial x} \frac{\partial}{\partial y'} U_{11} + \frac{1}{k_h^2} \frac{\partial^4}{\partial x' \partial z' \partial y \partial z} U_{22} \right) & \left(\frac{\partial}{\partial x} \frac{\partial}{\partial x'} U_{11} + \frac{1}{k_h^2} \frac{\partial^4}{\partial y' \partial z' \partial y \partial z} U_{22} \right) & -\frac{1}{k_h^2} \nabla_t'^2 \frac{\partial^2}{\partial y \partial z} U_{22} \\ -\frac{1}{k_h^2} \frac{\partial^2}{\partial x' \partial z'} \nabla_t^2 U_{22} & -\frac{1}{k_h^2} \frac{\partial^2}{\partial y' \partial z'} \nabla_t^2 U_{22} & \frac{1}{k_h^2} \nabla_t'^2 \nabla_t^2 U_{22} \end{bmatrix}\end{aligned}\quad (3.154)$$

$$\begin{aligned}
\mathcal{G}_{mm}^{\Gamma} &= \frac{1}{k_h^2} (\nabla \times \nabla \times \hat{z}) (\nabla' \times \nabla' \times \hat{z}) U_{11} + (\nabla \times \hat{z}) (\nabla' \times \hat{z}) U_{22} \\
&= \begin{bmatrix} \left(\frac{1}{k_h^2} \frac{\partial^4}{\partial x' \partial z' \partial x \partial z} U_{11} + \frac{\partial}{\partial y} \frac{\partial}{\partial y'} U_{22} \right) & \left(\frac{1}{k_h^2} \frac{\partial^4}{\partial y' \partial z' \partial x \partial z} U_{11} - \frac{\partial}{\partial y} \frac{\partial}{\partial x'} U_{22} \right) & -\frac{1}{k_h^2} \nabla_t'^2 \frac{\partial^2}{\partial x \partial z} U_{11} \\ \left(\frac{1}{k_h^2} \frac{\partial^4}{\partial x' \partial z' \partial y \partial z} U_{11} - \frac{\partial}{\partial x} \frac{\partial}{\partial y'} U_{22} \right) & \left(\frac{1}{k_h^2} \frac{\partial^4}{\partial y' \partial z' \partial y \partial z} U_{11} + \frac{\partial}{\partial x} \frac{\partial}{\partial x'} U_{22} \right) & -\frac{1}{k_h^2} \nabla_t'^2 \frac{\partial^2}{\partial y \partial z} U_{11} \\ -\frac{1}{k_h^2} \frac{\partial^2}{\partial x' \partial z'} \nabla_t^2 U_{11} & -\frac{1}{k_h^2} \frac{\partial^2}{\partial y' \partial z'} \nabla_t^2 U_{11} & \frac{1}{k_h^2} \nabla_t'^2 \nabla_t^2 U_{11} \end{bmatrix}
\end{aligned} \tag{3.155}$$

$$\begin{aligned}
\mathcal{G}_{me}^{\Gamma}(\mathbf{r}, \mathbf{r}') &= (\nabla \times \nabla \times \hat{z}) (\nabla' \times \hat{z}) U_{11} + (\nabla \times \hat{z}) [\nabla' \times (\nabla' \times \hat{z})] U_{22} \\
&= \begin{bmatrix} \left(\frac{\partial^3}{\partial x \partial z \partial y'} U_{11} + \frac{\partial^3}{\partial y \partial x' \partial z'} U_{22} \right) & \left(-\frac{\partial^3}{\partial x \partial z \partial x'} U_{11} + \frac{\partial^3}{\partial y \partial y' \partial z'} U_{22} \right) & -\nabla_t'^2 \frac{\partial}{\partial y} U_{22} \\ \left(\frac{\partial^3}{\partial y \partial z \partial y'} U_{11} - \frac{\partial^3}{\partial x \partial x' \partial z'} U_{22} \right) & -\left(\frac{\partial^3}{\partial y \partial z \partial x'} U_{11} + \frac{\partial^3}{\partial x \partial y' \partial z'} U_{22} \right) & \nabla_t'^2 \frac{\partial}{\partial x} U_{22} \\ -\nabla_t^2 \frac{\partial}{\partial y'} U_{11} & \nabla_t^2 \frac{\partial}{\partial x'} U_{11} & 0 \end{bmatrix}
\end{aligned} \tag{3.156}$$

$$\begin{aligned}
\mathcal{G}_{em}^{\Gamma}(\mathbf{r}, \mathbf{r}') &= (\nabla \times \hat{z}) [\nabla' \times (\nabla' \times \hat{z})] U_{11} + (\nabla \times \nabla \times \hat{z}) (\nabla' \times \hat{z}) U_{22} \\
&= \begin{bmatrix} \left(\frac{\partial^3}{\partial x \partial z \partial y'} U_{22} + \frac{\partial^3}{\partial y \partial x' \partial z'} U_{11} \right) & \left(-\frac{\partial^3}{\partial x \partial z \partial x'} U_{22} + \frac{\partial^3}{\partial y \partial y' \partial z'} U_{11} \right) & -\nabla_t'^2 \frac{\partial}{\partial y} U_{11} \\ \left(\frac{\partial^3}{\partial y \partial z \partial y'} U_{22} - \frac{\partial^3}{\partial x \partial x' \partial z'} U_{11} \right) & -\left(\frac{\partial^3}{\partial y \partial z \partial x'} U_{22} + \frac{\partial^3}{\partial x \partial y' \partial z'} U_{11} \right) & \nabla_t'^2 \frac{\partial}{\partial x} U_{11} \\ -\nabla_t^2 \frac{\partial}{\partial y'} U_{22} & \nabla_t^2 \frac{\partial}{\partial x'} U_{22} & 0 \end{bmatrix}
\end{aligned} \tag{3.157}$$

Here we explicitly list all the operator used in the derivation in details.

$$\nabla = \frac{\partial}{\partial x} \hat{x} + \frac{\partial}{\partial y} \hat{y} + \frac{\partial}{\partial z} \hat{z} \tag{3.158}$$

$$\nabla^2 = \frac{\partial}{\partial x^2} + \frac{\partial}{\partial y^2} + \frac{\partial}{\partial z^2} \tag{3.159}$$

$$\nabla_t^2 = \frac{\partial^2}{\partial x^2} + \frac{\partial^2}{\partial y^2} \tag{3.160}$$

$$\nabla \times \hat{z} = \frac{\partial}{\partial y} \hat{x} - \frac{\partial}{\partial x} \hat{y} \tag{3.161}$$

$$\nabla \times \nabla \times \hat{z} = \nabla (\nabla \cdot \hat{z}) - \nabla^2 \hat{z} = \frac{\partial^2}{\partial x \partial z} \hat{x} + \frac{\partial^2}{\partial y \partial z} \hat{y} - \nabla_t^2 \hat{z} \tag{3.162}$$

$$(\nabla \times \hat{z})(\nabla' \times \hat{z}) = \frac{\partial}{\partial y} \frac{\partial}{\partial y'} \hat{x} \hat{x} - \frac{\partial}{\partial y} \frac{\partial}{\partial x'} \hat{x} \hat{y} - \frac{\partial}{\partial x} \frac{\partial}{\partial y'} \hat{y} \hat{x} + \frac{\partial}{\partial x} \frac{\partial}{\partial x'} \hat{y} \hat{y} \tag{3.163}$$

3.4.2 Dyadic Green's Kernels in the Cylindrical Coordinate System

Similarly we can obtain the dyadic kernel form in cylindrical coordinate system by applying the following operators

$$\nabla = \hat{\rho} \frac{\partial}{\partial \rho} + \hat{\phi} \frac{1}{\rho} \frac{\partial}{\partial \phi} + \hat{z} \frac{\partial}{\partial z} \quad (3.164)$$

$$\nabla^2 = \frac{1}{\rho} \frac{\partial}{\partial \rho} \left[\rho \frac{\partial}{\partial \rho} \right] + \frac{1}{\rho^2} \frac{\partial^2}{\partial \phi^2} + \frac{\partial^2}{\partial z^2} \quad (3.165)$$

$$\nabla_t^2 = \frac{1}{\rho} \left(\frac{\partial}{\partial \rho} \left(\rho \frac{\partial}{\partial \rho} \right) + \frac{1}{\rho} \frac{\partial^2}{\partial \phi^2} \right) \quad (3.166)$$

$$\nabla \times \hat{z} = \hat{\rho} \frac{1}{\rho} \frac{\partial}{\partial \phi} - \hat{\phi} \frac{\partial}{\partial \rho} \quad (3.167)$$

$$\nabla \times \nabla \times (\hat{z}) = \hat{\rho} \left(\frac{\partial^2}{\partial z \partial \rho} \right) + \hat{\phi} \left(\frac{1}{\rho} \frac{\partial^2}{\partial z \partial \phi} \right) - \hat{z} \nabla_t^2 \quad (3.168)$$

$$(\nabla \times \hat{z})(\nabla' \times \hat{z}) = \frac{1}{\rho'} \frac{1}{\rho} \frac{\partial^2}{\partial \phi \partial \phi'} \hat{\rho} \hat{\rho} - \frac{1}{\rho} \frac{\partial^2}{\partial \phi \partial \rho'} \hat{\rho} \hat{\phi} - \frac{1}{\rho'} \frac{\partial^2}{\partial \rho \partial \phi'} \hat{\phi} \hat{\rho} + \frac{\partial^2}{\partial \rho \partial \rho'} \hat{\phi} \hat{\phi} \quad (3.169)$$

The formulation of dyadic kernels in cylindrical is cumbersome for example two components of \mathcal{G}_{ee}^Γ are

$$G_{ee,zz}^\Gamma(\mathbf{r}, \mathbf{r}') = \frac{1}{k_h^2} \nabla_t^2 \nabla_t'^2 U_{22} = -\frac{1}{k_h^2} \nabla_t'^2 G_{22}^\Gamma \quad (3.170)$$

$$G_{ee,\phi\phi}^\Gamma(\mathbf{r}, \mathbf{r}') = \frac{\partial^2}{\partial \rho \partial \rho'} U_{11} - \frac{1}{k_h^2 \rho'} \frac{\partial^3}{\partial \rho \partial z' \partial \phi'} U_{12} - \frac{1}{\rho} \frac{\partial^3}{\partial z \partial \phi \partial \rho'} U_{21} + \frac{1}{k_h^2 \rho \rho'} \frac{\partial^4}{\partial z \partial \phi \partial z' \partial \phi'} U_{22} \quad (3.171)$$

Hence we will not explicitly shown here.

CHAPTER 4. INCIDENT FIELD EVALUATION FOR PLANAR AND CYLINDRICAL STRUCTURES

Incident field evaluation is an important step of MoM implementation. Besides, it's also involved in the impedance variation evaluation, Eq.(3.103), due to flaws. The analytical solution of the field for a air-cored circular coil whose axis is perpendicular to planar conductor interface was studied by Dodd [9]. However usually only the electric field expression was shown due to the fact most of the integral equation models were developed and implemented for non-ferromagnetic materials. Here the explicit analytical expression for both electric and magnetic fields are summarized for a paralleled coil above half-space and slab, and a rotary coil in the borehole and tube.

Some assumption for calculating eddy current coil field:

- Frequency is low enough to apply quasi-static condition, say $f < 10\text{MHz}$ [9].
- The coil have a uniform current distribution over a rectangular cross section
- The coil field can be expressed as an integral superposition of single filament loop fields by integrating over the rectangular cross section

For quasi-static case, we have $k^2 = i\omega\mu_0\mu_r\sigma$, $\gamma = \sqrt{\kappa^2 - k^2} = \sqrt{\kappa^2 - i\omega\mu\sigma}$. For free space ($\sigma = 0$), we have $k^2 = 0$ and $\gamma = \kappa$.

4.1 Incident Field in Planar Layered Structure

4.1.1 The Fields for a Coil in Free-space

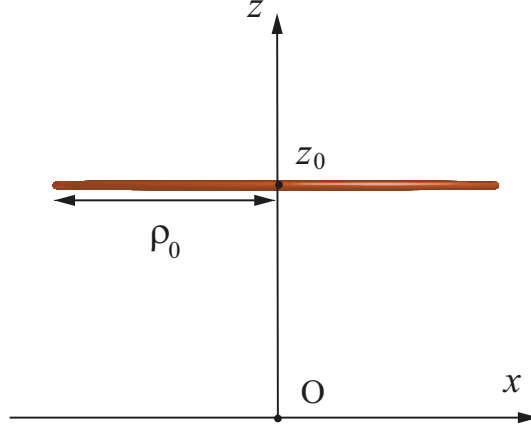


Figure 4.1: Horizontal circular filament loop in the unbounded space

The field of a filament loop with radius ρ_0 in free space, Fig. 4.1, can be obtained by applying method of separation of variables. To solve this equation, we divide the space into two infinite half spaces by $z = z_0$ plane and then account for the current discontinuity into boundary condition in terms of magnetic field. The governing equation and boundary conditions can be rewritten as

$$\nabla^2 \hat{\phi} E_\phi = 0 \quad (4.1)$$

$$[E_\phi]_{z=z_0} = 0 \quad (4.2)$$

$$\left[\frac{\partial E_\phi}{\partial z} \right]_{z=z_0} = -i\omega\mu I \delta(\rho - \rho_0) \quad (4.3)$$

By using separation of variables and applying the Hankel transform shown in Appendix C, the electric field can be expressed as

$$E_{\phi,air}^{loop}(\rho, z, \rho_0, z_0) = \frac{i\omega\mu_0 I}{2} \int_0^\infty J_1(\kappa\rho_0)\rho_0 J_1(\kappa\rho) e^{-\kappa|z-z_0|} d\kappa \quad (4.4)$$

where $J_1(z)$ is the first kind Bessel function.

An eddy current inductive coil with inner radius r_1 , outer radius r_2 and length ℓ locates in the free space, Fig. 4.2. The number of turns of the coil is N and the turn density is defined as

$$v = \frac{N}{\ell(r_2 - r_1)} \quad (4.5)$$

The total field can be obtained from single filament loop field by integrating over the cross section of coil.

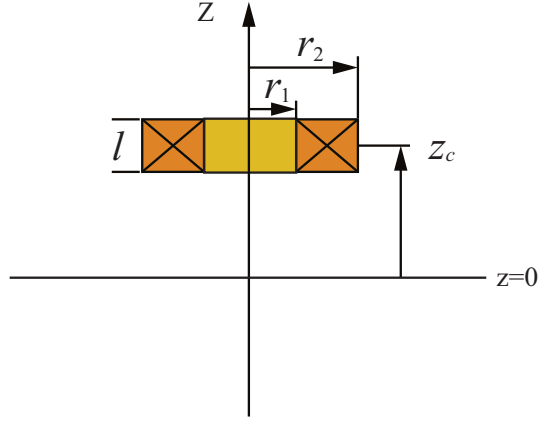


Figure 4.2: Horizontal coil in the unbounded space

Then the $E_\phi(\rho, z)$ can be expressed as

$$\begin{aligned} E_{\phi,coil}(\rho, z) &= v \int_{r_1}^{r_2} \int_{z_1}^{z_2} E_{\phi,air}^{loop}(\rho, z, \rho_0, z_0) d\rho_0 dz_0 \\ &= i\omega\mu_0 I v \int_0^\infty \frac{1}{\kappa^3} J_1(\kappa\rho) d\kappa \int_{\kappa r_1}^{\kappa r_2} J_1(x) x dx \int_{z_1}^{z_2} \frac{\kappa}{2} e^{-\kappa|z-z_0|} dz_0 \\ &= i\omega\mu_0 I v \int_0^\infty \frac{1}{\kappa^3} J_1(\kappa\rho) \chi(\kappa r_1, \kappa r_2) F(\kappa, z) d\kappa \end{aligned} \quad (4.6)$$

where

$$\chi(s_1, s_2) = \int_{s_1}^{s_2} J_1(x) x dx \quad (4.7)$$

and

$$F(\kappa, z) = \frac{\kappa}{2} \int_{z_1}^{z_2} e^{-\kappa|z-z_0|} dz_0$$

$$= \begin{cases} F_1(\kappa, z) = e^{-\kappa(z-z_c)} \sinh\left(\frac{\kappa\ell}{2}\right) & z > z_c + \frac{\ell}{2} \\ F_2(\kappa, z) = 1 - e^{-\frac{\kappa\ell}{2}} \cosh(\kappa(z-z_c)) & z_c + \frac{\ell}{2} \geq z \geq z_c - \frac{\ell}{2} \\ F_3(\kappa, z) = e^{\kappa(z-z_c)} \sinh\left(\frac{\kappa\ell}{2}\right) & z < z_c - \frac{\ell}{2} \end{cases} \quad (4.8)$$

If the coil is located in the conductive medium, we have $k^2 = i\omega\mu\sigma = i\omega\mu_0\mu_r\sigma$, $\gamma = \sqrt{\kappa^2 - k^2} = \sqrt{\kappa^2 - i\omega\mu\sigma}$. For a filament loop with radius ρ_0 , the electric field is expressed as

$$E_{\phi,lossy}^{loop}(\rho, z, \rho_0, z_0) = \frac{i\omega\mu I}{2} \int_0^\infty \frac{\kappa}{\gamma} J_1(\kappa\rho_0)\rho_0 J_1(\kappa\rho) e^{-\gamma|z-z_0|} d\kappa \quad (4.9)$$

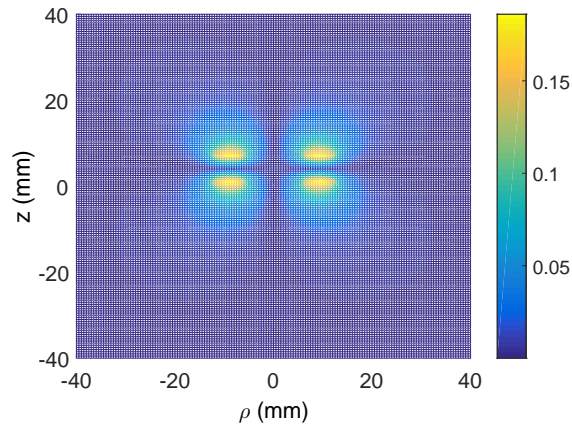
and

$$E_{\phi,coil}(\rho, z) = v \int_{r_1}^{r_2} \int_{z_1}^{z_2} E_{\phi,lossy}^{loop}(\rho, z, \rho_0, z_0) d\rho_0 dz_0$$

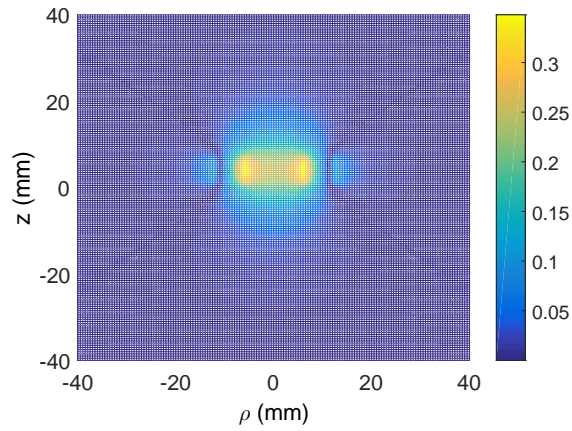
$$= i\omega\mu I v \int_0^\infty \frac{1}{\gamma^2 \kappa} J_1(\kappa\rho) d\kappa \int_{\kappa r_1}^{\kappa r_2} J_1(x) x d(x) \int_{z_1}^{z_2} \frac{\gamma}{2} e^{-\gamma|z-z_0|} dz_0 \quad (4.10)$$

$$= i\omega\mu I v \int_0^\infty \frac{1}{\gamma^2 \kappa} J_1(\kappa\rho) \chi(\kappa r_1, \kappa r_2) F(\gamma, z) d\kappa$$

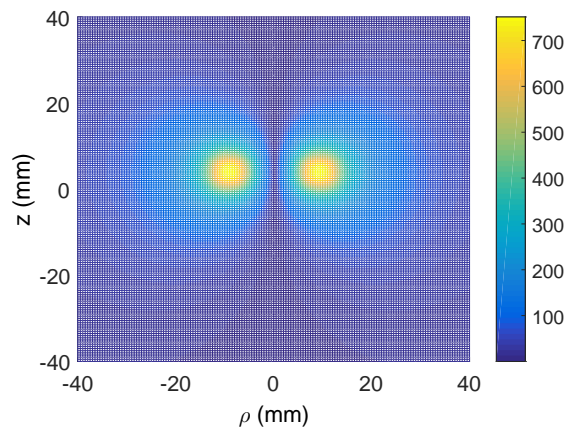
The cross-section of electric and magnetic field distribution of a coil in free space is calculated, Fig. 4.3. The section plane is cutting through the coil center. The frequency is 100 kHz and the coil size is the same as the TEM Problem 15, which is shown in Tab. 5.1. Note that the current excited current is assumed as 1 Ampere.



(a) $|B_r|$ component of the magnetic flux density of a coil in free space on a cross-section plane through the coil center



(b) $|B_z|$ component of the magnetic flux density of a coil in free space on a cross-section plane through the coil center



(c) $|E_\phi|$ component of the electric field of a coil in free space on a cross-section plane through the coil center

Figure 4.3: The electromagnetic fields of a coil in the free space

4.1.2 The Fields for a Coil above an Infinite Half-space Conductor

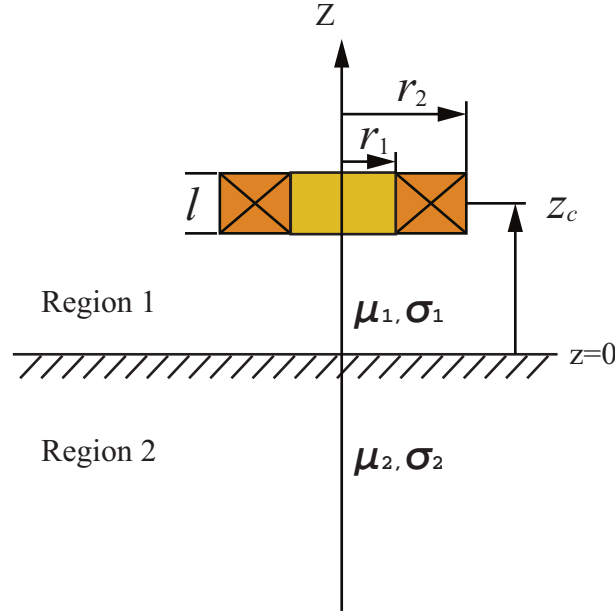


Figure 4.4: Horizontal coil above half-space conductive metal

When we put the coil above an infinite large planar conductor, the incident field which transmits from the coil to the air-conductor interface can be expressed as

$$E_{\phi,1}^0(\rho, z) = i\omega\mu_0 I v \int_0^{\infty} \frac{1}{\kappa^3} J_1(\kappa\rho) \chi(\kappa r_1, \kappa r_2) e^{\kappa(z-z_c)} \sinh\left(\frac{\kappa\ell}{2}\right) d\kappa \quad (4.11)$$

where $F(\kappa, z)$ with $z < z_c - \frac{\ell}{2}$ is chosen. The superscript 0 means incident field and subscript 1 denotes region 1. By using Maxwell's equation

$$\nabla \times \mathbf{E} = i\omega\mu_0 \mathbf{H} \quad (4.12)$$

Here we assume the region 1 is air. If it's conductive medium, a little modification is necessary as shown in previous section. For simplicity, the region 1 is always assumed as air unless stated.

So $\mu_1 = \mu_0$ and $\sigma_1 = 0$.

The magnetic fields are obtained

$$\begin{aligned} H_{z,1}^0 &= -i \frac{1}{\omega\mu_0} \frac{1}{\rho} \frac{\partial[\rho E_{\phi}]}{\partial\rho} \\ &= I v \int_0^{\infty} \frac{1}{\kappa^2} J_0(\kappa\rho) \chi(\kappa r_1, \kappa r_2) e^{\kappa(z-z_c)} \sinh\left(\frac{\kappa\ell}{2}\right) d\kappa \end{aligned} \quad (4.13)$$

where the relationship $[J_1(\kappa\rho)]' = \kappa J_1'(\kappa\rho) = \kappa J_0(\kappa\rho) - \frac{1}{\rho} J_1(\kappa\rho)$ (page 222) [102] is used to calculate H field.

$$\begin{aligned} H_{\rho,1}^0 &= -Iv \int_0^{\infty} \frac{1}{\kappa^3} J_1(\kappa\rho) \chi(\kappa r_1, \kappa r_2) F'(\kappa, z) d\kappa \\ &= -Iv \int_0^{\infty} \frac{1}{\kappa^2} J_1(\kappa\rho) \chi(\kappa r_1, \kappa r_2) e^{\kappa(z-z_c)} \sinh\left(\frac{\kappa\ell}{2}\right) d\kappa \end{aligned} \quad (4.14)$$

Based on scalar decomposition, we could generally express the E and H field by using TE and TM potential in a piece-wise homogeneous medium. For source free case, the electric field density and magnetic field density can be expressed as

$$\mathbf{E} = i\omega\mu [\nabla \times (\hat{z}\psi_1) + \nabla \times \nabla \times (\hat{z}\psi_2)] \quad (4.15)$$

$$\mathbf{H} = \nabla \times \nabla \times (\hat{z}\psi_1) + k^2 \nabla \times (\hat{z}\psi_2) \quad (4.16)$$

where ψ_1 denotes TE potential and ψ_2 denotes TM potential.

Above a half-space conductor plane, the total field is the combination of incident field and reflected field from interface. The potential ψ in the air and conductor can be expressed as follow separately in terms of reflection coefficient $\Gamma(\kappa)$ and transmission coefficient $T(\kappa)$,

$$\psi_{in}(\mathbf{r}) = \int_{-\infty}^{\infty} \int_{-\infty}^{\infty} \tilde{f}(k_x, k_y) e^{\kappa z} e^{i(k_x x + k_y y)} dk_x dk_y \quad (4.17)$$

$$\psi_r(\mathbf{r}) = \int_{-\infty}^{\infty} \int_{-\infty}^{\infty} \tilde{f}(k_x, k_y) \Gamma(\kappa) e^{-\kappa z} e^{i(k_x x + k_y y)} dk_x dk_y \quad (4.18)$$

in the air,

$$\psi_t(\mathbf{r}) = \int_{-\infty}^{\infty} \int_{-\infty}^{\infty} \tilde{f}(k_x, k_y) T(\kappa) e^{\gamma z} e^{i(k_x x + k_y y)} dk_x dk_y \quad (4.19)$$

in the conductor.

Here we assume the incident field always comes from region 1 into region 2, then $\Gamma(\kappa)$ and $T(\kappa)$ for TE and TM potentials are

$$\Gamma_{te}(\kappa) = \frac{\gamma_1/\gamma_2 - \mu_1/\mu_2}{\gamma_1/\gamma_2 + \mu_1/\mu_2} = \frac{\gamma_1\mu_2 - \gamma_2\mu_1}{\gamma_1\mu_2 + \gamma_2\mu_1} \quad (4.20)$$

$$T_{te}(\kappa) = \frac{2(\gamma_1/\gamma_2)(\mu_1/\mu_2)}{\gamma_1/\gamma_2 + \mu_1/\mu_2} = \frac{2\gamma_1\mu_1}{\gamma_1\mu_2 + \gamma_2\mu_1} = (\mu_1/\mu_2)[1 + \Gamma_{te}(\kappa)] \quad (4.21)$$

$$\Gamma_{tm}(\kappa) = \frac{\sigma_2\gamma_1 - \sigma_1\gamma_2}{\sigma_2\gamma_1 + \sigma_1\gamma_2} \quad (4.22)$$

$$T_{tm}(\kappa) = \frac{\sigma_1}{\sigma_2} [1 + \Gamma_{tm}(\kappa)] = \frac{2\sigma_1\gamma_1}{\sigma_2\gamma_1 + \sigma_1\gamma_2} \quad (4.23)$$

For the layered planar problem, the TE and TM modes are decoupled. It means the TE only causes the TE mode and vice versa. For the coil which is parallel with the interface of the air and conductor, there is only the TE component ψ_1 . we have known the incident E field as

$$\mathbf{E}_1^0 = i\omega\mu_0\nabla \times (\hat{z}\psi_{in}) = -i\omega\mu_0\hat{\phi}\frac{\partial\psi_{in}}{\partial\rho} = \hat{\phi}E_{\phi,1}^{in} = \hat{\phi}i\omega\mu_0Iv \int_0^\infty J_1(\kappa\rho)\mathfrak{S}(\kappa)e^{\kappa z}d\kappa \quad (4.24)$$

where $\mathfrak{S}(\kappa) = \frac{1}{\kappa^3}\chi(\kappa r_1, \kappa r_2)e^{-\kappa z_c} \sinh(\frac{\kappa\ell}{2})$. subscript 1 denotes the region 1.

Then the reflected field can be obtained

$$\mathbf{E}_1^{re} = \hat{\phi}E_{\phi,1}^{re} = \hat{\phi}i\omega\mu_0Iv \int_0^\infty \mathfrak{S}(\kappa)[\Gamma(\kappa)e^{-\kappa z}]J_1(\kappa\rho)d\kappa \quad (4.25)$$

The total field in the air region is then obtained as

$$E_{\phi,1}^{total} = i\omega\mu_0Iv \int_0^\infty \mathfrak{S}(\kappa)[e^{\kappa z} + \Gamma_{te}(\kappa)e^{-\kappa z}]J_1(\kappa\rho)d\kappa. \quad (4.26)$$

In the conductor region, the field is given as

$$\mathbf{E}_2 = i\omega\mu_2\nabla \times (\hat{z}\psi_t(\mathbf{r})) = \hat{\phi}i\omega\mu_0\mu_{r2}Iv \int_0^\infty J_1(\kappa\rho)\mathfrak{S}(\kappa)e^{\gamma z}\mathbf{T}_{te}(\kappa)d\kappa \quad (4.27)$$

Similar to free space case, the magnetic fields are

$$H_{\rho,2} = i\frac{1}{\omega\mu_2}\frac{\partial E_{\phi,2}}{\partial z} = -Iv \int_0^\infty \gamma J_1(\kappa\rho)\mathfrak{S}(\kappa)e^{\gamma z}\mathbf{T}_{te}(\kappa)d\kappa \quad (4.28)$$

$$H_{z,2} = -i\frac{1}{\omega\mu_2}\left[\frac{E_{\phi,2}}{\rho} + \frac{\partial E_{\phi,2}}{\partial\rho}\right] = Iv\left[\int_0^\infty \kappa J_0(\kappa\rho)\mathfrak{S}(\kappa)e^{\gamma z}\mathbf{T}_{te}(\kappa)d\kappa\right] \quad (4.29)$$

In addition, the impedance change of an air-cored coil in the air due to half-space conductor is obtained as

$$\Delta Z = -i\pi\omega\mu_0v^2 \int_0^\infty \frac{\chi^2(\kappa r_1, \kappa r_2)}{\kappa^6} (e^{-\kappa z_1} - e^{-\kappa z_2})^2 \Gamma_{te}(\kappa) d\kappa \quad (4.30)$$

where

$$2e^{-\kappa z_c} \sinh\left(\frac{\kappa \ell}{2}\right) = e^{-\kappa z_1} - e^{-\kappa z_2} \quad (4.31)$$

The electric field distribution of a coil above half-space conductor is calculated, Fig. 4.5. The frequency is 0.9 kHz. The coil size and conductor parameters are the same as the TEM Problem 15, which is shown in Tab. 5.1. The excited current is set as 1 Ampere.

From the calculated fields, we can clearly find that the tangential component E_ϕ obtained by the equations of the air region and conductor region separately is continuous which meets boundary conditions.

4.1.3 The Fields for a Coil above an Infinite Conductor Slab

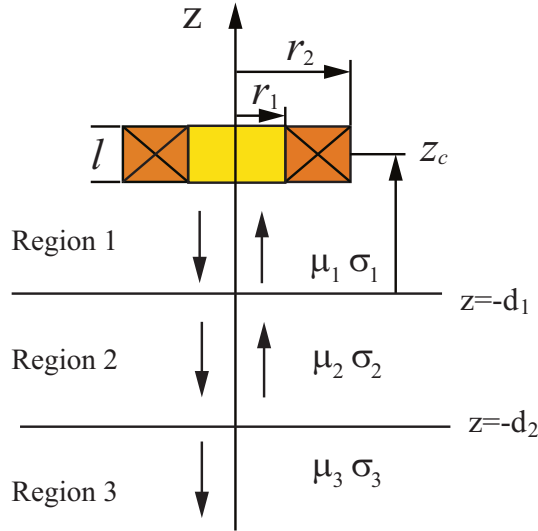
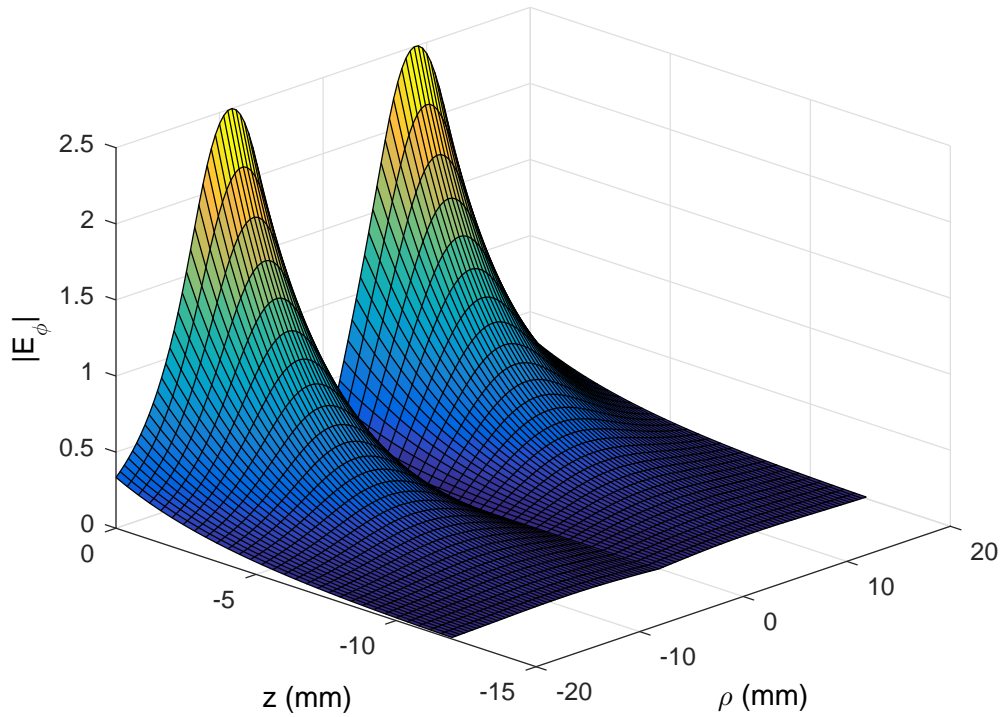
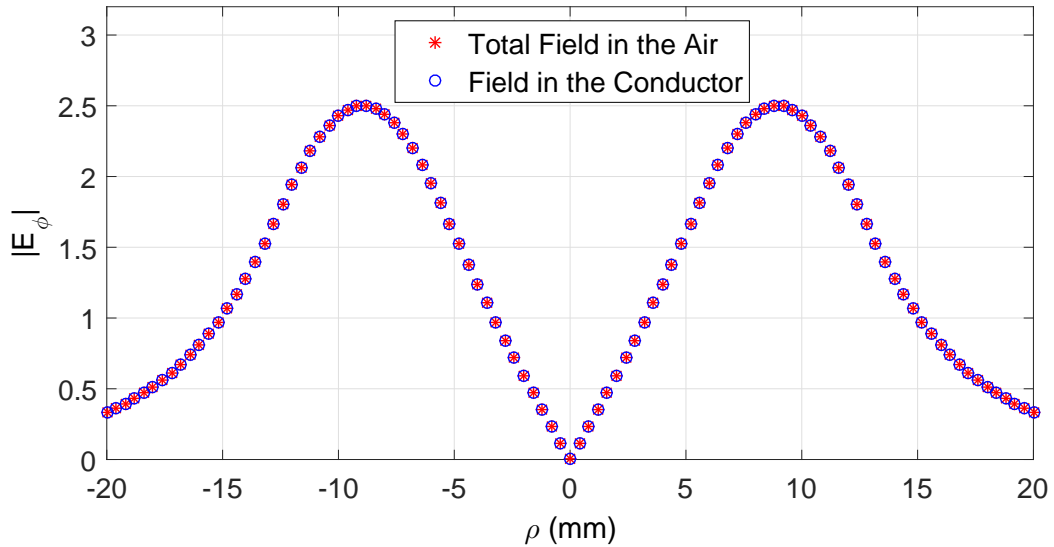


Figure 4.6: Horizontal coil above conductive slab

For a case where a metal slab is located in the free space. The coil is parallel with the interface of the air and conductor. So $\mu_1 = \mu_3 = \mu_0$ and $\sigma_1 = \sigma_3 = 0$. Only TE potential is



(a) $|E_\phi|$ field inside the conductor with a coil above



(b) The $|E_\phi|$ field at the half-space conductor interface, the fields are calculated separately by the formulation in the air and in the conductor

Figure 4.5: The electromagnetic fields of TEM Problem 15

involved. Refer to Fig. 4.6, the general TE potential expressions in three different regions can be written with unknown coefficients firstly as follow [90]

$$\begin{aligned}\psi_1 &= A_1[e^{\gamma_1 z} + \Gamma_{12}^g e^{-2\gamma_1 d_1} e^{-\gamma_1 z}] \\ \psi_2 &= A_2[e^{\gamma_2 z} + \Gamma_{23} e^{-2\gamma_2 d_2} e^{-\gamma_2 z}] \\ \psi_3 &= A_3 e^{\gamma_3 z}\end{aligned}\quad (4.32)$$

Γ_{12} means the reflection coefficient with the incident field coming from region 1 and reflected back to region 1. The superscript g of Γ_{12}^g indicates the total reflection coefficient which accounts for all the effects due to all the interface in region 1.

By imposing two constraint conditions at the interface $z = -d_1$, we have

$$A_2 e^{-\gamma_2 d_1} = T_{12} A_1 e^{-\gamma_1 d_1} + \Gamma_{21} A_2 \Gamma_{23} e^{-2\gamma_2 d_2 + \gamma_2 d_1} \quad (4.33)$$

due to that the downward field in region 2 is the sum of the transmitted field from region 1 and the reflected field from the interface at $z = -d_1$ and

$$\Gamma_{12}^g A_1 e^{-\gamma_1 d_1} = \Gamma_{12} A_1 e^{-\gamma_1 d_1} + T_{21} A_2 \Gamma_{23} e^{-2\gamma_2 d_2 + \gamma_2 d_1} \quad (4.34)$$

due to that the upward field in region 1 is the sum of the transmitted field from region 2 and the reflected field from the interface at $z = -d_1$. Now we can obtain

$$A_2 = \frac{T_{12} e^{(\gamma_2 - \gamma_1) d_1}}{1 - \Gamma_{21} \Gamma_{23} e^{-2\gamma_2 (d_2 - d_1)}} A_1 \quad (4.35)$$

$$\Gamma_{12}^g = \Gamma_{12} + \frac{T_{21} T_{12} \Gamma_{23} e^{-2\gamma_2 (d_2 - d_1)}}{1 - \Gamma_{21} \Gamma_{23} e^{-2\gamma_2 (d_2 - d_1)}} \quad (4.36)$$

This is similar to the reflection coefficient Γ_{in} in terms of S -parameters in the RF circuit [103].

$$\Gamma_{in} = S_{11} + \frac{S_{12} S_{21} \Gamma_{load}}{1 - S_{22} \Gamma_{load}} \quad (4.37)$$

If we add one layer more, we just need to replace the Γ_{23} by the general reflection coefficient Γ_{23}^g as

$$\Gamma_{12}^g = \Gamma_{12} + \frac{T_{12} \Gamma_{23}^g T_{21} e^{-2\gamma_2 (d_2 - d_1)}}{1 - \Gamma_{21} \Gamma_{23}^g e^{-2\gamma_2 (d_2 - d_1)}} \quad (4.38)$$

Now we have the TE potential in region 2 as

$$\psi_2 = A_1 \frac{T_{12} e^{(\gamma_2 - \gamma_1) d_1}}{1 - \Gamma_{21} \Gamma_{23}^g e^{-2\gamma_2 (d_2 - d_1)}} [e^{\gamma_2 z} + \Gamma_{23} e^{-2\gamma_2 d_2} e^{-\gamma_2 z}] \quad (4.39)$$

For simplicity, we assume $d_1 = 0$ and $d_2 = d$. d is the thickness of metal slab. Then the coefficient A_1 can be obtained by the following relationship

$$\begin{aligned}\mathbf{E}_1^0 &= i\omega\mu_1\nabla \times (\hat{z}\psi_{in}) = -i\omega\mu_1\hat{\phi}\frac{\partial\psi_{in}}{\partial\rho} \\ &= i\omega\mu_1\nabla \times (\hat{z}A_1e^{\gamma_1z}) = \hat{\phi}i\omega\mu_0Iv \int_0^\infty J_1(\kappa\rho)\mathfrak{S}(\kappa)e^{\kappa z}d\kappa\end{aligned}\quad (4.40)$$

Now the E field in the conductor region 2 could be expressed as

$$\begin{aligned}\mathbf{E}_2^{total} &= i\omega\mu_2\nabla \times (\hat{z}\psi_2(\mathbf{r})) \\ &= \hat{\phi}i\omega\mu_2Iv \int_0^\infty J_1(\kappa\rho)\mathfrak{S}(\kappa)\frac{T_{12}}{1-\Gamma_{21}\Gamma_{23}e^{-2\gamma_2d}}[e^{\gamma_2z} + \Gamma_{23}e^{-2\gamma_2d}e^{-\gamma_2z}]d\kappa\end{aligned}\quad (4.41)$$

If the slab is in the free space, namely region 3 is air, hence we have the reflection coefficient Γ_{ij} and transmission coefficient T_{ij} as

$$\begin{aligned}\Gamma_{23} = \Gamma_{21} &= \frac{\gamma_2\mu_1 - \gamma_1\mu_2}{\gamma_2\mu_1 + \gamma_1\mu_2} = \frac{\gamma_2 - \kappa\mu_{r2}}{\gamma_2 + \kappa\mu_{r2}} \\ T_{12} &= \frac{2\gamma_1\mu_1}{\gamma_1\mu_2 + \gamma_2\mu_1} = \frac{2\kappa}{\kappa\mu_{r2} + \gamma_2}\end{aligned}\quad (4.42)$$

Then we have the total TE potential in region 2 as

$$\psi_2 = A_12\kappa\frac{(\gamma_2 + \kappa\mu_{r2})e^{\gamma_2z} + (\gamma_2 - \kappa\mu_{r2})e^{-\gamma_2(z+2d)}}{(\gamma_2 + \kappa\mu_{r2})^2 - (\gamma_2 - \kappa\mu_{r2})^2e^{-2\gamma_2d}}\quad (4.43)$$

and the electric and magnetic fields in region 2 as

$$\mathbf{E}_2^{total} = \hat{\phi}i\omega\mu_2Iv \int_0^\infty J_1(\kappa\rho)\mathfrak{S}(\kappa) \left[2\kappa\frac{(\gamma_2 + \kappa\mu_{r2})e^{\gamma_2z} + (\gamma_2 - \kappa\mu_{r2})e^{-\gamma_2(z+2d)}}{(\gamma_2 + \kappa\mu_{r2})^2 - (\gamma_2 - \kappa\mu_{r2})^2e^{-2\gamma_2d}} \right] d\kappa\quad (4.44)$$

$$H_{\rho,2}^{total} = -Iv \int_0^\infty J_1(\kappa\rho)\mathfrak{S}(\kappa) \left[2\kappa\frac{(\gamma_2 + \kappa\mu_{r2})\gamma_2e^{\gamma_2z} - (\gamma_2 - \kappa\mu_{r2})\gamma_2e^{-\gamma_2(z+2d)}}{(\gamma_2 + \kappa\mu_{r2})^2 - (\gamma_2 - \kappa\mu_{r2})^2e^{-2\gamma_2d}} \right] d\kappa\quad (4.45)$$

$$H_{z,2}^{total} = Iv \int_0^\infty J_0(\kappa\rho)\mathfrak{S}(\kappa) \left[2\kappa^2\frac{(\gamma_2 + \kappa\mu_{r2})e^{\gamma_2z} + (\gamma_2 - \kappa\mu_{r2})e^{-\gamma_2(z+2d)}}{(\gamma_2 + \kappa\mu_{r2})^2 - (\gamma_2 - \kappa\mu_{r2})^2e^{-2\gamma_2d}} \right] d\kappa\quad (4.46)$$

If the slab is non-ferromagnetic material with $\mu_{r2} = 1$, then electric field in regio 2 reduces to

$$\mathbf{E}_2^{total} = \hat{\phi}i\omega\mu_2Iv \int_0^\infty J_1(\kappa\rho)\mathfrak{S}(\kappa) \left[2\kappa\frac{(\kappa + \gamma_2)e^{\gamma_2z} + (\gamma_2 - \kappa)e^{-\gamma_2(z+2d)}}{(\kappa + \gamma_2)^2 - (\gamma_2 - \kappa)^2e^{-2\gamma_2d}} \right] d\kappa\quad (4.47)$$

Similarly, The TE potential in region 3 can be obtained. By applying the constraint at interface $z = -d_2$, we have

$$A_3 e^{-\gamma_3 d_2} = T_{23} A_2 e^{-\gamma_2 d_2} \quad (4.48)$$

Then A_3 can be expressed in terms of A_2 as

$$A_3 = T_{23} A_2 e^{(\gamma_3 - \gamma_2) d_2} \quad (4.49)$$

By eliminating A_2 , we have

$$\psi_3 = A_1 \frac{T_{12} e^{(\gamma_2 - \gamma_1) d_1}}{1 - \Gamma_{21} \Gamma_{23} e^{-2\gamma_2 (d_2 - d_1)}} T_{23} e^{(\gamma_3 - \gamma_2) d_2} e^{\gamma_3 z} \quad (4.50)$$

Again, if the slab is located in the free space, $d_1 = 0$ and $d_2 = d$, we have

$$\psi_3 = A_1 \frac{4\kappa\gamma_2\mu_{r2} e^{(\kappa - \gamma_2)d} e^{\kappa z}}{(\gamma_2 + \kappa\mu_{r2})^2 - (\gamma_2 - \kappa\mu_{r2})^2 e^{-2\gamma_2 d}} \quad (4.51)$$

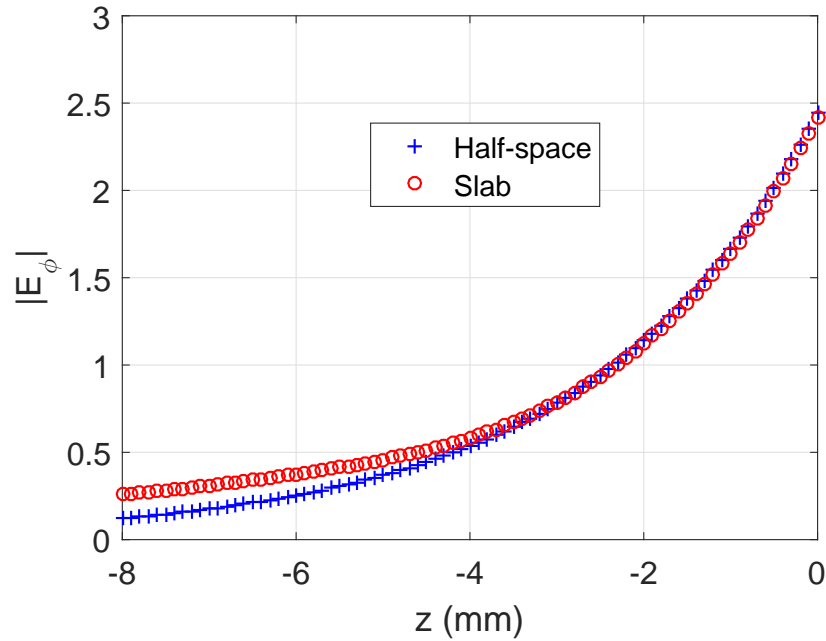
Once we have the TE potential, the electric and magnetic fields can be obtained. For example,

$$\begin{aligned} \mathbf{E}_3^{total} &= i\omega\mu_3 \nabla \times (\hat{z}\psi_3(\mathbf{r})) \\ &= \hat{\phi} i\omega\mu_3 I v \int_0^\infty J_1(\kappa\rho) \mathfrak{S}(\kappa) \frac{4\kappa\gamma_2\mu_{r2} e^{(\kappa - \gamma_2)d} e^{\kappa z}}{(\gamma_2 + \kappa\mu_{r2})^2 - (\gamma_2 - \kappa\mu_{r2})^2 e^{-2\gamma_2 d}} d\kappa \end{aligned} \quad (4.52)$$

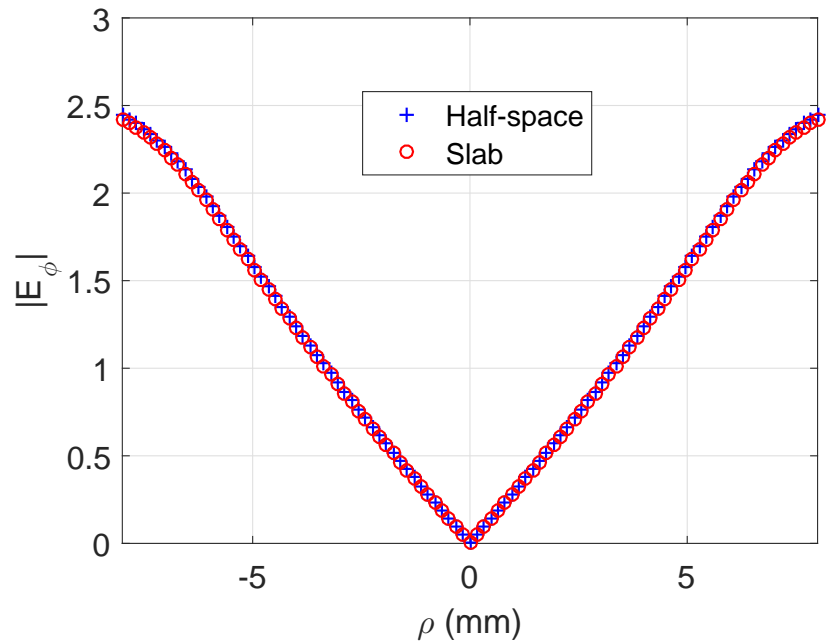
The electric field distribution of a coil above conductor slab is calculated, Fig. 4.7. The frequency is 0.9 kHz. The coil size and conductor parameters are the same as the TEM Problem 15, which is shown in Tab. 5.1. The excited current is set as 1 Ampere. The slab thickness is set as 6 mm.

4.2 Incident Field in Cylindrical Layered Structure

The EM fields of a rotary coil has been presented by Burke [33] and an alternative method was proposed by Bowler via single layer potential [104]. The more general case of a rotary coil with arbitrary orientation will be discussed in Chapter 7. In this section, the electric and magnetic fields of a rotary coil inside borehole and tube will be summarized.



(a) The comparison of $|E_\phi|$ fields along the z direction between half-space and slab conductor



(b) The comparison of $|E_\phi|$ fields at the half-space and slab interface

Figure 4.7: The electromagnetic fields of TEM Problem 15, the slab thickness is 6 mm

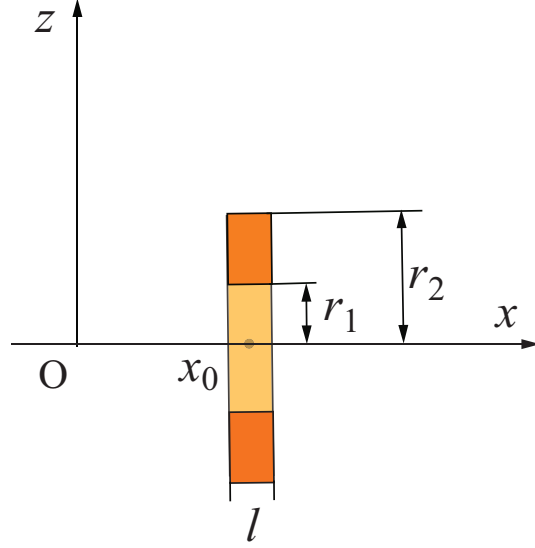


Figure 4.8: A rotary coil locates in free space

4.2.1 Incident Field in Free-space

The electric field and magnetic field in the source-free region can be expressed in terms of TE scalar potential ψ_1 and TM scalar potential ψ_2 as follow.

$$\mathbf{E} = i\omega\mu[\nabla \times (\hat{z}\psi_1) + \nabla \times \nabla \times (\hat{z}\psi_2)] \quad (4.53)$$

$$\mathbf{H} = \nabla \times \nabla \times (\hat{z}\psi_1) + k^2\nabla \times (\hat{z}\psi_2) \quad (4.54)$$

where μ is the permeability of medium. $k^2 = i\omega\mu\sigma$. σ is the conductivity of medium. Assuming the circular coil is in the air region, the magnetic field in the air is only determined by the TE potential, ψ_1 , since $k^2 = 0$. In the air region, the TE potential can be expressed as

$$\psi_{1c} = \sum_{m=-\infty}^{\infty} e^{im\varphi} \int_{-\infty}^{\infty} C_m(v) \begin{cases} I_m(|v|\rho) & \rho < \alpha_1 \\ K_m(|v|\rho) & \rho > \alpha_2 \end{cases} e^{ivz} dv, \quad (4.55)$$

here $C_m(v)$ is the source coefficients which is determined by the coil parameters. m is the index in azimuthal direction.

For a rotary coil whose axis is perpendicular to the axis of the z axis of the global coordinate system, $C_m(v)$ can be expressed as

$$\begin{aligned} C_m(v) &= \\ &= \frac{iIn_d}{v^2\pi^2} \sum_{n=-\infty}^{+\infty} \cos\left(\frac{n\pi}{2}\right) [I_{m+n}(|v||x_0+t|) - I_{m+n}(|v||x_0-t|)] \\ &\times \int_{r_1}^{r_2} \int_0^{\rho_0} I_n(|v||y_1|) \sin(v\sqrt{\rho_0^2 - y_1^2}) dy_1 d\rho_0 \end{aligned} \quad (4.56)$$

Here $n_d = N/l(r_2 - r_1)$ is the turn density, N is the filament turns of coil, $t = l/2$ is half of the coil axial length, r_1, r_2 is inner and outer radius of coil separately.

In free space, we can get magnetic flux density as due to $k^2 = 0$

$$\mathbf{B} = \nabla\Psi^0 = \nabla \left[\mu_0 \frac{\partial\psi_{1c}}{\partial z} \right] \quad (4.57)$$

Ψ^0 can be obtained by

$$\Psi^0 = \sum_{m=-\infty}^{\infty} e^{im\varphi} \int_{-\infty}^{\infty} \tilde{C}_m(v) \begin{cases} I_m(|v|\rho) & \rho < \alpha_1 \\ K_m(|v|\rho) & \rho > \alpha_2 \end{cases} e^{ivz} dv, \quad (4.58)$$

where $\tilde{C}_m(v) = iv\mu_0 C_m(v)$

Provided we know the source coefficients $\tilde{C}_m(v)$ of Ψ^0 , the magnetic field can be obtained by

$$\mathbf{B}^0 = \nabla\Psi^0 = \hat{\rho} \frac{\partial\Psi^0}{\partial\rho} + \hat{\phi} \frac{1}{\rho} \frac{\partial\Psi^0}{\partial\phi} + \hat{z} \frac{\partial\Psi^0}{\partial z} \quad (4.59)$$

For the coil inside borehole or tube, we have ($\rho > \alpha_2$) the incident magnetic flux density B

$$B_\rho^0 = \frac{\partial\Psi^0}{\partial\rho} = \sum_{m=-\infty}^{\infty} e^{im\varphi} \int_{-\infty}^{\infty} [K_m(|v|\rho)]' \tilde{C}_m(v) e^{ivz} dv \quad (4.60)$$

$$B_\phi^0 = \frac{1}{\rho} \frac{\partial\Psi^0}{\partial\phi} = im \sum_{m=-\infty}^{\infty} e^{im\varphi} \int_{-\infty}^{\infty} \frac{1}{\rho} K_m(|v|\rho) \tilde{C}_m(v) e^{ivz} dv \quad (4.61)$$

$$B_z^0 = \frac{\partial\Psi^0}{\partial z} = \sum_{m=-\infty}^{\infty} e^{im\varphi} \int_{-\infty}^{\infty} K_m(|v|\rho) iv \tilde{C}_m(v) e^{ivz} dv \quad (4.62)$$

The following recursion relationships of Bessel K function[102] are used in the derivation.

$$K'_m(z) = -K_{m-1}(z) - \frac{m}{z} K_m(z) \quad (4.63)$$

$$K'_m(z) = -K_{m+1}(z) + \frac{m}{z}K_m(z) \quad (4.64)$$

$$K'_m(z) = -\frac{K_{m+1}(z) + K_{m-1}(z)}{2} \quad (4.65)$$

4.2.2 Incident Field in the Conductive Region for a Borehole

Assuming the coil is inside the borehole. there will be reflection and transmission with the existence of the borehole. We can write the incident and reflected scalar potentials in the following form

$$\psi_1^0 = \sum_{m=-\infty}^{\infty} e^{im\varphi} \int_{-\infty}^{\infty} C_m(v) K_m(|v|\rho) e^{ivz} dv \quad (4.66)$$

$$\psi_1^{re} = \sum_{m=-\infty}^{\infty} e^{im\varphi} \int_{-\infty}^{\infty} C_m^{re}(v) I_m(|v|\rho) e^{ivz} dv \quad (4.67)$$

in the air region and

$$\psi_1^{(2)} = \sum_{m=-\infty}^{\infty} e^{im\varphi} \int_{-\infty}^{\infty} C_m^{(2)}(v) K_m(\gamma\rho) e^{ivz} dv \quad (4.68)$$

$$\psi_2^{(2)} = \sum_{m=-\infty}^{\infty} e^{im\varphi} \int_{-\infty}^{\infty} D_m^{(2)}(v) K_m(\gamma\rho) e^{ivz} dv \quad (4.69)$$

in the conductive region.

where $C_m^{re}(v) = \mathbf{\Gamma}_{12}^g(1,1)C_m(v)$. $C_m^{(2)}(v) = \mathbf{T}_{12}^g(1,1)C_m(v)$, $D_m^{(2)}(v) = \mathbf{T}_{12}^g(2,1)C_m(v)$ and $\gamma = \sqrt{v^2 - k^2}$. $\mathbf{\Gamma}_{12}^g$ is the non-normalized reflection matrix for region 1 to region 2. $\mathbf{\Gamma}_{12}^g(1,1)$ indicates the (1,1) component of reflection matrix $\mathbf{\Gamma}_{12}^g$. Similarly to $\mathbf{T}_{12}^g(2,1)$. $\mathbf{T}_{12}^g(2,2)$ and $\mathbf{T}_{12}^g(1,2)$ are vanished, which indicates no transmission related to TM mode. More details about reflection and transmission coefficients are in Appendix A. From Eq 4.53 and 4.54, we obtain

$$\tilde{H}_\rho = \frac{\partial^2 \tilde{\psi}_1}{\partial z \partial \rho} + imk^2 \frac{\tilde{\psi}_2}{\rho} \quad (4.70)$$

$$\tilde{E}_\rho = i\omega\mu \left(\frac{im}{\rho} \tilde{\psi}_1 + \frac{\partial^2}{\partial z \partial \rho} \tilde{\psi}_2 \right) \quad (4.71)$$

$$\tilde{H}_\phi = \frac{im}{\rho} \frac{\partial \tilde{\psi}_1}{\partial z} - k^2 \frac{\partial \tilde{\psi}_2}{\partial \rho} \quad (4.72)$$

$$\tilde{E}_\phi = -i\omega\mu \left(\frac{\partial \tilde{\psi}_1}{\partial \rho} - \frac{im}{\rho} \frac{\partial \tilde{\psi}_2}{\partial z} \right) \quad (4.73)$$

$$\tilde{H}_z = \frac{\partial^2 \tilde{\psi}_1}{\partial z^2} + k^2 \tilde{\psi}_1 \quad (4.74)$$

$$\tilde{E}_z = i\omega\mu \left(\frac{\partial^2 \tilde{\psi}_2}{\partial z^2} + k^2 \tilde{\psi}_2 \right) \quad (4.75)$$

The explicit expressions of electric field are summarized as follow

$$E_\rho = i\omega\mu \sum_{m=-\infty}^{\infty} e^{im\varphi} \int_{-\infty}^{\infty} e^{ivz} \left(\frac{im}{\rho} K_m(\gamma\rho) C_m^{(2)} + iv\gamma K_m'(\gamma\rho) D_m^{(2)} \right) dv \quad (4.76)$$

$$= i\omega\mu \sum_{m=-\infty}^{\infty} e^{im\varphi} \int_{-\infty}^{\infty} e^{ivz} \frac{1}{\rho} \left(im C_m^{(2)} + iv M_m(\gamma\rho) D_m^{(2)} \right) K_m(\gamma\rho) dv$$

$$E_\phi = -i\omega\mu \sum_{m=-\infty}^{\infty} e^{im\varphi} \int_{-\infty}^{\infty} e^{ivz} \left(\gamma K_m'(\gamma\rho) C_m^{(2)} + \frac{mv}{\rho} K_m(\gamma\rho) D_m^{(2)} \right) dv \quad (4.77)$$

$$= -i\omega\mu \sum_{m=-\infty}^{\infty} e^{im\varphi} \int_{-\infty}^{\infty} e^{ivz} \frac{1}{\rho} \left(M_m(\gamma\rho) C_m^{(2)} + mv D_m^{(2)} \right) K_m(\gamma\rho) dv$$

$$E_z = -i\omega\mu \sum_{m=-\infty}^{\infty} e^{im\varphi} \int_{-\infty}^{\infty} e^{ivz} \left(\gamma^2 K_m(\gamma\rho) D_m^{(2)} \right) dv \quad (4.78)$$

Table 4.1: Coil and borehole parameters

Coil Inner Raids, r_1	1.529mm
Coil Outer Raids, r_2	3.918mm
Coil Thickness	1.044mm
Number of Turns	305
Isolated DC Coil Inductance, L_0	465 μ H
Tube Inner Diameter	25mm
Tube Outer Diameter	300mm
Conductivity (MS/m)	23.05
Relative Magnetic Permeability, μ_r	1
Liftoff, λ	0.73mm

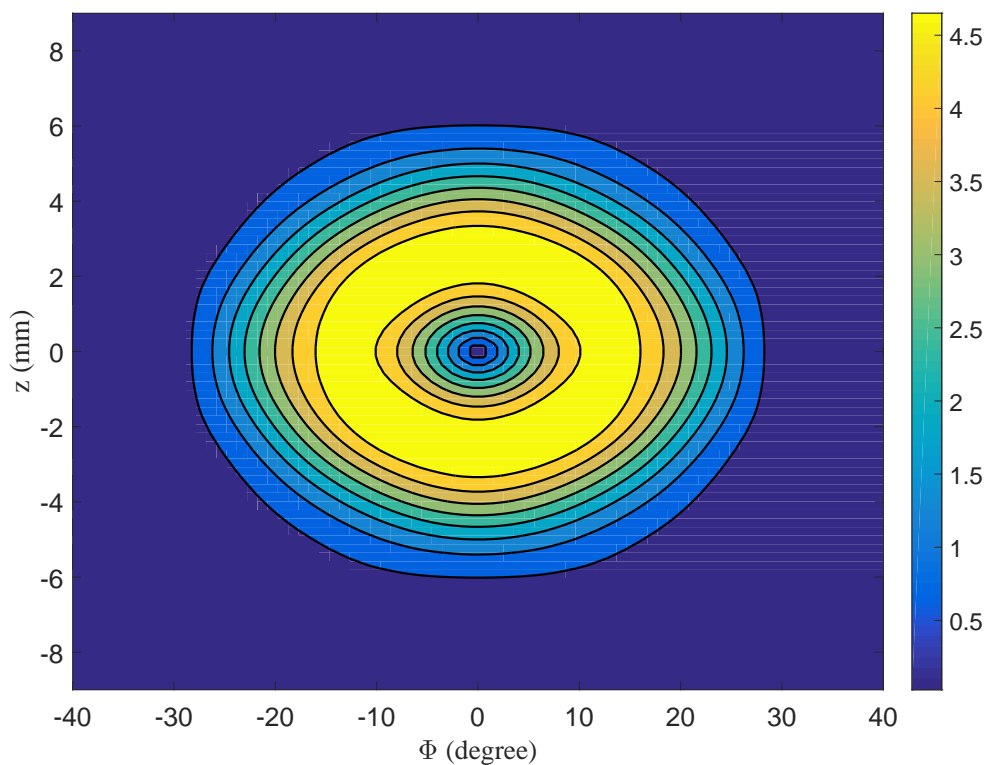


Figure 4.9: The $|E_\phi|$ field at the borehole interface

The electric field $|E_\phi|$ of a coil inside a borehole is calculated, Fig. 4.9. The frequency is 40 kHz. The coil size and borehole parameters are shown in Tab. 4.1 [19]. The excited current is set as 1 Ampere.

4.2.3 Incident Field in a Tube

The incident field inside the tube material can be obtained by using similar procedures as borehole. Based the above derivation, we can get the ψ_1 and ψ_2 potentials in the tube with inside source, which is used to calculate the incident field.

$$\begin{bmatrix} \tilde{\psi}_{1,\rho} \\ \tilde{\psi}_{2,\rho} \end{bmatrix}_2 = [K_m(\gamma_2\rho)\mathcal{I} + I_m(\gamma_2\rho)\mathbf{\Gamma}_{23}^g] \cdot [\mathcal{I} - \mathbf{\Gamma}_{21}^g \cdot \mathbf{\Gamma}_{23}^g]^{-1} \cdot \mathbf{T}_{12}^g \cdot \frac{\mathbf{a}_{1m}}{K_m(\gamma_1a)} \quad (4.79)$$

where

$$\frac{\mathbf{a}_{1m}}{K_m(\gamma_1a)} = \begin{bmatrix} C_m(v) \\ 0 \end{bmatrix} \quad (4.80)$$

Then we have

$$\begin{aligned} \begin{bmatrix} \tilde{\psi}_{1,\rho} \\ \tilde{\psi}_{2,\rho} \end{bmatrix}_2 &= \frac{K_m(\gamma_1a)}{K_m(\gamma_2a)} \left[K_m(\gamma_2\rho)\mathcal{I} + I_m(\gamma_2\rho) \frac{K_m(\gamma_2b)}{I_m(\gamma_2b)} \mathbf{\Gamma}_{23} \right] \\ &\cdot \left[\mathcal{I} - \frac{I_m(\gamma_2a)K_m(\gamma_2b)}{I_m(\gamma_2b)K_m(\gamma_2a)} \mathbf{\Gamma}_{21} \cdot \mathbf{\Gamma}_{23} \right]^{-1} \cdot \mathbf{T}_{12} \cdot \begin{bmatrix} C_m(v) \\ 0 \end{bmatrix} \end{aligned} \quad (4.81)$$

Defining

$$\left[\mathcal{I} - \frac{I_m(\gamma_2a)K_m(\gamma_2b)}{I_m(\gamma_2b)K_m(\gamma_2a)} \mathbf{\Gamma}_{21} \cdot \mathbf{\Gamma}_{23} \right]^{-1} \cdot \mathbf{T}_{12} = \mathbf{M} \quad (4.82)$$

$$\frac{K_m(\gamma_1a)}{K_m(\gamma_2a)} = \alpha \quad (4.83)$$

$$\frac{K_m(\gamma_2b)}{I_m(\gamma_2b)} = \beta \quad (4.84)$$

$$\begin{aligned} \begin{bmatrix} \tilde{\psi}_{1,\rho} \\ \tilde{\psi}_{2,\rho} \end{bmatrix}_2 &= \alpha [K_m(\gamma_2\rho)\mathcal{I} + I_m(\gamma_2\rho)\beta\mathbf{\Gamma}_{23}] \cdot \mathbf{M} \cdot \begin{bmatrix} C_m(v) \\ 0 \end{bmatrix} \\ &= \alpha \begin{bmatrix} K_m(\gamma_2\rho) + I_m(\gamma_2\rho)\beta\mathbf{\Gamma}_{23,(11)} & I_m(\gamma_2\rho)\beta\mathbf{\Gamma}_{23,(12)} \\ I_m(\gamma_2\rho)\beta\mathbf{\Gamma}_{23,(21)} & K_m(\gamma_2\rho) + I_m(\gamma_2\rho)\beta\mathbf{\Gamma}_{23,(22)} \end{bmatrix} \cdot \begin{bmatrix} M_{(11)}C_m(v) \\ M_{(21)}C_m(v) \end{bmatrix} \\ &= \alpha C_m(v) \begin{bmatrix} K_m(\gamma_2\rho) + I_m(\gamma_2\rho)\beta\mathbf{\Gamma}_{23,(11)} & I_m(\gamma_2\rho)\beta\mathbf{\Gamma}_{23,(12)} \\ I_m(\gamma_2\rho)\beta\mathbf{\Gamma}_{23,(21)} & K_m(\gamma_2\rho) + I_m(\gamma_2\rho)\beta\mathbf{\Gamma}_{23,(22)} \end{bmatrix} \cdot \begin{bmatrix} M_{(11)} \\ M_{(21)} \end{bmatrix} \end{aligned} \quad (4.85)$$

Then

$$\tilde{\psi}_{1,\rho} = \alpha C_m(v) \{ [K_m(\gamma_2\rho) + I_m(\gamma_2\rho)\beta\mathbf{\Gamma}_{23,(11)}] M_{(11)} + [I_m(\gamma_2\rho)\beta\mathbf{\Gamma}_{23,(12)}] M_{(21)} \} \quad (4.86)$$

$$\tilde{\psi}_{2,\rho} = \alpha C_m(v) \{ [I_m(\gamma_2\rho)\beta\Gamma_{23,(21)}] M_{(11)} + [K_m(\gamma_2\rho) + I_m(\gamma_2\rho)\beta\Gamma_{23,(22)}] M_{(21)} \} \quad (4.87)$$

Now the incident field in the tube can be obtained and expressed as

$$\tilde{E}_\rho = i\omega\mu\alpha C_m(v) \frac{1}{\rho} \left\{ \begin{array}{l} im [K_m(\gamma_2\rho) + I_m(\gamma_2\rho)\beta\Gamma_{23,(11)}] M_{(11)} \\ + im [I_m(\gamma_2\rho)\beta\Gamma_{23,(12)}] M_{(21)} \\ + i\kappa [\Lambda_m(\gamma_2\rho)I_m(\gamma_2\rho)\beta\Gamma_{23,(21)}] M_{(11)} \\ + i\kappa [M_m(\gamma_2\rho)K_m(\gamma_2\rho) + \Lambda_m(\gamma_2\rho)I_m(\gamma_2\rho)\beta\Gamma_{23,(22)}] M_{(21)} \end{array} \right\} \quad (4.88)$$

$$\tilde{E}_\phi = -i\omega\mu\alpha C_m(v) \frac{1}{\rho} \left\{ \begin{array}{l} [M_m(\gamma_2\rho)K_m(\gamma_2\rho) + \Lambda_m(\gamma_2\rho)I_m(\gamma_2\rho)\beta\Gamma_{23,(11)}] M_{(11)} \\ + [\Lambda_m(\gamma_2\rho)I_m(\gamma_2\rho)\beta\Gamma_{23,(12)}] M_{(21)} \\ + m\kappa [I_m(\gamma_2\rho)\beta\Gamma_{23,(21)}] M_{(11)} \\ + m\kappa [K_m(\gamma_2\rho) + I_m(\gamma_2\rho)\beta\Gamma_{23,(22)}] M_{(21)} \end{array} \right\} \quad (4.89)$$

$$\tilde{E}_z = -i\omega\mu\alpha C_m(v)\gamma_2^2 \{ [I_m(\gamma_2\rho)\beta\Gamma_{23,(21)}] M_{(11)} + [K_m(\gamma_2\rho) + I_m(\gamma_2\rho)\beta\Gamma_{23,(22)}] M_{(21)} \} \quad (4.90)$$

$$E_\rho = \sum_{m=-\infty}^{\infty} e^{im\varphi} \int_{-\infty}^{\infty} e^{i\kappa z} \tilde{E}_\rho d\kappa \quad (4.91)$$

$$E_\phi = \sum_{m=-\infty}^{\infty} e^{im\varphi} \int_{-\infty}^{\infty} e^{i\kappa z} \tilde{E}_\phi d\kappa \quad (4.92)$$

$$E_z = \sum_{m=-\infty}^{\infty} e^{im\varphi} \int_{-\infty}^{\infty} e^{i\kappa z} \tilde{E}_z d\kappa \quad (4.93)$$

The magnitude of electrical field distribution at the tube inner interface has been calculated, Fig. 8.8a in terms of distance in z direction and circumferential direction ($\phi \times a$). The eddy-current coil parameters and tube dimensions are summarized in Tab (7.1). Once obtaining the electrical field distribution, the magnitude of current distribution can be easily evaluated by multiplying the conductivity of tube material.

CHAPTER 5. COIL IMPEDANCE CHANGES DUE TO CRACKS IN FERROMAGNETIC PLANAR STRUCTURES

The eddy current modeling of the planar structure is an important topic due to that a lot of practical EC problems can be represented by simple structure modeling, for example the engine blade can be modeled as thin plate and the composite cabin shield can be modeled as planar-layered structure. In this chapter, we have implemented the MoM of half-space and thin slab for ferromagnetic conductive material based the formulation discussed in chapter 3. The theoretical predicted results were compared with existing benchmark experimental data. Excellent agreement was achieved.

5.1 Green's Function for an Unbounded Domain

The Green's function, $G_0(\mathbf{r}, \mathbf{r}')$, due to a point source in a homogeneous, linear and isotropic medium with conductivity σ and permeability μ satisfies the following equation

$$(\nabla^2 + k^2)G_0(\mathbf{r}, \mathbf{r}') = -\delta(\mathbf{r} - \mathbf{r}') \quad (5.1)$$

and the solution can be expressed as $G_0(\mathbf{r}, \mathbf{r}') = \frac{e^{ikR}}{4\pi R}$. But another alternative solution can be obtained by using 2-D Fourier transform.

By using 2-D Fourier transform, $G_0(\mathbf{r}, \mathbf{r}')$ could be expressed as the following form

$$G_0(\mathbf{r}, \mathbf{r}') = \frac{1}{(2\pi)^2} \int_{-\infty}^{\infty} \int_{-\infty}^{\infty} \tilde{G}_0(k_x, k_y, z, z') e^{ik_x x + ik_y y} e^{-i(k_x x' + k_y y')} dk_x dk_y \quad (5.2)$$

Substituting it back into Eq. 5.1, we have

$$\left[\frac{\partial^2}{\partial z^2} - \gamma^2 \right] \tilde{G}_0(k_x, k_y, z, z') = -\delta(z - z') \quad (5.3)$$

where $\gamma = \sqrt{k_x^2 + k_y^2 - k^2} = \sqrt{\kappa^2 - k^2}$, $k^2 = i\omega\mu\sigma$. $\tilde{G}_0(k_x, k_y, z, z')$ is also called the spectral domain Green function. If the medium is free space, $k^2 = i\omega\mu\sigma = 0$. The general solution of

$\tilde{G}_0(k_x, k_y, z, z')$ can be written as

$$\tilde{G}_0(k_x, k_y, z, z') = Ae^{-\gamma(z-z')} + Be^{\gamma(z-z')} \quad (5.4)$$

in terms of undetermined coefficient A and B . In the z dimension, the solution region can be divided as two parts, namely,

$$\tilde{G}_0(k_x, k_y, z, z') = Ae^{-\gamma(z-z')}$$

for $z - z' > 0$ and

$$\tilde{G}_0(k_x, k_y, z, z') = Be^{\gamma(z-z')}$$

for $z - z' < 0$. By taking the integration of Eq. 5.3 from $z' - \varepsilon$ to $z' + \varepsilon$ (ε is infinitesimal) and together with that the $\tilde{G}_0(k_x, k_y, z, z')$ should be continuous at $z = z'$, $\tilde{G}_0(k_x, k_y, z, z')$ is determined as

$$\tilde{G}_0(k_x, k_y, z, z') = \frac{1}{2\gamma} e^{-\gamma|z-z'|} \quad (5.5)$$

Now the green function becomes

$$G_0(\mathbf{r}, \mathbf{r}') = \frac{1}{(2\pi)^2} \int_{-\infty}^{\infty} \int_{-\infty}^{\infty} \frac{1}{2\gamma} e^{-\gamma|z-z'|} e^{ik_x(x-x')} e^{ik_y(y-y')} dk_x dk_y \quad (5.6)$$

5.2 Dyadic Green's Function for a Ferromagnetic Half-space Conductor

For half-space case, we assume the upper medium (region 1) has conductivity σ_1 and permeability μ_1 , the other half conductor has conductivity σ_2 and permeability μ_2 and the source is inside conductive region 2, Fig. 5.1. In order to get the dyadic kernel for half space, a set of scalar green functions, U_{ij} and U_0 in Eq. 3.134, need to be determined first.

We know the green function can be written as the sum of a singular part and a regular part as follow.

$$G_{ij}(\mathbf{r}, \mathbf{r}') = \delta_{ij} G_0(\mathbf{r}, \mathbf{r}') + G_{ij}^{\Gamma}(\mathbf{r}, \mathbf{r}') \quad (5.7)$$

Or

$$\tilde{G}_{ij}(k_x, k_y, z, z') = \delta_{ij} \tilde{G}_0(k_x, k_y, z, z') + \tilde{G}_{ij}^{\Gamma}(k_x, k_y, z, z') \quad (5.8)$$

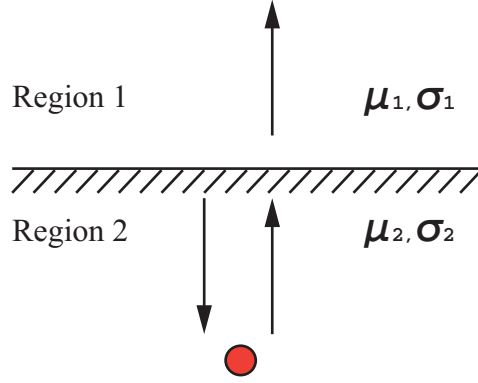


Figure 5.1: Half Space with Point Source in Region 2

in the spectral domain. $\tilde{G}_0(k_x, k_y, z, z')$ has been determined in the previous section. In the conductor, $\tilde{G}_{ij}^\Gamma(k_x, k_y, z, z')$ indicating the field migrating toward inside the conductor from the interface is represented as

$$\tilde{G}_{ij}^\Gamma(k_x, k_y, z, z') = \Gamma_{ij} \frac{1}{2\gamma_2} e^{\gamma_2 z} e^{\gamma_2 z'} \quad (5.9)$$

Or

$$G_{ij}^\Gamma = \frac{1}{(2\pi)^2} \int_{-\infty}^{\infty} \int_{-\infty}^{\infty} \Gamma_{ij} \frac{1}{2\gamma_2} e^{\gamma_2 z} e^{\gamma_2 z'} e^{ik_x(x-x')} e^{ik_y(y-y')} dk_x dk_y \quad (5.10)$$

where Γ_{ij} is the reflection coefficient of half space and $\Gamma_{ij} = 0 (i \neq j)$, which means the TE and TM modes are decoupled for planar structure. $\gamma_2 = \sqrt{k_x^2 + k_y^2 - k_2^2} = \sqrt{\kappa^2 - k_2^2}$, $k_2^2 = i\omega\mu_2\sigma_2$.

Based on definition $G_{ij}^\Gamma = -\nabla_i^2 U_{ij}$, we can easily have

$$\tilde{U}_{ij} = \frac{1}{\kappa^2} \tilde{G}_{ij}^\Gamma \quad (5.11)$$

where $\kappa^2 = k_x^2 + k_y^2$.

$$U_{11} = \frac{1}{(2\pi)^2} \int_{-\infty}^{\infty} \int_{-\infty}^{\infty} \frac{1}{\kappa^2} \frac{1}{2\gamma_2} \Gamma_{11} e^{\gamma_2(z+z')} e^{ik_x(x-x')} e^{ik_y(y-y')} dk_x dk_y \quad (5.12)$$

$$U_{22} = \frac{1}{(2\pi)^2} \int_{-\infty}^{\infty} \int_{-\infty}^{\infty} \frac{1}{\kappa^2} \frac{1}{2\gamma_2} \Gamma_{22} e^{\gamma_2(z+z')} e^{ik_x(x-x')} e^{ik_y(y-y')} dk_x dk_y \quad (5.13)$$

For eddy-current application, region 1 is usually air, $\Gamma_{11}(\kappa) = \frac{\gamma_2 - \kappa\mu_r 2}{\gamma_2 + \kappa\mu_r 2}$ and $\Gamma_{22}(\kappa) = -1$. Note that U_{ij} could be singular for $\kappa = 0$. However, we are using the scalar kernels to get the dyadic kernel rather than calculating the scalar kernels directly. In the end, it turns out the reflected part of dyadic kernel is not singular.

Now all four dyadic kernels can be obtained by substituting U_{ij} into Eq. 3.145, 3.148, 3.149 and 3.151 or

$$\mathcal{G}_{ee}^{\Gamma}(\mathbf{r}, \mathbf{r}') = (\nabla \times \hat{z})(\nabla' \times \hat{z})U_{11} + \frac{1}{k_h^2}[\nabla \times (\nabla \times \hat{z})][\nabla' \times (\nabla' \times \hat{z})]U_{22} \quad (5.14)$$

$$\mathcal{G}_{me}^{\Gamma}(\mathbf{r}, \mathbf{r}') = (\nabla \times \nabla \times \hat{z})(\nabla' \times \hat{z})U_{11} + (\nabla \times \hat{z})[\nabla' \times (\nabla' \times \hat{z})]U_{22} \quad (5.15)$$

$$\mathcal{G}_{mm}^{\Gamma}(\mathbf{r}, \mathbf{r}') = \frac{1}{k_h^2}(\nabla \times \nabla \times \hat{z})(\nabla' \times \nabla' \times \hat{z})U_{11} + (\nabla \times \hat{z})(\nabla' \times \hat{z})U_{22} \quad (5.16)$$

$$\mathcal{G}_{em}^{\Gamma}(\mathbf{r}, \mathbf{r}') = (\nabla \times \hat{z})(\nabla' \times \nabla' \times \hat{z})U_{11} + (\nabla \times \nabla \times \hat{z})(\nabla' \times \hat{z})U_{22} \quad (5.17)$$

where the host wave number is $k_h = k_2$. ∇_t^2 or $\nabla_t'^2$ will introduce $-\kappa^2 = -(k_x^2 + k_y^2)$. Since the cumbersome derivation of formulation, here we only show the final explicit expressions of reflected part of dyadic Green's functions for reference.

Then we have $\mathcal{G}_{ee}^{\Gamma}$

$$\mathcal{G}_{ee}^{\Gamma}(\mathbf{r}, \mathbf{r}') = \frac{1}{(2\pi)^2} \frac{1}{k_2^2} \int_{-\infty}^{\infty} \int_{-\infty}^{\infty} \frac{e^{\gamma_2(z+z')}}{2\gamma_2\kappa^2} \tilde{\mathcal{G}}_{ee}^{\Gamma} e^{ik_x(x-x')} e^{ik_y(y-y')} dk_x dk_y \quad (5.18)$$

where

$$\tilde{\mathcal{G}}_{ee}^{\Gamma} = \begin{bmatrix} k_2^2 k_y^2 \Gamma_{11} + \Gamma_{22} k_x^2 \gamma_2^2 & -k_2^2 k_x k_y \Gamma_{11} + \Gamma_{22} k_x k_y \gamma_2^2 & \Gamma_{22} \kappa^2 i k_x \gamma_2 \\ -k_2^2 k_x k_y \Gamma_{11} + \Gamma_{22} k_x k_y \gamma_2^2 & k_2^2 k_x^2 \Gamma_{11} + \Gamma_{22} k_y^2 \gamma_2^2 & \Gamma_{22} \kappa^2 i k_y \gamma_2 \\ -\Gamma_{22} \kappa^2 i k_x \gamma_2 & -\Gamma_{22} \kappa^2 i k_y \gamma_2 & \Gamma_{22} \kappa^4 \end{bmatrix} \quad (5.19)$$

Note that for the non-ferromagnetic problem, only $\hat{x}\hat{x}$ component is needed for narrow notch EC modeling [22]

$$\begin{aligned} G_{ee,xx}^{\Gamma}(\mathbf{r}, \mathbf{r}') &= \frac{\partial^2}{\partial y \partial y'} U_{11} + \frac{1}{k_2^2} \frac{\partial^4}{\partial x \partial z \partial x' \partial z'} U_{22} \\ &= \frac{1}{(2\pi)^2} \frac{1}{k_2^2} \int_{-\infty}^{\infty} \int_{-\infty}^{\infty} \frac{e^{\gamma_2(z+z')}}{2\gamma_2\kappa^2} [k_2^2 k_y^2 \Gamma_{11} + \Gamma_{22} k_x^2 \gamma_2^2] e^{ik_x(x-x')} e^{ik_y(y-y')} dk_x dk_y \end{aligned} \quad (5.20)$$

for $\mathcal{G}_{me}^{\Gamma}$

$$\mathcal{G}_{me}^{\Gamma}(\mathbf{r}, \mathbf{r}') = \frac{1}{(2\pi)^2} \int_{-\infty}^{\infty} \int_{-\infty}^{\infty} \frac{e^{\gamma_2(z+z')}}{2\kappa^2} \tilde{\mathcal{G}}_{me}^{\Gamma} e^{ik_x(x-x')} e^{ik_y(y-y')} dk_x dk_y \quad (5.21)$$

where

$$\tilde{\mathcal{G}}_{me}^{\Gamma} = \begin{bmatrix} k_x k_y \Gamma_{11} + k_x k_y \Gamma_{22} & -k_x^2 \Gamma_{11} + k_y^2 \Gamma_{22} & \Gamma_{22} \kappa^2 i k_y / \gamma_2 \\ k_y^2 \Gamma_{11} - k_x^2 \Gamma_{22} & -k_x k_y \Gamma_{11} - k_x k_y \Gamma_{22} & -\Gamma_{22} \kappa^2 i k_x / \gamma_2 \\ -\Gamma_{11} \kappa^2 i k_y / \gamma_2 & \Gamma_{11} \kappa^2 i k_x / \gamma_2 & 0 \end{bmatrix} \quad (5.22)$$

for \mathcal{G}_{mm}^Γ

$$\mathcal{G}_{mm}^\Gamma(\mathbf{r}, \mathbf{r}') = \frac{1}{(2\pi)^2} \frac{1}{k_2^2} \int_{-\infty}^{\infty} \int_{-\infty}^{\infty} \frac{e^{\gamma_2(z+z')}}{2\gamma_2\kappa^2} \tilde{\mathcal{G}}_{mm}^\Gamma e^{ik_x(x-x')} e^{ik_y(y-y')} dk_x dk_y \quad (5.23)$$

where

$$\tilde{\mathcal{G}}_{mm}^\Gamma = \begin{bmatrix} \Gamma_{11}k_x^2\gamma_2^2 + k_2^2k_y^2\Gamma_{22} & \Gamma_{11}k_xk_y\gamma_2^2 - k_2^2k_xk_y\Gamma_{22} & \Gamma_{11}\kappa^2ik_x\gamma_2 \\ \Gamma_{11}k_xk_y\gamma_2^2 - k_2^2k_xk_y\Gamma_{22} & \Gamma_{11}k_y^2\gamma_2^2 + k_2^2k_x^2\Gamma_{22} & \Gamma_{11}\kappa^2ik_y\gamma_2 \\ -\Gamma_{11}\kappa^2ik_x\gamma_2 & -\Gamma_{11}\kappa^2ik_y\gamma_2 & \Gamma_{11}\kappa^4 \end{bmatrix} \quad (5.24)$$

for \mathcal{G}_{em}^Γ

$$\mathcal{G}_{em}^\Gamma(\mathbf{r}, \mathbf{r}') = \frac{1}{(2\pi)^2} \int_{-\infty}^{\infty} \int_{-\infty}^{\infty} \frac{e^{\gamma_2(z+z')}}{2\kappa^2} \tilde{\mathcal{G}}_{em}^\Gamma e^{ik_x(x-x')} e^{ik_y(y-y')} dk_x dk_y \quad (5.25)$$

where

$$\tilde{\mathcal{G}}_{em}^\Gamma = \begin{bmatrix} k_xk_y\Gamma_{11} + k_xk_y\Gamma_{22} & k_y^2\Gamma_{11} - k_x^2\Gamma_{22} & \Gamma_{11}\kappa^2ik_y/\gamma_2 \\ -k_x^2\Gamma_{11} + k_y^2\Gamma_{22} & -k_xk_y\Gamma_{11} - k_xk_y\Gamma_{22} & -\Gamma_{11}\kappa^2ik_x/\gamma_2 \\ -\Gamma_{22}\kappa^2ik_y/\gamma_2 & \Gamma_{22}\kappa^2ik_x/\gamma_2 & 0 \end{bmatrix} \quad (5.26)$$

In order to simplify the numerical calculation, the artificial boundary conditions can be applied to transform the double integral into a double Fourier series representation. The boundary conditions, namely PEC at $x = 0, y = 0$ and PMC at $x = h_x, y = h_y$, are used, which can avoid the DC component in the series [99]. Then Eq. 5.12 and Eq. 5.13 can be expressed as

$$U_{11} = \frac{4}{h_x h_y} \sum_{i=1}^{\infty} \sum_{j=1}^{\infty} \frac{1}{\kappa_{ij}^2} \frac{1}{2\gamma_{2,ij}} \Gamma_{11,ij} e^{\gamma_{2,ij}(z+z')} \sin(k_{x,i}x) \sin(k_{x,i}x') \sin(k_{y,j}y) \sin(k_{y,j}y') \quad (5.27)$$

$$U_{22} = \frac{4}{h_x h_y} \sum_{i=1}^{\infty} \sum_{j=1}^{\infty} \frac{1}{\kappa_{ij}^2} \frac{1}{2\gamma_{2,ij}} \Gamma_{22,ij} e^{\gamma_{2,ij}(z+z')} \cos(k_{x,i}x) \cos(k_{x,i}x') \cos(k_{y,j}y) \cos(k_{y,j}y') \quad (5.28)$$

where $k_{x,i} = \frac{(2i-1)\pi}{2h_x}$, $k_{y,j} = \frac{(2j-1)\pi}{2h_y}$ and $i, j = 1, 2, 3, \dots$

Then we have

$$\mathcal{G}_{ee}^\Gamma(\mathbf{r}, \mathbf{r}') = \frac{2}{h_x h_y} \frac{1}{k_2^2} \sum_{i=1}^{\infty} \sum_{j=1}^{\infty} \frac{e^{\gamma_{2,ij}(z+z')}}{\gamma_{2,ij}\kappa_{ij}^2} \tilde{\mathcal{G}}_{ee}^\Gamma * \mathbf{F}_{ee}(x, x', y, y') \quad (5.29)$$

where $\tilde{\mathcal{G}}_{ee}^\Gamma$ and $\mathbf{F}_{ee}(x, x', y, y')$ are matrix

$$\tilde{\mathcal{G}}_{ee}^\Gamma = \begin{bmatrix} k_2^2k_{y,j}^2\Gamma_{11,ij} + \Gamma_{22,ij}k_{x,i}^2\gamma_{2,ij}^2 & -k_2^2k_{x,i}k_{y,j}\Gamma_{11,ij} + \Gamma_{22,ij}k_{x,i}k_{y,j}\gamma_{2,ij}^2 & -\Gamma_{22,ij}\kappa_{ij}^2k_{x,i}\gamma_{2,ij} \\ -k_2^2k_{x,i}k_{y,j}\Gamma_{11,ij} + \Gamma_{22,ij}k_{x,i}k_{y,j}\gamma_{2,ij}^2 & k_2^2k_{x,i}^2\Gamma_{11,ij} + \Gamma_{22,ij}k_{y,j}^2\gamma_{2,ij}^2 & -\Gamma_{22,ij}\kappa_{ij}^2k_{y,j}\gamma_{2,ij} \\ -\Gamma_{22,ij}\kappa_{ij}^2k_{x,i}\gamma_{2,ij} & -\Gamma_{22,ij}\kappa_{ij}^2k_{y,j}\gamma_{2,ij} & \Gamma_{22,ij}\kappa_{ij}^4 \end{bmatrix} \quad (5.30)$$

and

$$\mathbf{F}_{ee}(x, x', y, y') = \begin{bmatrix} \sin x \sin x' \cos y \cos y' & \sin x \cos x' \cos y \sin y' & \sin x \cos x' \cos y \cos y' \\ \cos x \sin x' \sin y \cos y' & \cos x \cos x' \sin y \sin y' & \cos x \cos x' \sin y \cos y' \\ \cos x \sin x' \cos y \cos y' & \cos x \cos x' \cos y \sin y' & \cos x \cos x' \cos y \cos y' \end{bmatrix} \quad (5.31)$$

Note that the arguments of sin or cos function are simplified by dropping off the $k_{x,i}$ or $k_{y,j}$.

The operator $.*$ means

$$\begin{bmatrix} a_{11} & a_{12} & a_{13} \\ a_{21} & a_{22} & a_{23} \\ a_{31} & a_{32} & a_{33} \end{bmatrix} .* \begin{bmatrix} b_{11} & b_{12} & b_{13} \\ b_{21} & b_{22} & b_{23} \\ b_{31} & b_{32} & b_{33} \end{bmatrix} = \begin{bmatrix} a_{11}b_{11} & a_{12}b_{12} & a_{13}b_{13} \\ a_{21}b_{21} & a_{22}b_{22} & a_{23}b_{23} \\ a_{31}b_{31} & a_{32}b_{32} & a_{33}b_{33} \end{bmatrix} \quad (5.32)$$

Similarly we have

$$\mathcal{G}_{mm}^{\Gamma}(\mathbf{r}, \mathbf{r}') = \frac{2}{h_x h_y} \frac{1}{k_2^2} \sum_{i=1}^{\infty} \sum_{j=1}^{\infty} \frac{e^{\gamma_{2,ij}(z+z')}}{\gamma_{2,ij} \kappa_{ij}^2} \tilde{G}_{mm}^{\Gamma} .* \mathbf{F}_{mm}(x, x', y, y') \quad (5.33)$$

where \tilde{G}_{mm}^{Γ} and $\mathbf{F}_{mm}(x, x', y, y')$ are matrix

$$\tilde{G}_{mm}^{\Gamma} = \begin{bmatrix} k_{x,i}^2 \gamma_{2,ij}^2 \Gamma_{11,ij} + \Gamma_{22,ij} k_{y,j}^2 k_{x,i}^2 & k_{x,i} k_{y,j} \gamma_{2,ij}^2 \Gamma_{11,ij} - \Gamma_{22,ij} k_{x,i}^2 k_{y,j} & \Gamma_{11,ij} \kappa_{ij}^2 k_{x,i} \gamma_{2,ij} \\ k_{x,i} k_{y,j} \gamma_{2,ij}^2 \Gamma_{11,ij} - \Gamma_{22,ij} k_{x,i}^2 k_{y,j} & \Gamma_{11,ij} k_{y,j}^2 \gamma_{2,ij}^2 + k_{x,i}^2 k_{y,j}^2 \Gamma_{22,ij} & \Gamma_{11,ij} \kappa_{ij}^2 k_{y,j} \gamma_{2,ij} \\ \Gamma_{11,ij} \kappa_{ij}^2 k_{x,i} \gamma_{2,ij} & \Gamma_{11,ij} \kappa_{ij}^2 k_{y,j} \gamma_{2,ij} & \Gamma_{11,ij} \kappa_{ij}^4 \end{bmatrix} \quad (5.34)$$

together with

$$\mathbf{F}_{mm}(x, x', y, y') = \begin{bmatrix} \cos x \cos x' \sin y \sin y' & \cos x \sin x' \sin y \cos y' & \cos x \sin x' \sin y \sin y' \\ \sin x \cos x' \cos y \sin y' & \sin x \sin x' \cos y \cos y' & \sin x \sin x' \cos y \sin y' \\ \sin x \cos x' \sin y \sin y' & \sin x \sin x' \sin y \cos y' & \sin x \sin x' \sin y \sin y' \end{bmatrix} \quad (5.35)$$

$$\mathcal{G}_{me}^{\Gamma}(\mathbf{r}, \mathbf{r}') = \frac{2}{h_x h_y} \sum_{i=1}^{\infty} \sum_{j=1}^{\infty} \frac{e^{\gamma_{2,ij}(z+z')}}{\kappa_{ij}^2} \tilde{G}_{me}^{\Gamma} .* \mathbf{F}_{me}(x, x', y, y') \quad (5.36)$$

where \tilde{G}_{me}^{Γ} and $\mathbf{F}_{me}(x, x', y, y')$ are matrix

$$\tilde{G}_{me}^{\Gamma} = \begin{bmatrix} k_{x,i}k_{y,j}\Gamma_{11,ij} + k_{x,i}k_{y,j}\Gamma_{22,ij} & -k_{x,i}^2\Gamma_{11,ij} + k_{y,j}^2\Gamma_{22,ij} & -\Gamma_{22,ij}\kappa_{ij}^2k_{y,j}/\gamma_{2,ij} \\ k_{y,j}^2\Gamma_{11,ij} - k_{x,i}^2\Gamma_{22,ij} & -k_{x,i}k_{y,j}\Gamma_{11,ij} - k_{x,i}k_{y,j}\Gamma_{22,ij} & \Gamma_{22,ij}\kappa_{ij}^2k_{x,i}/\gamma_{2,ij} \\ \Gamma_{11,ij}\kappa_{ij}^2k_{y,j}/\gamma_{2,ij} & -\Gamma_{11,ij}\kappa_{ij}^2k_{x,i}/\gamma_{2,ij} & 0 \end{bmatrix} \quad (5.37)$$

together with

$$\mathbf{F}_{me}(x, x', y, y') = \begin{bmatrix} \cos x \sin x' \sin y \cos y' & \cos x \cos x' \sin y \sin y' & \cos x \cos x' \sin y \cos y' \\ \sin x \sin x' \cos y \cos y' & \sin x \cos x' \cos y \sin y' & \sin x \cos x' \cos y \cos y' \\ \sin x \sin x' \sin y \cos y' & \sin x \cos x' \sin y \sin y' & 0 \end{bmatrix} \quad (5.38)$$

$$\mathcal{G}_{em}^{\Gamma}(\mathbf{r}, \mathbf{r}') = \frac{2}{h_x h_y} \sum_{i=1}^{\infty} \sum_{j=1}^{\infty} \frac{e^{\gamma_{2,ij}(z+z')}}{\kappa_{ij}^2} \tilde{G}_{em}^{\Gamma} * \mathbf{F}_{em}(x, x', y, y') \quad (5.39)$$

where \tilde{G}_{em}^{Γ} and $\mathbf{F}_{em}(x, x', y, y')$ are matrix

$$\tilde{G}_{em}^{\Gamma} = \begin{bmatrix} k_{x,i}k_{y,j}\Gamma_{11,ij} + k_{x,i}k_{y,j}\Gamma_{22,ij} & k_{y,j}^2\Gamma_{11,ij} - k_{x,i}^2\Gamma_{22,ij} & \Gamma_{11,ij}\kappa_{ij}^2k_{y,j}/\gamma_{2,ij} \\ -k_{x,i}^2\Gamma_{11,ij} + k_{y,j}^2\Gamma_{22,ij} & -k_{x,i}k_{y,j}\Gamma_{11,ij} - k_{x,i}k_{y,j}\Gamma_{22,ij} & -\Gamma_{11,ij}\kappa_{ij}^2k_{x,i}/\gamma_{2,ij} \\ -\Gamma_{22,ij}\kappa_{ij}^2k_{y,j}/\gamma_{2,ij} & \Gamma_{22,ij}\kappa_{ij}^2k_{x,i}/\gamma_{2,ij} & 0 \end{bmatrix} \quad (5.40)$$

together with

$$\mathbf{F}_{em}(x, x', y, y') = \begin{bmatrix} \sin x \cos x' \cos y \sin y' & \sin x \sin x' \cos y \cos y' & \sin x \sin x' \cos y \sin y' \\ \cos x \cos x' \sin y \sin y' & \cos x \sin x' \sin y \cos y' & \cos x \sin x' \sin y \sin y' \\ \cos x \cos x' \cos y \sin y' & \cos x \sin x' \cos y \cos y' & 0 \end{bmatrix} \quad (5.41)$$

When implementing the MoM, the volume integral evaluation is involved. A general formulation was achieved here for easily calculation purpose. Assuming a component of \mathcal{G}_{ee} dyadic Green's function can be generally expressed as follow

$$\mathcal{G}_{ee,xx}^{\Gamma}(\mathbf{r}, \mathbf{r}') = \frac{2}{h_x h_y} \sum_{i=1}^{\infty} \sum_{j=1}^{\infty} \Theta_{ij} \times e^{\gamma_{2,ij}(z+z')} \sin(k_{x,i}x) \sin(k_{x,i}x') \cos(k_{y,j}y) \cos(k_{y,j}y') \quad (5.42)$$

where Θ_{ij} has nothing to do with coordinates. So the volume integration within a specific volume cell will not affect this part. Then the integration of green function in a specific volume cell V_g can be expressed as

$$\int_{V_g} G_{ee,xx}^\Gamma(\mathbf{r}_q, \mathbf{r}') d\mathbf{r}' = \frac{16}{h_x h_y} \sum_{i=1}^{\infty} \sum_{j=1}^{\infty} \Theta_{ij} \frac{e^{\gamma_{2,ij}(z_q+z_g)}}{k_{x,i} k_{y,j} \gamma_{2,ij}} \sin(k_{x,i} x_q) \sin(k_{x,i} x_g) \cos(k_{y,j} y_q) \cos(k_{y,j} y_g) \sin(k_{x,i} \Delta x/2) \sin(k_{y,j} \Delta y/2) \sinh(\gamma_{2,ij} \Delta z/2) \quad (5.43)$$

Note that the integral evaluation of Green's function kernel can be sped up significantly by calculating some common parts first. For example $\frac{e^{\gamma_{2,ij}(z_q+z_g)}}{k_{x,i} k_{y,j} \gamma_{2,ij}}$, $\sin(k_{x,i} x_q)$, $\cos(k_{y,j} y_q)$ and $\cos(k_{y,j} y_g)$ depend on X_q , Y_q , X_g , Y_g and $Z_q + Z_g$. All the possible cases can be calculated first and saved as look-up table. Then the integral Eq. (5.43) can be obtained by checking the look-up table. The speed will be much faster than directly evaluation every time. Besides, $\sin(k_{x,i} \Delta x/2)$, $\sin(k_{y,j} \Delta y/2)$ and $\sinh(\gamma_{2,ij} \Delta z/2)$ in Eq. (5.43) only depend on Δx , Δy and Δz . Similar procedure can be implemented.

Another way to calculate the regular reflection integral part is to pre-calculate Green's kernel within big enough region first. Then the integral can be obtained by searching the Green function value table via numerical integral and interpolation. By analyzing the Green's function itself, we notice the value of Green's kernel only depends on $x - x'$, $y - y'$ and $z + z'$, based on which the calculation burden can be reduced. Such as $G_{ee,xx}^\Gamma$

$$G_{ee,xx}^\Gamma(\mathbf{r}, \mathbf{r}') = \frac{\partial^2}{\partial y \partial y'} U_{11} + \frac{1}{k_2^2} \frac{\partial^4}{\partial x \partial z \partial x' \partial z'} U_{22} = \frac{1}{(2\pi)^2} \frac{1}{k_2^2} \int_{-\infty}^{\infty} \int_{-\infty}^{\infty} \frac{e^{\gamma_2(z+z')}}{2\gamma_2 \kappa^2} [k_2^2 k_y^2 \Gamma_{11} + \Gamma_{22} k_x^2 \gamma_2^2] e^{ik_x(x-x')} e^{ik_y(y-y')} dk_x dk_y \quad (5.44)$$

As to the evaluation of Green's kernels, the truncated forms could be used to rapidly calculate, such as

$$G_{ee,xx}^\Gamma(\mathbf{r}, \mathbf{r}') = \frac{2}{h_x h_y} \frac{1}{k_2^2} \sum_{i=1}^{\infty} \sum_{j=1}^{\infty} \left\{ \frac{e^{\gamma_{2,ij}(z+z')}}{\gamma_{2,ij} \times \kappa_{ij}^2} [k_2^2 k_{y,j}^2 \Gamma_{11,ij} + \Gamma_{22,ij} k_{x,i}^2 \gamma_{2,ij}^2] \times \sin(k_{x,i} x) \sin(k_{x,i} x') \cos(k_{y,j} y) \cos(k_{y,j} y') \right\} \quad (5.45)$$

5.3 Dyadic Green's Function for a Ferromagnetic Conductive Slab

Again we assume the source is inside the conductor slab (region 2) with conductivity σ_2 and permeability μ_2 since we want to derive the dyadic green's function with the source in region 2. The upper medium (region 1) has conductivity σ_1 and permeability μ_1 and the below medium (region 3) has conductivity σ_3 and permeability μ_3 . In order to get the dyadic kernel for slab, the set of scalar green functions (Eq. 3.134) need to be determined first.

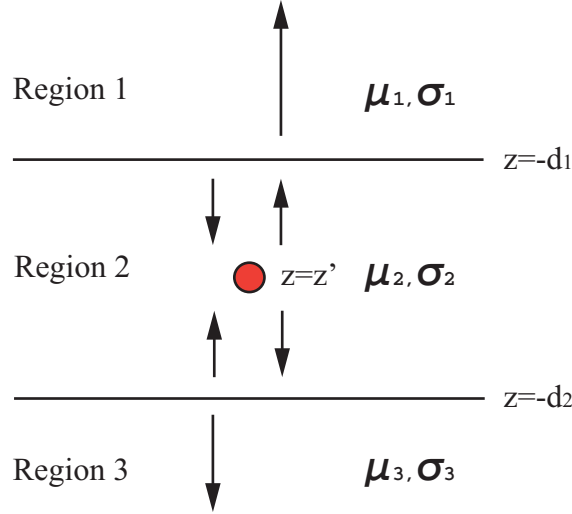


Figure 5.2: Slab with Embedded Point Source in Region 2

Similarly to half-space case, U_{ij} can be expressed as in the spectral domain form

$$\tilde{U}_{ij} = \frac{1}{\kappa^2} \frac{1}{2\gamma_2} [B e^{\gamma_2 z} + D e^{-\gamma_2 z}] \quad (5.46)$$

where the coefficient B and D can refer to Appendix A. By assuming that region 1 and region 3 are free space, $d_1 = 0$ and $d_2 = d$, which is the slab thickness, we have

$$\begin{aligned} \tilde{U}_{11} &= \frac{1}{\kappa^2} \frac{1}{2\gamma_2} \Gamma_{11} \frac{e^{\gamma_2(z+z')} + \Gamma_{11} e^{-2\gamma_2 d} [e^{\gamma_2(z-z')} + e^{-\gamma_2(z-z')}] + e^{-2\gamma_2 d} e^{-\gamma_2(z'+z)}}{1 - \Gamma_{11}^2 e^{-2\gamma_2 d}} \\ &= \frac{1}{\kappa^2} \frac{1}{2\gamma_2} R_{11} \end{aligned} \quad (5.47)$$

$$\begin{aligned} \tilde{U}_{22} &= \frac{1}{\kappa^2} \frac{1}{2\gamma_2} \Gamma_{22} \frac{e^{\gamma_2(z+z')} + \Gamma_{22} e^{-2\gamma_2 d} [e^{\gamma_2(z-z')} + e^{-\gamma_2(z-z')}] + e^{-2\gamma_2 d} e^{-\gamma_2(z'+z)}}{1 - \Gamma_{22}^2 e^{-2\gamma_2 d}} \\ &= \frac{1}{\kappa^2} \frac{1}{2\gamma_2} R_{22} \end{aligned} \quad (5.48)$$

where $\Gamma_{11} = \frac{\gamma_2 - \kappa \mu_{r2}}{\gamma_2 + \kappa \mu_{r2}}$, $\Gamma_{22} = -1$

We can also expressed the scalar kernels explicitly as

$$U_{11} = \frac{1}{(2\pi)^2} \int_{-\infty}^{\infty} \int_{-\infty}^{\infty} \frac{1}{\kappa^2} \frac{1}{2\gamma_2} R_{11} e^{ik_x(x-x')} e^{ik_y(y-y')} dk_x dk_y \quad (5.49)$$

$$U_{22} = \frac{1}{(2\pi)^2} \int_{-\infty}^{\infty} \int_{-\infty}^{\infty} \frac{1}{\kappa^2} \frac{1}{2\gamma_2} R_{22} e^{ik_x(x-x')} e^{ik_y(y-y')} dk_x dk_y \quad (5.50)$$

Now we have obtained the U_{ij} , the similar truncation procedures as half-space case did can be applied to get the dyadic Green function for the slab case. For example,

$$G_{mm,yy}^{\Gamma}(\mathbf{r}, \mathbf{r}') = \frac{2}{h_x h_y} \sum_{i=1}^{\infty} \sum_{j=1}^{\infty} \left\{ \frac{1}{k_2^2 \gamma_{2,ij} \times \kappa_{ij}^2} [\gamma_{2,ij}^2 k_{y,j}^2 R_{11,zz'} + k_2^2 k_{x,i}^2 R_{22}] \right. \\ \left. \times \sin(k_{x,i}x) \sin(k_{x,i}x') \cos(k_{y,j}y) \cos(k_{y,j}y') \right\} \quad (5.51)$$

$$G_{me,yx}^{\Gamma}(\mathbf{r}, \mathbf{r}') = \frac{2}{h_x h_y} \sum_{i=1}^{\infty} \sum_{j=1}^{\infty} \left\{ \frac{1}{\kappa_{ij}^2} [k_{y,j}^2 R_{11,z} - k_{x,i}^2 R_{22,z'}] \right. \\ \left. \times \sin(k_{x,i}x) \sin(k_{x,i}x') \cos(k_{y,j}y) \cos(k_{y,j}y') \right\} \quad (5.52)$$

where

$$\gamma_{2,ij}^2 R_{22,zz'} = \frac{\partial^2 R_{22}}{\partial z \partial z'} \quad (5.53)$$

$$\gamma_{2,ij}^2 R_{11,zz'} = \frac{\partial^2 R_{11}}{\partial z \partial z'} \quad (5.54)$$

$$\gamma_{2,ij} R_{11,z'} = \frac{\partial R_{11}}{\partial z'} \quad (5.55)$$

$$\gamma_{2,ij} R_{11,z} = \frac{\partial R_{11}}{\partial z} \quad (5.56)$$

or explicitly expressed as

$$R_{22,zz'} = \Gamma_{22} \frac{e^{\gamma_{2,ij}(z+z')} - \Gamma_{22} e^{-2\gamma_{2,ij}d} [e^{\gamma_{2,ij}(z-z')} + e^{-\gamma_{2,ij}(z-z')}] + e^{-2\gamma_{2,ij}d} e^{-\gamma_{2,ij}(z'+z)}}{1 - \Gamma_{22}^2 e^{-2\gamma_{2,ij}d}} \quad (5.57)$$

$$R_{11,zz'} = \Gamma_{11} \frac{e^{\gamma_{2,ij}(z+z')} - \Gamma_{11} e^{-2\gamma_{2,ij}d} [e^{\gamma_{2,ij}(z-z')} + e^{-\gamma_{2,ij}(z-z')}] + e^{-2\gamma_{2,ij}d} e^{-\gamma_{2,ij}(z'+z)}}{1 - \Gamma_{11}^2 e^{-2\gamma_{2,ij}d}} \quad (5.58)$$

$$R_{11,z} = \Gamma_{11} \frac{e^{\gamma_{2,ij}(z+z')} + \Gamma_{11} e^{-2\gamma_{2,ij}d} [e^{\gamma_{2,ij}(z-z')} - e^{-\gamma_{2,ij}(z-z')}] - e^{-2\gamma_{2,ij}d} e^{-\gamma_{2,ij}(z'+z)}}{1 - \Gamma_{11}^2 e^{-2\gamma_{2,ij}d}} \quad (5.59)$$

$$R_{11,z'} = \Gamma_{11} \frac{e^{\gamma_{2,ij}(z+z')} - \Gamma_{11} e^{-2\gamma_{2,ij}d} [e^{\gamma_{2,ij}(z-z')} - e^{-\gamma_{2,ij}(z-z')}] - e^{-2\gamma_{2,ij}d} e^{-\gamma_{2,ij}(z'+z)}}{1 - \Gamma_{11}^2 e^{-2\gamma_{2,ij}d}} \quad (5.60)$$

For simplicity, we explicitly express the dyadic kernels as follow for reference

$$\mathcal{G}_{ee}^{\Gamma}(\mathbf{r}, \mathbf{r}') = \frac{2}{h_x h_y} \frac{1}{k_2^2} \sum_{i=1}^{\infty} \sum_{j=1}^{\infty} \frac{1}{\gamma_{2,ij} \kappa_{ij}^2} \tilde{G}_{ee}^{\Gamma} * \mathbf{F}_{ee}(x, x', y, y') \quad (5.61)$$

where \tilde{G}_{ee}^Γ

$$\tilde{G}_{ee}^\Gamma = \begin{bmatrix} k_2^2 k_{y,j}^2 R_{11} + R_{22,zz'} k_{x,i}^2 \gamma_{2,ij}^2 & -k_2^2 k_{x,i} k_{y,j} R_{11} + R_{22,zz'} k_{x,i} k_{y,j} \gamma_{2,ij}^2 & -R_{22,z} \kappa_{ij}^2 k_{x,i} \gamma_{2,ij} \\ -k_2^2 k_{x,i} k_{y,j} R_{11} + R_{22,zz'} k_{x,i} k_{y,j} \gamma_{2,ij}^2 & k_2^2 k_{x,i}^2 R_{11} + R_{22,zz'} k_{y,j}^2 \gamma_{2,ij}^2 & -R_{22,z} \kappa_{ij}^2 k_{y,j} \gamma_{2,ij} \\ -R_{22,z'} \kappa_{ij}^2 k_{x,i} \gamma_{2,ij} & -R_{22,z'} \kappa_{ij}^2 k_{y,j} \gamma_{2,ij} & R_{22} \kappa_{ij}^4 \end{bmatrix} \quad (5.62)$$

$$\mathcal{G}_{mm}^\Gamma(\mathbf{r}, \mathbf{r}') = \frac{2}{h_x h_y} \frac{1}{k_2^2} \sum_{i=1}^{\infty} \sum_{j=1}^{\infty} \frac{1}{\gamma_{2,ij} \kappa_{ij}^2} \tilde{G}_{mm}^\Gamma \cdot * \mathbf{F}_{mm}(x, x', y, y') \quad (5.63)$$

where \tilde{G}_{mm}^Γ

$$\tilde{G}_{mm}^\Gamma = \begin{bmatrix} k_{x,i}^2 \gamma_{2,ij}^2 R_{11,zz'} + R_{22} k_2^2 k_{y,j}^2 & k_{x,i} k_{y,j} \gamma_{2,ij}^2 R_{11,zz'} - R_{22} k_2^2 k_{x,i} k_{y,j} & R_{11,z} \kappa_{ij}^2 k_{x,i} \gamma_{2,ij} \\ k_{x,i} k_{y,j} \gamma_{2,ij}^2 R_{11,zz'} - R_{22} k_2^2 k_{x,i} k_{y,j} & k_{y,j}^2 \gamma_{2,ij}^2 R_{11,zz'} + R_{22} k_2^2 k_{x,i}^2 & R_{11,z} \kappa_{ij}^2 k_{y,j} \gamma_{2,ij} \\ R_{11,z'} \kappa_{ij}^2 k_{x,i} \gamma_{2,ij} & R_{11,z'} \kappa_{ij}^2 k_{y,j} \gamma_{2,ij} & R_{11} \kappa_{ij}^4 \end{bmatrix} \quad (5.64)$$

$$\mathcal{G}_{me}^\Gamma(\mathbf{r}, \mathbf{r}') = \frac{2}{h_x h_y} \sum_{i=1}^{\infty} \sum_{j=1}^{\infty} \frac{1}{\kappa_{ij}^2} \tilde{G}_{me}^\Gamma \cdot * \mathbf{F}_{me}(x, x', y, y') \quad (5.65)$$

where \tilde{G}_{me}^Γ

$$\tilde{G}_{me}^\Gamma = \begin{bmatrix} k_{x,i} k_{y,j} R_{11,z} + k_{x,i} k_{y,j} R_{22,z'} & -k_{x,i}^2 R_{11,z} + k_{y,j}^2 R_{22,z'} & -R_{22} \kappa_{ij}^2 k_{y,j} / \gamma_{2,ij} \\ k_{y,j}^2 R_{11,z} - k_{x,i}^2 R_{22,z'} & -k_{x,i} k_{y,j} R_{11,z} - k_{x,i} k_{y,j} R_{22,z'} & R_{22} \kappa_{ij}^2 k_{x,i} / \gamma_{2,ij} \\ R_{11} \kappa_{ij}^2 k_{y,j} / \gamma_{2,ij} & -R_{11} \kappa_{ij}^2 k_{x,i} / \gamma_{2,ij} & 0 \end{bmatrix} \quad (5.66)$$

$$\mathcal{G}_{em}^\Gamma(\mathbf{r}, \mathbf{r}') = \frac{2}{h_x h_y} \sum_{i=1}^{\infty} \sum_{j=1}^{\infty} \frac{1}{\kappa_{ij}^2} \tilde{G}_{em}^\Gamma \cdot * \mathbf{F}_{em}(x, x', y, y') \quad (5.67)$$

where \tilde{G}_{em}^Γ

$$\tilde{G}_{em}^\Gamma = \begin{bmatrix} k_{x,i} k_{y,j} R_{11,z'} + R_{22,z} k_{x,i} k_{y,j} & k_{y,j}^2 R_{11,z'} - R_{22,z} k_{x,i}^2 & R_{11} \kappa_{ij}^2 k_{y,j} / \gamma_{2,ij} \\ -k_{x,i}^2 R_{11,z'} + R_{22,z} k_{y,j}^2 & -k_{x,i} k_{y,j} R_{11,z'} - R_{22,z} k_{x,i} k_{y,j} & -R_{11} \kappa_{ij}^2 k_{x,i} / \gamma_{2,ij} \\ -R_{22} \kappa_{ij}^2 k_{y,j} / \gamma_{2,ij} & R_{22} \kappa_{ij}^2 k_{x,i} / \gamma_{2,ij} & 0 \end{bmatrix} \quad (5.68)$$

The \mathbf{F} matrix is the same as that half-space case has. When implementing the MoM, the volume integral evaluation is involved. A general formulation was also achieved here for easy calculation purpose. Assuming a component of dyadic Green's function can be generally expressed as follow

$$G^\Gamma(\mathbf{r}, \mathbf{r}') = \frac{2}{h_x h_y} \sum_{i=1}^{\infty} \sum_{j=1}^{\infty} \Theta_{ij}(z, z') \sin(k_{x,i}x) \sin(k_{x,i}x') \cos(k_{y,j}y) \cos(k_{y,j}y') \quad (5.69)$$

Then the volume integral is obtained as

$$\begin{aligned} & \int_{V_g} G^\Gamma(\mathbf{r}_q, \mathbf{r}') d\mathbf{r}' \\ &= \frac{2}{h_x h_y} \sum_{i=1}^{\infty} \sum_{j=1}^{\infty} \sin(k_{x,i}x_q) \cos(k_{y,j}y_q) \left[\int_{z_g} \Theta_{ij}(z_q, z') dz' \right] \int_{S_g} \sin(k_{x,i}x') \cos(k_{y,j}y') dx' dy' \\ &= \frac{2}{h_x h_y} \sum_{i=1}^{\infty} \sum_{j=1}^{\infty} \left\{ \frac{8}{k_{x,i} k_{y,j} \gamma_{2,ij}} \Theta_{ij}(z_q, z_g) \sin(k_{x,i}x_q) \sin(k_{x,i}x_g) \cos(k_{y,j}y_q) \right. \\ & \quad \left. \cos(k_{y,j}y_g) \sin(k_{x,i}\Delta x/2) \sin(k_{y,j}\Delta y/2) \sinh(\gamma_{ij}\Delta z/2) \right\} \end{aligned} \quad (5.70)$$

5.4 Singularity of \mathcal{G}_{ee} , \mathcal{G}_{mm} in an Unbounded Domain

The notation used in the singularity formulation is summarized as follow

1. $G = \frac{e^{ikR}}{4\pi R}$

Denote the Green's function in unbounded domain and $R = |\mathbf{r} - \mathbf{r}'|$

2. $G_0 = \frac{1}{4\pi R}$

Denote the static Green's function in unbounded domain.

3. $\mathcal{G}_0 = [\mathcal{I} + \nabla\nabla]G = [\mathcal{I} + \nabla'\nabla']G$

Denote the dyadic Green's function in unbounded domain.

4. $\mathbf{F}(\mathbf{r}, t) = \text{Re}[\mathbf{F}(\mathbf{r})e^{j\omega t}] = \text{Re}[\mathbf{F}(\mathbf{r})e^{-i\omega t}]$

5. $\mathcal{G}(\mathbf{r}, \mathbf{r}') = \mathcal{G}_0(\mathbf{r}, \mathbf{r}') + \mathcal{G}^\Gamma(\mathbf{r}, \mathbf{r}')$

The dyadic Green's function in the layered medium can be expressed as the sum of the unbounded part and the reflection part, which accounts for the boundary conditions.

Evaluation of the integral involving the singularity in the source region is a key step in the analysis yet not all authors reveal their approach. Although the topic has been treated in the literature[105, 106, 76] which extract the singular region V_ϵ containing $\mathbf{r}' = \mathbf{r}$ and achieve explicit expressions for limiting case of an infinitesimal exclusion volume V_ϵ or finite special V_ϵ shapes such as sphere, cylinder and cube, sphere and cylinder exclusions are not convenient for integral calculation of the rest regular part of element volume containing singularity and these exclusions will lead to very poor approximations when the cells have high aspect ratios happened in narrow crack case. In this article we provide simple analytical expressions, which is easy to implement and avoids the singularity extraction, to use in controlling the accuracy of terms on the diagonal of the matrix.

In the matrix element evaluation of \mathbf{A}^{ee} and \mathbf{A}^{mm} , we will get involved with the following integral as (5.71).

$$\mathcal{I}_{qq}^0 = k^2 \int_{V_q} \mathcal{G}_0(\mathbf{r}_q, \mathbf{r}') dv' \quad (5.71)$$

Here \mathcal{I}_{qq}^0 is dyad. V_q is integral region of one specific volume element, \mathbf{r}_q is the matching-point inside element V_q , which is at the center of the cell. k is the wave number. The \mathcal{I}_{qq}^0 can also be expressed as follow

$$\mathcal{I}_{qq}^0 = k^2 \sum_i I_0 \hat{x}_i \hat{x}_i + \sum_i \sum_j I_{ij} \hat{x}_i \hat{x}_j \quad (5.72)$$

Where \hat{x}_i, \hat{x}_j with $i, j \in \{1, 2, 3\}$ correspond to $\hat{x}, \hat{y}, \hat{z}$ for rectangular system. I_0 and I_{ij} are one specific component of the dyad.

$$I_0 = \int_{V_q} G(\mathbf{r}, \mathbf{r}') dv' \quad (5.73)$$

$$I_{ij} = \int_{V_q} \frac{\partial^2 G(\mathbf{r}, \mathbf{r}')}{\partial x'_i \partial x'_j} dv' = B_{ij} + C_{ij} \quad (5.74)$$

$$B_{ij} = \int_{V_q} \frac{\partial^2 (G - G_0)}{\partial x'_i \partial x'_j} dv' \quad (5.75)$$

$$C_{ij} = \int_{V_q} \frac{\partial^2 G_0(\mathbf{r}, \mathbf{r}')}{\partial x'_i \partial x'_j} dv' = \frac{\partial^2}{\partial x'_i \partial x'_j} \int_{V_q} G_0(\mathbf{r}, \mathbf{r}') dv' \quad (5.76)$$

For cube and sphere exclusion[106], $C_{ij} = -\frac{1}{3} \delta_{ij}$. For other aspect ratio cuboid, it might be obtained by using Eq 5.90 and Eq 5.91.

For simplicity, here we set $\mathbf{r}_q = 0$ and drop the prime '. Then $R = \sqrt{x^2 + y^2 + z^2}$. The I_0 and B_{ij} can be rewritten as

$$I_0 = \frac{1}{4\pi} \int_{V_g} \frac{e^{ikR}}{R} dv \quad (5.77)$$

$$B_{ij} = \int_{V_g} \left[\frac{\partial^2}{\partial x_i \partial x_j} (G(R) - G_0(R)) \right] dv \quad (5.78)$$

$$C_{ij} = \frac{\partial^2}{\partial x_i \partial x_j} \int_{V_g} G_0(R) dv \quad (5.79)$$

Since the exclusion region might be different shapes. Here we will discuss the cube and sphere separately. Note that for cuboid element, we can just set the exclusion region the same as the cell itself to avoid the exclusion procedure.

5.4.1 Cuboidal Exclusion Region

In a specific volume cell V_g with the dimension $h_x \times h_y \times h_z$. it contains the exclusion region V_ε . Here we set the $V_\varepsilon = V_g$ for simplicity.

5.4.1.1 Evaluation of I_0

By using series expansion, we obtain

$$\frac{e^{ikR}}{R} \approx \sum_{n=0}^N \frac{(ik)^n R^{n-1}}{n!} \quad (5.80)$$

Here N is truncation number. $n \in [0, 1, 2, \dots, N]$. Then the I_0 is reduced to

$$I_0 \approx \frac{1}{4\pi} \sum_{n=0}^N \frac{(ik)^n}{n!} \int_{-\frac{h_x}{2}}^{\frac{h_x}{2}} \int_{-\frac{h_y}{2}}^{\frac{h_y}{2}} \int_{-\frac{h_z}{2}}^{\frac{h_z}{2}} R^{n-1} dx dy dz = \frac{1}{4\pi} \sum_{n=0}^N \frac{(ik)^n}{n!} S_n \quad (5.81)$$

The evaluation of different n terms are discussed and shown as follow.

- $n = 0$

$$S_0 = \int_{V_g} \frac{1}{R} dx dy dz \quad (5.82)$$

which can be integrated analytically by using the following primitive function or indefinite function

$$\int \frac{1}{R} dx dy dz = F(x, y, z) + F(y, z, x) + F(z, x, y) \quad (5.83)$$

$$F(x, y, z) = xy \ln \left[\sqrt{x^2 + y^2 + z^2} + z \right] - \frac{x^2}{2} \tan^{-1} \left[\frac{yz}{x \sqrt{x^2 + y^2 + z^2}} \right] \quad (5.84)$$

- $n = 1$

$$S_1 = h_x h_y h_z \quad (5.85)$$

- $n > 1$ can be easily calculated by numerical integral method.

By using the above method, the calculation of I_0 can be done quickly and accurately.

5.4.1.2 Evaluation of B_{ij} and C_{ij}

Similarly, we have

$$G - G_0 \approx \frac{1}{4\pi} \sum_{n=1}^N \frac{(ik)^n R^{n-1}}{n!} \quad (5.86)$$

by applying the series expansion and hence we obtain

$$B_{ij} \approx \frac{1}{4\pi} \sum_{n=1}^N \frac{(ik)^n}{n!} \int_{V_g} \frac{\partial^2 R^{n-1}}{\partial x_i \partial x_j} dv = \frac{1}{4\pi} \sum_{n=1}^N \frac{(ik)^n}{n!} S_{n,ij} \quad (5.87)$$

By expressing the differentiation operator explicitly, we obtain

$$B_{ij}(i = j) \approx \frac{1}{4\pi} \sum_{n=1}^N \frac{(ik)^n}{n!} \int_{V_g} \{(n-1)R^{n-3} + (n-1)(n-3)x_i^2 R^{n-5}\} dv \quad (5.88)$$

$$B_{ij}(i \neq j) \approx \frac{1}{4\pi} \sum_{n=1}^N \frac{(ik)^n}{n!} \int_{V_g} \{(n-1)(n-3)x_i x_j R^{n-5}\} dv \quad (5.89)$$

Similarly to I_0 , the evaluation of different n terms are discussed and shown as follow.

- $n = 0$ is the C_{ij} . And this also occurs in adjacent cell integral evaluation, we can use the following indefinite function [107]

$$\Phi_1(x, y, z) = \int \frac{\partial^2}{\partial x^2} R^{-1} dv = -\tan^{-1} \left[\frac{yz}{xR} \right] \quad (5.90)$$

$$\Phi_2(x, y, z) = \int \frac{\partial^2}{\partial x \partial y} R^{-1} dv = \ln(R + z) \quad (5.91)$$

- $n = 1$

$$S_{1,ij}(i = j) = S_{1,ij}(i \neq j) = 0 \quad (5.92)$$

- $n = 2$

$$\Phi_1(x, y, z) = \int \frac{\partial^2}{\partial x^2} R dv = xy \ln(R + z) + xz \ln(R + y) - x^2 \tan^{-1} \frac{yz}{xR} \quad (5.93)$$

$$\Phi_2(x, y, z) = \int \frac{\partial^2}{\partial x \partial y} R dv = \frac{1}{2} Rz + \frac{x^2 + y^2}{2} \ln(R + z) \quad (5.94)$$

- $n = 3$

$$B_{3,ij}(i = j) = \frac{1}{4\pi} \frac{(ik)^3}{3!} 2h_x h_y h_z \quad (5.95)$$

$$B_{3,ij}(i \neq j) = 0 \quad (5.96)$$

- $n = 4$

$$\begin{aligned} \Phi_1(x, y, z) &= \int \frac{\partial^2}{\partial x^2} R^3 dv \\ &= \frac{x}{2} \left[2yzR + y(y^2 + 3x^2) \ln(R + z) + z(z^2 + 3x^2) \ln(R + y) - 2x^3 \tan^{-1} \frac{yz}{xR} \right] \end{aligned} \quad (5.97)$$

$$\Phi_2(x, y, z) = \int \frac{\partial^2}{\partial x \partial y} R^3 dv = \frac{1}{8} \left[[2R^2 + 3(x^2 + y^2)] zR + 3(x^2 + y^2)^2 \ln(R + z) \right] \quad (5.98)$$

- $n = 5$

$$\Phi_1(x, y, z) = \int \frac{\partial^2}{\partial x^2} R^4 dv = \frac{4}{3} x [yz(R^2 + 2x^2)] \quad (5.99)$$

$$\Phi_2(x, y, z) = \int \frac{\partial^2}{\partial x \partial y} R^4 dv = (x^2 + y^2)^2 z + \frac{2}{3} (x^2 + y^2) z^3 + \frac{1}{5} z^5 \quad (5.100)$$

- $n > 5$ could be easily calculate by applying numerical integral method. The contribution after 5th term is usually negligible. However the routines should include the flexibility of choosing how many terms to have.

When the product kR is bigger enough, we need the adjust the truncation term number to make sure singular integration accuracy.

5.4.2 Spherical Exclusion Region

In a specific volume cell, it contains the sphere exclusion region V_ε with the radius a .

5.4.2.1 Evaluation of I_0

$$I_0 = \int_{V_\varepsilon} G dv = \frac{1}{4\pi} \int_{V_\varepsilon} \frac{e^{ikr}}{r} r^2 d\Omega dr = \int_{V_\varepsilon} r e^{ikr} dr = \frac{-1}{k^2} [1 + e^{ika} (ika - 1)] \quad (5.101)$$

Here $d\Omega$ is the differential Teriradian.

5.4.2.2 Evaluation of B_{ij}

By using the identities shown Appendix C for spherical coordinate system, we can easily get the following useful equations.

$$\int_{-\pi/2}^{\pi/2} \int_{-\pi}^{\pi} \hat{r}\hat{r} \sin \theta d\theta d\phi = \frac{4}{3}\pi\mathcal{I} = \left(\frac{4}{3}\pi\hat{x}\hat{x} + \frac{4}{3}\pi\hat{y}\hat{y} + \frac{4}{3}\pi\hat{z}\hat{z} \right) \quad (5.102)$$

$$\nabla\nabla G = \frac{e^{ikr}}{4\pi r} \left(\hat{r}\hat{r} \left(\frac{-k^2 r^2 - 3ikr + 3}{r^2} \right) + \left(\frac{ikr - 1}{r^2} \right) \mathcal{I} \right) \quad (5.103)$$

$$\nabla\nabla G_0 = \frac{1}{4\pi r} \left(3\hat{r}\hat{r} \frac{1}{r^2} - \mathcal{I} \frac{1}{r^2} \right) \quad (5.104)$$

Based Eq 5.102, Eq 5.103, Eq 5.104 and some formulation manipulations, the following result can be obtained

$$\int_{V_\varepsilon} \nabla\nabla[G - G_0]dv = -\mathcal{I} \frac{k^2}{3} \int_0^a r e^{ikr} dr = \mathcal{I} \frac{1}{3} \left(1 + e^{ika}(ika - 1) \right) \quad (5.105)$$

Hence we have

$$B_{ij} = \frac{1}{3} \delta_{ij} \left(1 + e^{ika}(ika - 1) \right) \quad (5.106)$$

5.4.2.3 Evaluation of C_{ij}

For sphere exclusion [106], we have

$$C_{ij} = -\frac{1}{3} \delta_{ij} \quad (5.107)$$

Now, we can find a very simple expression can be achieved with sphere exclusion for the singular integral shown as follow

$$\mathcal{I}_{qg}^0 = \left[-1 - \frac{2}{3} e^{ika}(ika - 1) \right] \mathcal{I} \quad (5.108)$$

5.4.3 Integral Evaluation in Regular Region

When the V_q is not the same region as V_g , the integral, \mathcal{I}_{gg}^0 , is regular and the following equations can be used to evaluate it numerically.

$$\frac{\partial^2 G(\mathbf{r}, \mathbf{r}')}{\partial x'_i \partial x'_i} = k^2 \left\{ -\cos^2 \theta_i - \frac{i}{kR} \left[1 + \frac{i}{kR} \right] [3\cos^2 \theta_i - 1] \right\} G(\mathbf{r}, \mathbf{r}') \quad (5.109)$$

$$\frac{\partial^2 G(\mathbf{r}, \mathbf{r}')}{\partial x'_i \partial x'_j} = k^2 \cos \theta_i \cos \theta_j \left\{ -1 - \frac{3i}{kR} \left[1 + \frac{i}{kR} \right] \right\} G(\mathbf{r}, \mathbf{r}') \quad (5.110)$$

where $\cos \theta_i = \frac{x_i - x'_i}{R}$ and $R = |\mathbf{r} - \mathbf{r}'|$.

Another way is to use the formulation derived for the singular integral directly and its advantage is quick calculation.

5.4.3.1 Spherical Exclusion Case

For V_ε is sphere exclusion, It might be tedious to do the remaining region ($V_g - V_\varepsilon$) integral. Another way to achieve it is setting the Green's function part as piece-wise function

$$\mathcal{G}_0(\mathbf{r}, \mathbf{r}') = \begin{cases} 0 & \mathbf{r} \in V_\varepsilon \\ \mathcal{G}_0(\mathbf{r}, \mathbf{r}') & \mathbf{r} \notin V_\varepsilon \end{cases} \quad (5.111)$$

Then now we can use the numerical method to calculate the integral within the whole element region V_g .

5.4.3.2 Adjacent Cell Integral Calculation

Around one cell, there are six adjacent cells which is also very singular. Analytical evaluation for these cells are preferable. For these 6 cells, we can easily to find that

- I_0 of 6 cells are the same. (the distance between adjacent cell to singular cell is the same)
- I_{ij} of 6 cells are not the same.
- shift the cell with the positive and negative value, we will get different $I_0 + I_{ij}$. However, the diagonal elements will be the same if the absolute shift is the same. The off-diagonal elements will have opposite signs between negative and positive shifts.

for example, the cell with shift $(a, 0, 0)$ and the cell with shift $(-a, 0, 0)$ will have the same diagonal elements. However, the element related with x partial derivative will have opposite signs since shift is in the x direction. ($\frac{\partial^2}{\partial x_i^2}$ will not affect the sign. $\frac{\partial^2}{\partial x_i \partial x_j}$ in different direction will introduce different sign.) So we can pre-calculate all the I for all the possible distance between any two of mesh cells. Then the specific I value can be picked based on shifting property discussed above.

5.5 Singularity of \mathcal{G}_{em} , \mathcal{G}_{me}

\mathcal{G}_{em}^0 can be expressed as follow in the unbounded domain

$$\begin{aligned} \mathcal{G}_{me}^0 &= \nabla G \times \mathcal{I} = -\nabla' G \times \mathcal{I} \\ &= \begin{bmatrix} 0 & -\frac{\partial G}{\partial z} & \frac{\partial G}{\partial y} \\ \frac{\partial G}{\partial z} & 0 & -\frac{\partial G}{\partial x} \\ -\frac{\partial G}{\partial y} & \frac{\partial G}{\partial x} & 0 \end{bmatrix} = \begin{bmatrix} 0 & \frac{\partial G}{\partial z'} & -\frac{\partial G}{\partial y'} \\ -\frac{\partial G}{\partial z'} & 0 & \frac{\partial G}{\partial x'} \\ \frac{\partial G}{\partial y'} & -\frac{\partial G}{\partial x'} & 0 \end{bmatrix} \end{aligned} \quad (5.112)$$

where $G = \frac{e^{ikR}}{4\pi R}$ denoting the Green's function in unbounded domain. The singular integral involved can be expressed as

$$I = \int_{V_g} \mathcal{G}_{me}^0(\mathbf{r}, \mathbf{r}') dv' \quad (5.113)$$

it is a 3×3 matrix and the diagonal components are zeros. And we denote

$$I_i = \frac{1}{4\pi} \int_{V_g} \frac{\partial}{\partial x'_i} \left(\frac{e^{ikR}}{R} \right) dv' \quad (5.114)$$

For simplicity, we set $\mathbf{r} = 0$ and drop the prime symbol ', we have

$$I_i \approx \frac{1}{4\pi} \sum_{n=0}^N \frac{(ik)^n}{n!} \int_{V_g} \frac{\partial R^{n-1}}{\partial x_i} dv = \frac{1}{4\pi} \sum_{n=0}^N S_n \quad (5.115)$$

S_n can also be written in the form

$$S_n = \frac{(ik)^n}{n!} \int_{V_g} (n-1) R^{n-3} x_i dv \quad (5.116)$$

The the similar procedure used in \mathcal{G}_{ee} can be applied to every term.

5.6 Singularity Treatment Verification by Calculation of RCS of a Dielectric Sphere

The validation of the proposed singularity treatment is done by comparing the RCS of a dielectric sphere with the analytical Mie's series solution. The sphere parameters and calculation frequency are $f = 300$ MHz, $\epsilon_r = 2.56$ and $\mu_r = 1$. The radius of sphere is 0.15λ

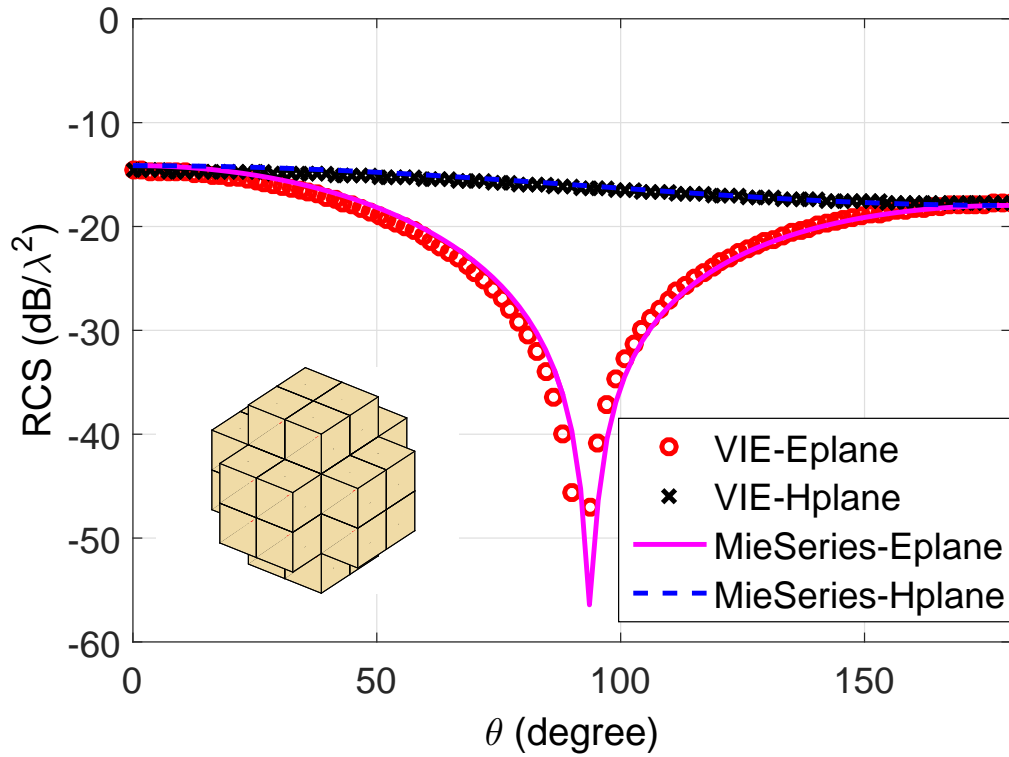


Figure 5.3: RCS results comparison between VIE method and Mie-series with 32 cells

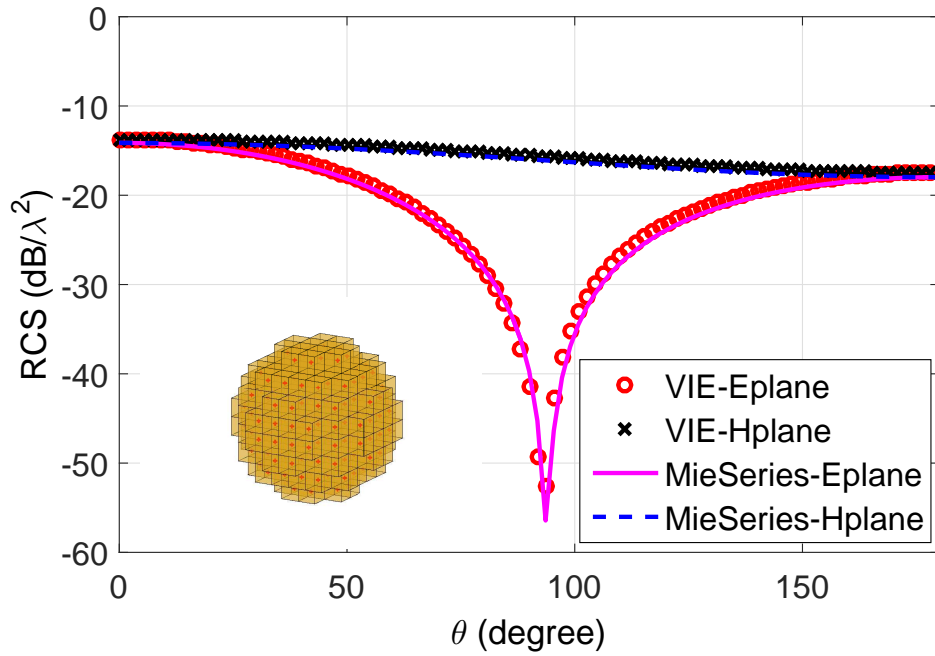


Figure 5.4: RCS results comparison between VIE method and Mie-series with 280 cells

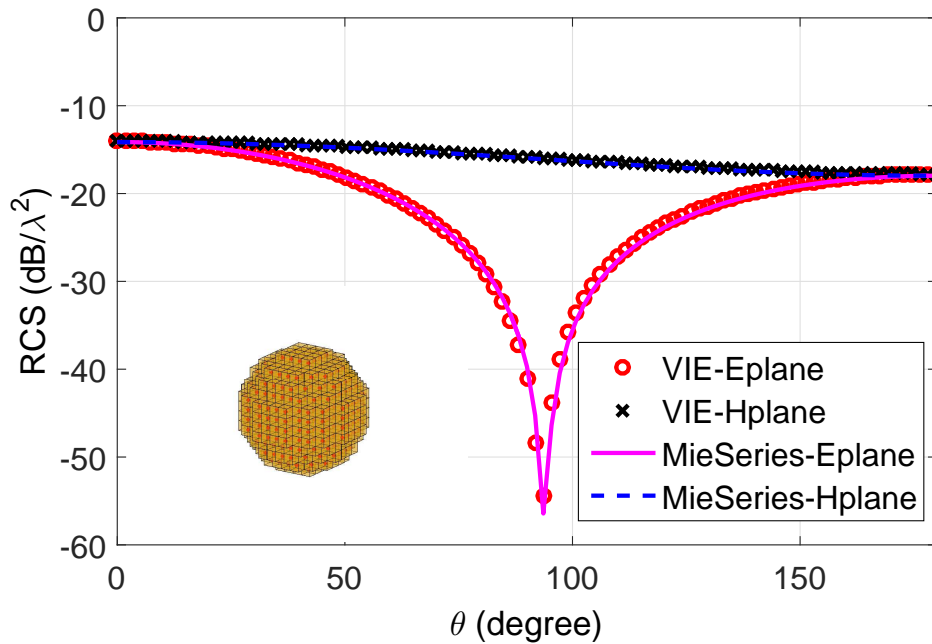


Figure 5.5: RCS results comparison between VIE method and Mie-series with 912 cells

5.7 Modeling Verification for Non-ferromagnetic Material

5.7.1 Experiment 1: Conductor Plate with a Rectangular Crack

The parameters of test experiment 1 [22] is shown in Tab. 5.1. The frequency is 900 Hz and the corresponding skin-depth is $\delta = 3.033\text{mm}$. The mesh size is $N_x \times N_y \times N_z = 1 \times 8 \times 8$.

Table 5.1: Coil and crack parameters for Team Workshop Problem 15

Coil Inner Raids, r_1	6.15mm
Coil Outer Raids, r_2	12.4mm
Coil Thickness	6.15mm
Number of Turns	3790
Liftoff	0.88mm
Crack Depth	5mm
Crack Width	0.28mm
Crack Length	12.6mm
Slab Thickness	12.22mm
Conductivity (MS/m)	30.6
Relative Magnetic Permeability, μ_r	1

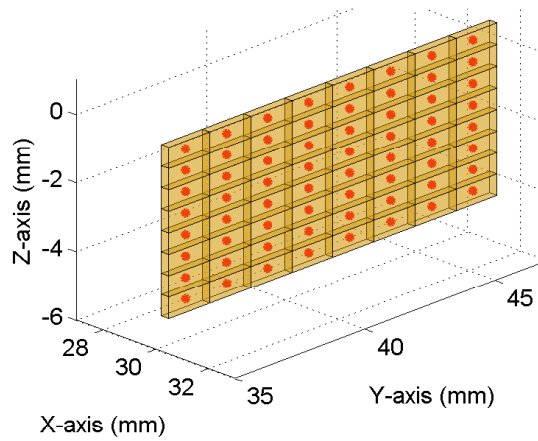


Figure 5.6: The mesh of the crack region of TEM Problem 15

The detailed comparison between the model predicted data and experimental data are shown in Fig. 5.7 and Fig. 5.8.

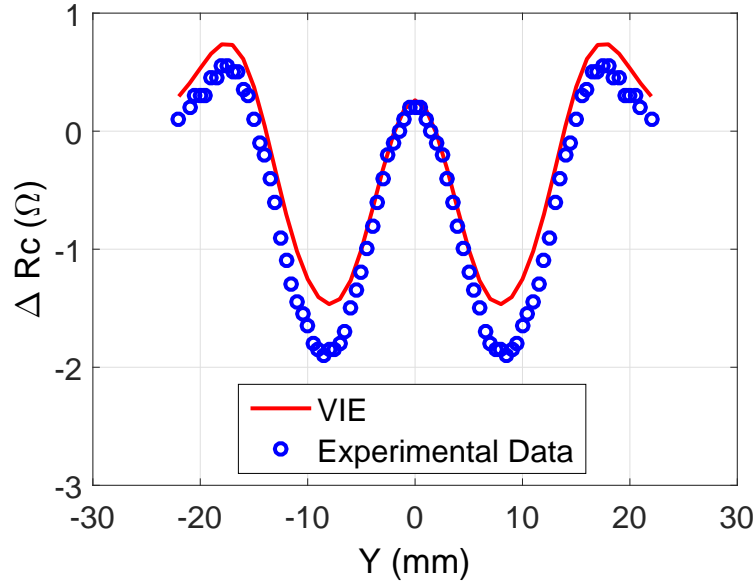


Figure 5.7: Comparison between experimental and theoretical result of resistance changes of TEM Problem 15 at 900 Hz

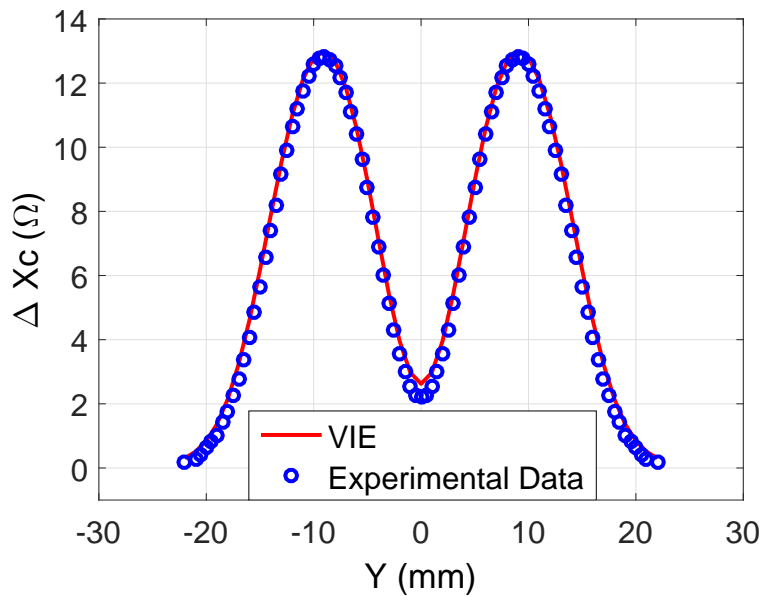


Figure 5.8: Comparison between experimental and theoretical result of reactance changes of TEM Problem 15 at 900 Hz

5.7.2 Experiment 2: Conductor Plate with a Semi-elliptical Crack

The parameters of test experiment 2 [16] is shown in Tab. 5.2. The frequency are 1027 Hz and 2081 Hz and the corresponding skin-depth are $\delta = 3.31\text{mm}$ and $\delta = 2.325\text{mm}$. The mesh size is $N = 96$.

Table 5.2: Coil and crack parameters for experiment 2

Coil Inner Raids, r_1	2.51mm
Coil Outer Raids, r_2	7.38mm
Coil Thickness	4.99mm
Number of Turns	4000
Liftoff	0.3mm
Crack Depth	8.61mm
Crack Width	0.33mm
Crack Length	22.1mm
Slab Thickness	24mm
Conductivity (MS/m)	22.62
Relative Magnetic Permeability, μ_r	1

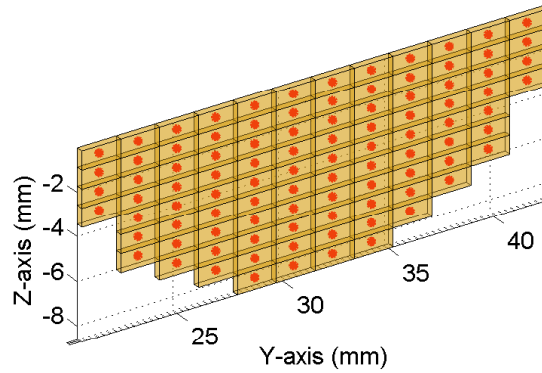


Figure 5.9: The mesh of the crack region of experiment 2

The detailed comparison between the model predicted data and experimental data are shown in Fig. 5.10 and Fig. 5.13.

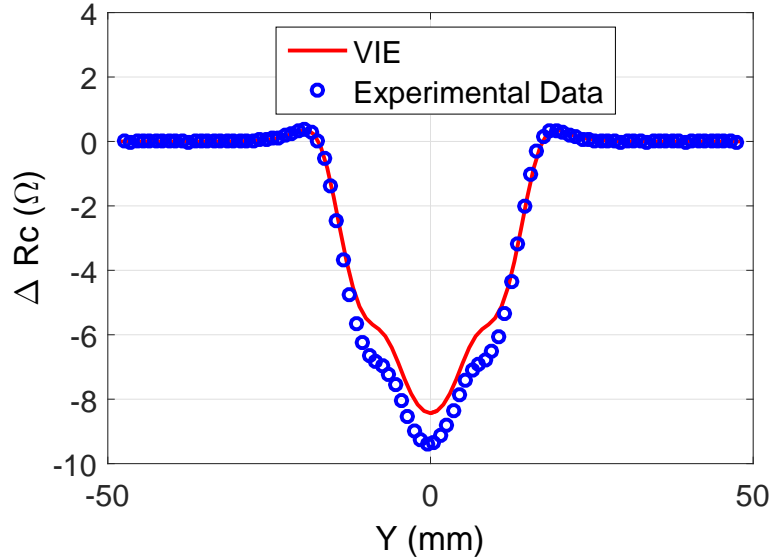


Figure 5.10: Comparison between experimental and theoretical result of resistance changes of experiment 2 at 1027 Hz

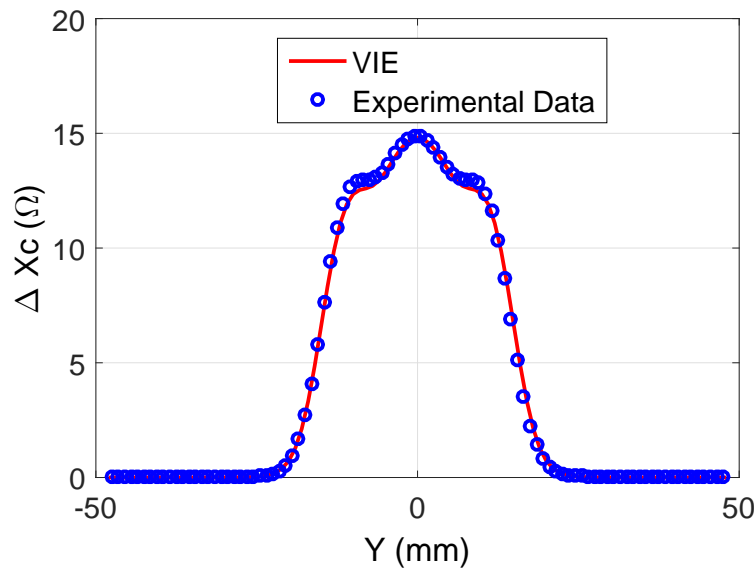


Figure 5.11: Comparison between experimental and theoretical result of reactance changes of experiment 2 at 1027 Hz

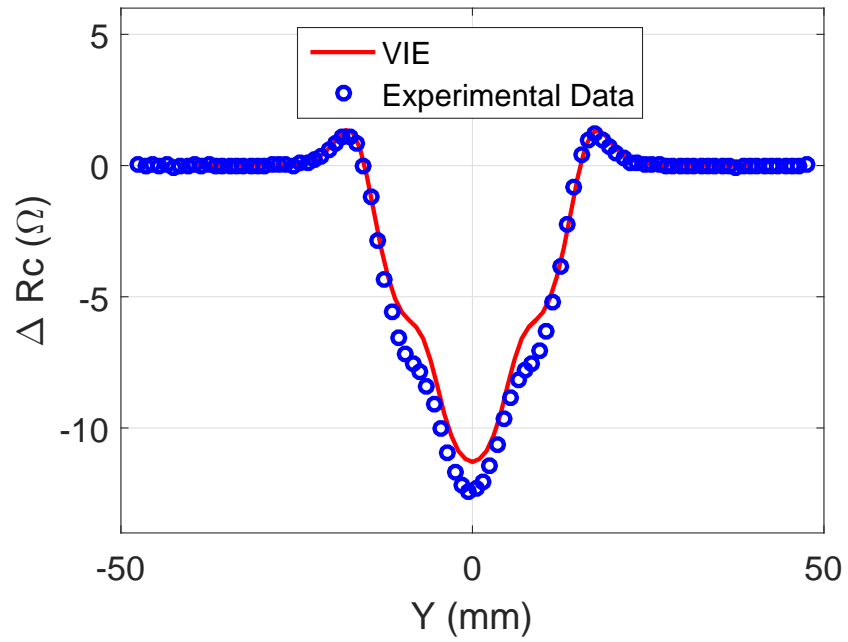


Figure 5.12: Comparison between experimental and theoretical result of resistance changes of experiment 2 at 2081 Hz

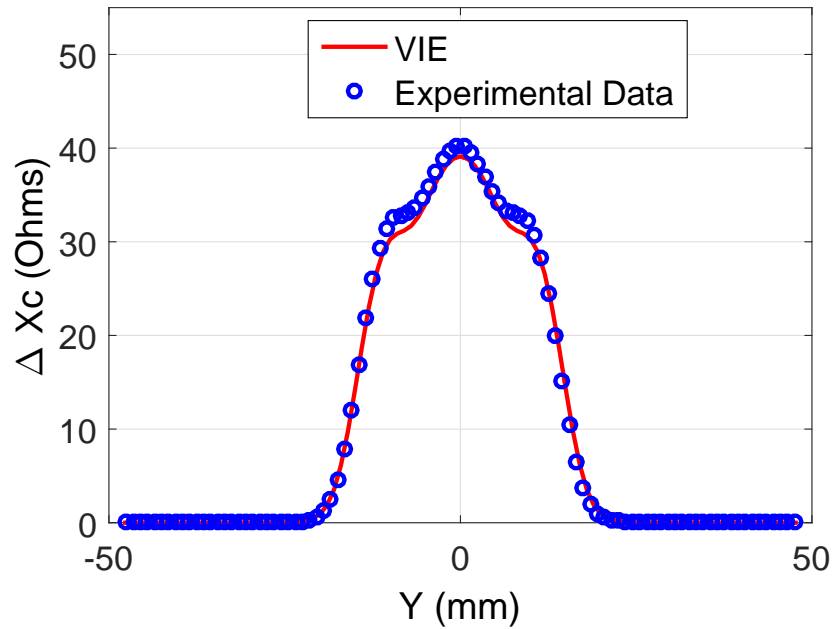


Figure 5.13: Comparison between experimental and theoretical result of reactance changes of experiment 2 at 2081 Hz

5.7.3 Experiment 3: Conductor Plate with a Through-thickness Crack

The parameters of test experiment 3 [99] is shown in Tab. 5.3. The frequency are 630 Hz and 2500 Hz and the corresponding skin-depth are $\delta = 4.807mm$ and $\delta = 2.4131mm$. The mesh size is $N_x \times N_y \times N_z = 1 \times 15 \times 3$.

Table 5.3: Coil and crack parameters for experiment 3

Coil Inner Raids, r_1	4.975mm
Coil Outer Raids, r_2	9.805mm
Coil Thickness	4.02mm
Number of Turns	399
Liftoff	0.05mm
Crack Depth	2mm
Crack Width	0.234mm
Crack Length	29.893mm
Slab Thickness	2mm
Conductivity (MS/m)	17.4
Relative Magnetic Permeability, μ_r	1

The detailed comparison between the model predicted data and experimental data are shown from Fig. 5.14 to Fig. 5.19.

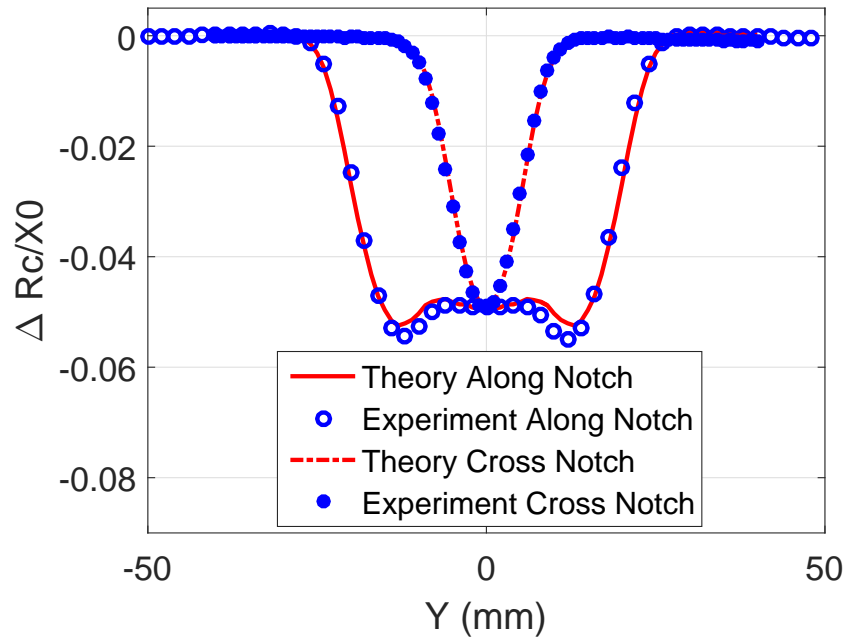


Figure 5.14: Comparison between model prediction and experiment of resistance changes at 0.631 kHz

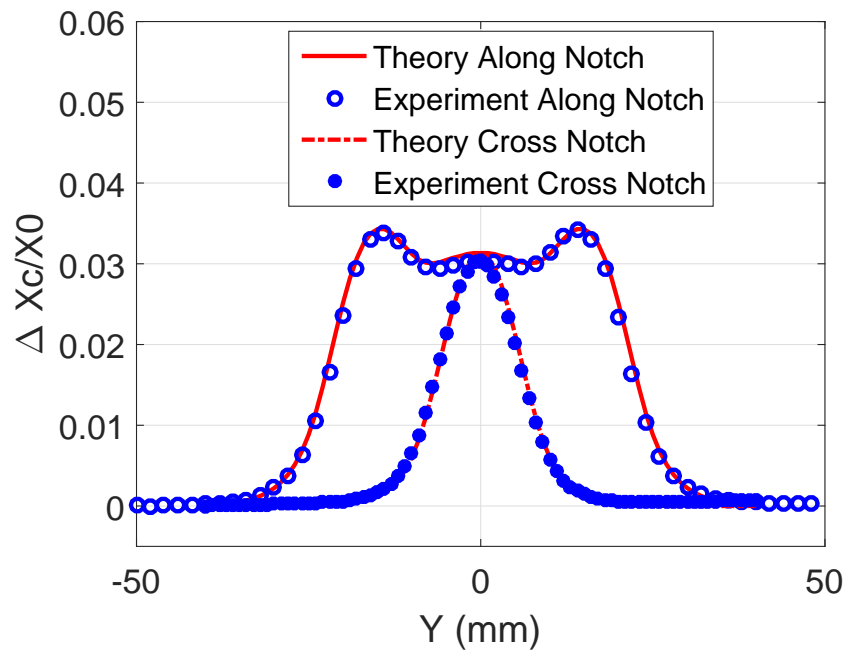


Figure 5.15: Comparison between model prediction and experiment of resistance changes at 0.631 kHz

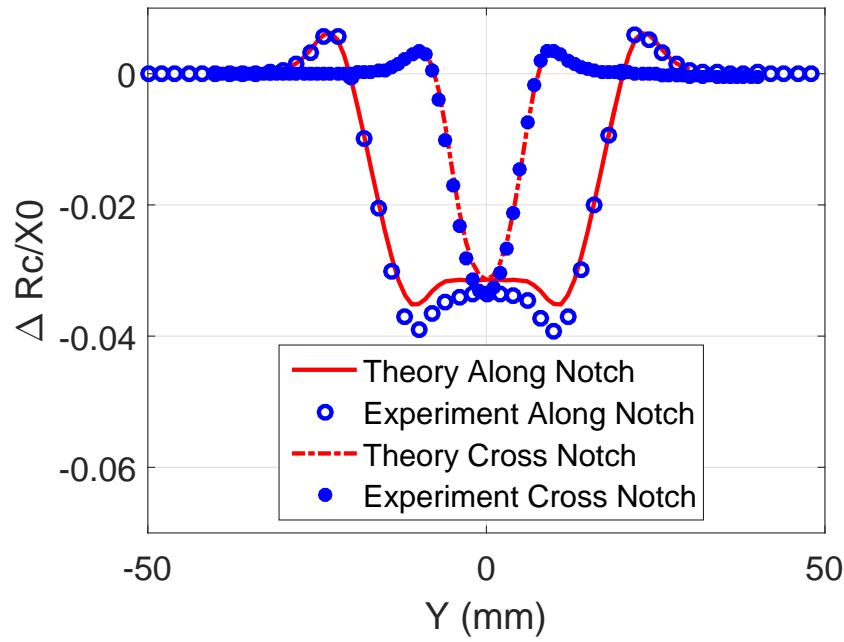


Figure 5.16: Comparison between model prediction and experiment of resistance changes at 2.5 kHz

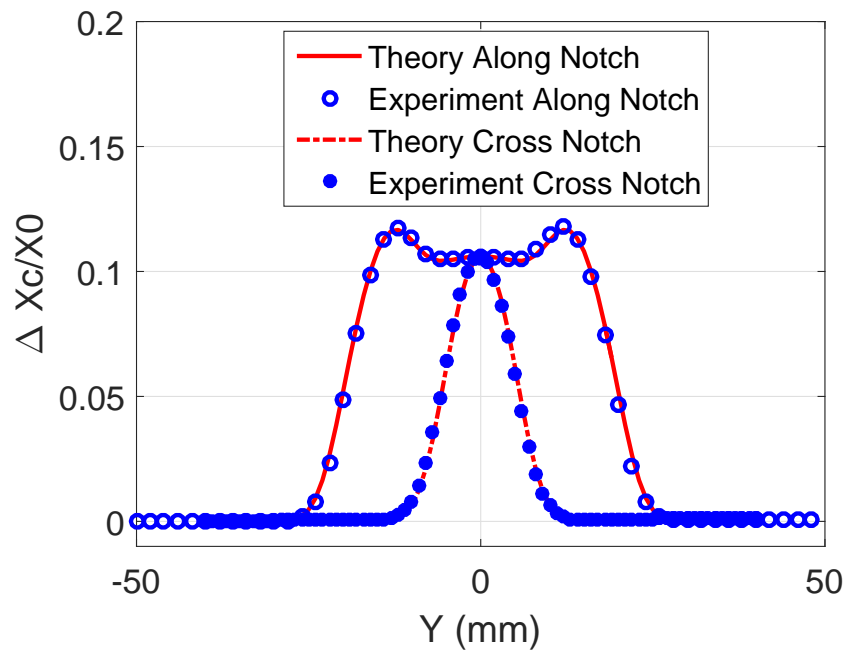


Figure 5.17: Comparison between model prediction and experiment of resistance changes at 2.5 kHz

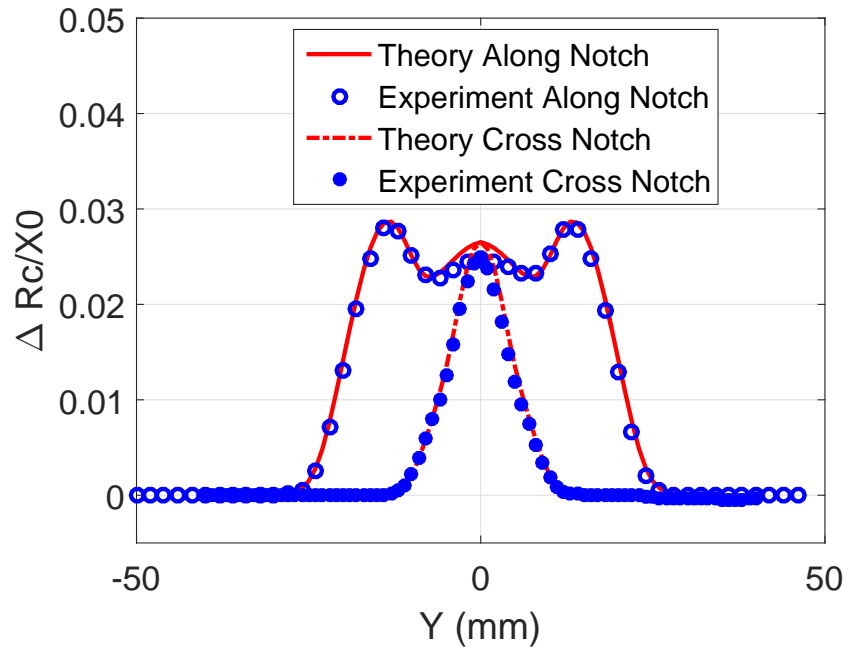


Figure 5.18: Comparison between model prediction and experiment of resistance changes at 10 kHz

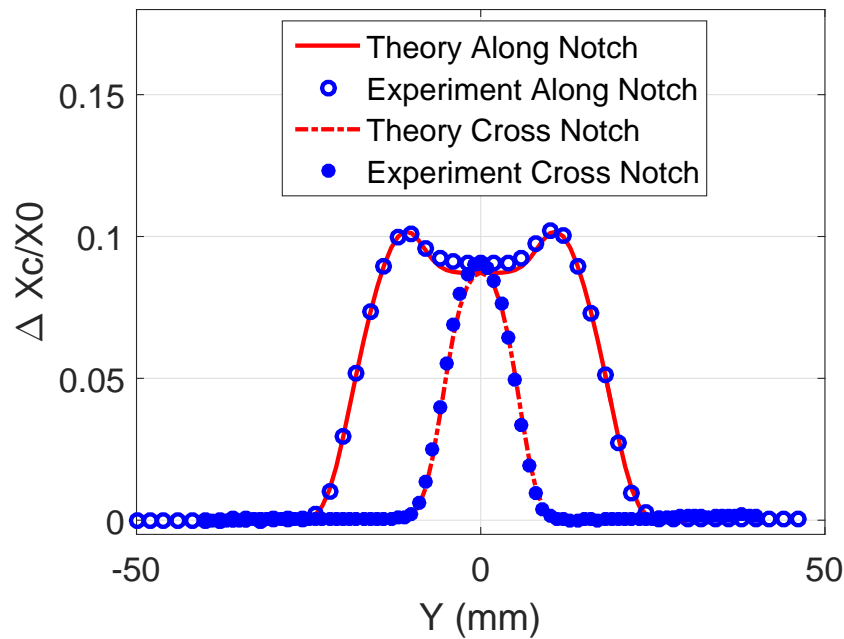


Figure 5.19: Comparison between model prediction and experiment of resistance changes at 10 kHz

CHAPTER 6. EXPERIMENTAL VALIDATION AND RESULTS OF FERROMAGNETIC SPECIMEN

In this chapter, the coil impedance change due to non-through semi-elliptical notch in ferromagnetic steel specimen is tested to obtain reference data results for comparison with theoretical and computational models. First, eddy current metallic test specimens have been designed, purchased and delivered for carrying out a series of controlled measurements on simulated defects in the form of notches produced by electrical discharge machining (EDM). 316 and 304 austenitic stainless steel are used extensively in fast reactors for the reactor vessel, primary pipe work, and heat exchangers and they are non-ferromagnetic. However, candidate materials for fuel cladding and heater exchanger tube in fast reactors are likely to fall into ferromagnetic steels, such as 9Cr-1Mo, oxide dispersion strengthened (ODS). etc. In particular there has been a long standing effort in Japan and France (at CEA) to study the properties of oxide dispersed steel (ODS), as a likely candidate for use in the high neutron flux environment surrounding the nuclear fuel. Because ODS steel is not commonly available, we are using 440 SS test specimens with a high chrome content. These are likely to have similar electromagnetic properties to those of ODS steel including a similar permeability. Then the experiments with along-the-notch scan, across-the-notch scan and 2-D scan are carried out. The experimental results are also compared with theoretical predictions based on numerical calculation. In order to get the theoretical predictions, the conductivity σ and relative permeability μ_r of 440 SS specimen are obtained first by using ACPD method [108, 109]. Then the coil liftoff from the specimen surface was determined based on the multi-frequency impedance data and theoretical model correlation. In the end, good agreement is obtained between measurement data and model prediction.

6.1 Eddy-current Impedance Measurement System

Eddy current inspection under fast reactor coolant particularly sodium will require a high performance test instrument. The system we have chosen is based on a lock-in amplifier from Zurich Instruments. In order that it operates as a key component in an eddy current test system we have added auxiliary circuits included a precision resistor with the aim of achieving a high sensitivity measurements and automatic data acquisition of the eddy current probe impedance changes due to flaws.

The eddy-current impedance measurement system, which includes two sub-systems: the signal acquisition system and the DUT-probe system, is set up first. The signal acquisition system, Fig. 6.2, is primarily responsible for the probe signal sampling, quantization, post-processing, data storage and communication with control-computer. This subsystem comprises power supply, lock-in amplifier and impedance add-on module. Voltage amplitude and phase measurements of the probe can be made accurately using the lock-in amplifier. The one being used in this project from Zurich Instruments is shown in Fig. 6.2. In order to convert the voltage data to a change in impedance, an add-on circuit is needed.

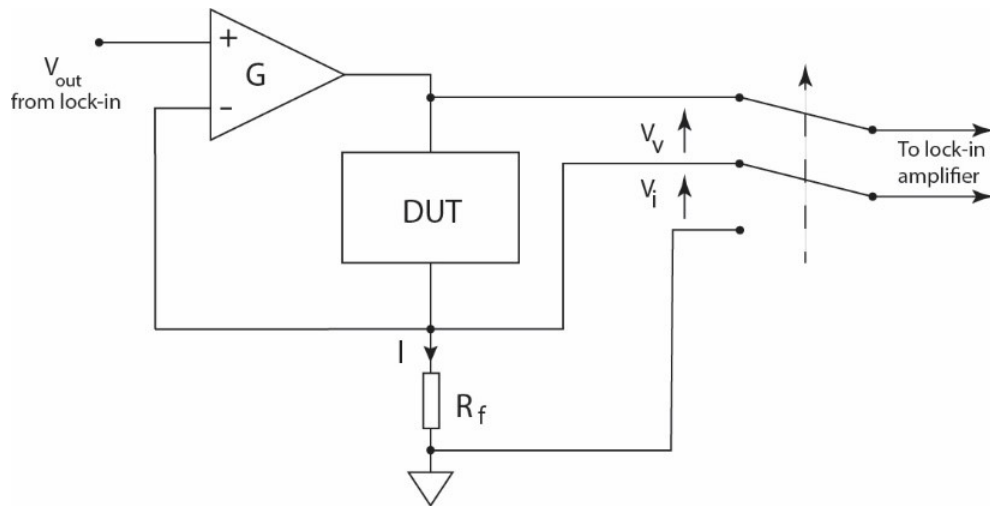


Figure 6.1: Impedance add-on circuit structure

The basic configuration of add-on circuit is shown in Fig. 6.1. The trans-conductance amplifier G provided current to the device under test (DUT). The lock-in amplifier measures

both the potential drop across the DUT and the voltage drop across the standard resistor to determine the impedance.

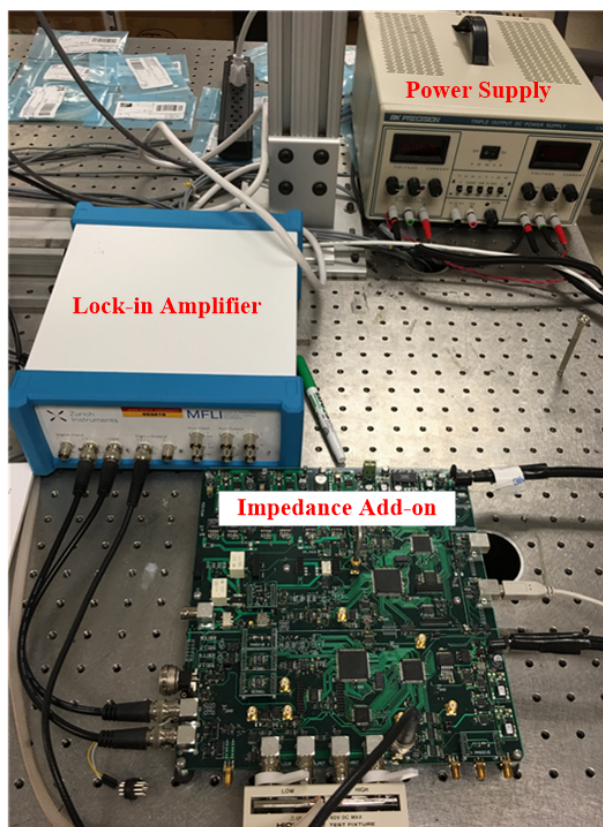


Figure 6.2: Eddy-current impedance measurement system which includes power supply, lock-in amplifier and impedance add-on module

The add-on circuit together with a lock-in amplifier provides a digital output of the amplitude and phase of the input voltage which can be switched between the voltage across an eddy current probe coil and the voltage across a known standard resistor carrying the probe current. My colleague, Yuan Ji, did the circuit design, layout and debug. In order to make our test system robust from power supply interference and ESD, the ESD protection and voltage regulation are also integrated in the add-on circuit.

The DUT-probe system is shown in Fig. 6.3. The eddy-current probe, Fig.6.4, is mounted on a computer-controlled z-stage with 5 micron resolution. The specimen is mounted on the platform which constitutes xy-stage with 5 micron resolution, a rotary stage and a manually

adjusted tilt stage from bottom up. In order to have a quick and stable connection to the probe, the BNC connector is used as a standard connection type for all the probes.

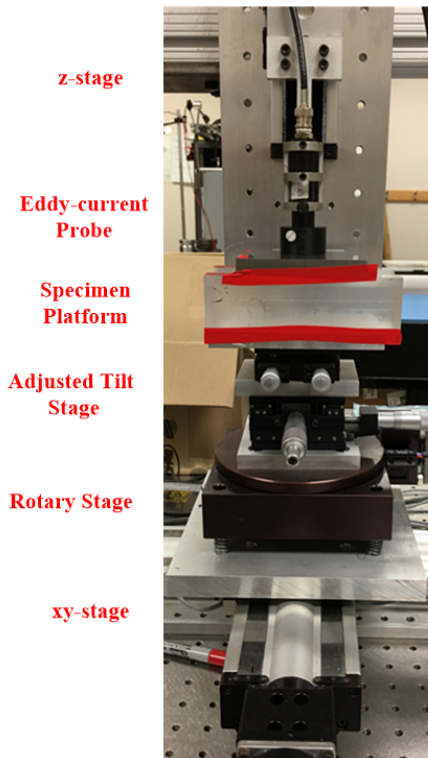


Figure 6.3: Experimental bench used to measure the coil impedance change due to the narrow notch in the 440SS steel slab

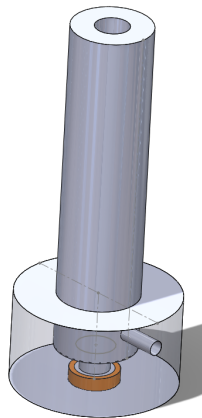


Figure 6.4: Eddy-current probe structure

6.2 Measurement of Conductivity and Permeability

In predicting the eddy current probe signals due to notches in ferromagnetic material it is necessary to know both the electrical conductivity σ and relative magnetic permeability μ_r of the material. Although eddy current measurements of conductivity can be done reliably for non-magnetic material, it has inherent uncertainties for magnetic material. This is due to the fact that eddy current probe impedance changes on an unflawed plate at moderate high frequencies depends on the product of the conductivity and permeability. At low frequencies the parameters are to some extent separable, at least in principle but the eddy current signal weakens and becomes less easy to measure. This is because the induced current depends on the rate of change of the field which diminishes as the frequency is decreased.

A more effective way of finding both electrical conductivity and magnetic permeability accurately is by using a four point probe [108]. Because the current is injected via two contact pins there is no inherent reduction in the injected current as a function of frequency and measurement can be carried out with a DC current or preferably at very low frequency to eliminate thermal-electric effects. The measurements of potential drop using two pick-up pins at low frequency is then dependent on conductivity with very little contribution from the permeability. This happens when the skin depth is much greater than the pin separation. At high frequency, the pick-up voltage is like the eddy current measurement; dependent on the product of electrical conductivity and permeability, but as one approaches the direct current limit, it tends toward a dependence on conductivity only.

The ACPD test bench is shown in Fig. 6.5, which comprises platform, specimen and probe from bottom up. In order to observe the in-homogeneous properties of material conductivity and permeability due to different positions, the test is repeated four times at different positions.

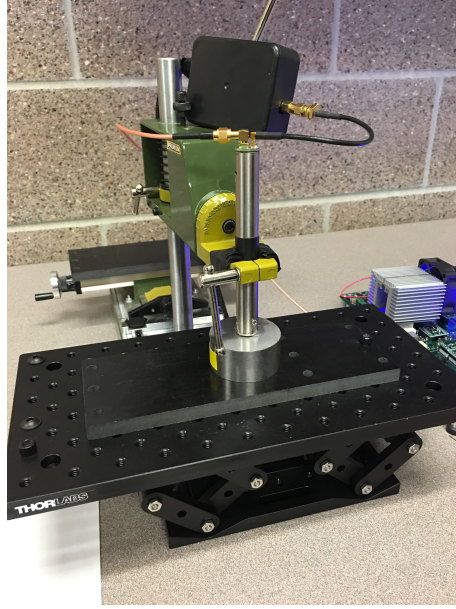


Figure 6.5: ACPD test bench for measuring specimen conductivity and permeability

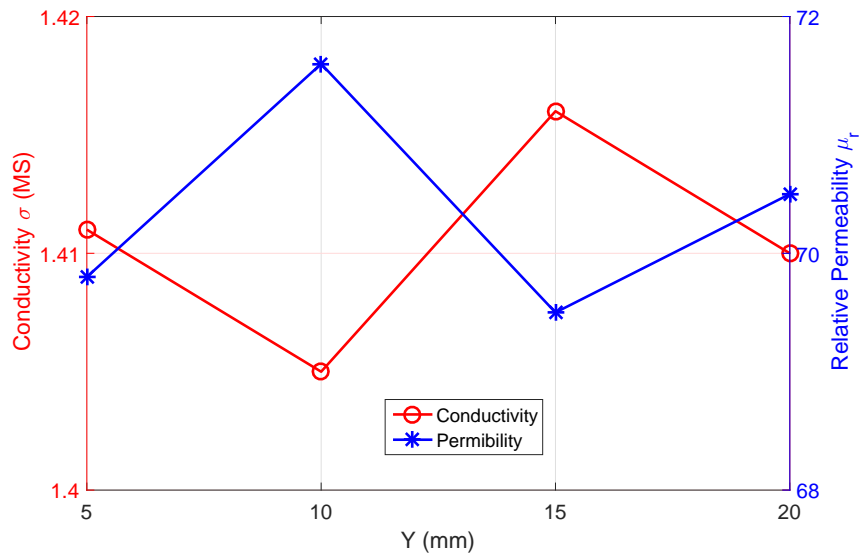


Figure 6.6: The variation of specimen conductivity and permeability in terms of position

The result are shown in Fig. 6.6. The conductivity has the mean $\sigma = 1.41Ms/m$ and 0.4% variation. The permeability has the mean $\mu_r = 70.3$ and 2% variation.

6.3 Experiment Data for a Ferromagnetic Steel Specimen with a Semi-elliptical Notch

6.3.1 13 mm Thick Slab Specimen

The 13mm 440SS steel specimen has the dimension $100\text{mm} \times 100\text{mm} \times 13\text{mm}$ ($L \times W \times H$). The semi-elliptical notch is located at the center with the dimension $8.026\text{mm} \times 0.16\text{mm} \times 1.999\text{mm}$, Fig. 6.7.

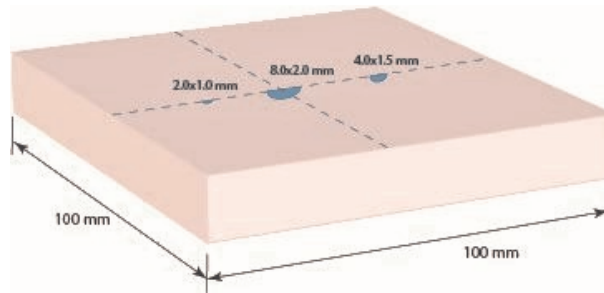


Figure 6.7: Thick 440SS steel slab specimen with semi-elliptical notch

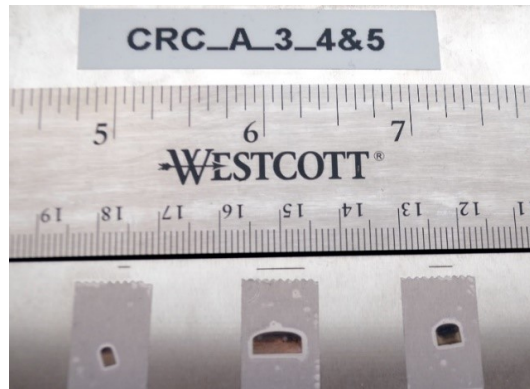


Figure 6.8: 8 mm notch (middle one) in 13mm thick specimen with the EDM cutting tool

6.3.1.1 Liftoff Determination by Multi-frequency Scan

In order to determine the probe liftoff, the impedance variation due to the presence of the flawless specimen is obtained at different frequency. Then the theoretical equivalent liftoff is obtained by fitting the multi-frequency impedance variation data via the theoretical impedance variation formulation, Eq. 4.30. The theoretical and experimental data comparison are shown

in Fig. 6.9 and 6.10. The equivalent liftoff 0.82 mm is used.

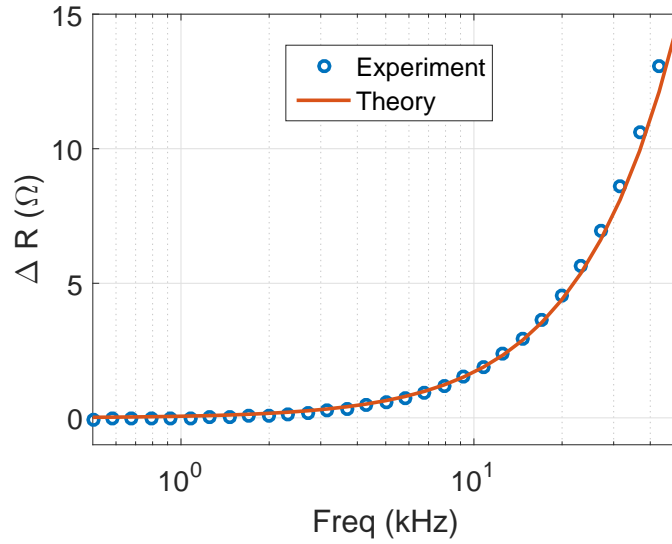


Figure 6.9: The resistance change of a circular coil above a flawless 440SS slab as a function of frequency

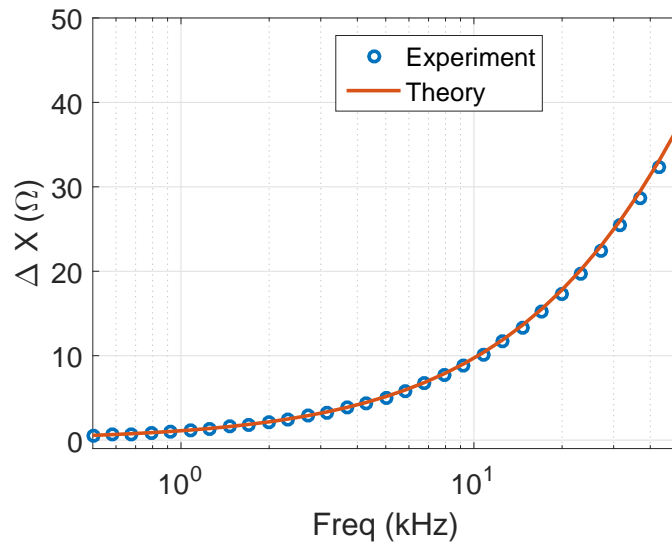
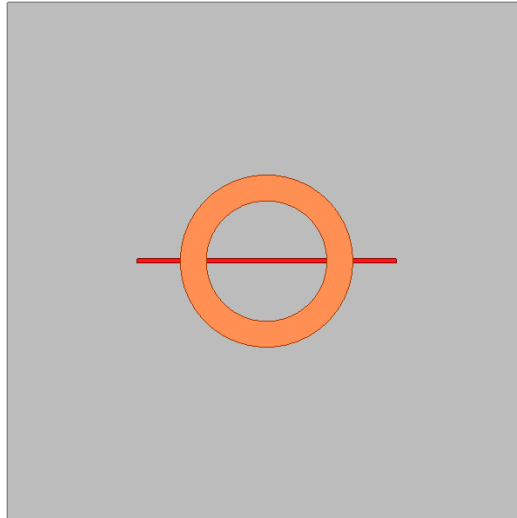


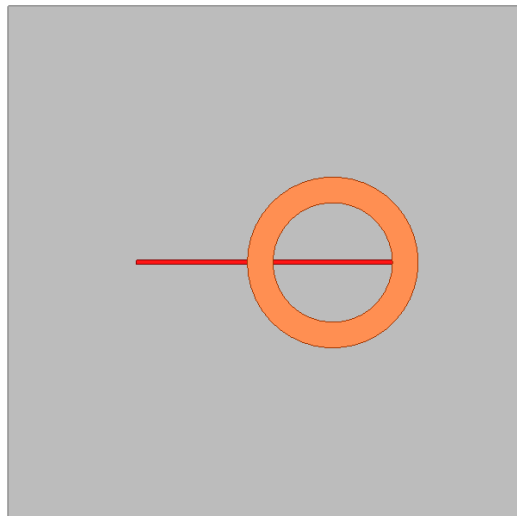
Figure 6.10: The reactance change of a circular coil above a flawless 440SS slab as a function of frequency

6.3.1.2 Impedance Variation along the Notch

In this experiment, the eddy-current probe is scanned along the notch, Fig. 6.11. Several frequencies are tested. More detailed parameters of eddy-current probe, test specimen, notch size and test conditions are shown in Tab. 6.1. The comparison between prediction and experimental data are summarized as follows.



(a) Eddy current coil is centered above the notch



(b) Eddy current coil is centered above the notch and scanned along the notch

Figure 6.11: Along the notch scan diagram

Table 6.1: Probe coil 1, 13 mm specimen and notch parameters

Coil Inner Radius, r_1	2.82 mm
Coil Outer Radius, r_2	4.51 mm
Coil Width	1.78 mm
Number of Turns	306
Liftoff	0.82 mm
Notch Depth	1.999 mm
Notch Width	0.160 mm
Notch Length	8.026 mm
404SS Steel Specimen Thickness	13 mm
Conductivity (MS/m)	1.41
Relative Magnetic Permeability, μ_r	70.3

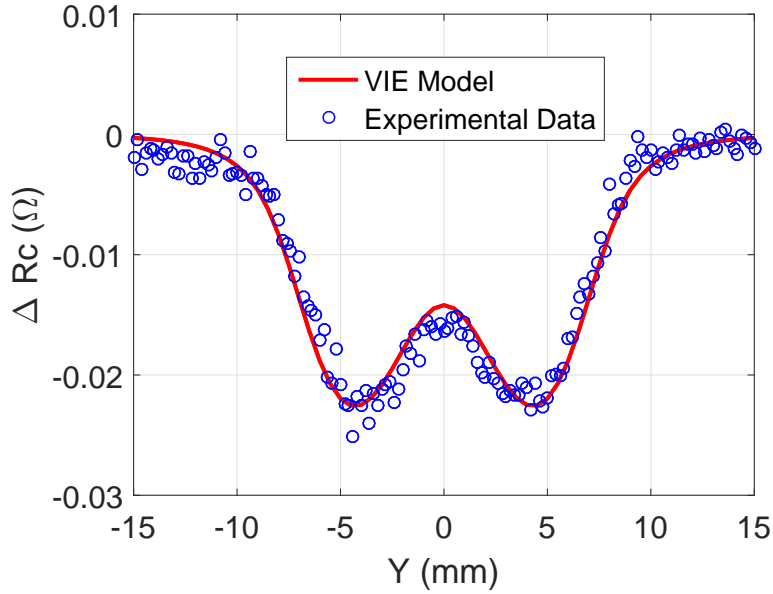


Figure 6.12: Comparison between model prediction and experimental data of resistance variation at 3 kHz

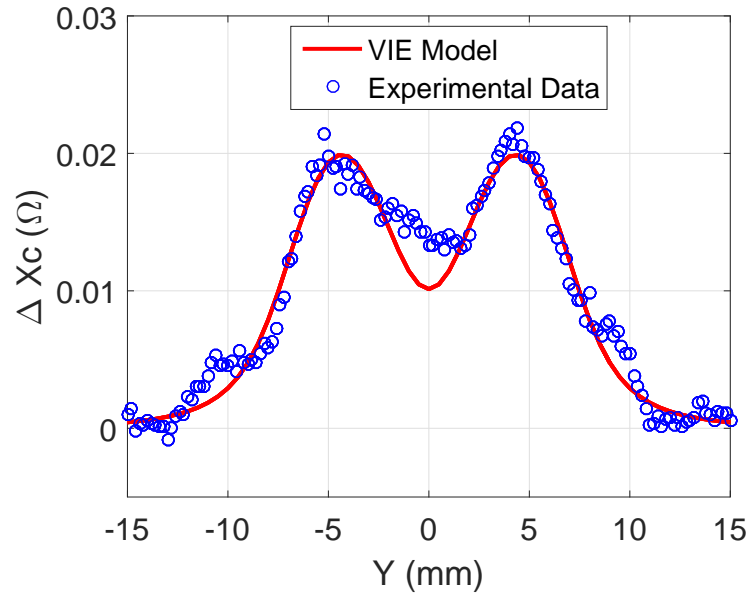


Figure 6.13: Comparison between model prediction and experimental data of reactance variation at 3 kHz

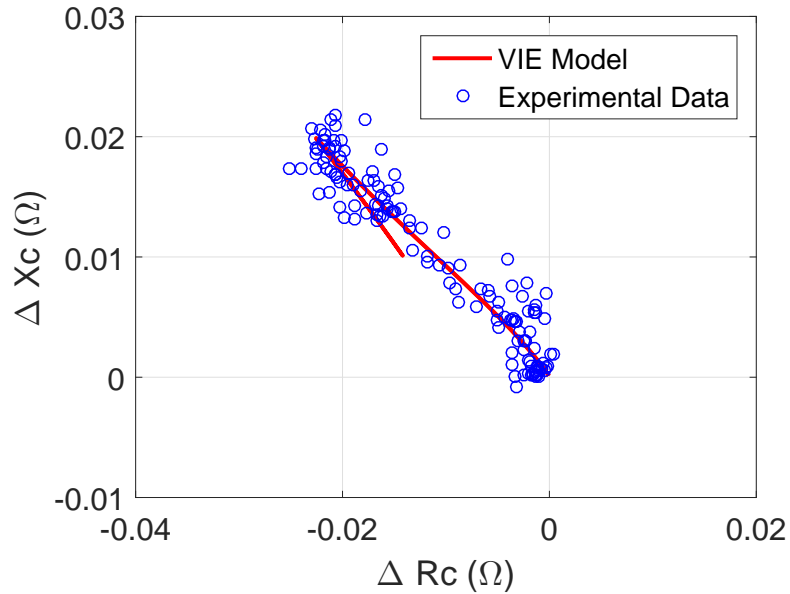


Figure 6.14: Comparison between model prediction and experimental data of impedance variation in impedance plane at 3 kHz

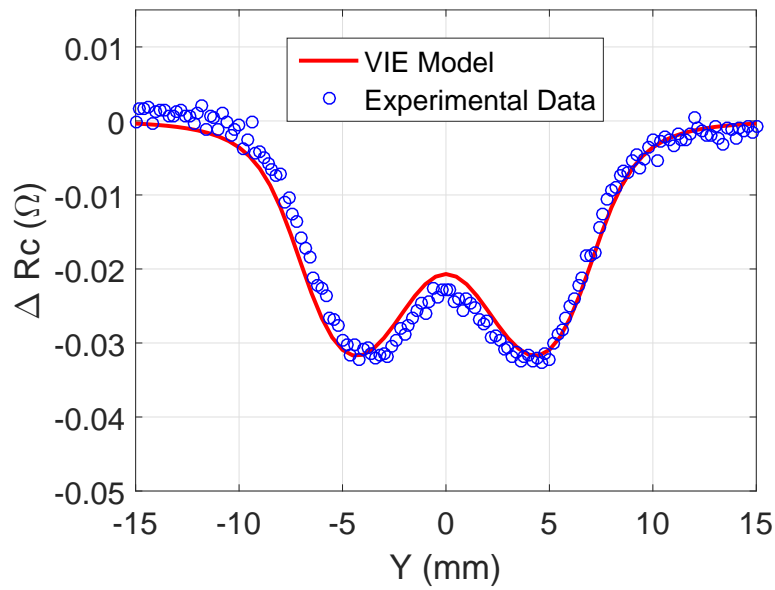


Figure 6.15: Comparison between model prediction and experimental data of resistance variation at 4 kHz

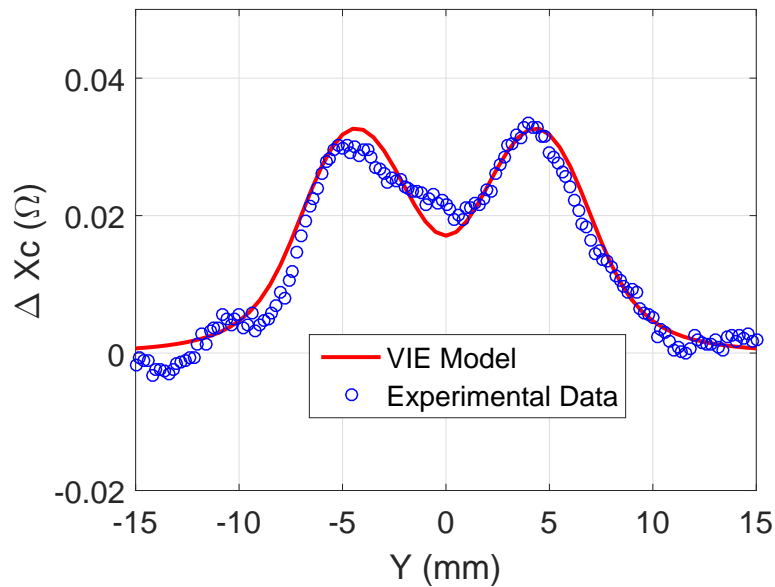


Figure 6.16: Comparison between model prediction and experimental data of reactance variation at 4 kHz

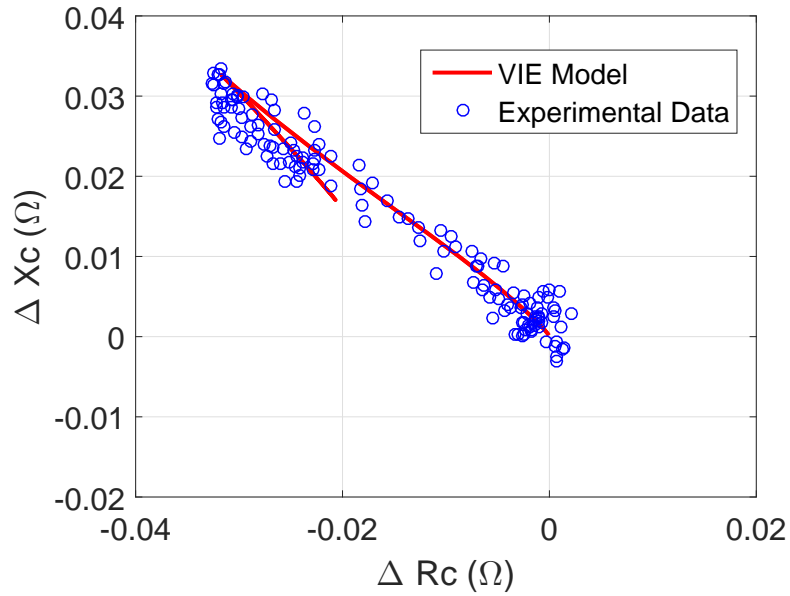


Figure 6.17: Comparison between model prediction and experimental data of impedance variation in impedance plane at 4 kHz

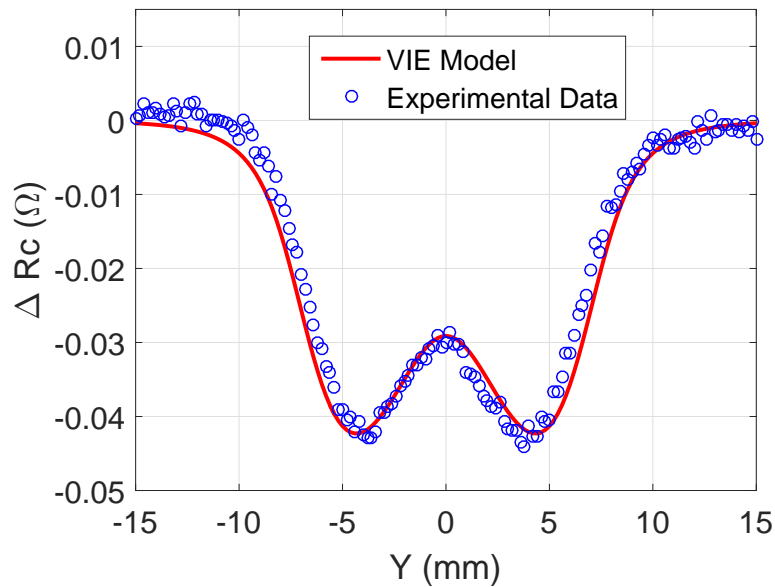


Figure 6.18: Comparison between model prediction and experimental data of resistance variation at 5 kHz

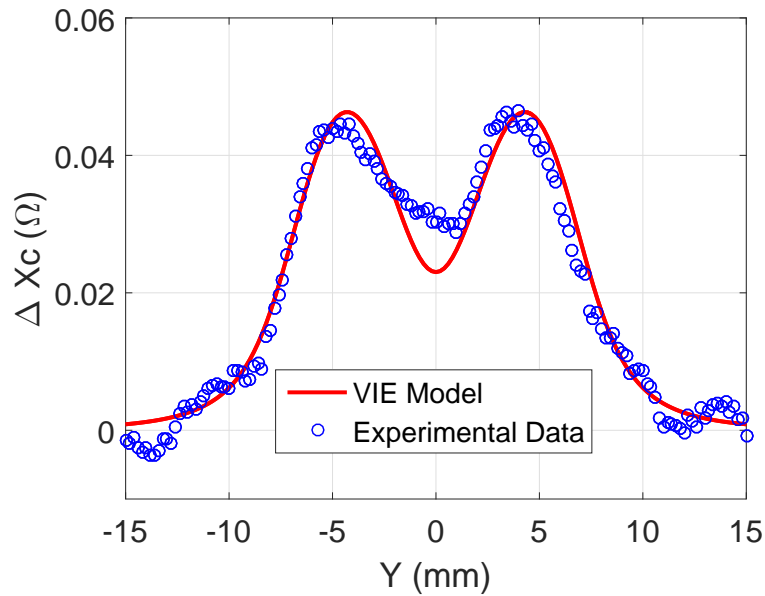


Figure 6.19: Comparison between model prediction and experimental data of reactance variation at 5 kHz

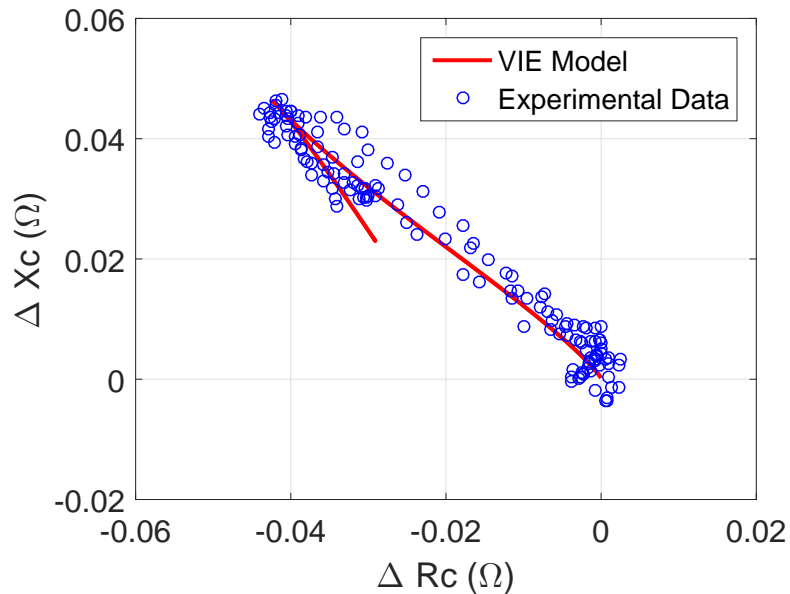
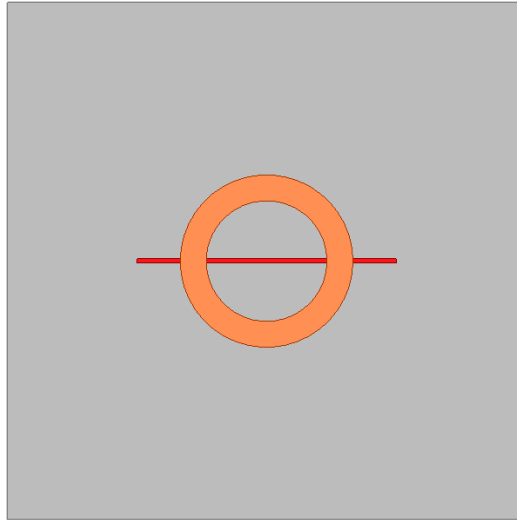


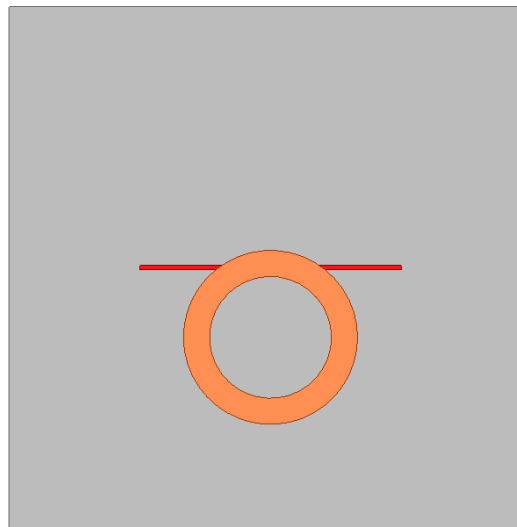
Figure 6.20: Comparison between model prediction and experimental data of impedance variation in impedance plane at 5 kHz

6.3.1.3 Impedance Variation across the Notch

In this experiment, the eddy-current probe is scanned across the notch, Fig. 6.21. Several frequencies are tested. More detailed parameters of eddy-current probe, test specimen, notch size and test conditions are shown in Tab. 6.1. The comparison between prediction and experimental data are summarized as follows.



(a) Eddy current coil is centered above the notch



(b) Eddy current coil is centered above the notch and scanned across the notch

Figure 6.21: Across the notch scan diagram

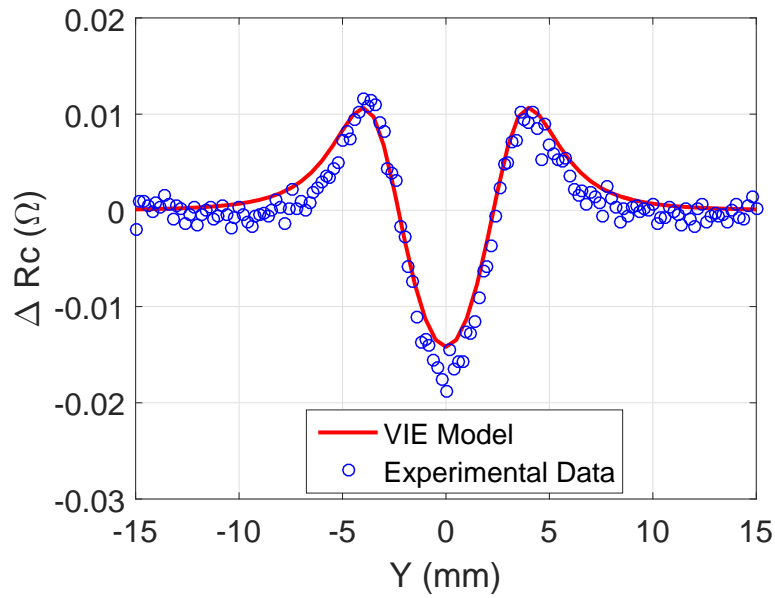


Figure 6.22: Comparison between model prediction and experimental data of resistance variation at 3 kHz

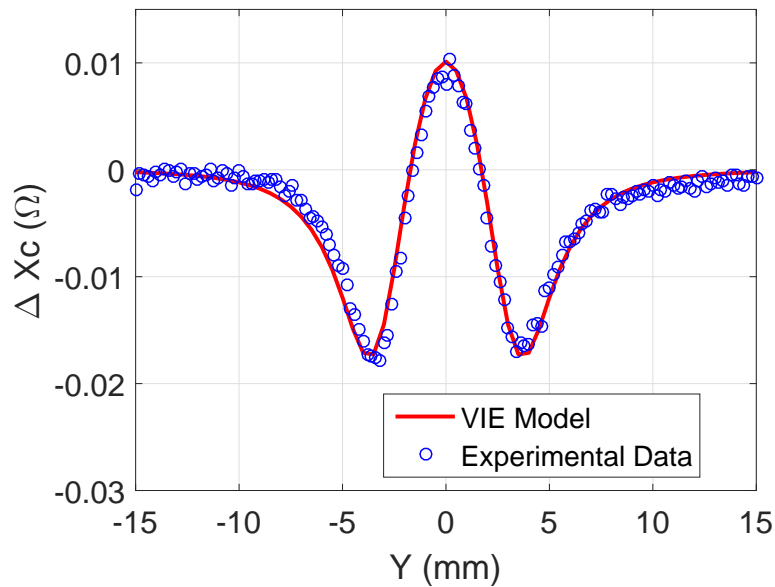


Figure 6.23: Comparison between model prediction and experimental data of reactance variation at 3 kHz

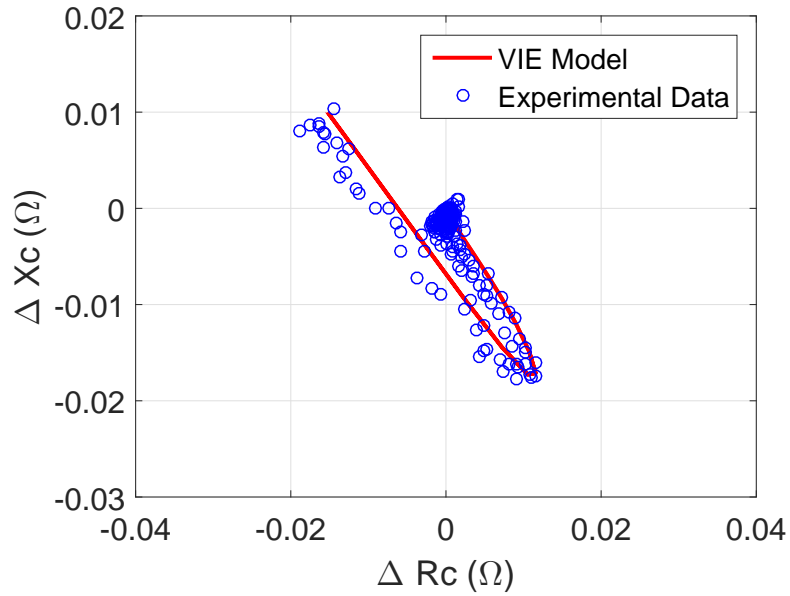


Figure 6.24: Comparison between model prediction and experimental data of impedance variation in impedance plane at 3 kHz

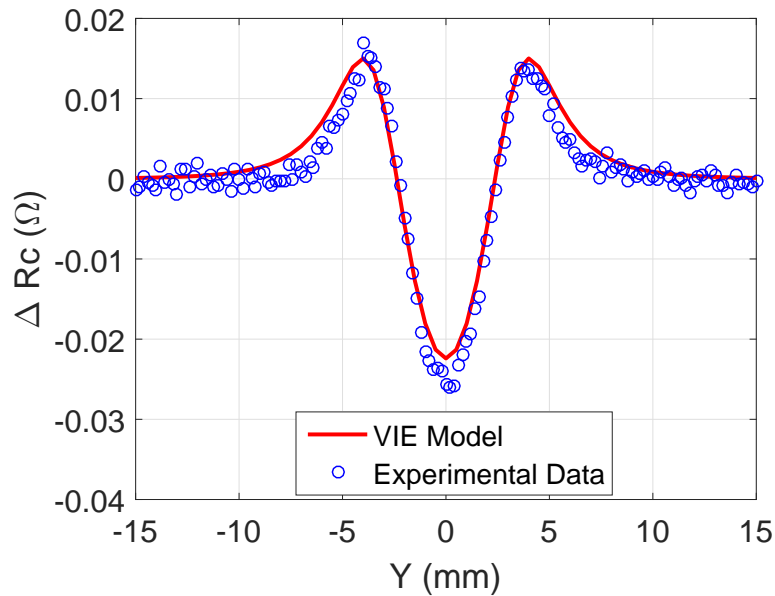


Figure 6.25: Comparison between model prediction and experimental data of resistance variation at 4 kHz

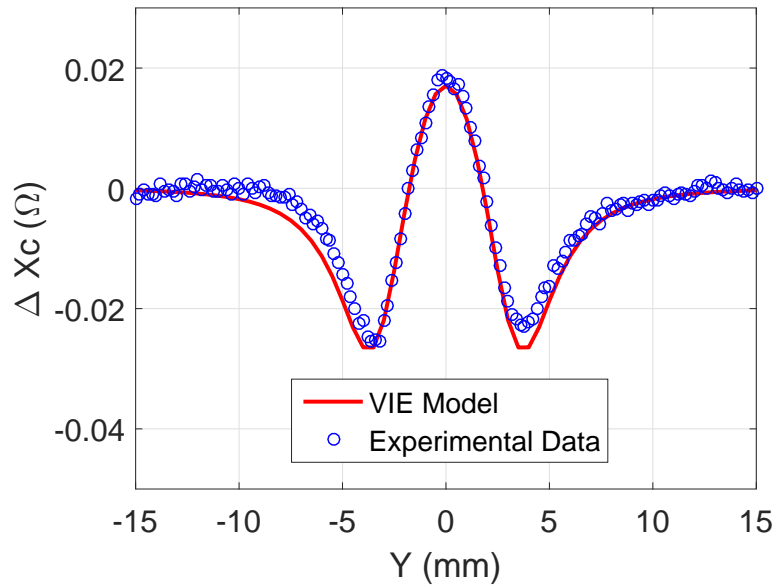


Figure 6.26: Comparison between model prediction and experimental data of reactance variation at 4 kHz

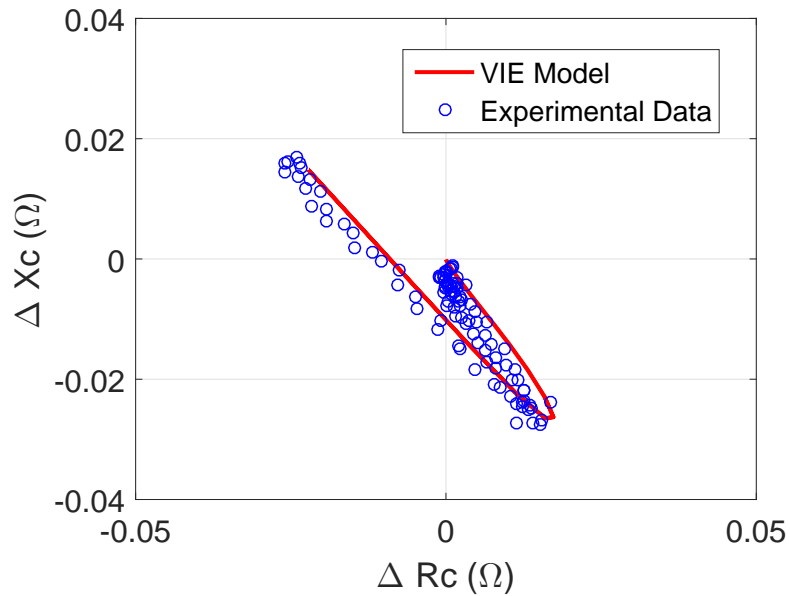


Figure 6.27: Comparison between model prediction and experimental data of impedance variation in impedance plane at 4 kHz

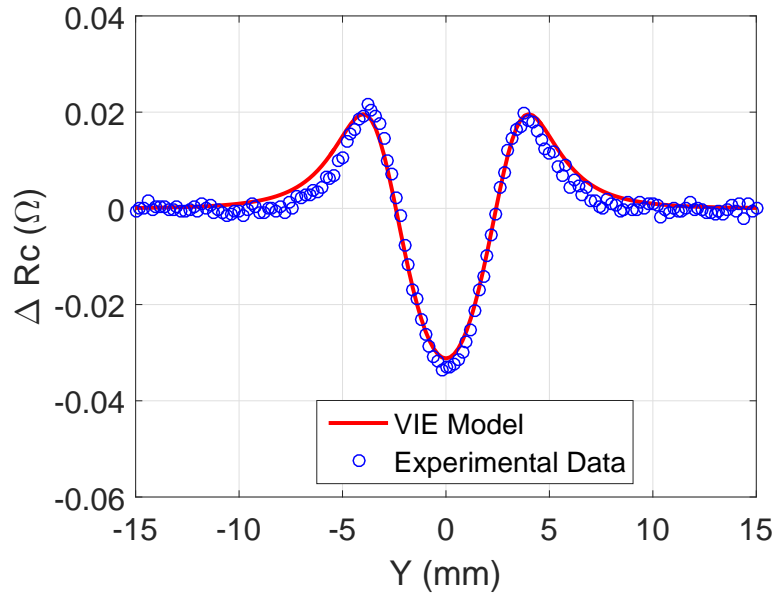


Figure 6.28: Comparison between model prediction and experimental data of resistance variation at 5 kHz

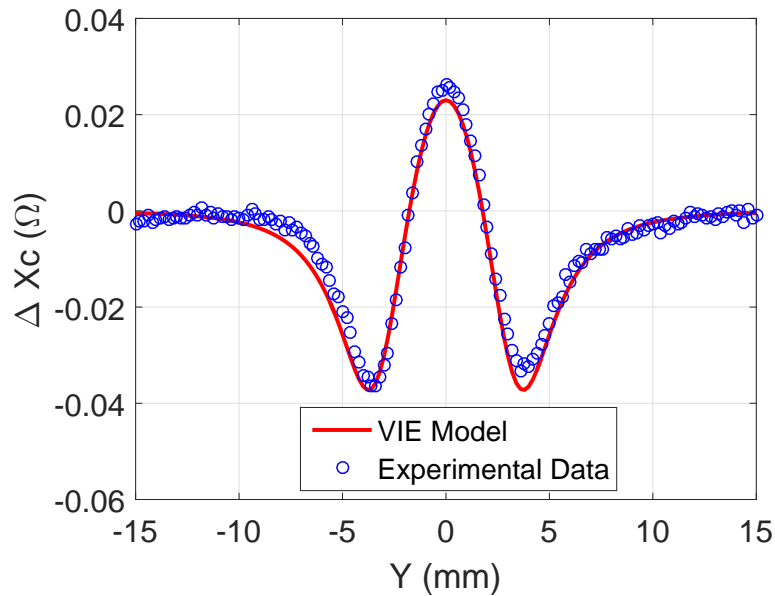


Figure 6.29: Comparison between model prediction and experimental data of reactance variation at 5 kHz

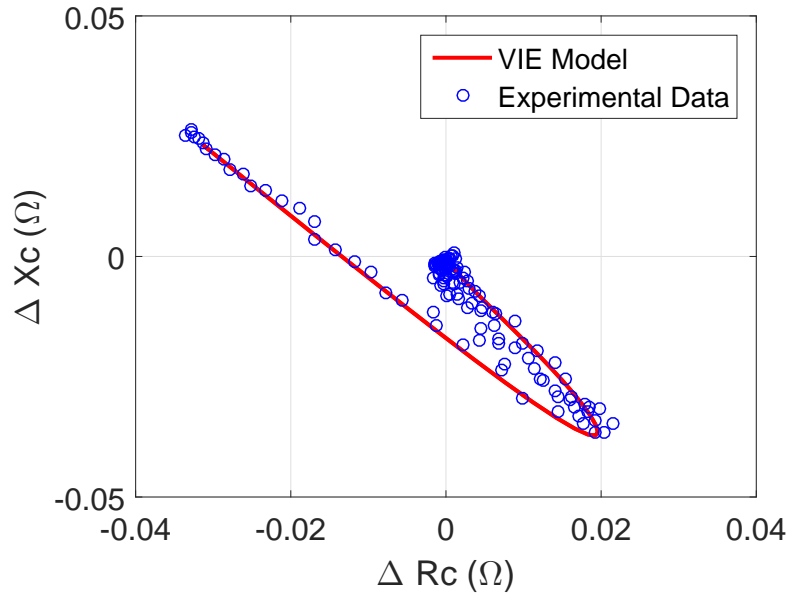


Figure 6.30: Comparison between model prediction and experimental data of impedance variation in impedance plane at 5 kHz

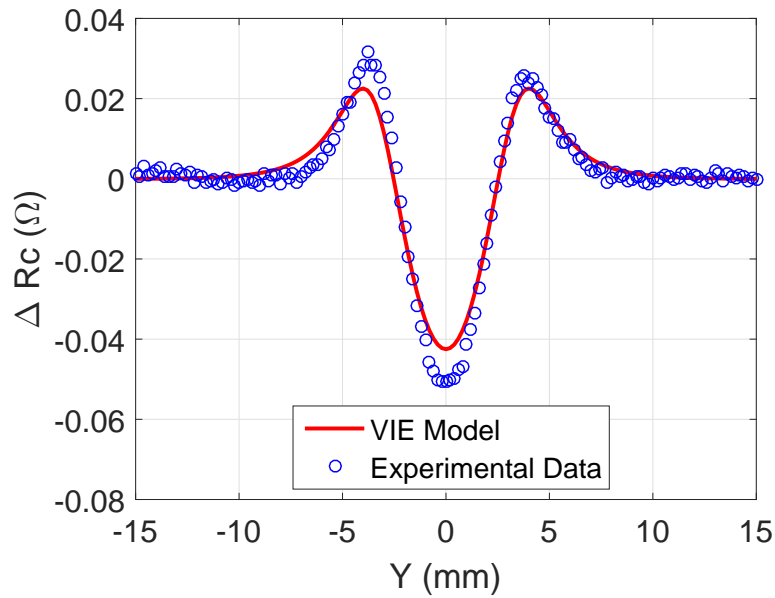


Figure 6.31: Comparison between model prediction and experimental data of resistance variation at 7 kHz

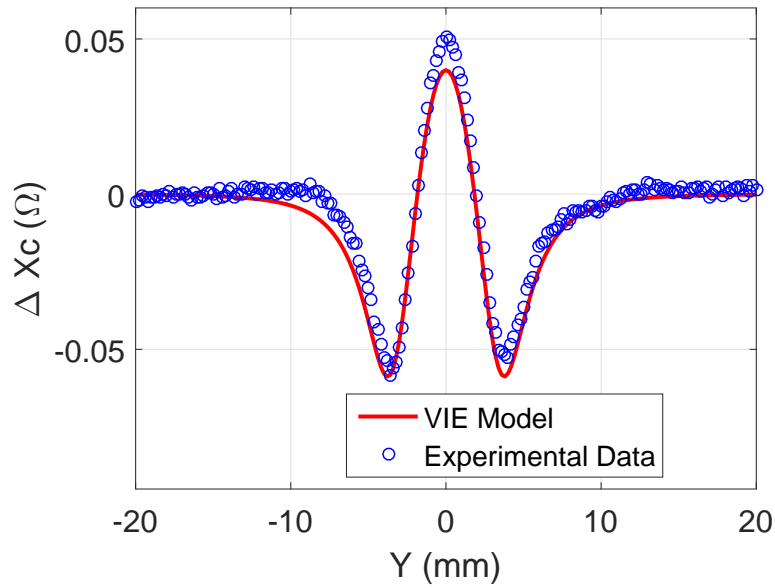


Figure 6.32: Comparison between model prediction and experimental data of reactance variation at 7 kHz

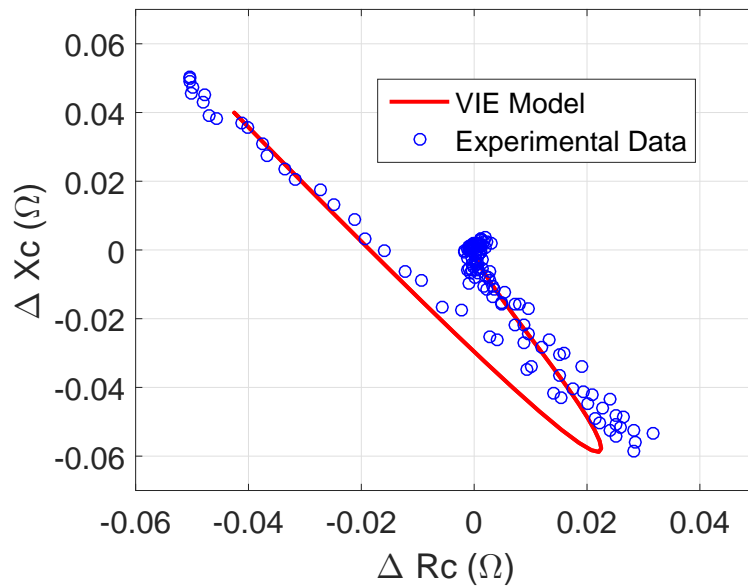


Figure 6.33: Comparison between model prediction and experimental data of impedance variation in impedance plane at 7 kHz

From the comparison, we can find the good agreement between the model prediction and experimental data is achieved. Besides, we can find the along-the-notch scan data is more noisy than that of across-the-notch data. The reason might be that the interaction between nearby notch due to there is not enough distance between three notches in the along-the-notch direction. On the contrary, there is no other notch in the across-the-notch direction.

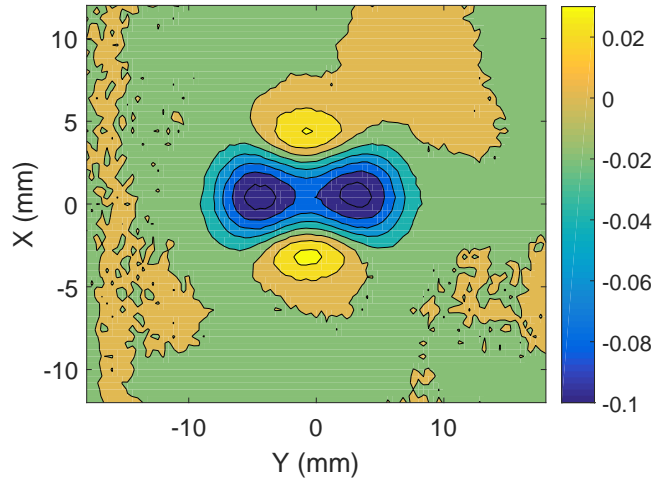


Figure 6.34: Impedance real part variation contour of 13mm specimen at 10kHz with semi-elliptical notch based on experiment

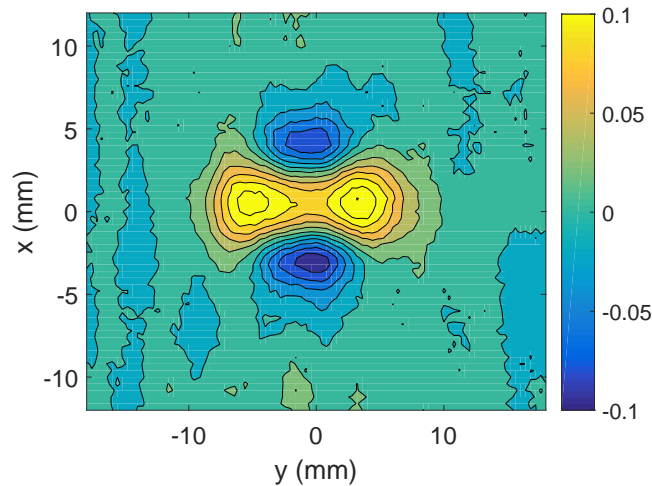


Figure 6.35: Impedance imaginary part variation contour of 13mm specimen at 10kHz with semi-elliptical notch based on experiment

6.3.1.4 Impedance Variation 2-D Image

There are many factors which could introduce impedance change noise. For example the specimen surface curve, in-homogeneous of material properties. residual stress etc. In order to have a better observation about the impedance variation in terms of position, the impedance change image is obtained by the 2D impedance scan, Figs. 6.34 and 6.35.

From the 2-D impedance variation image, we can clearly observe the linear pattern of the reactance part due to the lift-off variation caused by specimen curve.

6.3.2 3 mm Thin Slab Specimen

The 3mm 440 SS slab specimen has the dimension $100\text{mm} \times 100\text{mm} \times 2.93\text{mm}$ ($L \times W \times H$). The semi-elliptical notch is located at the center with the dimension $6.026\text{mm} \times 0.146\text{mm} \times 1.504\text{mm}$, Fig. 6.36. More detailed parameters of eddy-current probe, test specimen, notch size and test conditions are shown in Tab. 6.2.

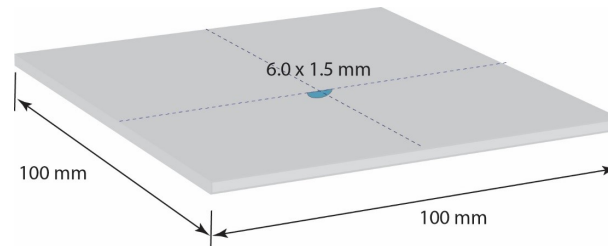


Figure 6.36: Thin 440SS steel slab specimen with semi-elliptical notch

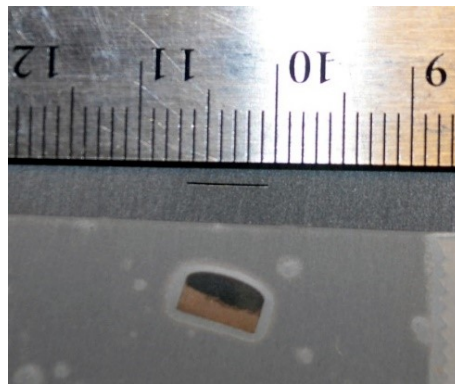


Figure 6.37: 6 mm notch in 3mm thick specimen with the EDM cutting tool

6.3.2.1 Impedance Variation along the Notch

In this experiment, the eddy-current probe is scanned along the notch. The frequency is 10 kHz and the corresponding skin-depth is $\delta = 0.5066\text{mm}$. Note that the electrical field interaction is dominant due to that the magnetic field intensity is tangential to the notch surface. The mesh size used in calculation is $N_x \times N_y \times N_z = 1 \times 10 \times 40$.

Table 6.2: Probe coil 1, 3 mm specimen and notch parameters

Coil Inner Radius, r_1	2.82 mm
Coil Outer Radius, r_2	4.51 mm
Coil Width	1.78 mm
Number of Turns	306
Liftoff	0.4 mm
Notch Depth	1.504 mm
Notch Width	0.146 mm
Notch Length	6.026 mm
404SS Steel Specimen Thickness	2.93mm
Conductivity (MS/m)	1.41
Relative Magnetic Permeability, μ_r	70.3

The comparison between the model predicted data and experimental data are shown in Fig. 6.38 and Fig. 6.39 and the good agreement is achieved. The RMS impedance noise of the circuit is about $2\text{ m}\Omega$. The discrepancy away from the notch could be caused by inhomogeneous of steel conductivity, permeability, lift-off variation due to non-flat surface and residual stress due to the fabrication procedure. Besides, the constant relative permeability is assumed and this might not be good enough to characterize the ferromagnetic metal.

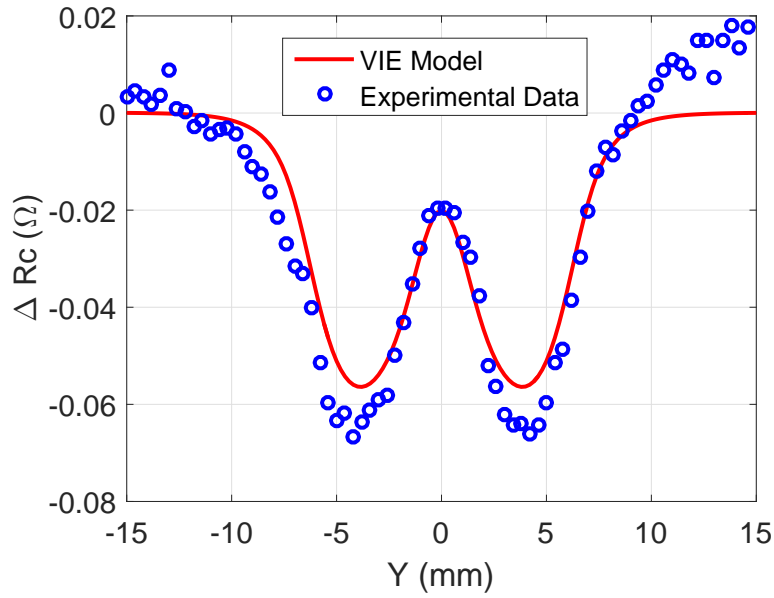


Figure 6.38: Comparison between model prediction and experiment data of resistance variation at 10 kHz

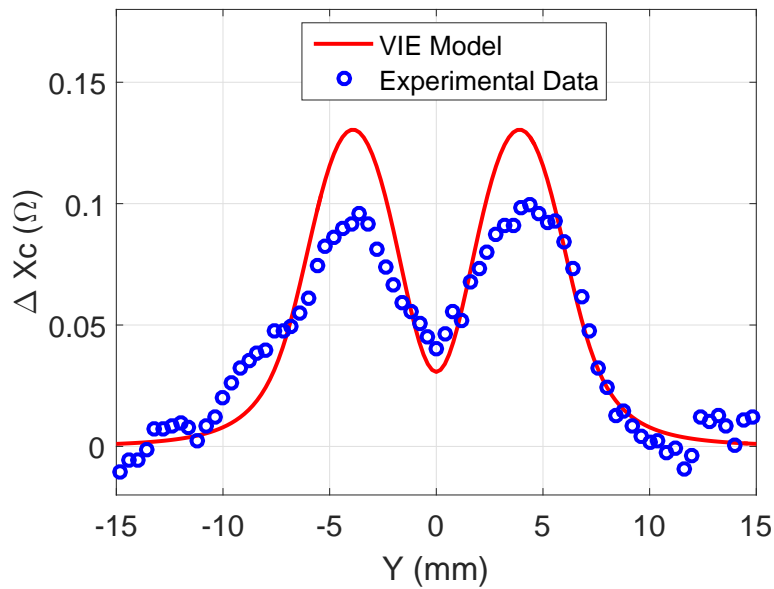


Figure 6.39: Comparison between model prediction and experiment data of reactance variation at 10 kHz

6.3.2.2 Impedance Variation across the Notch

The experiment with the eddy-current probe scan cross over the notch is carried out. The parameters of test experiment are the same as Tab. 6.2. The comparison between model prediction and experimental data are shown in Figs. 6.40 and 6.41.

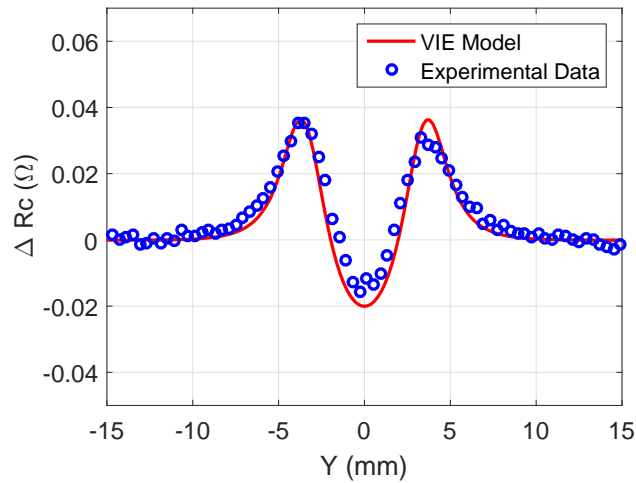


Figure 6.40: Comparison between model prediction and experiment of resistance changes at 10 kHz for across-the-notch scan

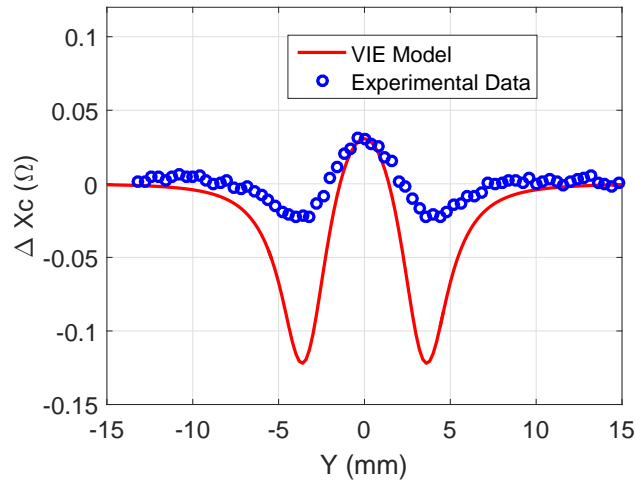


Figure 6.41: Comparison between model prediction and experiment of reactance changes at 10 kHz for across-the-notch scan

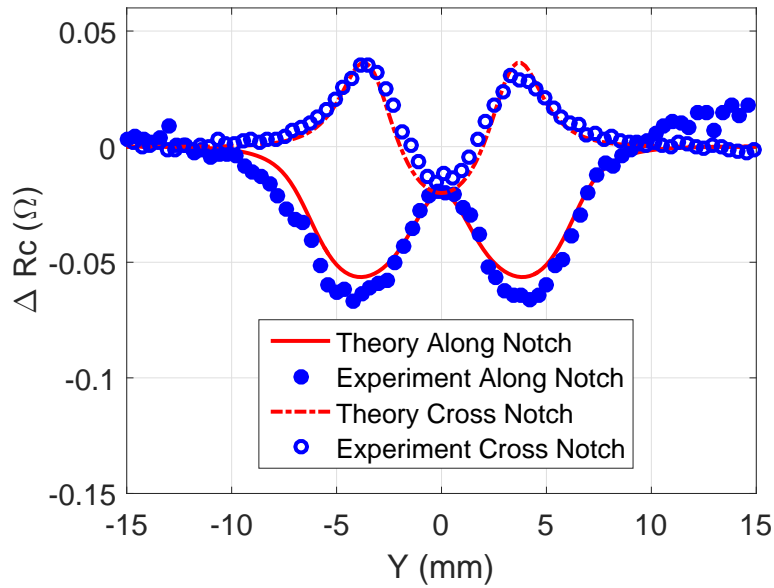


Figure 6.42: Comparison between model prediction and experiment of resistance changes at 10 kHz for both scans

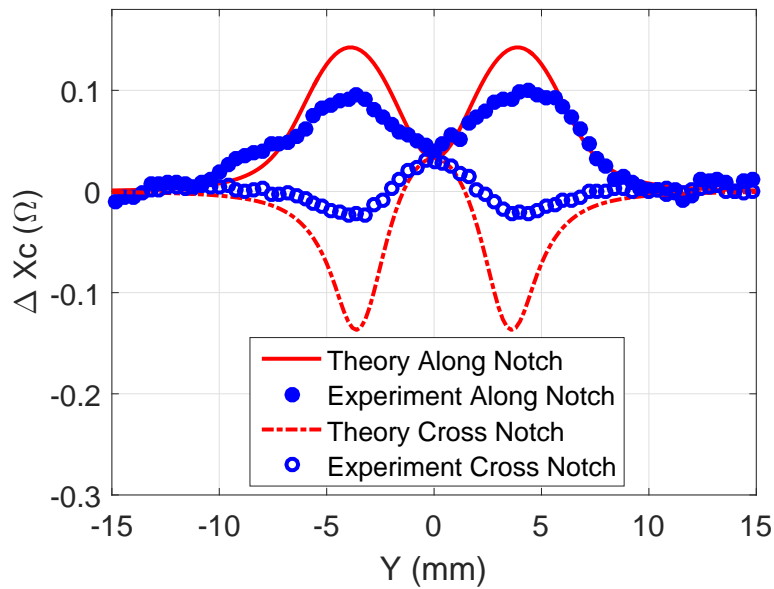


Figure 6.43: Comparison between model prediction and experiment of resistance changes at 10 kHz for both scans

Contrary to along-the-notch scan, the magnetic field interaction is stronger due to that the magnetic field intensity is mostly perpendicular to the notch surface. And this causes an interesting effect on the impedance change that the across-the-notch scan has opposite effect on the impedance change, Figs 6.42 and 6.43. This means one introduces a local maximum point and another will cause a local minimum point. Compared with non-ferromagnetic metal result, this is special to ferromagnetic metal and might be useful to distinguish the real crack signal from disturbing signals. For better comparison, the impedance variation of both scans are shown in Fig.6.42 and Fig. 6.43.

6.3.2.3 Impedance Variation 2-D Image

There are many factors which could introduce impedance change noise. For example inhomogeneous of material properties. residual stress etc. In order to have a better observation about the impedance variation in terms of position, The impedance change image is obtained by the 2D impedance scan, Figs. 6.44 and 6.45.

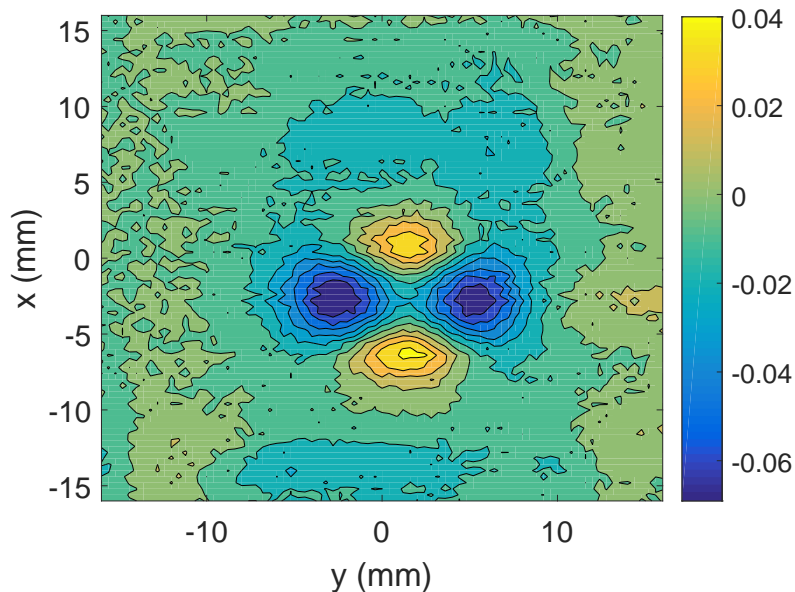


Figure 6.44: Impedance real part variation contour of 3mm specimen at 10kHz with semi-elliptical notch

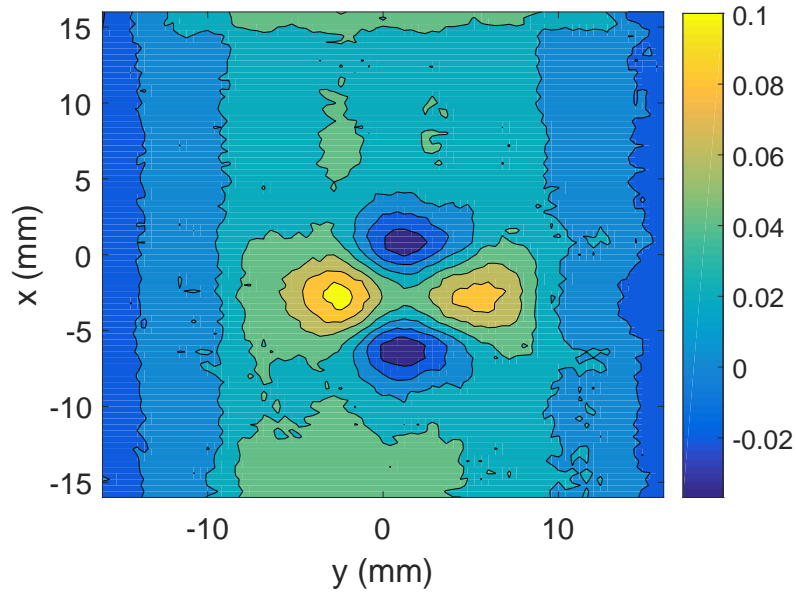


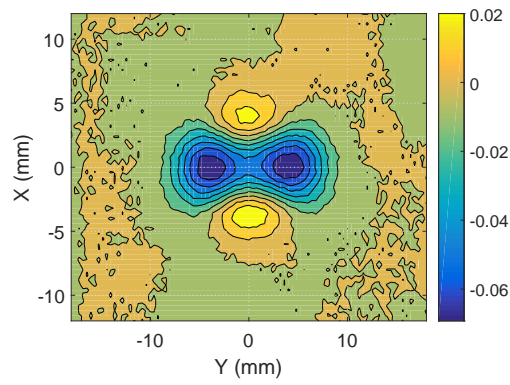
Figure 6.45: Impedance imaginary part variation contour of 3mm specimen at 10kHz with semi-elliptical notch

From the 2-D impedance variation image, we can clearly observe the linear pattern of the reactance part due to the lift-off variation caused by specimen curve. Besides, the opposite effect between along-the-notch scan and across-the-notch scan can also be found.

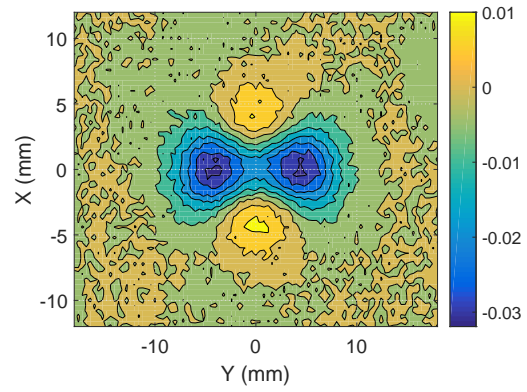
6.4 Liftoff Effect on Probability of Detection

The liftoff will affect the impedance variation significantly. In this section, we analyze the different liftoff effect on the impedance change signal quality. The specimen used in this test is the 13mm 440 stainless steel and the probe coil 1.

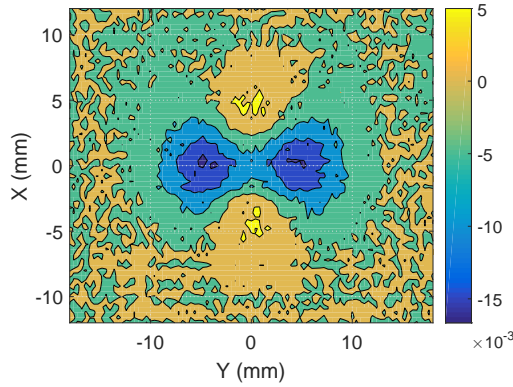
The liftoff is from 1.35mm to 6.35mm with the step 1mm and denoted as No.1 to No.6. The test frequency is 10kHz. The real part of impedance variation contour are shown as follows:



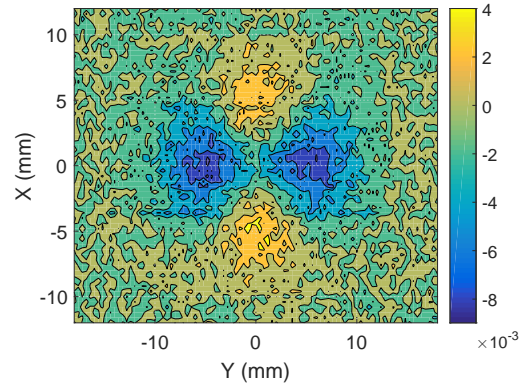
(a) Liftoff No. 1



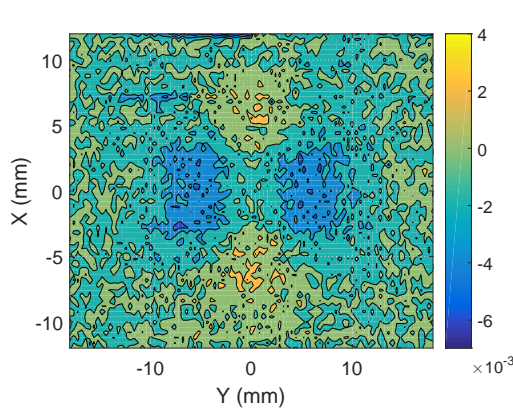
(b) Liftoff No. 2



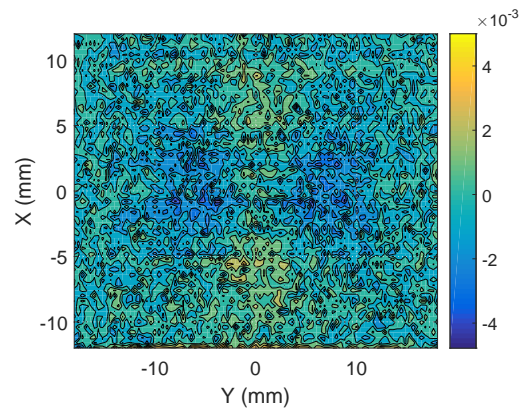
(c) Liftoff No. 3



(d) Liftoff No. 4



(e) Liftoff No. 5



(f) Liftoff No. 6

Figure 6.46: The real part of impedance variation contour in terms of different liftoff based on experiment

The imaginary part of impedance variation contour are shown as follows:

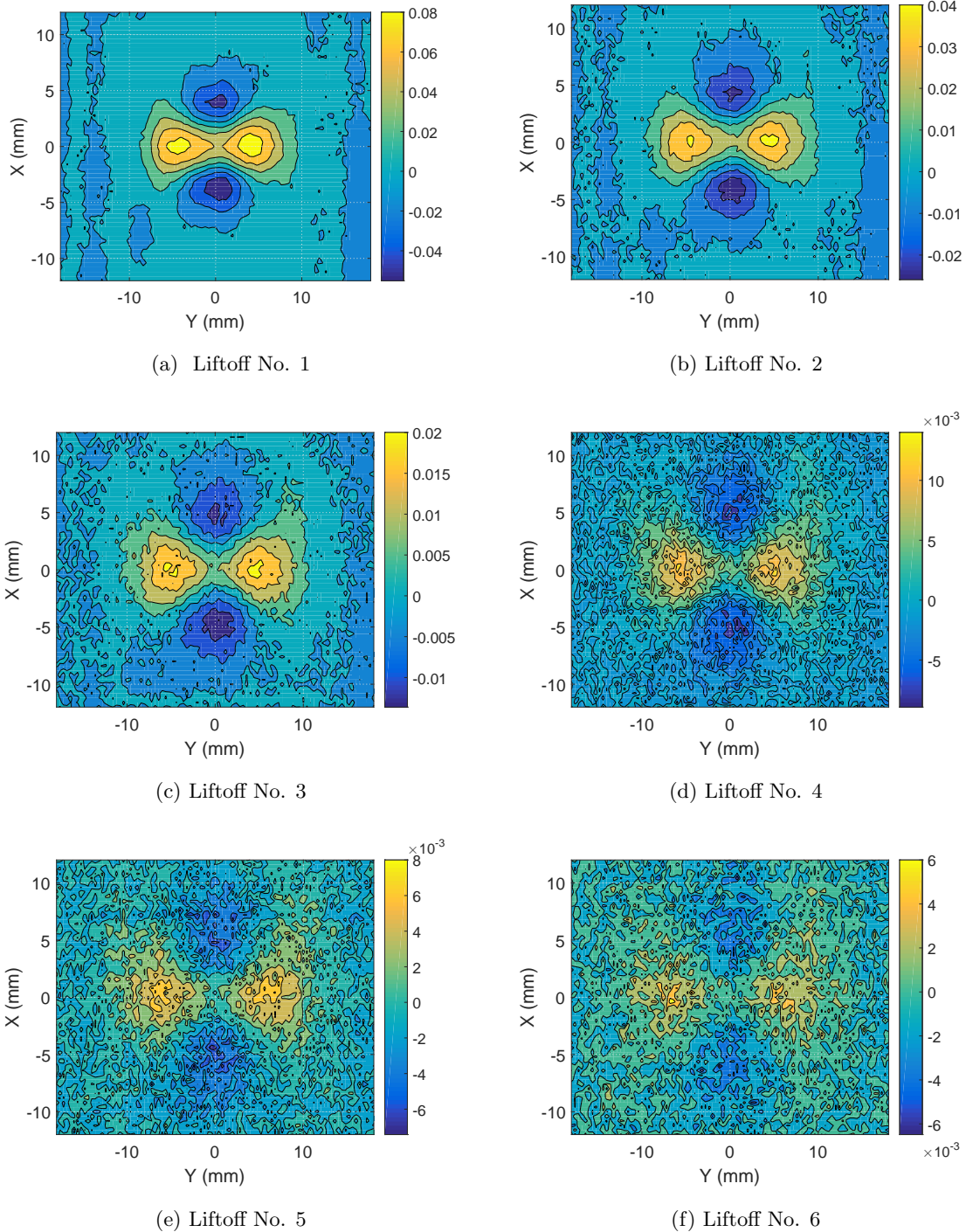


Figure 6.47: The imaginary part of impedance variation contour in terms of different liftoff based on experiment

As the liftoff increases, the crack signal will decrease due to the bigger liftoff compared with the baseline. Hence the probability of detection (POD) the rack will decrease. A classic POD model can be expressed as with logic link function in terms of crack length [110]

$$POD(x) = \frac{e^{\beta_0 + \beta_1 \ln(x)}}{1 + e^{\beta_0 + \beta_1 \ln(x)}} \quad (6.1)$$

Where x is the crack size and POD is the corresponding probability. β_0 and β_1 are the coefficients which can be estimated as the well-known linear regression estimates of $\ln \left[\frac{POD}{1-POD} \right]$ on $\ln(x)$.

Similarly, here a modified POD formulation for the effect of liftoff can be written as

$$POD(x) = \frac{1}{1 + e^{\beta_0 + \beta_1 \ln(x)}} \quad (6.2)$$

or

$$\ln \left[\frac{1 - POD}{POD} \right] = \beta_0 + \beta_1 \ln(x) \quad (6.3)$$

Where x is the liftoff and POD is the corresponding probability. β_0 and β_1 are the coefficients which can be estimated by the linear regression estimates of $\ln \left[\frac{1-POD}{POD} \right]$ on $\ln(x)$. Then the POD is obtained as shown in Fig.6.48

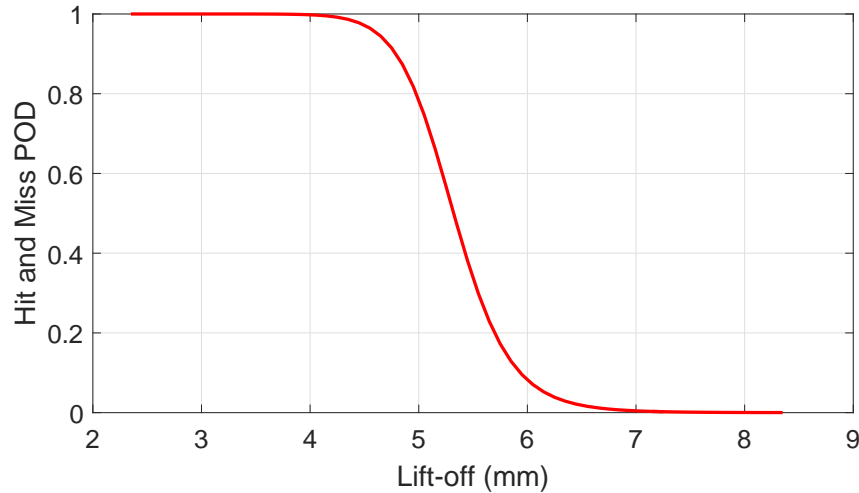


Figure 6.48: The POD curve as a function of liftoff

6.5 The Comparison of the Impedance Variation between Ferromagnetic and Non-ferromagnetic Steel

In order to have a better understanding of the effect on the impedance changes due to the ferromagnetic steel, the 2-D impedance variation simulation based on our numerical model is done for both ferromagnetic 440 steel and non-ferromagnetic steel. The probe, notch size and specimen parameters are the same, shown in Tab. 6.1, except the relative permeability of non-ferromagnetic steel is 1. The frequency is set as 5 kHz in all the simulation. The results of simulation are summarized as follow.

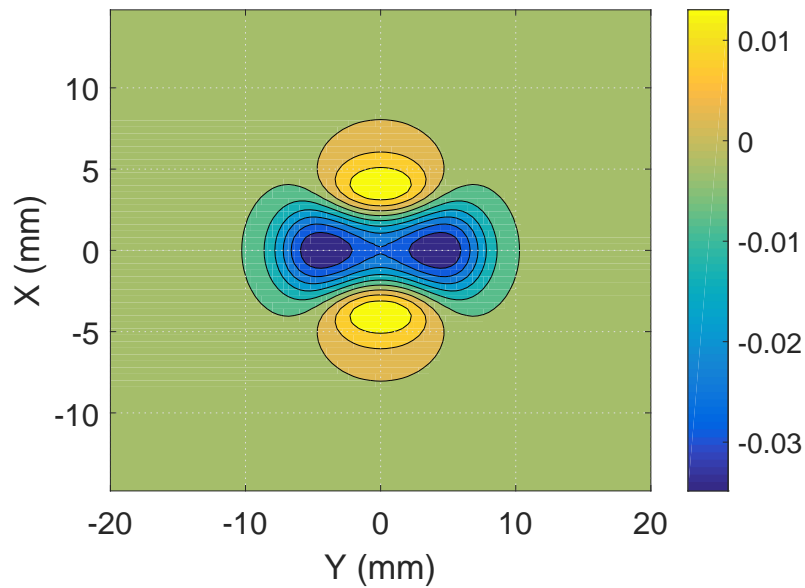


Figure 6.49: The simulated 2-D resistance variance due to the semi-elliptical notch of ferromagnetic steel

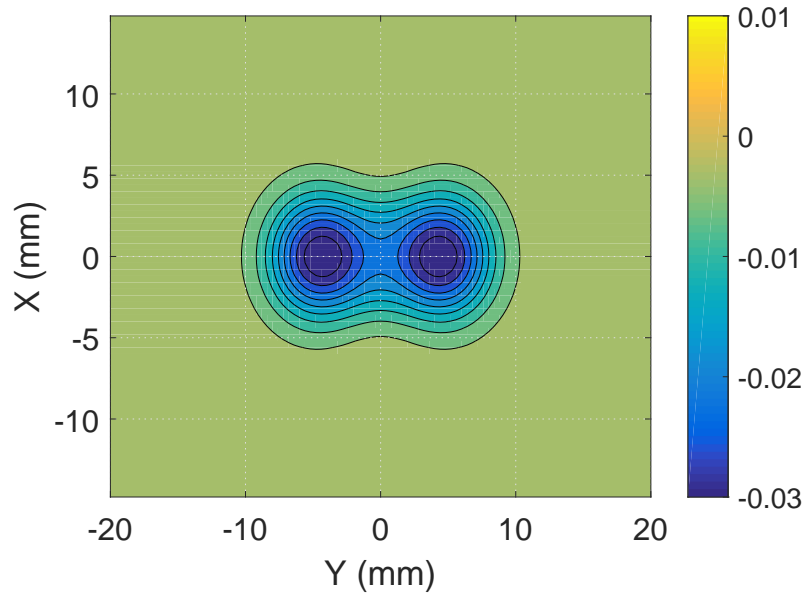


Figure 6.50: The simulated 2-D resistance variance due to the semi-elliptical notch of non-ferromagnetic steel

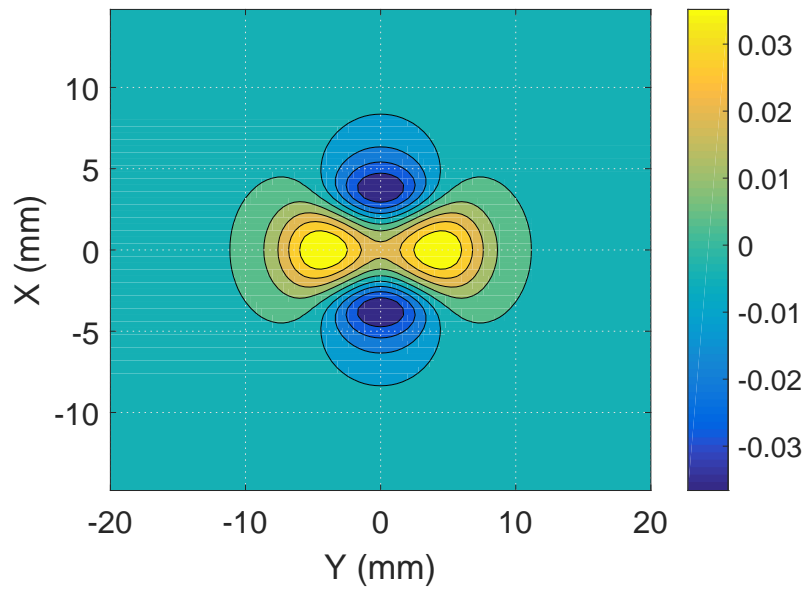


Figure 6.51: The simulated 2-D reactance variance due to the semi-elliptical notch of ferromagnetic steel

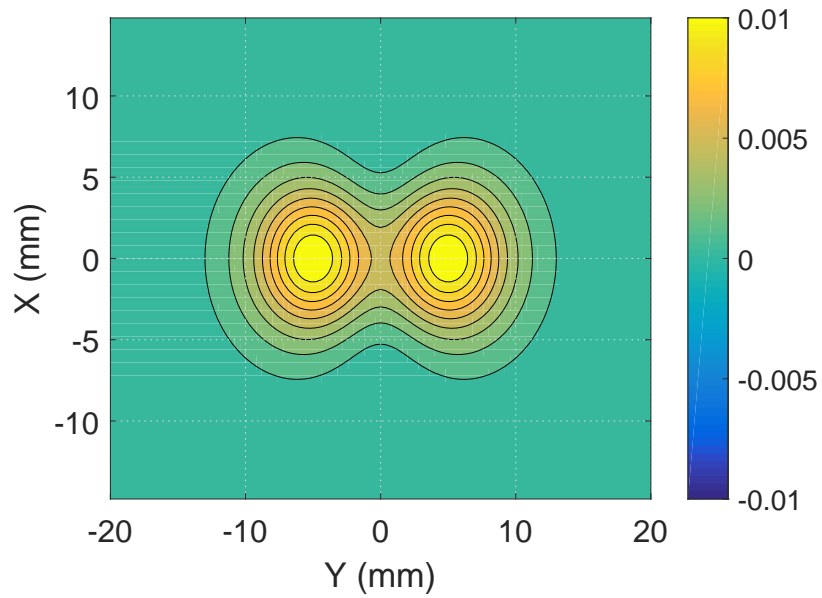


Figure 6.52: The simulated 2-D reactance variance due to the semi-elliptical notch of non-ferromagnetic steel

From the simulation, we can find an interesting phenomenon. The impedance variation of ferromagnetic steel along the notch scan and across the notch scan will have opposite sign. However, both scans will have the same sign for non-ferromagnetic conductor.

CHAPTER 7. ARBITRARY ORIENTATION INDUCTION COIL INTERACTING WITH CYLINDRICAL STRUCTURES

(A draft journal paper)

7.1 Abstract

We determine the electromagnetic field of an induction coil orientation with respect to a nearby conductive tube. The results can be used in modeling inspection for flaws or for sensing the location of a cylindrical surface. To derive the expressions for the coil field, we determine first the field of a circular current filament. The coil field is then obtained by integration of the filament field over the coil cross-section. Expressions for the electromagnetic field of an internal or external coil in the vicinity of a tube can be determined in this way. Also the coil impedance variation can be evaluated accounting for the effect of frequency, angle of azimuthal rotation and of polar tilt as well as the coil location with respect to the tube. Applications of the results include inductive position sensing and eddy current nondestructive evaluation.

7.2 Introduction

The analysis of circular coil fields and their interaction with conductive plates and circular rods or the corresponding planar and cylindrical layered systems are studied to enhance the theory of induced current and its applications. An important motivation for the analysis is to produce formula that are available for fast and accurate calculations and which can be easily embedded in codes that predict numerical results for a variety of configurations. At an early stage in these developments, analytical formula were found for the field and impedance of a circular coil whose axis is normal to the surface of a planar plate and a coil coaxial with a

circularly cylindrical conductor such as a tube[9], a configuration that is used for example in the inspection of heat exchanger tubes by bobbin coils in the power industry. Following these early results, expressions have been derived for the field of an arbitrary tilted coil above a plate [34] and recently for the case of a circular coil whose axis is arbitrary with respect to the axis of a tube or hole [24]. In this article we give an alternative solution to this problem.

The analysis of coil-tube interaction in general, requires two coordinate systems; one local and one global, the latter being cylindrical coordinates referenced to the tube axis. The free space electromagnetic field due to an arbitrary source coil is a solution of Laplace equation which can be expressed as general form in cylindrical coordinates. The field equation contains an arbitrary source function and in general its derivation will require local coordinates. A basic example of an eddy current problem using two coordinate systems is that of a coil whose axis is parallel to that of a tube [32]. In that case we simply have two cylindrical coordinate systems with parallel axes. In another example, the axis of a circular induction coil is perpendicular to that of a uniform bore-hole or tube. The analytical expression for the field and impedance of a coil in this case was found by using the Biot-Savart law to give a result in terms of an infinite integral [27]. This is done first for a circular filament and the result integrated over the coil cross section to get the coil field. Later, the derivation of the circular filament field with its axis perpendicular to that of a tube was formulated as a single layer potential problem [111, 20]. This means that the scalar potential represents the filament field in a way that is analogous to that of a uniformly charged disk; a problem in which there is a jump in the normal gradient of the scalar potential across the disc. An integral expression for the coil source function was derived in integral form and then expressed in series form convenient for numerical calculations. Practical applications of this configuration include a circumferentially-sensitive pancake coil array and a rotary probe in a tube. In this article, we take a similar approach to that in [111] but extend the analysis to determine the coil function for one with an arbitrary orientation using cylindrical polar and Cartesian coordinates for both local and global coordinate systems. The solution is in the form of an integral but this could be transformed into series form by using the similar procedure to that in [104]. The coil field once calculated can be used as the incident field in the integral equation for the numerical calculation of coil-flaw

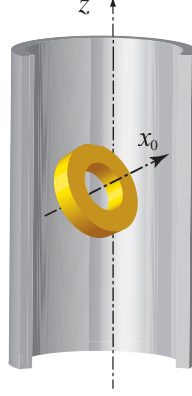


Figure 7.1: A circular induction coil of arbitrary orientation inside a conductive tube

interaction. Then the impedance variation due to a flaw can be determined by using reciprocity and the volume equivalence principle [104]. In addition, one can potentially use the present solution as the foundation for including the effect a ferrite core on the probe field [49, 112].

7.3 Field Analysis

7.3.1 Scalar Decomposition of the Field

A quasi-static time-harmonic field varying as the real part of $e^{-i\omega t}$ can be represented by the transverse electric (TE) potential ψ_1 and transverse magnetic (TM) potential ψ_2 defined with respect to the unit vector \hat{z} , which is the direction of the global coordinate axis and also the tube axis, Fig. 7.1. In the source-free region, we can express the magnetic field intensity as

$$\mathbf{H} = \nabla \times \nabla \times (\hat{z}\psi_1) + k^2 \nabla \times (\hat{z}\psi_2) \quad (7.1)$$

and electric field intensity as

$$\mathbf{E} = i\omega\mu [\nabla \times (\hat{z}\psi_1) + \nabla \times \nabla \times (\hat{z}\psi_2)] \quad (7.2)$$

where $k^2 = i\omega\mu_0\mu_r\sigma$, with μ_0 the free space permeability, μ_r is the relative permeability of the tube material and σ is the electric conductivity of the material. For a conductive region both scalar potentials satisfy the Helmholtz equation

$$(\nabla^2 + k^2)\psi_i = 0 \quad i = 1, 2. \quad (7.3)$$

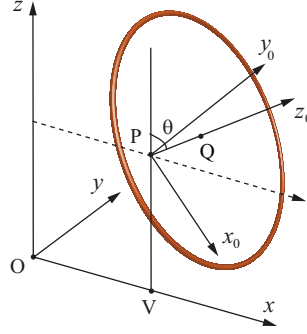


Figure 7.2: Circular filament centered at the point Q in the plane $x_0 = x'_0$ having radius ρ_0 . The azimuthal rotation angle is ϕ and θ is the polar tilt angle.

For non-conductive regions, $k^2 = 0$ and the transverse potentials satisfy the Laplace equation. In which case (7.1) reduces to

$$\mathbf{H} = \nabla \frac{\partial \psi_1}{\partial z}. \quad (7.4)$$

Note that the magnetic field is defined solely in terms of the TE potential ψ_1 in a non-conductive region. This is similar to the case where the magnetic field is written in terms of a magnetic scalar potential as $\mathbf{H} = \nabla \Phi$. In both cases we have to deal with a conflict with Ampère's law which requires that $\nabla \times \mathbf{H} \neq 0$ in region where electric current flows. Even if an explicit field representation in the region of the current is not used, we still have to avoid a conflict with the circuital law. The difficulty is traditionally overcome by introducing a discontinuity in the magnetic potential [95], in which case it is referred to as a double layer potential; physically equivalent to a magnetic dipole layer. In effect a surrogate source has been introduced that gives rise the same field as the filament current. Similarly with the TE potential, one chooses the appropriate discontinuity to be in the normal gradient of ψ_1 at a planar circular surface bounded by the current filament in which case the discontinuity in the TE scalar function means it is a single layer potential [113].

7.3.2 Field of a Circular Current Filament

Consider a circular filament centered at point Q , Fig. 7.2, coaxial with the local x_0 -coordinate axis. Relative to the global x -axis, the x_0 -axis can be located by an azimuthal rotation through an angle ϕ about a point P located at $(x, y, z) = (x_1, 0, 0)$. Also the z_0 -axis

is tilted through a polar angle θ relative to the line PV which is parallel to the global z -axis while the x_0 rotates and the y_0 axis remains in the xy -plane. The filament lies in the plane $x_0 = x'_0$ where x'_0 is a constant for a given filament. Later we treat x'_0 and the filament radius, ρ'_0 , as a variables of integration to determine the coil field from that of the filament.

The magnetic field of the filament expressed in terms of the TE potential ψ_0 , defined with respect to x_0 -direction is $\mathbf{H} = \nabla \times \nabla \times (\hat{x}_0 \psi_0)$ but again the potential satisfies Laplace equation in which case

$$\mathbf{H} = \nabla \frac{\partial \psi_0}{\partial x_0}. \quad (7.5)$$

Recovering a solution in terms of ψ_1 is done by simply using

$$\frac{\partial \psi_1}{\partial z} = \frac{\partial \psi_0}{\partial x_0} \quad (7.6)$$

To ensure the continuity of tangential electric field, ψ_0 must be continuous on S_0 . To conform to a restricted form of the circuital law, that the line integral cannot cross the chosen surface bounded by the filament, we introduce the following discontinuity on S_0

$$\left[\frac{\partial \psi_0}{\partial x_0} \right]_{S_0} = -I, \quad (7.7)$$

where the subscripted square bracket indicates the discontinuity at the surface S_0 .

Since ψ_0 is a solution of the Laplace equation, it can be expressed using Fourier transforms and cylindrical polar coordinates defined with respect to the z -axis as

$$\psi_0(\mathbf{r}) = \frac{I}{4\pi^2} \sum_{m=-\infty}^{\infty} e^{im\varphi} \int_{-\infty}^{\infty} D_m(v) \begin{matrix} I_m(|v|\rho) & \rho < s_1 \\ K_m(|v|\rho) & \rho > s_2 \end{matrix} e^{ivz} dv, \quad (7.8)$$

where the source function, $D_m(v)$, is to be determined in the present case for a filament in the plane $x_0 = x'_0$ centered at Q, Fig. 7.2 . The radial limit, s_1 is the upper limit of the solution containing $I_m(|v|\rho)$ which is the shortest distance between the z -axis and a point on the filament. Similarly, the lower radial limit of the $K_m(|v|\rho)$ solution, s_2 , is the largest radial distance between the z -axis and a point on the filament. We shall not need the solution in the region $s_1 < \rho < s_2$.

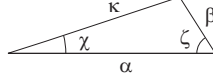


Figure 7.3: Triangle used to relate addition theorem variables using the cosine rule.

By using Green's second theorem [89] for a single layer potential, ψ_0 can be determined from

$$\psi_0 = I \int_{S_0} G(\mathbf{r}|\mathbf{r}') dS' = \frac{I}{4\pi} \int_{S_0} \frac{1}{R} dS' \quad (7.9)$$

where the integration with respect to the source coordinates is over the surface S_0 . A consequence of the dependence of R on $\mathbf{r} - \mathbf{r}'$ is that we need a sign reversal compared with (7.6) to get

$$\frac{\partial \psi_1}{\partial z} = -\frac{\partial \psi_0}{\partial x'_0}. \quad (7.10)$$

Once ψ_0 is found, then ψ_1 can be recovered from (7.10). Given that R can be expressed as [114]

$$\frac{1}{R} = \frac{1}{\pi} \sum_{m=-\infty}^{\infty} e^{im(\varphi-\varphi')} \int_{-\infty}^{\infty} I_m(|v|\rho_{<}) K_m(|v|\rho_{>}) e^{iv(z-z')} dv \quad (7.11)$$

where $\rho_{>}$ is the greater and $\rho_{<}$ the lesser of ρ and ρ' one can substitute (7.11) into (7.9) and compare with (7.8) to get

$$D_m(v) = e^{-im\varphi'} \int_{S_0} \begin{array}{l} K_m(|v|\rho') \\ I_m(|v|\rho') \end{array} e^{-ivz'} dS' \quad \begin{array}{l} \rho < s_1 \\ \rho > s_2 \end{array}. \quad (7.12)$$

where $D_m(v)$ is the filament source function which can be evaluated using a co-ordinate transform.

7.3.3 Coordinate Transform

Next we consider the transformation of (7.12) to define a more tractable form for the integration using Graf's addition theorem [115]. It involves two relationships; one applicable for $\rho < s_1$ and the other for $\rho > s_2$. Respectively these are

$$K_\nu(s) e^{-\nu x} = \sum_{n=-\infty}^{\infty} K_{\nu+n}(\alpha) I_n(\beta) e^{-in\zeta} \quad (7.13)$$

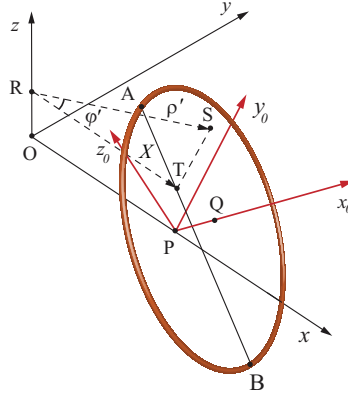


Figure 7.4: Circular filament centered at point Q. The filament surface S_0 intersects with $y = 0$ plane at the line AB

and

$$I_\nu(s)e^{-\nu x} = \sum_{n=-\infty}^{\infty} (-1)^n I_{\nu+n}(\alpha) I_n(\beta) e^{-m\zeta} \quad (7.14)$$

where the arguments are related by the cosine rule: $\kappa^2 = \alpha^2 + \beta^2 - 2\alpha\beta \cos \zeta$, applied to the triangle shown in Fig. 7.3. We use (7.14) applied in the source integral in Eq. (7.12) when $\rho > s_2$, and the field is therefore represented by the singular Bessel function series. A similar procedure is used for $\rho < s_1$ and the roles of the Bessel functions are reversed.

The addition theorem is used with reference to $\triangle RST$, Fig. 7.4 and also with reference to $\triangle RUT$ shown in Fig. 7.5, adjacent to $\triangle RST$. Applying the addition theorem to both triangles, leads to a splitting of the integration into two parts at the line AB where the filament disk intersects the $y = 0$ plane. We shall define the limits of the integration at this boundary using a local Cartesian coordinates x_0, y_0, z_0 .

With the origin of the local coordinates on the x axis at $x = x_1$; the point P in Fig. 7.2, global coordinates are related to the local coordinates as follows:

$$x = x_0 \cos \phi \cos \theta - y_0 \sin \phi - z_0 \cos \phi \sin \theta + x_1 \quad (7.15)$$

$$y = x_0 \cos \theta \sin \phi + y_0 \cos \phi - z_0 \sin \theta \sin \phi \quad (7.16)$$

$$z = x_0 \sin \theta + z_0 \cos \theta \quad (7.17)$$

The surface S_0 , bounded by the filament, is in the plane $x_0 = x'_0$ and coaxial with the x_0

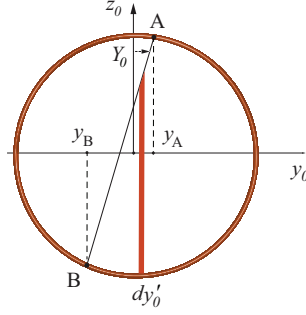


Figure 7.6: Integration over the surface S_0 bounded by the circular filament is divided at the line AB into two parts. The linear function $Y_0(z_0)$, shown in the diagram, defines the perpendicular distance of this line from the plane $y_0 = 0$. In carrying out the intergration over z'_0 one needs to set the limits at the filament and at the line AB depending on the value of y'_0 .

The integration over the filament disk is with respect to the local source coordinates y'_0 and z'_0 . The limits of the integration wth respect to y'_0 are defined using the points y_A , and y_B which are y_0 -coordinates of the points A and B, Fig. 7.6. The limits are also defined by the filaments boundary at which

$$y_0^2 + z_0^2 = \rho_0^2. \quad (7.23)$$

For the case where $\varphi' > 0$ the y'_0 integral is from y_B to ρ_0 . For the case where $\varphi' < 0$ the integration is from $-y_A$ to ρ_0 To find expressions for y_A , and y_B , put $y_0 = Y_0(z_0)$ in (7.23) to find points on the line AB. Then use the resulting equation to eliminate z_0 from (7.18). The result is a quadratic equation for Y_0 whose solutions are

$$y_A = \frac{-x'_0 \cos \phi \sin \phi \cos \theta + \xi}{\cos^2 \phi + \sin^2 \phi \sin^2 \theta} \quad (7.24)$$

$$y_B = \frac{-x'_0 \cos \phi \sin \phi \cos \theta - \xi}{\cos^2 \phi + \sin^2 \phi \sin^2 \theta} \quad (7.25)$$

where

$$\xi = \sin \phi \sin \theta \sqrt{\rho_0^2 (\cos^2 \phi + \sin^2 \phi \sin^2 \theta) - x_0'^2 \sin^2 \phi \cos^2 \theta} \quad (7.26)$$

The limits of z'_0 are determined by the line AB and the filament itself, Fig. 7.6. For $\varphi' > 0$, the low limit of the integration with respect to z'_0 is $-a(y'_0)$ where $a(y'_0) = \sqrt{\rho_0^2 - y_0'^2}$, taking the positive root. But the upper limit is $Z_a(y'_0)$ defined as a piece-wise function

$$z_a(y'_0) = \begin{cases} Z_0(y'_0) & y_B \leq y'_0 < y_A \\ a(y'_0) & y_A \leq y'_0 < \rho_0 \end{cases} \quad (7.27)$$

Similarly, for $\varphi' < 0$, the low limit of integration is $Z_b(y'_0)$ defined as

$$z_b(y'_0) = \begin{cases} -a(y'_0) & -\rho_0 \leq y'_0 < y_B \\ Z_0(y'_0) & y_B \leq y'_0 < y_A \end{cases} \quad (7.28)$$

and the upper limit is $a(y'_0)$.

Now by substituting (7.21) and (7.22) into (7.12) and applying the limits discussed above, we can rewrite (7.12) as

$$D_m(v) = \sum_{n=-\infty}^{\infty} e^{in(\frac{\pi}{2}+\phi)} \left\{ \int_{y_B}^{\rho_0} \int_{-a}^{z_a} I_{m+n}(|v|X) I_n(|v|[y'_0 - Y_0]) e^{-ivz'} dz'_0 dy'_0 + (-1)^n \int_{-\rho_0}^{y_A} \int_{z_b}^a I_{m+n}(|v|X) I_n(|v|[y'_0 - Y_0]) e^{-ivz'} dz'_0 dy'_0 \right\} \quad (7.29)$$

where $z' = x'_0 \sin \theta + z'_0 \cos \theta$ using the coordinate transform (7.17), $a = \sqrt{\rho_0^2 - y_0'^2}$ and note that Y_0 is a function of z'_0 .

Now we have transformed the global prime source coordinates of source coefficient calculation into local prime source coordinates. Note that the above derivation has included the effect of filament offset on the x_0 axis so as to simplify the derivation of source coefficient of coil. In order to verify and get the insights of the effect of either azimuthal or polar tilt, the azimuthal and polar tilt special case will be analyzed separately.

7.3.4 Circular Filament with an Azimuthal Tilt

When the polar tilt angle $\theta = 0^\circ$, the filament has only an azimuthal tilt. The filament is centered at point P and the z_0 -axis, referring to Fig. 7.2, now becomes parallel to z -axis of the global coordinate. By substituting $\theta = 0^\circ$ into (7.18), (7.20), (7.24) and (7.25), we get

$$Y_0 = -x'_0 \tan \phi \quad (7.30)$$

$$X = \frac{x'_0}{\cos \phi} + x_1 \quad (7.31)$$

$$y_A = y_B = -x'_0 \tan \phi \quad (7.32)$$

Similarly, z_a , z_b and z' can be reduced as following by setting $\theta = 0^\circ$

$$z_a = -z_b = \sqrt{\rho_0^2 - y_0'^2} \quad (7.33)$$

$$z' = x_0' \sin \theta + z_0' \cos \theta = z_0' \quad (7.34)$$

Substituting these equations back into (7.29) and putting $\Delta\rho = x_0' \tan \phi$, we get

$$D_m(v) = \frac{2}{v} \sum_{n=-\infty}^{+\infty} e^{in(\frac{\pi}{2}+\phi)} I_{m+n}(|v|X) [f_n(-\Delta\rho, -\Delta\rho, \rho_0) + (-1)^n f_n(\Delta\rho, \Delta\rho, \rho_0)] \quad (7.35)$$

where

$$f_n(r_1, r_2, \rho_0) = \int_{r_1}^{\rho_0} I_n(|v||\xi - r_2|) \sin(v\sqrt{\rho_0^2 - \xi^2}) d\xi \quad (7.36)$$

and we use

$$\int_{-\sqrt{\rho_0^2 - y_0'^2}}^{\sqrt{\rho_0^2 - y_0'^2}} e^{-ivz_0'} dz_0' = \frac{2}{v} \sin(v\sqrt{\rho_0^2 - y_0'^2}) \quad (7.37)$$

due to that the Bessel function I_{m+n} and I_n are independent from z_0' and the inner integral can be evaluated analytically.

Note that if the tilt angle ϕ is big enough or the circular coil is long in the axial direction, some filaments of the coil might be totally above or below the xz -plane. Then only one $f_n(r_1, r_2, \rho_0)$ function in (7.35) will be included and the integral limit will from $-\rho_0$ to ρ_0 .

7.3.5 Circular Filament with a Polar Tilt

When the polar tilt angle $\phi = 0^\circ$, the filament has only a polar tilt as shown. The y_0 -axis, referring to Fig. 7.2, now becomes parallel to y -axis of the global coordinate. By substituting $\phi = 0^\circ$ into (7.18), (7.20), (7.24) and (7.25), we get

$$Y_0 = 0 \quad (7.38)$$

$$X = x_0' \cos \theta - z_0' \sin \theta + x_1 \quad (7.39)$$

$$y_A = y_B = 0 \quad (7.40)$$

Similarly, z_a , z_b and z' can be reduced as following by setting $\phi = 0^\circ$

$$z_a = -z_b = \sqrt{\rho_0^2 - y_0'^2} \quad (7.41)$$

$$z' = x_0' \sin \theta + z_0' \cos \theta \quad (7.42)$$

Substituting these equations into (7.29), we get

$$D_m(v) = 2 \sum_{n=-\infty}^{+\infty} \cos\left(\frac{n\pi}{2}\right) e^{-ivx'_0 \sin\theta} \int_0^{\rho_0} I_n(|v||y'_0|) \int_{-\sqrt{\rho_0^2 - y_0'^2}}^{\sqrt{\rho_0^2 - y_0'^2}} I_{m+n}(|v|X) e^{-ivz'_0 \cos\theta} dz'_0 dy'_0 \quad (7.43)$$

After integrating with respect to y'_0 and z'_0 over the surface of the filament disk, the source coefficient $D_m(v)$ for $\rho > s_2$ can be obtained. Note that only even n is needed to calculate the $D_m(v)$ since it will vanish for odd n .

7.3.6 Rotary Filament

The rotary filament case can be gotten easily by setting $\theta = 0^\circ$ and $\phi = 0^\circ$. It also can be achieved by setting $\theta = 0^\circ$ for polar tilt case or setting $\phi = 0^\circ$ for azimuthal tilt case. Here we substitute $\theta = 0^\circ$ into the expressions of the polar tilt case. Then (7.42) and (7.39) reduce to

$$z' = z'_0 \quad (7.44)$$

$$X = x'_0 + x_1 \quad (7.45)$$

Substituting these two equations into (7.43) and using (7.37), $D_m(v)$ reduces to

$$D_m(v) = \frac{4}{v} \sum_{n=-\infty}^{+\infty} \cos\left(n\frac{\pi}{2}\right) I_{m+n}(|v|X) \int_0^{\rho_0} I_n(|v||y'_0|) \sin(v\sqrt{\rho_0^2 - y_0'^2}) dy'_0 \quad (7.46)$$

Note that only even n is needed to calculate the $D_m(v)$ since it will vanish for odd n .

7.4 Free Space Coil Field

Now we know how to get TE potential ψ_0 for filament with arbitrary orientation. Similarly, we express ψ_1 for the coil in free space just as we have ψ_0 for the circular filament

$$\psi_1(\mathbf{r}) = \frac{I}{4\pi^2} \sum_{m=-\infty}^{\infty} e^{im\varphi} \int_{-\infty}^{\infty} C_m(v) \begin{cases} I_m(|v|\rho) & \rho < \beta_1 \\ K_m(|v|\rho) & \rho > \beta_2 \end{cases} e^{ivz} dv \quad (7.47)$$

where the radial limits, β_1 and β_2 , are respectively the shortest and longest distances from z -axis to a point on the coil. Associated Bessel function $I_m(z)$ is used for $\rho < \beta_1$ and $K_m(z)$ is used for $\rho > \beta_2$.

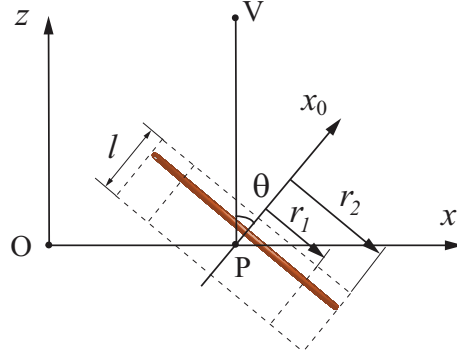


Figure 7.7: The cross-section view of a circular coil at $y = 0$ plane with polar tilt angle θ is shown in dashed outline. The coil is centered at point P and one filament loop of the coil is also shown to illustrate the filament superposition

By using (7.10) and integrating the filament field with respect to x'_0 and ρ_0 over the coil cross-section, we obtain the source coefficient for the coil field

$$C_m(v) = \frac{-\nu}{iv} \int_{r_1}^{r_2} [D_m(v, x'_0 = l/2) - D_m(v, x'_0 = -l/2)] d\rho_0 \quad (7.48)$$

where $\nu = N/l(r_2 - r_1)$ is the turns density of the coil, N is filament turns of a coil, l is the length of coil in the axial direction. r_1 and r_2 are the inner radius and outer radius of the coil separately shown in Fig. 7.7.

For azimuthal tilt, substituting (7.35) into (7.48), $C_m(v)$ is expressed as

$$\begin{aligned} C_m(v) &= \frac{-2\nu}{iv^2} \sum_{n=-\infty}^{+\infty} e^{in(\frac{\pi}{2}+\phi)} [I_{m+n}(|v|\frac{l}{2\cos\phi} + x_1|) \\ &\quad - (-1)^n I_{m+n}(|v|\frac{-l}{2\cos\phi} + x_1|)] \\ &\quad \times [F_n(r_1, r_2, -\Delta\rho) + (-1)^n F_n(r_1, r_2, \Delta\rho)] \end{aligned} \quad (7.49)$$

where

$$F_n(\chi_1, \chi_2, \eta) = \int_{\chi_1}^{\chi_2} \int_{\eta}^{\rho_0} I_n(|v||\xi - \eta|) \sin(v\sqrt{\rho_0^2 - \xi^2}) d\xi d\rho_0 \quad (7.50)$$

We can find $C_m(v)$ is an odd function of v .

For polar tilt, substituting (7.43) into (7.48), $C_m(v)$ is expressed as

$$C_m(v) = \frac{-2\nu}{iv} \sum_{n=-\infty}^{+\infty} \cos\left(\frac{n\pi}{2}\right) \left[e^{-iv\frac{l}{2}\sin\theta} - e^{iv\frac{l}{2}\sin\theta} \right] F_n(v) \quad (7.51)$$

$$F_n(v) = \int_{r_1}^{r_2} \int_0^{\rho_0} I_n(|v||y'_0|) \int_{-a}^a I_{m+n}(|v|X) e^{-ivz'_0 \cos \theta} dz'_0 dy'_0 d\rho_0 \quad (7.52)$$

where $a = \sqrt{\rho_0^2 - y_0'^2}$ and note that $C_m(v) = 0$ for all odd n and conjugates of $C_m(-v)$ and $C_m(v)$.

For rotary Coil, substituting (7.46) into (7.48), $C_m(v)$ is expressed as

$$\begin{aligned} C_m(v) &= \frac{-4\nu}{iv^2} \sum_{n=-\infty}^{+\infty} \cos\left(n\frac{\pi}{2}\right) \\ &\times \left[I_{m+n}(|v||x_1 + \frac{l}{2}|) - I_{m+n}(|v||x_1 - \frac{l}{2}|) \right] \\ &\times \int_{r_1}^{r_2} \int_0^{\rho_0} I_n(|v||y'_0|) \sin(v\sqrt{\rho_0^2 - y_0'^2}) dy'_0 d\rho_0 \end{aligned} \quad (7.53)$$

Note that $C_m(v) = 0$ for all odd n and $C_m(v)$ is an odd function of v .

7.5 Coil Impedance Change and Experiment

Consider the internal surface S_1 of the tube enclosing the eddy-current probe source whose current density is \mathbf{J}_1 and which generates electric field $\mathbf{E}_1^{(0)}$. Another field $\mathbf{E}_1^{(\Gamma)}$ in this region arises from the induced current in the tube, which is outside the region. Corresponding magnetic fields are $\mathbf{H}_1^{(0)}$ and $\mathbf{H}_1^{(\Gamma)}$. According to the Lorentz reciprocity theorem the volume integral of $\mathbf{E}_1^{(\Gamma)} \cdot \mathbf{J}_1$ can be expressed as a surface integral[89] and according to the reaction principle, the negative of the reaction equates to the power delivered to the source due to the presence of induced current. Thus

$$I^2 \Delta Z = - \int_{\Omega} \mathbf{E}_1^{(\Gamma)} \cdot \mathbf{J}_1 dv = - \oint_{S_0} [\mathbf{E}_1^{(0)} \times \mathbf{H}_1^{(\Gamma)} - \mathbf{E}_1^{(\Gamma)} \times \mathbf{H}_1^{(0)}] \cdot d\mathbf{S} \quad (7.54)$$

where ΔZ is the coil impedance due to the presence of the induced current and one takes S_1 to be an infinite circular cylinder inside the tube at its surface whose radius is a . In terms of transverse electric potentials,

$$I^2 \Delta Z = -i\omega\mu_0 a \int_{-\pi}^{\pi} \int_{-\infty}^{\infty} \frac{\partial \psi_1^{(\Gamma)}}{\partial z} \left(\frac{\partial^2 \psi_1^{(0)}}{\partial z \partial \rho} \right) - \frac{\partial \psi_1^{(0)}}{\partial z} \left(\frac{\partial^2 \psi_1^{(\Gamma)}}{\partial z \partial \rho} \right) d\varphi dz \quad (7.55)$$

where $\psi_1^{(0)}$ is the TE potential without the presence of tube and $\psi_1^{(\Gamma)}$ is the TE potential due to the presence of tube. By a transformation developed from Parseval's relation

$$\Delta Z = \frac{i\omega\mu_0}{4\pi^2} \sum_m \int_{-\infty}^{\infty} v^2 C_{-m}(-v) \Gamma_m(v) C_m(v) dv \quad (7.56)$$

where $\Gamma_m(v)$ represents the reflection at the internal surface of the tube [104].

7.5.1 Model Predicted Results

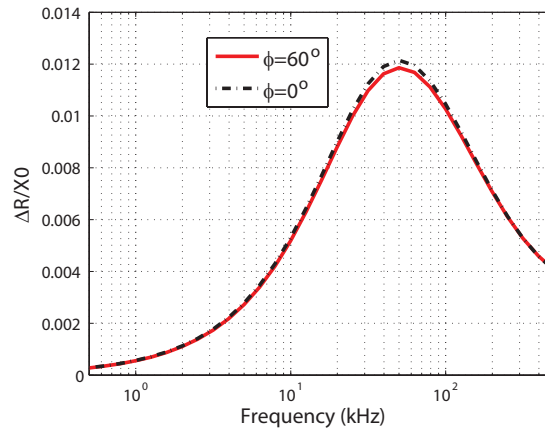


Figure 7.8: The effect of tilted angle ϕ on normalized resistance changes for a circular coil with different ϕ inside a tube

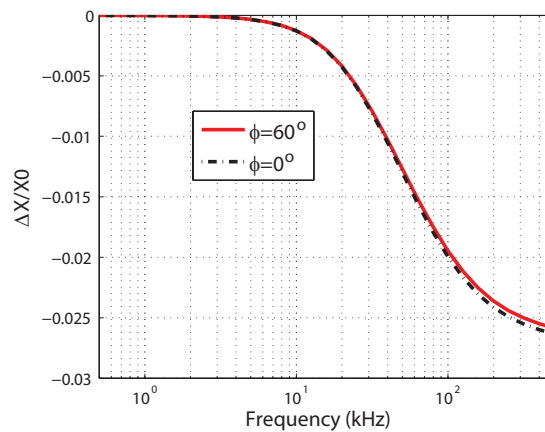


Figure 7.9: The effect of tilted angle ϕ on normalized reactance changes for a circular coil inside a tube

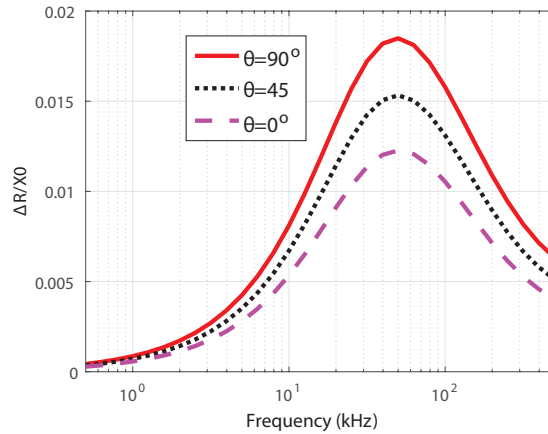


Figure 7.10: The effect of tilted angle θ on normalized resistance changes for a circular coil with different θ inside a tube

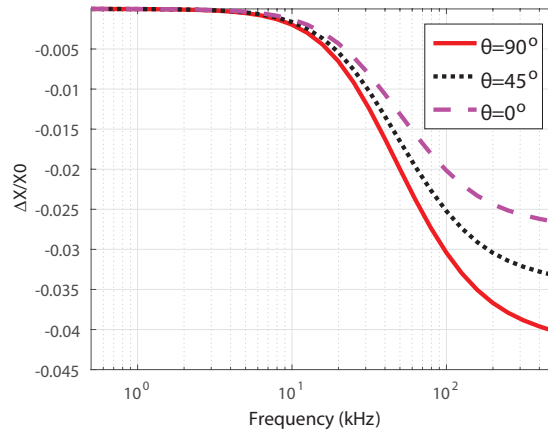


Figure 7.11: The effect of tilted angle θ on normalized reactance changes for a circular coil with different θ inside a tube

The impedance changes have been calculated based on the proposed model shown from Fig. 7.8 to Fig. 7.11 for a coil in an inconel 600 tube ($\mu_r = 1$) of conductivity 0.84 MS/m. The coil and tube parameters are given in the Table 7.1 except that the liftoff is increased by the amount 3.918 mm to make sure it will not intersect with tube with biggest tilt angle $\theta = 90^\circ$ or $\phi = 90^\circ$. But it will make the impedance variation smaller compared with rotary coil case with $\phi = \theta = 0^\circ$ due to larger liftoff.

The azimuthal tilt effect on impedance variations are shown in Fig. 7.8 and Fig. 7.9. All the impedance data is normalized by isolated coil reactance, $X_0 = \omega L_0$. We can find $\phi = 0^\circ$ case has the strongest impedance changes and azimuthal tilt will reduce the coil impedance changes compared with rotary coil ($\phi = 0^\circ$). But the changes are not significant because the distance of the coil from the tube inner surface doesn't change a lot ϕ , especially for larger liftoff and small coil. The polar tilt effect on impedance variations are shown in Fig. 7.10 and Fig. 7.11. We can easily find polar tilt will increase the impedance changes and $\theta = 90^\circ$ (now it reduces to offset bobbin case) has biggest reaction. One reason is the probe coil is not close to the tube inside surface to avoid the probe intersect with tube for big tilt angle case. So bigger polar tilt angle will make the coil closer to the tube surface and has stronger reaction.

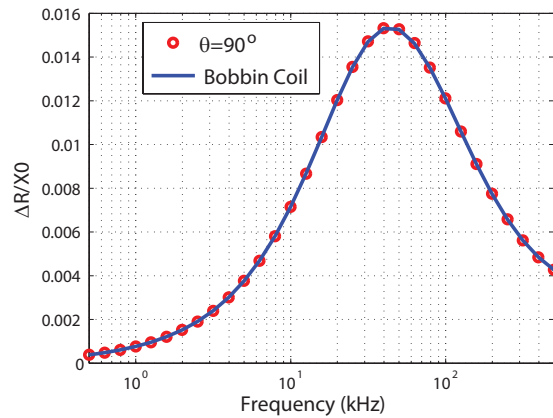


Figure 7.12: Comparison between coaxial bobbin coil and polar tilt coil with $\theta = 90^\circ$ and $x_1 = 0$ of normalized resistance changes for a coil inside a tube of different frequency

Table 7.1: Coil and inconel steam generator tube parameters for experiment

Coil Inner Raids, r_1	$1.529 \pm 0.004\text{mm}$
Coil Outer Raids, r_2	$3.918 \pm 0.003\text{mm}$
Coil Thickness	$1.044 \pm 0.005\text{mm}$
Number of Turns	305
Isolated DC Coil Inductance, L_0	$465\mu\text{H}$
Tube Inner Diameter	$16.64 \pm 0.025\text{mm}$
Tube Outer Diameter	$18.99 \pm 0.025\text{mm}$
Conductivity (MS/m)	0.84
Relative Magnetic Permeability, μ_r	1
Coil Center Liftoff, λ	1.757mm

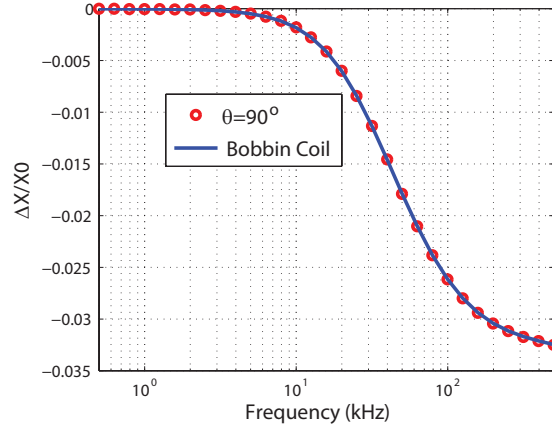


Figure 7.13: Comparison between coaxial bobbin coil and polar tilt coil with $\theta = 90^\circ$ and $x_1 = 0$ of normalized reactance changes for a coil inside a tube of different frequency

In order to verify the polar tilt result, we also calculate the impedance changes of co-axial bobbin coil inside the tube [9], which can be used to compare with the polar tilt coil by setting $\theta = 90^\circ$ and $x_1 = 0$. The comparison are shown in Fig (7.12) and Fig (7.13). Both of them agree with each other perfectly.

The magnitude of electrical field distribution at the tube inner interface has been calculated in order to observe the tilt effect shown in Fig. 7.14 in terms of distance in z direction and angles (Φ) in the circumferential direction at frequency 10kHz. The eddy-current coil and tube parameters are summarized in Tab (7.2). Once obtaining the electrical field distribution,

the magnitude of current distribution can be easily evaluated by multiplying the conductivity of tube material. From the Fig. 7.14, one can find both polar tilt and azimuthal tilt will concentrate more current in the area where is closer to the coil. However, the tilt in azimuthal direction will increase the maximum current density magnitude more effective than polar tilt. The reason could be that the electrical field generated by the coil is more tangential at the central area in circumferential direction.

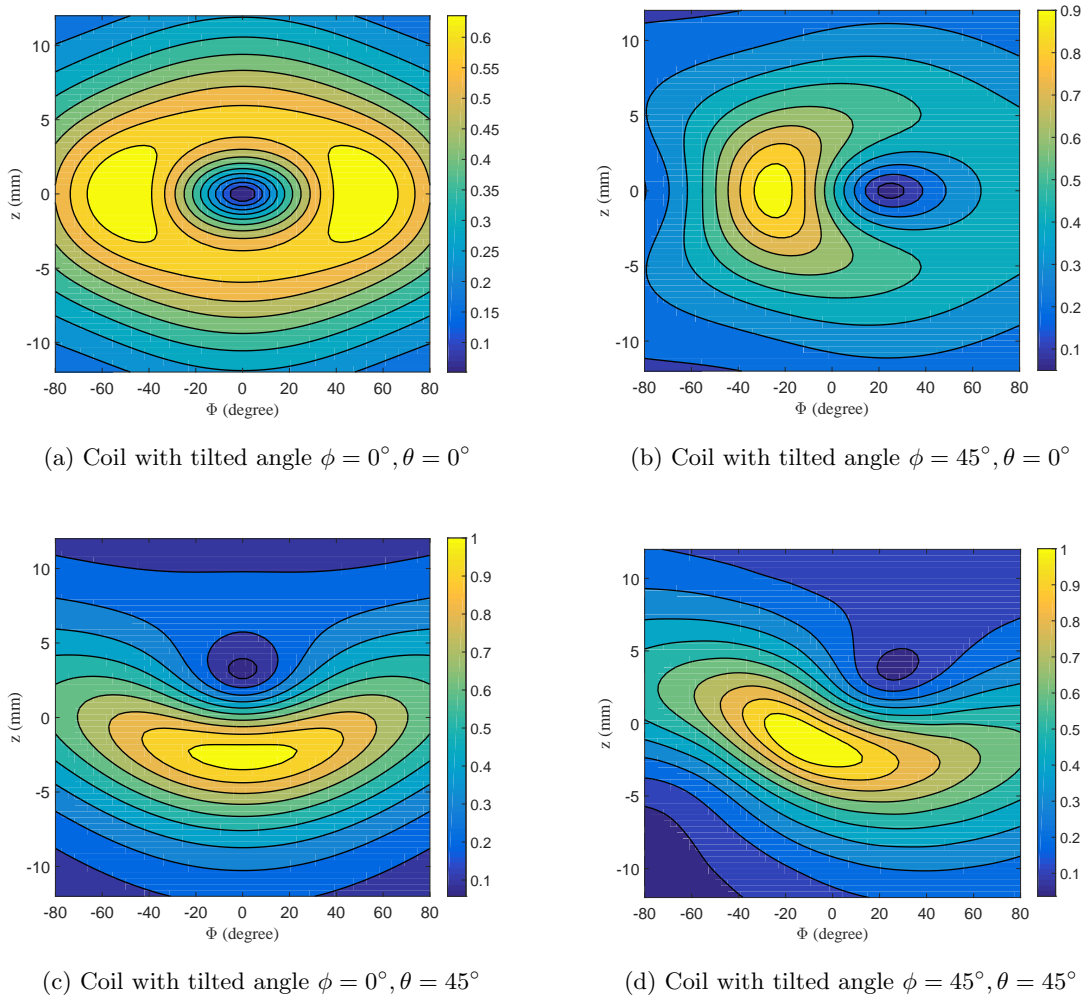


Figure 7.14: The $|\mathbf{E}|$ distribution at the tube inner interface. a is the tube inner radius. The induced current can be obtained by multiplying conductivity of the conductor.

Table 7.2: Coil and inconel steam generator tube parameters for theoretical calculation

Coil Inner Raids, r_1	$1.529 \pm 0.004\text{mm}$
Coil Outer Raids, r_2	$3.918 \pm 0.003\text{mm}$
Coil Thickness	$1.044 \pm 0.005\text{mm}$
Number of Turns	305
Isolated DC Coil Inductance, L_0	$465\mu\text{H}$
Tube Inner Diameter	$16.64 \pm 0.025\text{mm}$
Tube Outer Diameter	$18.99 \pm 0.025\text{mm}$
Conductivity (MS/m)	0.84
Relative Magnetic Permeability, μ_r	1
Coil Center Liftoff, λ	5.675mm

7.5.2 Experimental Results

The experiment of a coil with axis orthogonal tilted ($\theta = 0^\circ, \phi = 0^\circ$) have been carried out in order to acquire coil impedance variation due to the tube. The tube is inconel steam generator tube. The coil and tube parameters are given in the Table 7.1. Although the conductivity of the tube could be done by using an eddy current conductivity meter, the instruments are inaccurate for samples that are not flat. instead we use the multi-frequency impedance data provided here to determine both effective lift-off and effective tube conductivity. The impedance variation comparison of the experimental ΔZ and theoretical calculations are shown in Fig. 7.15 and Fig. 7.16. Following the usual practice in eddy-current NDE, all the impedance data is normalized by isolated coil reactance, $X_0 = \omega L_0$. In order to get enough accuracy, we take 41 terms of m , 20 terms of n . From the comparison, we can find that the theoretical ΔZ due to coil are in excellent agreement with the experimental results.

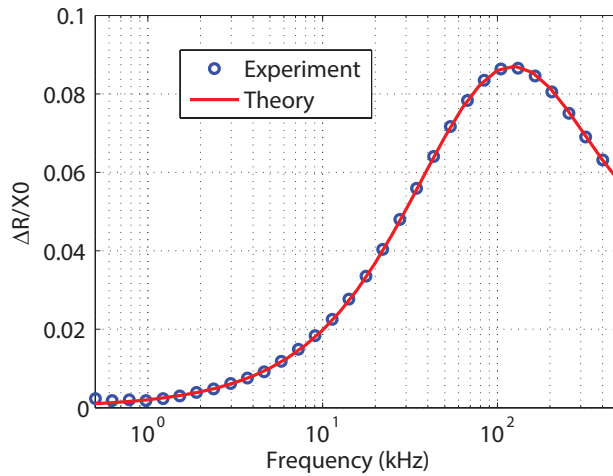


Figure 7.15: Comparison between experimental and theoretical result of normalized resistance changes for a coil inside a tube of different frequency

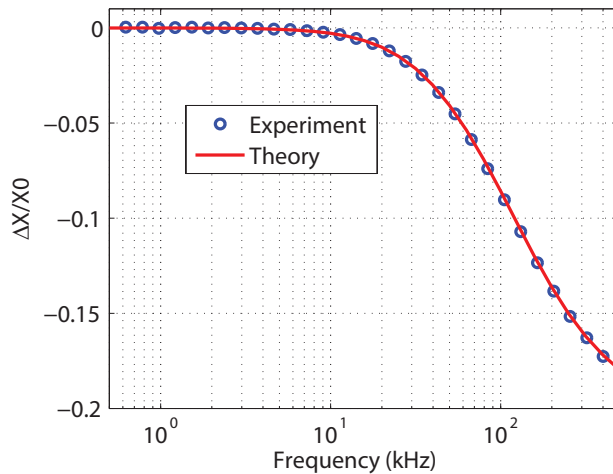


Figure 7.16: Comparison between experimental and theoretical result of normalized reactance changes for a coil inside a tube of different frequency

7.5.3 Conclusion

This paper proposes a new analytical model for obtaining the electromagnetic field of circular coil with arbitrary orientation inside or outside a tube. The source coefficients are obtained first based on coordinate transform. Then the field and impedance changes due to tube can

be determined. The field calculated could be used as the incident field in the integral equation for the numerical calculation. Besides, the effects of azimuthal and polar tilt on impedance variation have been analyzed separately. The calculated rotary coil impedance variations are compared with the experimental results and good agreement is achieved. The co-axial bobbin coil model inside tube is also calculated for better comparison. This theory can serve as a model for determining the probe position and orientation with respect to a tube based on impedance variations.

CHAPTER 8. ARBITRARY ORIENTATION INDUCTION COIL INTERACTING WITH PLANAR STRUCTURES

(A draft journal paper)

8.1 Abstract

In this article, simple closed-form analytical expressions for the electromagnetic field of a circular eddy-current probe coil with arbitrary orientation above a conductive half-space or slab are derived. The electromagnetic fields are evaluated first for a arbitrary titled circular filament loop in the free space by using addition theorem and coordinator transform. Then the field of a circular eddy-current coil is obtained by integrating the filament field over the cross section of coil. The eddy current induced in the conductive half-space is calculated and analyzed in terms of different titled angles. The impedance changes are also evaluated analytically and are verified by comparing with the Dodd's model whose coil axis is perpendicular with the planar surface. The model are expected to be useful for eddy-current signal noise analysis and rapid incident field calculation in the numerical methods models.

8.2 Introduction

The analysis of coil fields and the impedance change of a circular air-cored coil whose axis is perpendicular to the surface of a layered conducting half-space have been studied by Dodd and Deeds [9], which served as the basis for many eddy current non-destructive evaluation (NDE) models [29, 79]. In addition, the coil with its axis parallel to the planar surface aimed to model the coil used in the electrical current perturbation method for crack detection was developed by Burke [31]. However, in the practical applications, the geometric effect produced

by uncontrolled relative liftoff shift and coil tilt could induce highly undesirable signal added as noise to the useful flaw signals and the simple coil models fail to capture these effects. Later, the field distribution due to a circular current loop with arbitrary position above plate was studied [116]. In order to make the model more general, an analytical expression of fields and impedance change for an coil with arbitrary orientation was derived [34]. But all the expressions require evaluation of a double infinite integral expansion, which is not computation-friendly.

In this paper, an alternative method for the problem of a circular coil with arbitrary position and orientation is proposed. The problem is first transferred to a single layer problem by using scalar decomposition of field and applying specific boundary conditions on the scalar potential [111]. Then the remarkably simple closed-form expressions of field and impedance change for a circular coil due to presence of half-space or slab are provided in terms of coil position and tilt angle. The induced eddy current in the conductive half-space of different tilted angle is evaluated and presented. Meanwhile, the comparison of the impedance change between proposed model and Dodd's model is also done and shows excellent agreement. All the expressions only require one integral and one summation rather than double infinite integral, which will be better for rapid calculation and numerical implementation.

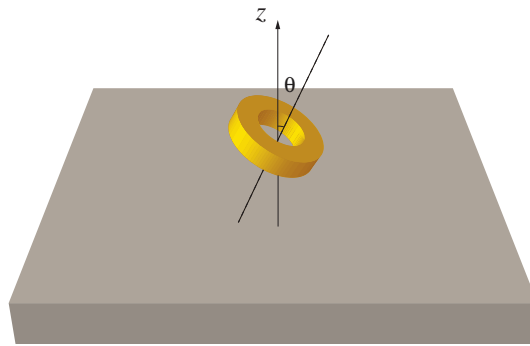


Figure 8.1: An air-cored circular coil located above conductive plate. The coil axis (dash line) has a polar tilted angle θ relative to z axis

The theoretical results are useful in wobble noise analysis [32] and the numerical method for fast evaluation of incident field term of volume integral method, which is widely used in the simulation of the probe-flaw problem [117]. In addition, one can potentially extend this

solution to include the effect of a ferrite core [49].

8.3 Circular Filament Field and Source Function Evaluation

8.3.1 Scalar Decomposition of the Fields

A quasi-static time-harmonic field varying as the real part of $e^{-i\omega t}$ can be represented by the transverse electric (TE) potential ψ_1 and transverse magnetic (TM) potential ψ_2 . Both are defined with respect to the unit vector \hat{z} , which is the direction of the global coordinate axis. In the source-free region, we can express the magnetic field intensity as

$$\mathbf{H} = \nabla \times \nabla \times \hat{z}\psi_1 + k^2 \nabla \times \hat{z}\psi_2 \quad (8.1)$$

and electric field intensity as

$$\mathbf{E} = i\omega\mu [\nabla \times \hat{z}\psi_1 + \nabla \times \nabla \times \hat{z}\psi_2] \quad (8.2)$$

where $k^2 = i\omega\mu_0\mu_r\sigma$, μ_0 is free space permeability, μ_r is relative permeability of the material and σ is the electric conductivity of the material. For a conductive region both potentials satisfy the Helmholtz equation. However, for non-conductive regions, both scalar potentials satisfy the Laplace equation due to $k^2 = 0$, in which case (8.1) reduces to

$$\mathbf{H} = \nabla \frac{\partial \psi_1}{\partial z}. \quad (8.3)$$

Note that now the magnetic field is only determined by TE potential ψ_1 .

8.3.2 Field of a Tilted Circular Filament Loop

A circular filament loop with arbitrary orientation and radius ρ_0 excited by AC current I can be modeled as Fig. 8.2. (x, y, z) is the global coordinate system and (x_0, y_0, z_0) is the local coordinate system whose origin is at point P with global coordinates as $(x_c, 0, z_c)$. Relative to the global z axis, the local z_0 axis can be located by rotating the z_0 axis through a polar angle θ relative to the line VP which is parallel to the global z axis.

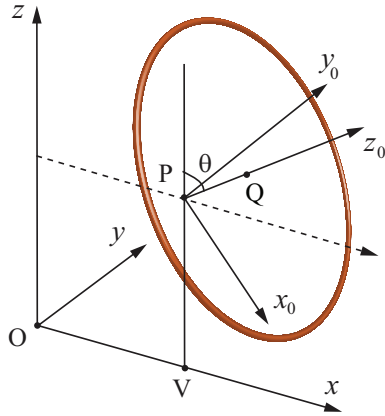


Figure 8.2: Circular filament centered at the point Q in the plane $z_0 = z'_0$ having radius ρ_0 . The axis of the circular loop coincides with z_0 axis

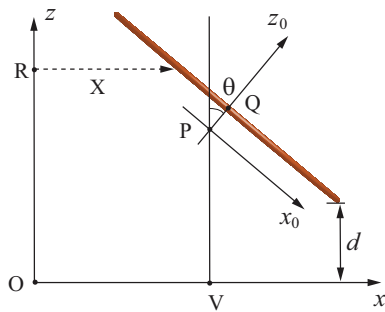


Figure 8.3: A circular filament loop with titled angle θ in the free-space. The cross-section view shows the $y = 0$ plane.

The filament lies in the plane $z_0 = z'_0$ centered at point Q on z_0 axis, where z'_0 is a constant for a given filament. Later we treat it as a variable to determine the coil field based on filament field. The angle θ is the tilted angle of filament and d is the smallest distance from any point of the filament loop to the xy - plane, Fig. 8.3. The transformation between the global coordinate system and the local coordinate system is obtained as

$$x = x_0 \cos \theta + z_0 \sin \theta + x_c \quad (8.4)$$

$$y = y_0 \quad (8.5)$$

$$z = -x_0 \sin \theta + z_0 \cos \theta + z_c \quad (8.6)$$

Instead of obtaining ψ_1 directly, we first use the TE potential ψ_0 defined with preferred direction in z_0 , Fig. 8.3, to represent the field. Similarly, the potential ψ_0 also satisfies Laplace equation

$$\mathbf{H} = \nabla \frac{\partial \psi_0}{\partial z_0}. \quad (8.7)$$

Once ψ_0 is solved, ψ_1 is easily recovered by the relationship

$$\frac{\partial \psi_1}{\partial z} = \frac{\partial \psi_0}{\partial z_0} \quad (8.8)$$

To ensure the continuity of tangential electric field, ψ_0 is continuous on S_0 . To satisfy the circuital law, the following discontinuity on S_0 is introduced [111]

$$\left[\frac{\partial \psi_0}{\partial z_0} \right]_{S_0} = -I \quad (8.9)$$

and it's a single layer potential.

Since ψ_0 satisfies the Laplace equation, it can be expressed in cylindrical coordinates following the method of separation of variables in the general form as

$$\psi_0(\rho, \phi, z) = \frac{I}{4\pi} \sum_{m=-\infty}^{\infty} e^{im\phi} \int_0^{\infty} D_m(\kappa) J_m(\kappa\rho) \begin{cases} e^{-\kappa z} & z > z_{\max} \\ e^{\kappa z} & z < z_{\min} \end{cases} d\kappa, \quad (8.10)$$

where $D_m(\kappa)$ is the source function of a circular filament loop and is to be determined. The limit z_{\max} , which is the the largest coordinate value of a point on the filament in z axis, is lower limit of $e^{-\kappa z}$ solution. Similarly, the limit z_{\min} , which is the smallest coordinate value of a point on the filament in the z axis, is the upper limit of $e^{\kappa z}$ solution. We shall not need he filed of region $z_{\min} < z < z_{\max}$.

By using Green's second theorem for a single layer potential ψ_0 , we have

$$\psi_0 = \frac{I}{4\pi} \int_{S_0} \frac{1}{R} dS' \quad (8.11)$$

where the integration is over the surface S_0 bounded by the filament in terms of source coordinates. Since of $R = |\mathbf{r} - \mathbf{r}'|$ and \mathbf{r}' denotes the source coordinate, we have

$$\frac{\partial \psi_1}{\partial z} = -\frac{\partial \psi_0}{\partial z'_0} \quad (8.12)$$

Given that we can express $1/R$ using addition theorem as [95]

$$\frac{1}{R} = \sum_{m=-\infty}^{\infty} e^{im(\phi-\phi')} \int_0^{\infty} J_m(\kappa\rho) J_m(\kappa\rho') e^{-\kappa|z-z'|} d\kappa \quad (8.13)$$

By substituting (8.13) into (8.11) and comparing with (8.10), the source coefficient $D_m(\kappa)$ is obtained as

$$D_m(\kappa) = \int_{S_0} e^{-im\phi'} J_m(\kappa\rho') \begin{cases} e^{\kappa z'} & z > z_{\max} \\ e^{-\kappa z'} & z < z_{\min} \end{cases} dS', \quad (8.14)$$

where $D_m(\kappa)$ is the source function which will be evaluated using Graf's addition theorem and the coordinate transformation as shown in (8.4), (8.5) and (8.6).

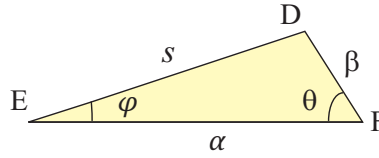


Figure 8.4: The triangle DEF used to relate addition theorem variables

8.3.3 Source Coefficient Evaluation

In order to evaluate (8.14), the following addition theorem based on triangle DEF, Fig. 8.4, is used. [115]

$$J_v(s)e^{-iv\phi} = \sum_{n=-\infty}^{n=\infty} J_{v+n}(\alpha) J_n(\beta) e^{-in\theta} \quad (8.15)$$

Here the addition theorem is used with reference to ΔRTS , Fig. 8.5 and ΔRUT , Fig. 8.6. By applying the addition theorem to both triangles, we let $s = \kappa\rho'$, $\alpha = \kappa X$ and $\beta = \kappa|y'_0|$ for $\phi' > 0$ to obtain

$$J_m(\kappa\rho') e^{-im\phi'} = \sum_{n=-\infty}^{\infty} J_{m+n}(\kappa X) J_n(\kappa|y'_0|) e^{-in\pi/2} \quad (8.16)$$

and for $\phi' < 0$

$$J_m(\kappa\rho') e^{-im\phi'} = \sum_{n=-\infty}^{\infty} J_{m+n}(\kappa X) J_n(\kappa|y'_0|) e^{in\pi/2} \quad (8.17)$$

where $X = x'_0 \cos \theta + z'_0 \sin \theta + x_c$ is the shortest distance from any point on the surface S_0 bounded by filament to the z axis.

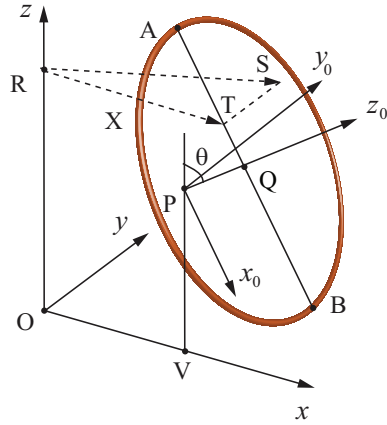


Figure 8.5: Circular filament centered at point Q. the filament surface S_0 intersects with $y = 0$ plane at the line AB, which split the S_0 into two parts. The triangles ΔRTS shows how Graf's addition theorem is applied on it

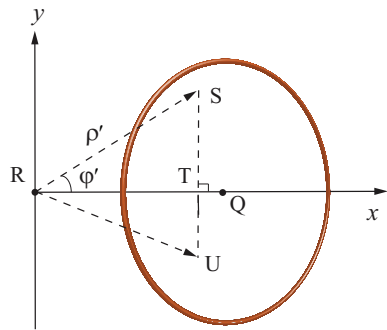


Figure 8.6: The plane view of a tilted circular filament loop. The triangles ΔRTS and ΔRTU are used to transform the global source coordinates to local coordinates by Graf's addition theorem

The integration limits are determined by the filament itself. For both $\phi' > 0$ and $\phi' < 0$, the low limit of the integration with respect to z'_0 is $-a(y'_0)$ where $a(y'_0) = \sqrt{\rho_0^2 - y_0'^2}$, taking the positive root. The upper limit is a . By substituting (8.16) and (8.17) into (8.14) and the integration limits discussed above, we have

$$D_m(\kappa) = 2 \sum_{n=-\infty}^{\infty} \cos\left(\frac{n\pi}{2}\right) \int_0^{\rho_0} J_n(\kappa y') \int_{-a}^a J_{m+n}(\kappa X) \begin{matrix} e^{\kappa z'} \\ e^{-\kappa z'} \end{matrix} dx'_0 dy'_0, \quad \begin{matrix} z > z_{\max} \\ z < z_{\min} \end{matrix} \quad (8.18)$$

where $z' = -x'_0 \sin \theta + z'_0 \cos \theta + z_c$

8.4 Coil Field Analysis

8.4.1 Coil Field in the Free-space

Similarly to the TE potential of a circular filament current loop, the TE potential of circular the eddy-current coil can also be expressed in the form

$$\psi_{1,c}(\rho, \phi, z) = \frac{I}{4\pi} \sum_{m=-\infty}^{\infty} e^{im\phi} \int_0^{\infty} C_m(\kappa) J_m(\kappa \rho) \begin{matrix} e^{-\kappa z} \\ e^{\kappa z} \end{matrix} d\kappa, \quad \begin{matrix} z > z_{\max} \\ z < z_{\min} \end{matrix} \quad (8.19)$$

where $C_m(\kappa)$ is the coil source coefficient which is need to be determined.

By using (8.12), we have

$$C_m(\kappa) \begin{matrix} -\kappa \\ \kappa \end{matrix} = -v \int_{r_1}^{r_2} [D_m(\rho_0, z'_0 = l/2, \kappa) - D_m(\rho_0, z'_0 = -l/2, \kappa)] d\rho_0, \quad \begin{matrix} z > z_{\max} \\ z < z_{\min} \end{matrix} \quad (8.20)$$

where $v = N/l(r_2 - r_1)$ is the turn density, which is only determined by coil parameters, Fig. 8.7.

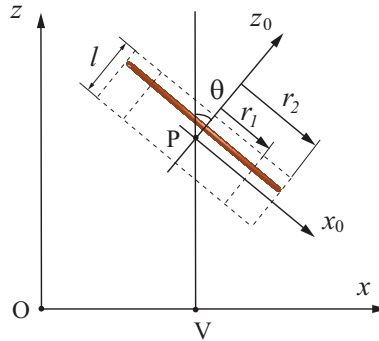
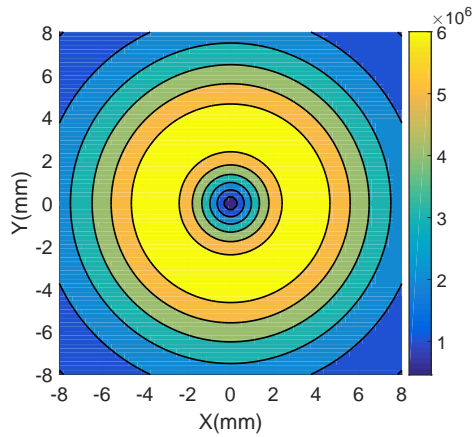
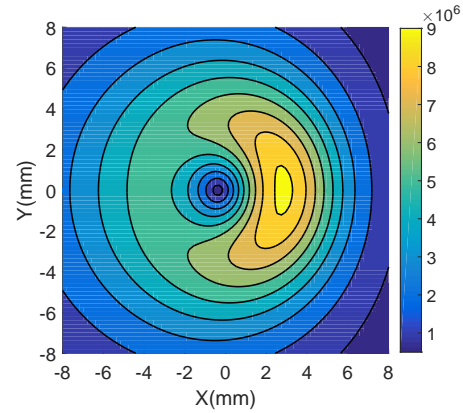


Figure 8.7: The cross-section view of a tilted circular coil is shown in dashed outline. The coil is centered at point P and one filament loop of the coil is also shown to illustrate the filament superposition

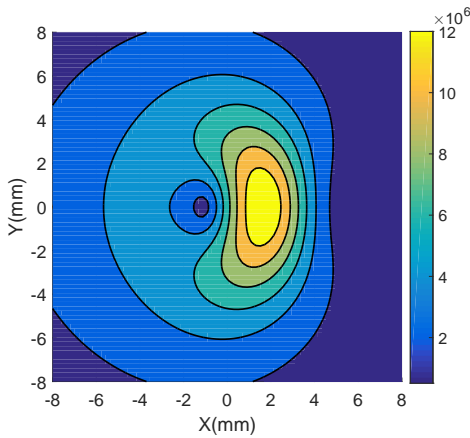
8.4.2 Induced Eddy Current in the Conductive Half-space



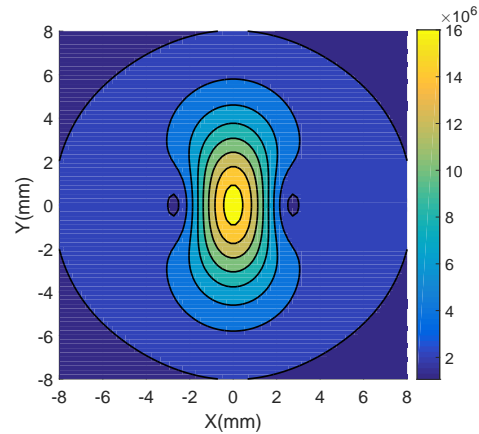
(a) Amplitude Contour of eddy currents with titled angle $\theta = 0^\circ$



(b) Amplitude Contour of eddy currents with titled angle $\theta = 30^\circ$



(c) Amplitude Contour of eddy currents with titled angle $\theta = 60^\circ$



(d) Amplitude Contour of eddy currents with titled angle $\theta = 90^\circ$

Figure 8.8: Amplitude Contour of eddy currents induced on the surface of a conductive half-space by a circular coil with different titled angle

Assuming a air-cored circular coil is located above a conductive half-space with conductivity σ and relative permeability μ_r , the induced eddy current in the conductive half-space is

expressed by applying (8.2) and $J = \sigma E$ as

$$J_\rho = i\omega\mu\sigma \frac{I}{4\pi} \sum_{m=-\infty}^{\infty} e^{im\phi} \int_0^{\infty} imC_m(\kappa)T_{te}(\kappa)\frac{1}{\rho}J_m(\kappa\rho)e^{\gamma z}d\kappa \quad (8.21)$$

$$J_\phi = -i\omega\mu\sigma \frac{I}{4\pi} \sum_{m=-\infty}^{\infty} e^{im\phi} \int_0^{\infty} C_m(\kappa)T_{te}(\kappa)J'_m(\kappa\rho)e^{\gamma z}d\kappa \quad (8.22)$$

where $T_{te}(\kappa)$ is the transmission coefficient. For half-space it has the form

$$T_{te}(\kappa) = \frac{2\kappa}{\kappa\mu_{r2} + \gamma_2} \quad (8.23)$$

In order to have a better understanding of the effect of tilt, the induced eddy current with different tilted angle is evaluated and shown in Fig. 8.8. The coil size and specimen parameters are summarized in Tab. 8.1.

Table 8.1: Coil and specimen parameters

Coil Inner Radius, r_1	1.529mm
Coil Outer Radius, r_2	3.918mm
Coil Thickness, l	1.044mm
Number of Turns, N	305
Isolated DC Coil Inductance, L_0	465 μ H
Conductivity (MS/m)	20.0
Relative Magnetic Permeability, μ_r	1
Coil Center Liftoff, z_c	4.522mm

8.5 Impedance Variation

S_0 is the arbitrary surface which includes the scatter here its the conductor.

$$I^2\Delta Z = i\omega\mu \int_0^{2\pi} \int_0^{\infty} \left[\frac{\partial\psi_1^r}{\partial z} \frac{\partial^2\psi_1^0}{\partial z^2} - \frac{\partial\psi_1^0}{\partial z} \frac{\partial^2\psi_1^r}{\partial z^2} \right] \rho d\phi d\rho \quad (8.24)$$

Then the impedance change is expressed as

$$\Delta Z = \frac{-i\omega\mu}{4\pi} \sum_{m=-\infty}^{\infty} (-1)^m \int_0^{\infty} \kappa^2 C_{-m}(\kappa) \Gamma_{te}(\kappa) C_m(\kappa) d\kappa \quad (8.25)$$

where $\Gamma_{te}(\kappa)$ is the reflection coefficient. For half-space it has the form

$$\Gamma_{te}(\kappa) = \frac{\kappa\mu r_2 - \gamma_2}{\kappa\mu r_2 + \gamma_2} \quad (8.26)$$

If the tilted angle is zero, the problem reduces to model proposed by Dodd [9] and the impedance variance can be evaluated by the following equation.

$$\Delta Z = -i\pi\omega\mu_0v^2 \int_0^{\infty} \frac{\chi^2(\kappa r_1, \kappa r_2)}{\kappa^6} (e^{-\kappa z_1} - e^{-\kappa z_2})^2 \Gamma_{te}(\kappa) d\kappa \quad (8.27)$$

where $z_1 = z_c - l/2$, $z_2 = z_c + l/2$,

$$\chi(\kappa r_1, \kappa r_2) = \chi(\kappa r_2) - \chi(\kappa r_1) \quad (8.28)$$

and

$$\chi(\alpha) = \int_0^{\alpha} J_1(x) x dx = \frac{\pi\alpha}{2} [J_1(\alpha)\mathbf{H}_0(\alpha) - J_0(\alpha)\mathbf{H}_1(\alpha)] \quad (8.29)$$

$\mathbf{H}_0(\alpha)$ and $\mathbf{H}_1(\alpha)$ are Struve functions [102].

The impedance variation based on the our formulation and horizontal coil formulation are obtained individually. The coil size and specimen parameters are shown in Tab. 7.1 except the coil center liftoff, z_c , is set as 1.522mm. The comparison is shown as follow.

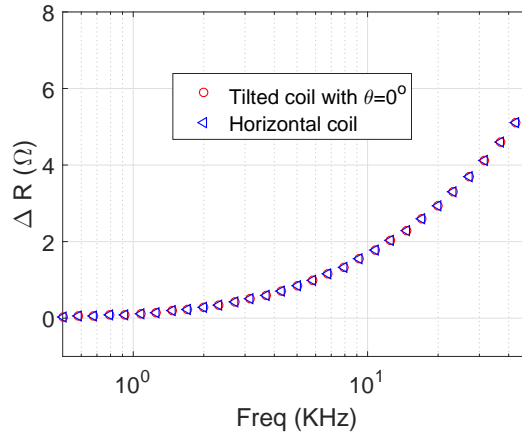


Figure 8.9: The comparison of resistance variation between tilted coil with titled angle $\theta = 0^\circ$ and horizontal coil formulation due to the existence of half-space conductor

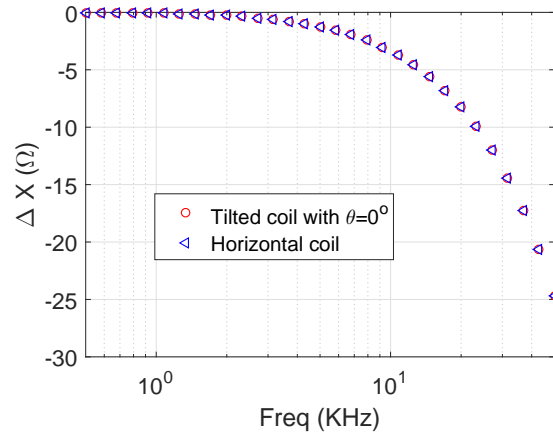


Figure 8.10: The comparison of reactance variation between tilted coil with titled angle $\theta = 0^\circ$ and horizontal coil formulation due to the existence of half-space conductor

8.6 Conclusion

This paper proposes a new analytical model for obtaining the electromagnetic field of circular coil with arbitrary orientation above a conductive half-space. This analytical solution can be used in the wobble noise analysis and repaid calculation of incident field involved in the MoM calculation.

APPENDIX A. REFLECTION AND TRANSMISSION COEFFICIENT FOR PLANARLY AND CYLINDRICALLY LAYERED MEDIUM

A.1 Reflection and Transmission in a Cartesian Coordinate System

A.1.1 Half Space Coefficients

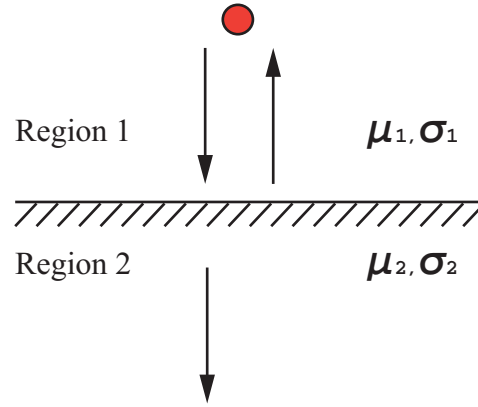


Figure A.1: Half-space medium with source in region 1

In the source free region, the fields can be expressed in terms of TE scalar potential ψ_1 and TM scalar potential ψ_2 .

$$\mathbf{H} = \nabla \times \nabla \times (\hat{z}\psi_1) + k^2 \nabla \times (\hat{z}\psi_2) \quad (\text{A.1})$$

$$\mathbf{E} = i\omega\mu[\nabla \times (\hat{z}\psi_1) + \nabla \times \nabla \times (\hat{z}\psi_2)] \quad (\text{A.2})$$

where μ is the permeability of medium.

In the Cartesian coordinate system, we have

$$\mathbf{H} = \hat{x} \left(\frac{\partial^2 \psi_1}{\partial x \partial z} + k^2 \frac{\partial \psi_2}{\partial y} \right) + \hat{y} \left(\frac{\partial^2 \psi_1}{\partial y \partial z} - k^2 \frac{\partial \psi_2}{\partial x} \right) - \hat{z} \nabla_t^2 \psi_1 \quad (\text{A.3})$$

$$\mathbf{E} = \hat{x} i\omega\mu \left(\frac{\partial \psi_1}{\partial y} + \frac{\partial^2 \psi_2}{\partial x \partial z} \right) + \hat{y} i\omega\mu \left(-\frac{\partial \psi_1}{\partial x} + \frac{\partial^2 \psi_2}{\partial y \partial z} \right) - \hat{z} i\omega\mu \nabla_t^2 \psi_2 \quad (\text{A.4})$$

Assuming both of potentials have the forms

$$\psi = A_1[e^{\gamma_1 z} + R_{12}e^{-\gamma_1 z}] \quad (\text{A.5})$$

for region 1, and

$$\psi = A_1[T_{12}e^{\gamma_2 z}] \quad (\text{A.6})$$

for region 2 separately. R_{12} indicates the reflection coefficient for the field comes from region 1 and is reflected back to region 1. T_{12} indicates the reflection coefficient for the field transmitting from region 1 to region 2.

The reflection and transmission coefficients can be obtained by applying boundary conditions that the tangential components of E and H fields should be continuous at the interface.

The continuity of E field introduces

$$[\mu_i \psi_1] |_{z=z_c} = 0, \left[\mu_i \frac{\partial \psi_2}{\partial z} \right] |_{z=z_c} = 0 \quad (\text{A.7})$$

and that the continuity of H indicates

$$\left[\frac{\partial \psi_1}{\partial z} \right] |_{z=z_c} = 0, [\mu_i \sigma_i \psi_2] |_{z=z_c} = 0 \quad (\text{A.8})$$

where subscript i indicates the region. In the end, we have the reflection and transmission coefficients for TE potential as

$$R_{te,12}(\kappa) = \frac{\gamma_1/\gamma_2 - \mu_1/\mu_2}{\gamma_1/\gamma_2 + \mu_1/\mu_2} = \frac{\gamma_1\mu_2 - \gamma_2\mu_1}{\gamma_1\mu_2 + \gamma_2\mu_1} \quad (\text{A.9})$$

$$T_{te,12}(\kappa) = \frac{2(\gamma_1/\gamma_2) \times (\mu_1/\mu_2)}{\gamma_1/\gamma_2 + \mu_1/\mu_2} = \frac{2\gamma_1\mu_1}{\gamma_1\mu_2 + \gamma_2\mu_1} = \frac{\mu_1}{\mu_2} [1 + R_{te,12}(\kappa)] \quad (\text{A.10})$$

Similarly to TM potential, we have

$$R_{tm,12}(\kappa) = \frac{\sigma_2\gamma_1 - \sigma_1\gamma_2}{\sigma_2\gamma_1 + \sigma_1\gamma_2} \quad (\text{A.11})$$

$$T_{tm,12}(\kappa) = \frac{\sigma_1}{\sigma_2} [1 + R_{tm,12}(\kappa)] = \frac{2\sigma_1\gamma_1}{\sigma_2\gamma_1 + \sigma_1\gamma_2} \quad (\text{A.12})$$

A.1.2 Slab with a Source Above It

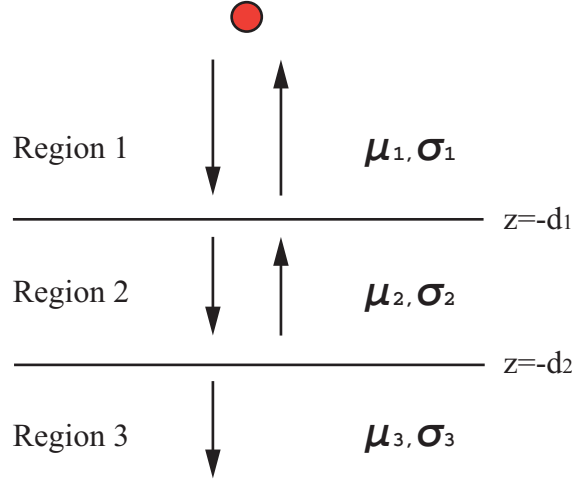


Figure A.2: Infinite large slab with source in region 1

The general potential expressions for three different regions, namely region 1, 2 and 3, can be written with undetermined coefficients firstly as follow individually [90].

$$\begin{aligned}\psi &= A_1[e^{\gamma_1 z} + R_{12}^g e^{-2\gamma_1 d_1} e^{-\gamma_1 z}] \\ \psi &= A_2[e^{\gamma_2 z} + R_{23} e^{-2\gamma_2 d_2} e^{-\gamma_2 z}] \\ \psi &= A_3 e^{\gamma_3 z}\end{aligned}\tag{A.13}$$

where A_1, A_2 and A_3 are the undermined coefficient for corresponding region. The subscript indicates different region, Fig. A.2. R_{12}^g represents the total reflection coefficient, indicated by superscript g , not only due to the $z = -d_1$ interface.

Since the downward field in region 2 is the sum of the transmitted field from region 1 and the reflected field from the interface at $z = -d_1$, we have

$$A_2 e^{-\gamma_2 d_1} = T_{12} A_1 e^{-\gamma_1 d_1} + R_{21} A_2 R_{23} e^{-2\gamma_2 d_2 + \gamma_2 d_1}\tag{A.14}$$

Similarly, since the upward field in region 1 is the sum of the transmitted field from region 2 and the reflected field from the interface at $z = -d_1$, we obtain

$$R_{12}^g A_1 e^{-\gamma_1 d_1} = R_{12} A_1 e^{-\gamma_1 d_1} + T_{21} A_2 R_{23} e^{-2\gamma_2 d_2 + \gamma_2 d_1}\tag{A.15}$$

Now we can obtain

$$A_2 = \frac{T_{12}e^{(\gamma_2-\gamma_1)d_1}}{1 - R_{21}R_{23}e^{-2\gamma_2(d_2-d_1)}} A_1 \quad (\text{A.16})$$

$$R_{12}^g = R_{12} + \frac{T_{21}T_{12}R_{23}e^{-2\gamma_2(d_2-d_1)}}{1 - R_{21}R_{23}e^{-2\gamma_2(d_2-d_1)}} \quad (\text{A.17})$$

which is similar to the reflection coefficient Γ_{in} in terms of S -parameters used in the RF circuit.

$$\Gamma_{in} = S_{11} + \frac{S_{12}S_{21}\Gamma_{load}}{1 - S_{22}\Gamma_{load}} \quad (\text{A.18})$$

If we add one more layer, we just need to replace the R_{23} by the general reflection coefficient R_{23}^g as

$$R_{12}^g = R_{12} + \frac{T_{12}R_{23}^g T_{21}e^{-2\gamma_2(d_2-d_1)}}{1 - R_{21}R_{23}^g e^{-2\gamma_2(d_2-d_1)}} \quad (\text{A.19})$$

Now we have the potential in region 2 as

$$\psi = A_1 \frac{T_{12}e^{(\gamma_2-\gamma_1)d_1}}{1 - R_{21}R_{23}e^{-2\gamma_2(d_2-d_1)}} [e^{\gamma_2 z} + R_{23}e^{-2\gamma_2 d_2} e^{-\gamma_2 z}] \quad (\text{A.20})$$

At the interface $z = -d_2$, we have the following constrain

$$A_3 e^{-\gamma_3 d_2} = T_{23} A_2 e^{-\gamma_2 d_2} \quad (\text{A.21})$$

Then coefficient A_3 can be represented in terms of A_1 . The potential in region 3 can reduce to

$$\psi = A_1 \frac{T_{12}e^{(\gamma_2-\gamma_1)d_1}}{1 - R_{21}R_{23}e^{-2\gamma_2(d_2-d_1)}} T_{23} e^{(\gamma_3-\gamma_2)d_2} e^{\gamma_3 z} \quad (\text{A.22})$$

Note that all the formulation are valid for both TE potential, ψ_1 , and TM potential, ψ_2 , by just substituting the corresponding R and T coefficients.

A.1.3 Slab with an Internal Source

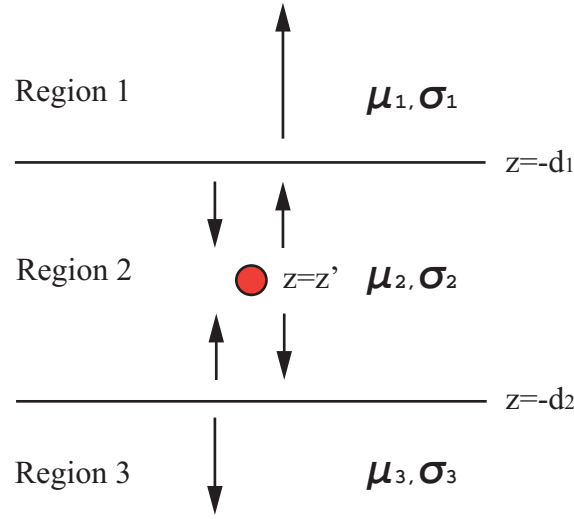


Figure A.3: Slab with Embedded Source in Region 2

The z variation of the potentials in the region 2, Fig. A.3, can be expressed as the sum of three components, namely the first one in the unbounded domain, the second one reflected by the up interface at $z = -d_1$ and the third one reflected by the down interface at $z = -d_2$.

$$\tilde{\psi}(z, z') = e^{-\gamma_2|z-z'|} + Be^{\gamma_2 z} + De^{-\gamma_2 z} \quad (\text{A.23})$$

with the undetermined coefficients B and D , which could be solved by applying constraint conditions at the interfaces.

Since the downward field at $z = -d_1$ should be the sum of the reflected field due to unbounded upward one and that due to reflection at $z = -d_2$, we have

$$Be^{-\gamma_2 d_1} = R_{21}[e^{-\gamma_2|d_1+z'|} + De^{\gamma_2 d_1}] \quad (\text{A.24})$$

R_{ij} denotes the reflection coefficient for the field coming from region i to region j and is reflected back to region i .

Similarly, the upward field at $z = -d_2$ should be the sum of the reflected field due to unbounded downward one and that due to reflection at $z = -d_1$. So we have

$$De^{\gamma_2 d_2} = R_{23}[e^{-\gamma_2|d_2+z'|} + Be^{-\gamma_2 d_2}] \quad (\text{A.25})$$

By solving the above two equations, we obtain

$$Be^{-\gamma_2 d_1} = R_{21} \frac{e^{-\gamma_2 |d_1+z'|} + R_{23} e^{-\gamma_2 |d_2+z'|} e^{\gamma_2 (d_1-d_2)}}{1 - R_{21} R_{23} e^{2\gamma_2 (d_1-d_2)}} \quad (\text{A.26})$$

$$De^{\gamma_2 d_2} = R_{23} \frac{e^{-\gamma_2 |d_2+z'|} + R_{21} e^{-\gamma_2 |d_1+z'|} e^{\gamma_2 (d_1-d_2)}}{1 - R_{21} R_{23} e^{2\gamma_2 (d_1-d_2)}} \quad (\text{A.27})$$

By substituting Eq. A.27 back into Eq. A.23, we have

$$\tilde{\psi}_+(z, z') = [e^{\gamma_2 z'} + e^{-\gamma_2 (2d_2+z')} R_{23}] [e^{-\gamma_2 z} + e^{\gamma_2 (2d_1+z)} R_{21}] M^{-1} \quad (\text{A.28})$$

$$\tilde{\psi}_-(z, z') = [e^{-\gamma_2 z'} + e^{\gamma_2 (2d_1+z')} R_{21}] [e^{\gamma_2 z} + e^{-\gamma_2 (2d_2+z)} R_{23}] M^{-1} \quad (\text{A.29})$$

where $M = 1 - R_{21} R_{23} e^{2\gamma_2 (d_1-d_2)}$, $\tilde{\psi}_+(z, z')$ denotes the variation in the region below $z = -d_1$ and above the source $z = z'$ and $\tilde{\psi}_-(z, z')$ denotes the variation in the region below $z = z'$ and above the source $z = -d_2$.

The regular term or reflection term can be expressed as

$$\tilde{\psi}^\Gamma(z, z') = \left[\begin{array}{l} R_{21} e^{\gamma_2 (2d_1+z')} e^{\gamma_2 z} + R_{21} R_{23} e^{-\gamma_2 (d_2+z')} e^{\gamma_2 (2d_1-d_2)} e^{\gamma_2 z} \\ + R_{23} e^{-\gamma_2 (2d_2+z')} e^{-\gamma_2 z} + R_{23} R_{21} e^{\gamma_2 (d_1+z')} e^{\gamma_2 (d_1-2d_2)} e^{-\gamma_2 z} \end{array} \right] M^{-1} \quad (\text{A.30})$$

For slab in the air, we have $R_{21} = R_{23} = R$. And we assume $d_1 = 0$. Now the M reduce to

$$M = 1 - R^2 e^{-2\gamma_2 d_2} \quad (\text{A.31})$$

$$\tilde{\psi}^\Gamma(z, z') = R \frac{e^{\gamma_2 (z'+z)} + R e^{-2\gamma_2 d_2} e^{\gamma_2 (z-z')} + e^{-2\gamma_2 d_2} e^{-\gamma_2 (z+z')} + R e^{-2\gamma_2 d_2} e^{-\gamma_2 (z-z')}}{1 - R^2 e^{-2\gamma_2 d_2}} \quad (\text{A.32})$$

A.2 Reflection and Transmission in a Cylindrical Coordinate System

In the source free region, the fields can be expressed in terms of TE scalar potential, ψ_1 , and TM scalar potential, ψ_2 , as

$$\mathbf{H} = \nabla \times \nabla \times (\hat{z}\psi_1) + k^2 \nabla \times (\hat{z}\psi_2) \quad (\text{A.33})$$

$$\mathbf{E} = i\omega\mu[\nabla \times (\hat{z}\psi_1) + \nabla \times \nabla \times (\hat{z}\psi_2)] \quad (\text{A.34})$$

where μ is the permeability of medium.

The explicit expressions are

$$\mathbf{H} = \hat{\rho} \left(\frac{\partial^2 \psi_1}{\partial z \partial \rho} + k^2 \frac{1}{\rho} \frac{\partial \psi_2}{\partial \phi} \right) + \hat{\phi} \left(\frac{1}{\rho} \frac{\partial^2 \psi_1}{\partial z \partial \phi} - k^2 \frac{\partial \psi_2}{\partial \rho} \right) - \hat{z} \frac{1}{\rho} \left(\frac{\partial}{\partial \rho} \left(\rho \frac{\partial \psi_1}{\partial \rho} \right) + \frac{1}{\rho} \frac{\partial^2 \psi_1}{\partial \phi^2} \right) \quad (\text{A.35})$$

$$\mathbf{E} = \hat{\rho} i \omega \mu \left(\frac{1}{\rho} \frac{\partial \psi_1}{\partial \phi} + \frac{\partial^2 \psi_2}{\partial z \partial \rho} \right) + \hat{\phi} i \omega \mu \left(-\frac{\partial \psi_1}{\partial \rho} + \frac{1}{\rho} \frac{\partial^2 \psi_2}{\partial z \partial \phi} \right) - \hat{z} i \omega \mu \frac{1}{\rho} \left(\frac{\partial}{\partial \rho} \left(\rho \frac{\partial \psi_2}{\partial \rho} \right) + \frac{1}{\rho} \frac{\partial^2 \psi_2}{\partial \phi^2} \right) \quad (\text{A.36})$$

$$H_z = -\nabla_t^2 \psi_1 = \frac{\partial^2 \psi_1}{\partial z^2} + k^2 \psi_1 \quad (\text{A.37})$$

$$E_z = -i \omega \mu \nabla_t^2 \psi_2 = i \omega \mu \left(\frac{\partial^2 \psi_2}{\partial z^2} + k^2 \psi_2 \right) \quad (\text{A.38})$$

Note that

$$\nabla_t^2 = \frac{1}{\rho} \left(\frac{\partial}{\partial \rho} \left(\rho \frac{\partial}{\partial \rho} \right) + \frac{1}{\rho} \frac{\partial^2}{\partial \phi^2} \right) \quad (\text{A.39})$$

By using Fourier transform, we can express the potentials in the following spectral form

$$\psi_1 = \sum_{m=-\infty}^{\infty} e^{im\phi} \int_{-\infty}^{\infty} e^{ikz} \tilde{\psi}_{1,\rho} d\kappa = \sum_{m=-\infty}^{\infty} e^{im\phi} \tilde{\psi}_1 \quad (\text{A.40})$$

$$\psi_2 = \sum_{m=-\infty}^{\infty} e^{im\phi} \int_{-\infty}^{\infty} e^{ikz} \tilde{\psi}_{2,\rho} d\kappa = \sum_{m=-\infty}^{\infty} e^{im\phi} \tilde{\psi}_2 \quad (\text{A.41})$$

where

$$\tilde{\psi}_1(\rho, m, z) = \int_{-\infty}^{\infty} e^{ikz} \tilde{\psi}_{1,\rho} d\kappa \quad (\text{A.42})$$

$$\tilde{\psi}_2(\rho, m, z) = \int_{-\infty}^{\infty} e^{ikz} \tilde{\psi}_{2,\rho} d\kappa, \quad (\text{A.43})$$

and $\tilde{\psi}_{1,\rho}$ and $\tilde{\psi}_{2,\rho}$ satisfies the Bessel equation

$$\tilde{\psi}_\rho + \tilde{\psi}_\rho \frac{1}{\rho} - \left(\gamma^2 + \frac{m^2}{\rho^2} \right) \tilde{\psi}_\rho = 0 \quad (\text{A.44})$$

where $\gamma = \sqrt{\kappa^2 - k^2}$. The general solution of it is

$$\tilde{\psi}_\rho = A_m I_m(\gamma \rho) + B_m K_m(\gamma \rho) \quad (\text{A.45})$$

Then we can express the spectral domain potentials $\tilde{\psi}_{1,\rho}$ and $\tilde{\psi}_{2,\rho}$ in the matrix form,

$$\begin{bmatrix} \tilde{\psi}_{1,\rho} \\ \tilde{\psi}_{2,\rho} \end{bmatrix} = I_m(\gamma \rho) \begin{bmatrix} a_{te,m} \\ a_{tm,m} \end{bmatrix} = I_m(\gamma \rho) \mathbf{a}_m \quad (\text{A.46})$$

for the incoming field, and

$$\begin{bmatrix} \tilde{\psi}_{1,\rho} \\ \tilde{\psi}_{2,\rho} \end{bmatrix} = K_m(\gamma\rho) \begin{bmatrix} a_{te,m} \\ a_{tm,m} \end{bmatrix} = K_m(\gamma\rho) \mathbf{a}_m \quad (\text{A.47})$$

for the outgoing field. Here $\mathbf{a}_m = \begin{bmatrix} a_{te,m} \\ a_{tm,m} \end{bmatrix}$ is the source coefficients determined by the source.

A.2.1 Borehole with an Internal Source

A borehole structure with source in the borehole is shown in Fig. A.4. In order to make the region clear, from the inner to outside, the index will increase and start at 1. Hence the source here is in region 1.

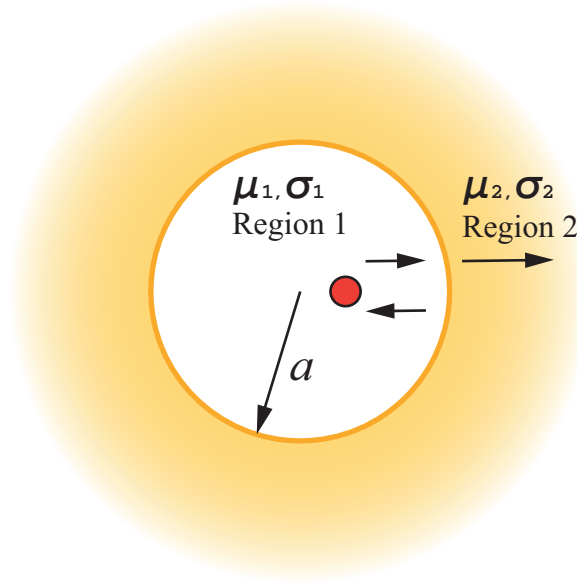


Figure A.4: Borehole structure with the source in region 1. The radius of hole is a

In the region 1, we express the TE and TM potentials generally as

$$\begin{aligned} \begin{bmatrix} \tilde{\psi}_{1,\rho} \\ \tilde{\psi}_{2,\rho} \end{bmatrix}_1 &= \begin{bmatrix} \frac{K_m(\gamma_1\rho)}{K_m(\gamma_1a)} \mathbf{I} + \frac{I_m(\gamma_1\rho)}{I_m(\gamma_1a)} \mathbf{\Gamma}_{12} \end{bmatrix} \mathbf{a}_{1m} \\ &= \left[K_m(\gamma_1\rho) \mathbf{I} + I_m(\gamma_1\rho) \frac{K_m(\gamma_1a)}{I_m(\gamma_1a)} \mathbf{\Gamma}_{12} \right] \frac{\mathbf{a}_{1m}}{K_m(\gamma_1a)} \end{aligned} \quad (\text{A.48})$$

where $\mathbf{a}_{1\mathbf{m}}$ is the source coefficient, $\mathbf{\Gamma}_{12}^g = \frac{K_m(\gamma_1 a)}{I_m(\gamma_1 a)} \mathbf{\Gamma}_{12}$ is the non-normalized reflection coefficient from region 1 to region 2. The diagonal components of $\mathbf{\Gamma}_{12}^g$ denote the self-interaction reflection. And the other two components denote the coupling between TE and TM modes. In region 2, we have

$$\begin{bmatrix} \tilde{\psi}_{1,\rho} \\ \tilde{\psi}_{2,\rho} \end{bmatrix}_2 = \left[\frac{K_m(\gamma_2 \rho)}{K_m(\gamma_2 a)} \mathbf{T}_{12} \right] \mathbf{a}_{1\mathbf{m}} = \left[K_m(\gamma_2 \rho) \frac{K_m(\gamma_1 a)}{K_m(\gamma_2 a)} \mathbf{T}_{12} \right] \frac{\mathbf{a}_{1\mathbf{m}}}{K_m(\gamma_1 a)} \quad (\text{A.49})$$

$\mathbf{T}_{12}^g = \frac{K_m(\gamma_1 a)}{K_m(\gamma_2 a)} \mathbf{T}_{12}$ is the non-normalized transmission coefficient. The diagonal components of $\frac{K_m(\gamma_1 a)}{K_m(\gamma_2 a)} \mathbf{T}_{12}$ denote the self-interaction transmission coefficient. And the other two denote the coupling between TE and TM modes.

In order to get the reflection and transmission coefficients, we need to apply the continuous BCs at the borehole interface. We can express the electric and magnetic field in the spectral form as

$$\tilde{H}_\rho = \frac{\partial^2 \tilde{\psi}_1}{\partial z \partial \rho} + imk^2 \frac{\tilde{\psi}_2}{\rho} \quad (\text{A.50})$$

$$\tilde{E}_\rho = i\omega\mu \left(\frac{im}{\rho} \tilde{\psi}_1 + \frac{\partial^2}{\partial z \partial \rho} \tilde{\psi}_2 \right) \quad (\text{A.51})$$

$$\tilde{H}_\phi = \frac{im}{\rho} \frac{\partial \tilde{\psi}_1}{\partial z} - k^2 \frac{\partial \tilde{\psi}_2}{\partial \rho} \quad (\text{A.52})$$

$$\tilde{E}_\phi = -i\omega\mu \left(\frac{\partial \tilde{\psi}_1}{\partial \rho} - \frac{im}{\rho} \frac{\partial \tilde{\psi}_2}{\partial z} \right) \quad (\text{A.53})$$

$$\tilde{H}_z = \frac{\partial^2 \tilde{\psi}_1}{\partial z^2} + k^2 \tilde{\psi}_1 \quad (\text{A.54})$$

$$\tilde{E}_z = i\omega\mu \left(\frac{\partial^2 \tilde{\psi}_2}{\partial z^2} + k^2 \tilde{\psi}_2 \right) \quad (\text{A.55})$$

Then we have the z-components as follow in the matrix form

$$\begin{bmatrix} \tilde{H}_z \\ \tilde{E}_z / i\omega \end{bmatrix} = -\gamma_s^2 \boldsymbol{\mu}_s \begin{bmatrix} \tilde{\psi}_{1,\rho} \\ \tilde{\psi}_{2,\rho} \end{bmatrix} \quad (\text{A.56})$$

where s is the region index, $\gamma_s = \sqrt{\kappa^2 - k_s^2}$, $k_s^2 = i\omega\mu_0\mu_{r,s}\sigma_s$, and $\boldsymbol{\mu}_s = \begin{bmatrix} 1 & 0 \\ 0 & \mu_0\mu_{r,s} \end{bmatrix} =$

$\begin{bmatrix} 1 & 0 \\ 0 & \mu_s \end{bmatrix}$ is the μ matrix for region s .

Similarly, we have the ϕ -components as follow in the matrix form

$$\begin{bmatrix} \tilde{H}_\phi \\ \tilde{E}_\phi/i\omega \end{bmatrix} = \boldsymbol{\mu}_s \begin{bmatrix} \frac{im}{\rho} \partial_z & -k_s^2 \partial_\rho \\ -\partial_\rho & \frac{im}{\rho} \partial_z \end{bmatrix} \begin{bmatrix} \tilde{\psi}_1 \\ \tilde{\psi}_2 \end{bmatrix} = -\boldsymbol{\mu}_s \begin{bmatrix} \frac{m\kappa}{\rho} & k_s^2 \partial_\rho \\ \partial_\rho & \frac{m\kappa}{\rho} \end{bmatrix} \begin{bmatrix} \tilde{\psi}_{1,\rho} \\ \tilde{\psi}_{2,\rho} \end{bmatrix} \quad (\text{A.57})$$

By using continuous boundary condition that the tangential component in region 1 and region 2 should be continuous at the interface, we can easily obtain at the interface $\rho = a$

$$\gamma_1^2 \boldsymbol{\mu}_1 \begin{bmatrix} \tilde{\psi}_{1,\rho} \\ \tilde{\psi}_{2,\rho} \end{bmatrix}_1 = \gamma_2^2 \boldsymbol{\mu}_2 \begin{bmatrix} \tilde{\psi}_{1,\rho} \\ \tilde{\psi}_{2,\rho} \end{bmatrix}_2 \quad (\text{A.58})$$

$$\boldsymbol{\mu}_1 \begin{bmatrix} m\kappa & k_1^2 \rho \partial_\rho \\ \rho \partial_\rho & m\kappa \end{bmatrix} \begin{bmatrix} \tilde{\psi}_{1,\rho} \\ \tilde{\psi}_{2,\rho} \end{bmatrix}_1 = \boldsymbol{\mu}_2 \begin{bmatrix} m\kappa & k_2^2 \rho \partial_\rho \\ \rho \partial_\rho & m\kappa \end{bmatrix} \begin{bmatrix} \tilde{\psi}_{1,\rho} \\ \tilde{\psi}_{2,\rho} \end{bmatrix}_2 \quad (\text{A.59})$$

By substituting Eq A.48 and A.49 into the above equations, we can get

$$\gamma_1^2 \boldsymbol{\mu}_1 [\mathbf{I} + \boldsymbol{\Gamma}_{12}] = \gamma_2^2 \boldsymbol{\mu}_2 \mathbf{T}_{12} \quad (\text{A.60})$$

$$\boldsymbol{\mu}_1 [\mathbf{M}_m(\gamma_1 a) \mathbf{I} + \boldsymbol{\Lambda}_m(\gamma_1 a) \boldsymbol{\Gamma}_{12}] = \boldsymbol{\mu}_2 \mathbf{M}_m(\gamma_2 a) \mathbf{T}_{12} \quad (\text{A.61})$$

Here

$$\begin{aligned} \mathbf{M}_m(\gamma_2 a) &= \begin{bmatrix} m\kappa & k_2^2 M_m(\gamma_2 a) \\ M_m(\gamma_2 a) & m\kappa \end{bmatrix} \\ \mathbf{M}_m(\gamma_1 a) &= \begin{bmatrix} m\kappa & k_1^2 M_m(\gamma_1 a) \\ M_m(\gamma_1 a) & m\kappa \end{bmatrix} \\ \boldsymbol{\Lambda}_m(\gamma_1 a) &= \begin{bmatrix} m\kappa & k_1^2 \Lambda_m(\gamma_1 a) \\ \Lambda_m(\gamma_1 a) & m\kappa \end{bmatrix} \end{aligned} \quad (\text{A.62})$$

Here we defining

$$\Lambda_m(x) = \frac{x I'_m(x)}{I_m(x)}, M_m(x) = \frac{x K'_m(x)}{K_m(x)} \quad (\text{A.63})$$

We can easily have

$$\Lambda_m(x) - M_m(x) = \frac{x(I'_m K_m - I_m K'_m)}{I_m K_m} = \frac{1}{I_m K_m} \quad (\text{A.64})$$

By solving the Eq. A.60 and A.61, we have

$$\boldsymbol{\Gamma}_{12} = \mathbf{Q}^{-1} \gamma_2^2 \boldsymbol{\mu}_1 [\boldsymbol{\Lambda}_m(\gamma_1 a) - \mathbf{M}_m(\gamma_1 a)] - \mathbf{I} \quad (\text{A.65})$$

where $\mathbf{Q} = \gamma_2^2 \boldsymbol{\mu}_1 \boldsymbol{\Lambda}_m(\gamma_1 a) - \gamma_1^2 \boldsymbol{\mu}_2 \mathbf{M}_m(\gamma_2 a) \boldsymbol{\mu}_2^{-1} \boldsymbol{\mu}_1$.

We notice that

$$[\boldsymbol{\Lambda}_m(\gamma_1 a) - \mathbf{M}_m(\gamma_1 a)] = \frac{1}{I_m(\gamma_1 a) K_m(\gamma_1 a)} \begin{bmatrix} 0 & k_1^2 \\ 1 & 0 \end{bmatrix} \quad (\text{A.66})$$

Then $\boldsymbol{\Gamma}_{12}$ reduces to

$$\boldsymbol{\Gamma}_{12} = \frac{\gamma_2^2}{I_m(\gamma_1 a) K_m(\gamma_1 a)} \mathbf{Q}^{-1} \begin{bmatrix} 0 & k_1^2 \\ \mu_1 & 0 \end{bmatrix} - \mathbf{I} \quad (\text{A.67})$$

The transmission coefficient matrix is obtained as

$$\mathbf{T}_{12} = \frac{\gamma_1^2}{\gamma_2^2} \boldsymbol{\mu}_2^{-1} \boldsymbol{\mu}_1 [\mathbf{I} + \boldsymbol{\Gamma}_{12}] = \frac{\gamma_1^2}{\gamma_2^2} \begin{bmatrix} 1 + \Gamma^{11} & \Gamma^{12} \\ \mu_1 \mu_2^{-1} \Gamma^{21} & \mu_1 \mu_2^{-1} (1 + \Gamma^{22}) \end{bmatrix} \quad (\text{A.68})$$

Or

$$\mathbf{T}_{12} = \gamma_1^2 \boldsymbol{\mu}_2^{-1} \boldsymbol{\mu}_1 \mathbf{Q}^{-1} [\boldsymbol{\Lambda}_m(\gamma_1 a) - \mathbf{M}_m(\gamma_1 a)] \quad (\text{A.69})$$

If air is in region 1 and conductive material is in region 2, we have the reflection and transmission coefficients of TE potential due to TE source as [104]

$$\boldsymbol{\Gamma}_{12}(1, 1) = -\frac{m^2 k_2^2 \mu_{r2} + M_m(\gamma_2 a) [\gamma_2^2 M_m(|\kappa|a) - \kappa^2 \mu_{r2} M_m(\gamma_2 a)]}{m^2 k_2^2 \mu_{r2} + M_m(\gamma_2 a) [\gamma_2^2 \Lambda_m(|\kappa|a) - \kappa^2 \mu_{r2} M_m(\gamma_2 a)]} \quad (\text{A.70})$$

and

$$\mathbf{T}_{12}(1, 1) = \frac{\kappa^2 M_m(\gamma_2 a) [\Lambda_m(|\kappa|a) - M_m(|\kappa|a)]}{m^2 k_2^2 \mu_{r2} + M_m(\gamma_2 a) [\gamma_2^2 \Lambda_m(|\kappa|a) - \kappa^2 \mu_{r2} M_m(\gamma_2 a)]} \quad (\text{A.71})$$

Furthermore, if it's the coaxial bobbin coil problem, $m = 0$ is applied. Then we have

$$\boldsymbol{\Gamma}_{12}^g(1, 1) = -\frac{[\kappa \mu_{r2} K_0(\kappa a) K_1(\gamma_2 a) - \gamma_2 K_0(\gamma_2 a) K_1(\kappa a)]}{[\gamma_2 K_0(\gamma_2 a) I_1(\kappa a) + \kappa \mu_{r2} K_1(\gamma_2 a) I_0(\kappa a)]} \quad (\text{A.72})$$

A.2.2 Borehole with an External Source

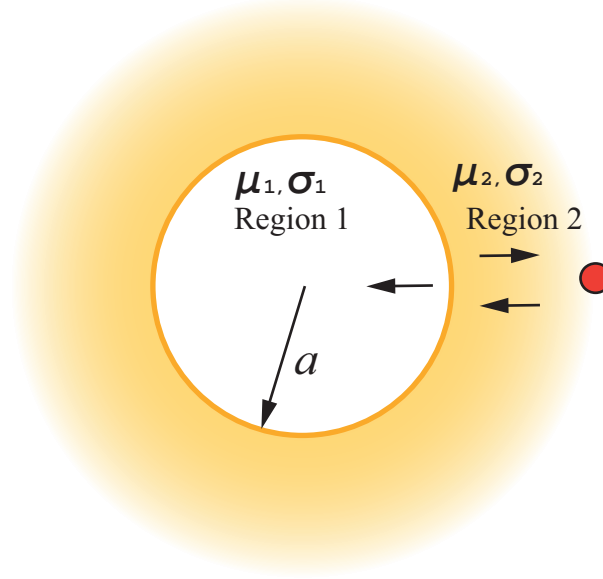


Figure A.5: Borehole structure with the source in region 2. The radius of hole is a

Similarly to the derivation of borehole with the source in region 1, we expressed the spectral domain potentials in region 1 as,

$$\begin{bmatrix} \tilde{\psi}_{1,\rho} \\ \tilde{\psi}_{2,\rho} \end{bmatrix}_1 = \left[\frac{I_m(\gamma_1 \rho)}{I_m(\gamma_1 a)} \mathbf{T}_{21} \right] = [I_m(\gamma_1 \rho) \mathbf{T}_{21}^g] \frac{\mathbf{a}_{2m}}{I_m(\gamma_2 a)} \quad (\text{A.73})$$

$\mathbf{T}_{21}^g = \frac{I_m(\gamma_2 a)}{I_m(\gamma_1 a)} \mathbf{T}_{21}$ is the general transmission coefficient. And in region 2, we have

$$\begin{aligned} \begin{bmatrix} \tilde{\psi}_{1,\rho} \\ \tilde{\psi}_{2,\rho} \end{bmatrix}_2 &= \left[\frac{I_m(\gamma_2 \rho)}{I_m(\gamma_2 a)} \mathbf{I} + \frac{K_m(\gamma_2 \rho)}{K_m(\gamma_2 a)} \mathbf{\Gamma}_{21} \right] \mathbf{a}_{2m} \\ &= [I_m(\gamma_2 \rho) \mathbf{I} + K_m(\gamma_2 \rho) \mathbf{\Gamma}_{21}^g] \frac{\mathbf{a}_{2m}}{I_m(\gamma_2 a)} \end{aligned} \quad (\text{A.74})$$

$\mathbf{\Gamma}_{21}^g = \frac{I_m(\gamma_2 a)}{K_m(\gamma_2 a)} \mathbf{\Gamma}_{21}$ is the general reflection coefficient.

By applying BCs at the interface $\rho = a$, we have

$$\gamma_1^2 \boldsymbol{\mu}_1 \begin{bmatrix} \tilde{\psi}_{1,\rho} \\ \tilde{\psi}_{2,\rho} \end{bmatrix}_1 = \gamma_2^2 \boldsymbol{\mu}_2 \begin{bmatrix} \tilde{\psi}_{1,\rho} \\ \tilde{\psi}_{2,\rho} \end{bmatrix}_2 \quad (\text{A.75})$$

and

$$\boldsymbol{\mu}_1 \begin{bmatrix} m\kappa & k_1^2 \rho \partial_\rho \\ \rho \partial_\rho & m\kappa \end{bmatrix} \begin{bmatrix} \tilde{\psi}_{1,\rho} \\ \tilde{\psi}_{2,\rho} \end{bmatrix}_1 = \boldsymbol{\mu}_2 \begin{bmatrix} m\kappa & k_2^2 \rho \partial_\rho \\ \rho \partial_\rho & m\kappa \end{bmatrix} \begin{bmatrix} \tilde{\psi}_{1,\rho} \\ \tilde{\psi}_{2,\rho} \end{bmatrix}_2 \quad (\text{A.76})$$

By substituting Eq. A.73 and A.74, we obtain

$$\gamma_1^2 \boldsymbol{\mu}_1 [\mathbf{T}_{21}] = \gamma_2^2 \boldsymbol{\mu}_2 [\mathbf{I} + \boldsymbol{\Gamma}_{21}] \quad (\text{A.77})$$

$$\boldsymbol{\mu}_1 \boldsymbol{\Lambda}_m(\gamma_1 a) [\mathbf{T}_{21}] = \boldsymbol{\mu}_2 [\boldsymbol{\Lambda}_m(\gamma_2 a) \mathbf{I} + \mathbf{M}_m(\gamma_2 a) \boldsymbol{\Gamma}_{21}] \quad (\text{A.78})$$

By solving the above two equations, we obtain

$$\boldsymbol{\Gamma}_{21} = \gamma_1^2 \mathbf{Q}^{-1} \boldsymbol{\mu}_2 [\boldsymbol{\Lambda}_m(\gamma_2 a) - \mathbf{M}_m(\gamma_2 a)] - \mathbf{I} \quad (\text{A.79})$$

where

$$\mathbf{Q} = \gamma_2^2 \boldsymbol{\mu}_1 \boldsymbol{\Lambda}_m(\gamma_1 a) \boldsymbol{\mu}_1^{-1} \boldsymbol{\mu}_2 - \gamma_1^2 \boldsymbol{\mu}_2 \mathbf{M}_m(\gamma_2 a) \quad (\text{A.80})$$

Note that

$$[\boldsymbol{\Lambda}_m(\gamma_2 a) - \mathbf{M}_m(\gamma_2 a)] = \frac{1}{I_m(\gamma_2 a) K_m(\gamma_2 a)} \begin{bmatrix} 0 & k_2^2 \\ 1 & 0 \end{bmatrix} \quad (\text{A.81})$$

then Eq.A.79 can be rewritten as

$$\boldsymbol{\Gamma}_{21} = \frac{\gamma_1^2}{I_m(\gamma_2 a) K_m(\gamma_2 a)} \mathbf{Q}^{-1} \begin{bmatrix} 0 & k_2^2 \\ \mu_2 & 0 \end{bmatrix} - \mathbf{I} \quad (\text{A.82})$$

The transmission coefficient matrix is solved as

$$\mathbf{T}_{21} = \frac{\gamma_2^2}{\gamma_1} \boldsymbol{\mu}_1^{-1} \boldsymbol{\mu}_2 [\mathbf{I} + \boldsymbol{\Gamma}_{21}] = \frac{\gamma_2^2}{\gamma_1} \begin{bmatrix} 1 & 0 \\ 0 & \mu_2 \mu_1^{-1} \end{bmatrix} [\mathbf{I} + \boldsymbol{\Gamma}_{21}] \quad (\text{A.83})$$

Or

$$\mathbf{T}_{21} = \gamma_2^2 \boldsymbol{\mu}_1^{-1} \boldsymbol{\mu}_2 \mathbf{Q}^{-1} \boldsymbol{\mu}_2 [\boldsymbol{\Lambda}_m(\gamma_2 a) - \mathbf{M}_m(\gamma_2 a)] \quad (\text{A.84})$$

Actually, In order to get the non-normalized $\boldsymbol{\Gamma}$ and \mathbf{T} (the similar definition in [90]), we can use the following relationship

- From region 1 to region 2

$$\boldsymbol{\Gamma}_{12}^g = \frac{K_m(\gamma_1 a)}{I_m(\gamma_1 a)} \boldsymbol{\Gamma}_{12} \quad (\text{A.85})$$

$$\mathbf{T}_{12}^g = \frac{K_m(\gamma_1 a)}{K_m(\gamma_2 a)} \mathbf{T}_{12} \quad (\text{A.86})$$

- From region 2 to region 1

$$\mathbf{\Gamma}_{21}^g = \frac{I_m(\gamma_2 a)}{K_m(\gamma_2 a)} \mathbf{\Gamma}_{21} \quad (\text{A.87})$$

$$\mathbf{T}_{21}^g = \frac{I_m(\gamma_2 a)}{I_m(\gamma_1 a)} \mathbf{T}_{21} \quad (\text{A.88})$$

A.2.3 Tube with an Internal Source

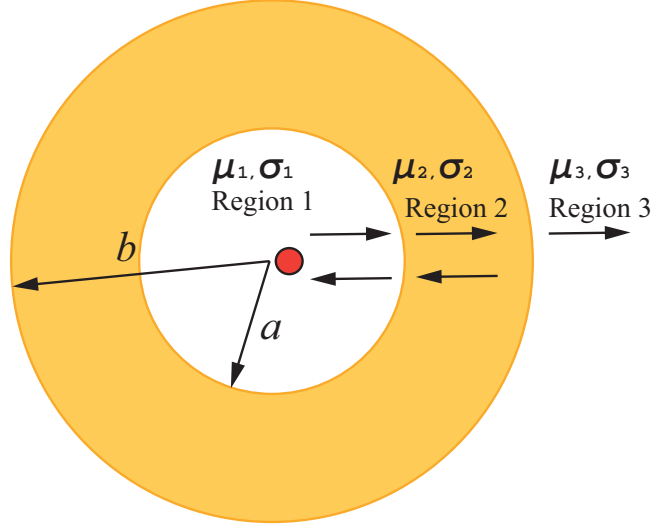


Figure A.6: Tube structure with the source in region 1

First, we express the spectral domain potentials in the general form for region 1, 2 and 3 as

$$\begin{bmatrix} \tilde{\psi}_{1,\rho} \\ \tilde{\psi}_{2,\rho} \end{bmatrix}_1 = \begin{bmatrix} K_m(\gamma_1 \rho) \mathbf{I} + \frac{I_m(\gamma_1 \rho)}{I_m(\gamma_1 a)} \tilde{\mathbf{\Gamma}}_{12} \\ \frac{K_m(\gamma_1 a)}{K_m(\gamma_1 \rho)} \mathbf{I} \end{bmatrix} \cdot \mathbf{a}_{1m} \quad (\text{A.89})$$

$$\begin{bmatrix} \tilde{\psi}_{1,\rho} \\ \tilde{\psi}_{2,\rho} \end{bmatrix}_2 = \begin{bmatrix} K_m(\gamma_2 \rho) \mathbf{I} + \frac{I_m(\gamma_2 \rho)}{I_m(\gamma_2 b)} \mathbf{\Gamma}_{23} \\ \frac{K_m(\gamma_2 b)}{K_m(\gamma_2 \rho)} \mathbf{I} \end{bmatrix} \cdot \mathbf{a}_{2m} \quad (\text{A.90})$$

$$\begin{bmatrix} \tilde{\psi}_{1,\rho} \\ \tilde{\psi}_{2,\rho} \end{bmatrix}_3 = \begin{bmatrix} K_m(\gamma_3 \rho) \\ K_m(\gamma_3 b) \end{bmatrix} \cdot \mathbf{a}_{3m} \quad (\text{A.91})$$

where $\tilde{\mathbf{\Gamma}}_{12}$ is the total reflection coefficient due to the effect of all the interface not only the $\rho = a$ interface. At interface $\rho = a$, we have two constraints. one is the outgoing field in region 2 is the sum of the transmitted field of the incident field in region 1 and the reflected field

from incoming field in region 2. Another one is the incoming field in region 1 is the sum of the transmitted field comes from incoming field in region 2 and the field reflected from outgoing field in region 1.

Then we can get

$$\frac{\mathbf{a}_{2m}}{K_m(\gamma_2 b)} = \mathbf{T}_{12}^g \frac{\mathbf{a}_{1m}}{K_m(\gamma_1 a)} + \mathbf{\Gamma}_{21}^g \mathbf{\Gamma}_{23} \frac{\mathbf{a}_{2m}}{I_m(\gamma_2 b)} \quad (\text{A.92})$$

$$\tilde{\mathbf{\Gamma}}_{12} \frac{\mathbf{a}_{1m}}{I_m(\gamma_1 a)} = \mathbf{\Gamma}_{12}^g \frac{\mathbf{a}_{1m}}{K_m(\gamma_1 a)} + \mathbf{T}_{21}^g \mathbf{\Gamma}_{23} \frac{\mathbf{a}_{2m}}{I_m(\gamma_2 b)} \quad (\text{A.93})$$

Or in the normalized form as

$$\frac{\mathbf{a}_{2m}}{K_m(\gamma_2 b)} = \frac{K_m(\gamma_1 a)}{K_m(\gamma_2 a)} \mathbf{T}_{12} \frac{\mathbf{a}_{1m}}{K_m(\gamma_1 a)} + \frac{I_m(\gamma_2 a)}{K_m(\gamma_2 a)} \mathbf{\Gamma}_{21} \mathbf{\Gamma}_{23} \frac{K_m(\gamma_2 b)}{I_m(\gamma_2 b)} \frac{\mathbf{a}_{2m}}{K_m(\gamma_2 b)} \quad (\text{A.94})$$

$$\tilde{\mathbf{\Gamma}}_{12} \frac{\mathbf{a}_{1m}}{I_m(\gamma_1 a)} = \frac{K_m(\gamma_1 a)}{I_m(\gamma_1 a)} \mathbf{\Gamma}_{12} \frac{\mathbf{a}_{1m}}{K_m(\gamma_1 a)} + \frac{I_m(\gamma_2 a)}{I_m(\gamma_1 a)} \mathbf{T}_{21} \mathbf{\Gamma}_{23} \frac{K_m(\gamma_2 b)}{I_m(\gamma_2 b)} \frac{\mathbf{a}_{2m}}{K_m(\gamma_2 b)} \quad (\text{A.95})$$

From Eq.A.92, we have

$$\mathbf{a}_{2m} = \frac{K_m(\gamma_2 b)}{K_m(\gamma_2 a)} \left[\mathbf{I} - \frac{I_m(\gamma_2 a) K_m(\gamma_2 b)}{I_m(\gamma_2 b) K_m(\gamma_2 a)} \mathbf{\Gamma}_{21} \cdot \mathbf{\Gamma}_{23} \right]^{-1} \cdot \mathbf{T}_{12} \cdot \mathbf{a}_{1m} \quad (\text{A.96})$$

Then substituting it into Eq.A.93, we obtain

$$\tilde{\mathbf{\Gamma}}_{12}^g = \mathbf{\Gamma}_{12}^g + \mathbf{T}_{21}^g \cdot \mathbf{\Gamma}_{23}^g (\mathbf{I} - \mathbf{\Gamma}_{21}^g \cdot \mathbf{\Gamma}_{23}^g)^{-1} \cdot \mathbf{T}_{12}^g = \frac{K_m(\gamma_1 a)}{I_m(\gamma_1 a)} \tilde{\mathbf{\Gamma}}_{12} \quad (\text{A.97})$$

in the non-normalized form and

$$\tilde{\mathbf{\Gamma}}_{12} = \mathbf{\Gamma}_{12} + \frac{I_m(\gamma_2 a) K_m(\gamma_2 b)}{I_m(\gamma_2 b) K_m(\gamma_2 a)} \mathbf{T}_{21} \cdot \mathbf{\Gamma}_{23} \left[\mathbf{I} - \frac{I_m(\gamma_2 a) K_m(\gamma_2 b)}{I_m(\gamma_2 b) K_m(\gamma_2 a)} \mathbf{\Gamma}_{21} \cdot \mathbf{\Gamma}_{23} \right]^{-1} \cdot \mathbf{T}_{12} \quad (\text{A.98})$$

in the normalized form.

Note that here $\tilde{\mathbf{\Gamma}}_{12}$ is the normalized reflection coefficient. Here $\gamma_1^2 = \kappa^2 - k_1^2$, $\gamma_2^2 = \kappa^2 - k_2^2$, $k_1^2 = i\omega\mu_0\mu_{r1}\sigma_1$, $k_2^2 = i\omega\mu_0\mu_{r2}\sigma_2$

The potentials in region 2 is

$$\begin{bmatrix} \tilde{\psi}_{1,\rho} \\ \tilde{\psi}_{2,\rho} \end{bmatrix}_2 = [K_m(\gamma_2 \rho) \mathbf{I} + I_m(\gamma_2 \rho) \mathbf{\Gamma}_{23}^g] [\mathbf{I} - \mathbf{\Gamma}_{21}^g \mathbf{\Gamma}_{23}^g]^{-1} \mathbf{T}_{12}^g \frac{\mathbf{a}_{1m}}{K_m(\gamma_1 a)} \quad (\text{A.99})$$

A.2.4 Tube with a Source between inner and outer surface

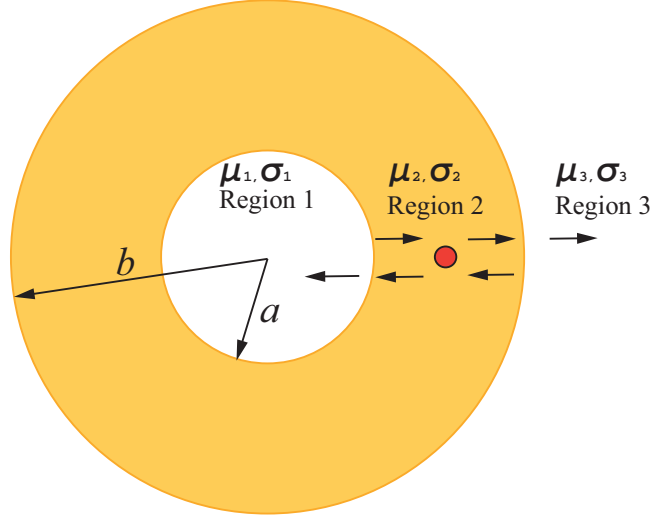


Figure A.7: Tube with source in region 2

The Green's function due to point source can be expressed as the sum of three components, namely the first one in the unbounded domain, the second one reflected by the inner interface and the third one reflected by the outsider interface[90]

$$\begin{bmatrix} \tilde{G}_{11} & \tilde{G}_{12} \\ \tilde{G}_{21} & \tilde{G}_{22} \end{bmatrix} = \tilde{\mathbf{G}} = I_m(\gamma_2 \rho_{<}) K_m(\gamma_2 \rho_{>}) \mathbf{I} + K_m(\gamma_2 \rho) \mathbf{A}_m + I_m(\gamma_2 \rho) \mathbf{B}_m \quad (\text{A.100})$$

The outward field at $\rho = a$ should be the sum of the reflected field due to unbounded inward one and that due to reflection at $\rho = b$.

$$\mathbf{A}_m = \frac{I_m(\gamma_2 a)}{K_m(\gamma_2 a)} \mathbf{\Gamma}_{21} \cdot [K_m(\gamma_2 \rho') \mathbf{I} + \mathbf{B}_m] = \mathbf{\Gamma}_{21}^g \cdot [K_m(\gamma_2 \rho') \mathbf{I} + \mathbf{B}_m] \quad (\text{A.101})$$

The inward field at $\rho = b$ should be the sum of the reflected field due to unbounded inward one and that due to reflection at $\rho = a$.

$$\mathbf{B}_m = \frac{K_m(\gamma_2 b)}{I_m(\gamma_2 b)} \mathbf{\Gamma}_{23} \cdot [I_m(\gamma_2 \rho') \mathbf{I} + \mathbf{A}_m] = \mathbf{\Gamma}_{23}^g \cdot [I_m(\gamma_2 \rho') \mathbf{I} + \mathbf{A}_m] \quad (\text{A.102})$$

Then we can get

$$\mathbf{A}_m = \mathbf{M}_+ \mathbf{\Gamma}_{21}^g \cdot [K_m(\gamma_2 \rho') \mathbf{I} + I_m(\gamma_2 \rho') \mathbf{\Gamma}_{23}^g] \quad (\text{A.103})$$

$$\mathbf{B}_m = \mathbf{M}_- \mathbf{\Gamma}_{23}^g [I_m(\gamma_2 \rho') \mathbf{I} + K_m(\gamma_2 \rho') \mathbf{\Gamma}_{21}^g] \quad (\text{A.104})$$

where

$$\mathbf{M}_+ = [\mathbf{I} - \mathbf{\Gamma}_{21}^g \cdot \mathbf{\Gamma}_{23}^g]^{-1}, \mathbf{M}_- = [\mathbf{I} - \mathbf{\Gamma}_{23}^g \cdot \mathbf{\Gamma}_{21}^g]^{-1} \quad (\text{A.105})$$

or

$$\mathbf{M}_+ = \left[\mathbf{I} - \frac{I_m(\gamma_2 a) K_m(\gamma_2 b)}{I_m(\gamma_2 b) K_m(\gamma_2 a)} \mathbf{\Gamma}_{21} \cdot \mathbf{\Gamma}_{23} \right]^{-1} \quad (\text{A.106})$$

$$\mathbf{M}_- = \left[\mathbf{I} - \frac{I_m(\gamma_2 a) K_m(\gamma_2 b)}{I_m(\gamma_2 b) K_m(\gamma_2 a)} \mathbf{\Gamma}_{23} \cdot \mathbf{\Gamma}_{21} \right]^{-1} \quad (\text{A.107})$$

Note that following relationships can be obtained

$$\mathbf{\Gamma}_{23}^g \cdot \mathbf{M}_+ = \mathbf{M}_- \cdot \mathbf{\Gamma}_{23}^g \quad (\text{A.108})$$

$$\mathbf{M}_+ \cdot \mathbf{\Gamma}_{21}^g = \mathbf{\Gamma}_{21}^g \cdot \mathbf{M}_- \quad (\text{A.109})$$

Then the regular term can be expressed as

$$\begin{aligned} \tilde{\mathbf{G}}^\Gamma &= K_m(\gamma_2 \rho) \mathbf{A}_m + I_m(\gamma_2 \rho) \mathbf{B}_m \\ &= K_m(\gamma_2 \rho') \frac{I_m(\gamma_2 a)}{K_m(\gamma_2 a)} \left[K_m(\gamma_2 \rho) \mathbf{I} + I_m(\gamma_2 \rho) \frac{K_m(\gamma_2 b)}{I_m(\gamma_2 b)} \mathbf{\Gamma}_{23} \right] \mathbf{M}_+ \mathbf{\Gamma}_{21} \\ &\quad + I_m(\gamma_2 \rho') \frac{K_m(\gamma_2 b)}{I_m(\gamma_2 b)} \left[I_m(\gamma_2 \rho) \mathbf{I} + K_m(\gamma_2 \rho) \frac{I_m(\gamma_2 a)}{K_m(\gamma_2 a)} \mathbf{\Gamma}_{21} \right] \mathbf{M}_- \mathbf{\Gamma}_{23} \\ &= K_m(\gamma_2 \rho') [K_m(\gamma_2 \rho) \mathbf{I} + I_m(\gamma_2 \rho) \mathbf{\Gamma}_{23}^g] \mathbf{M}_+ \mathbf{\Gamma}_{21}^g \\ &\quad + I_m(\gamma_2 \rho') [I_m(\gamma_2 \rho) \mathbf{I} + K_m(\gamma_2 \rho) \mathbf{\Gamma}_{21}^g] \mathbf{M}_- \mathbf{\Gamma}_{23}^g \end{aligned} \quad (\text{A.110})$$

A.2.5 Tube with an External Source

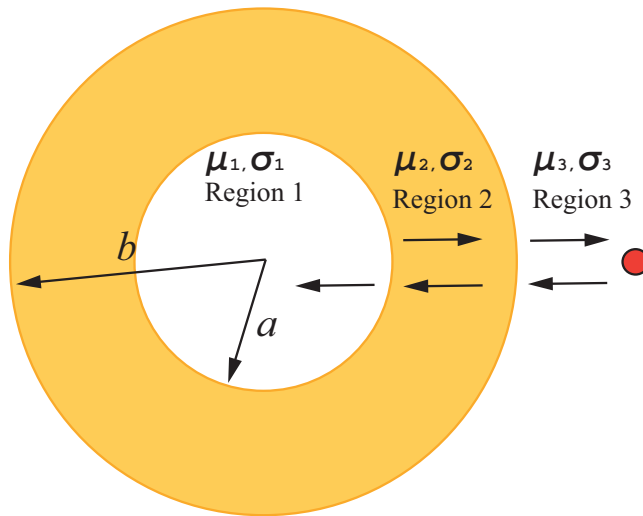


Figure A.8: Tube with source in region 3

First, we expressed the potentials in different regions as

$$\begin{bmatrix} \tilde{\psi}_{1,\rho} \\ \tilde{\psi}_{2,\rho} \end{bmatrix}_1 = \left[\frac{K_m(\gamma_1 \rho)}{K_m(\gamma_1 a)} \right] \mathbf{a}_{1\mathbf{m}} \quad (\text{A.111})$$

$$\begin{bmatrix} \tilde{\psi}_{1,\rho} \\ \tilde{\psi}_{2,\rho} \end{bmatrix}_2 = \left[\frac{I_m(\gamma_2 \rho)}{I_m(\gamma_2 a)} \mathbf{I} + \frac{K_m(\gamma_2 \rho)}{K_m(\gamma_2 a)} \mathbf{\Gamma}_{21} \right] \mathbf{a}_{2\mathbf{m}} \quad (\text{A.112})$$

$$\begin{bmatrix} \tilde{\psi}_{1,\rho} \\ \tilde{\psi}_{2,\rho} \end{bmatrix}_3 = \left[\frac{I_m(\gamma_3 \rho)}{I_m(\gamma_3 b)} \mathbf{I} + \frac{K_m(\gamma_3 \rho)}{K_m(\gamma_3 b)} \tilde{\mathbf{\Gamma}}_{32} \right] \mathbf{a}_{3\mathbf{m}} \quad (\text{A.113})$$

Similarly to source inside tube case, we have two constraints at the interface $\rho = b$ to obtain two equations as follow

$$\frac{\mathbf{a}_{2\mathbf{m}}}{I_m(\gamma_2 a)} \mathbf{I} = \mathbf{T}_{32}^g \frac{\mathbf{a}_{3\mathbf{m}}}{I_m(\gamma_3 b)} \mathbf{I} + \mathbf{\Gamma}_{23}^g \mathbf{\Gamma}_{21} \frac{\mathbf{a}_{2\mathbf{m}}}{K_m(\gamma_2 a)} \quad (\text{A.114})$$

$$\tilde{\mathbf{\Gamma}}_{32} \frac{\mathbf{a}_{3\mathbf{m}}}{K_m(\gamma_3 b)} = \mathbf{\Gamma}_{32}^g \frac{\mathbf{a}_{3\mathbf{m}}}{I_m(\gamma_3 b)} + \mathbf{T}_{23}^g \mathbf{\Gamma}_{21} \frac{\mathbf{a}_{2\mathbf{m}}}{K_m(\gamma_2 a)} \quad (\text{A.115})$$

By solving Eq.A.114, we have

$$\mathbf{a}_{2\mathbf{m}} = \frac{I_m(\gamma_2 a)}{I_m(\gamma_3 b)} [\mathbf{I} - \mathbf{\Gamma}_{23}^g \mathbf{\Gamma}_{21}^g]^{-1} \mathbf{T}_{32}^g \mathbf{a}_{3\mathbf{m}} \quad (\text{A.116})$$

Substituting Eq.A.115, we obtain

$$\tilde{\mathbf{\Gamma}}_{32}^g = \mathbf{\Gamma}_{32}^g + \mathbf{T}_{23}^g \mathbf{\Gamma}_{21}^g [\mathbf{I} - \mathbf{\Gamma}_{23}^g \mathbf{\Gamma}_{21}^g]^{-1} \mathbf{T}_{32}^g = \frac{I_m(\gamma_3 b)}{K_m(\gamma_3 b)} \tilde{\mathbf{\Gamma}}_{32} \quad (\text{A.117})$$

in the non-normalized form, and

$$\tilde{\mathbf{\Gamma}}_{32} = \mathbf{\Gamma}_{32} + \frac{I_m(\gamma_2 a) K_m(\gamma_2 b)}{I_m(\gamma_2 b) K_m(\gamma_2 a)} \mathbf{T}_{23} \cdot \mathbf{\Gamma}_{21} \left(\mathbf{I} - \frac{I_m(\gamma_2 a) K_m(\gamma_2 b)}{I_m(\gamma_2 b) K_m(\gamma_2 a)} \mathbf{\Gamma}_{23} \cdot \mathbf{\Gamma}_{21} \right)^{-1} \cdot \mathbf{T}_{32} \quad (\text{A.118})$$

in the normalized form.

The TE and TM potentials in the tube metal is

$$\begin{bmatrix} \tilde{\psi}_{1,\rho} \\ \tilde{\psi}_{2,\rho} \end{bmatrix}_2 = [I_m(\gamma_2 \rho) \mathbf{I} + K_m(\gamma_2 \rho) \mathbf{\Gamma}_{21}^g] [\mathbf{I} - \mathbf{\Gamma}_{23}^g \mathbf{\Gamma}_{21}^g]^{-1} \mathbf{T}_{32}^g \frac{\mathbf{a}_{3\mathbf{m}}}{I_m(\gamma_3 b)} \quad (\text{A.119})$$

APPENDIX B. BOBBIN COIL CO-AXIAL WITH BOREHOLE AND TUBE STRUCTURES

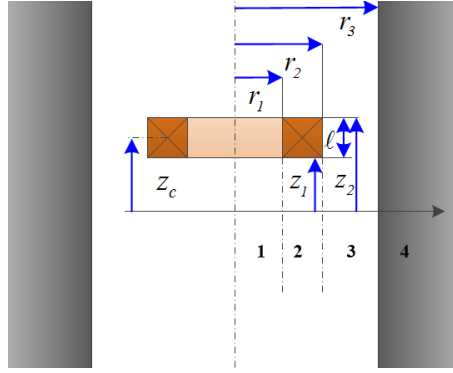


Figure B.1: A eddy current coil located inside coaxial with borehole, the number 1,2,3,4 indicates different region

The coil impedance changes inside a borehole whose axis is co-axis with that of borehole, Fig. B.1 can be obtained by

$$\Delta Z = -8i\omega\mu_0v^2 \int_0^\infty \sin^2\left(\frac{\kappa\ell}{2}\right) \frac{1}{\kappa^6} \psi_I^2(\kappa r_1, \kappa r_2) \Gamma(\kappa) d\kappa \quad (\text{B.1})$$

where v is the turn density and Γ is the reflection coefficient of a source inside the borehole shown as follow

$$\Gamma(\kappa) = \frac{\kappa K_0(\kappa r_3) K_1(\gamma r_3) - (\gamma/\mu_r) K_0(\gamma r_3) K_1(\kappa r_3)}{(\gamma/\mu_r) K_0(\gamma r_3) I_1(\kappa r_3) + \kappa K_1(\gamma r_3) I_0(\kappa r_3)} \quad (\text{B.2})$$

Function ψ_I and ψ_K can be found in Appendix C. $\gamma = \sqrt{\kappa^2 - k^2}$. $k^2 = i\omega\mu\sigma$. μ_r and σ are the relative permeability and conductivity of conductive material.

The reflection and transmission coefficient with source inside can be expressed more generally as

$$\Gamma^{i,i+1}(\kappa) = \frac{(\gamma_i/\mu_{r,i})K_0(\gamma_i r_i)K_1(\gamma_{i+1} r_i) - (\gamma_{i+1}/\mu_{r,i+1})K_0(\gamma_{i+1} r_i)K_1(\gamma_i r_i)}{(\gamma_{i+1}/\mu_{r,i+1})K_0(\gamma_{i+1} r_i)I_1(\gamma_i r_i) + (\gamma_i/\mu_{r,i})K_1(\gamma_{i+1} r_i)I_0(\gamma_i r_i)} \quad (\text{B.3})$$

here i is the region index. $\Gamma^{i,i+1}(\kappa)$ is the reflection coefficient from region i to region $i+1$ with the source in region i . Similarly, we have transmission coefficient with source inside as

$$T^{i,i+1}(\kappa) = \frac{(1/r_i \mu_{r,i})}{(\gamma_{i+1}/\mu_{r,i+1})K_0(\gamma_{i+1} r_i)I_1(\gamma_i r_i) + (\gamma_i/\mu_{r,i})K_1(\gamma_{i+1} r_i)I_0(\gamma_i r_i)} \quad (\text{B.4})$$

For source outside, we have

$$\Gamma^{i+1,i}(\kappa) = \frac{(\gamma_{i+1}/\mu_{r,i+1})I_0(\gamma_{i+1} r_i)I_1(\gamma_i r_i) - (\gamma_i/\mu_{r,i})I_1(\gamma_{i+1} r_i)I_0(\gamma_i r_i)}{(\gamma_{i+1}/\mu_{r,i+1})K_0(\gamma_{i+1} r_i)I_1(\gamma_i r_i) + (\gamma_i/\mu_{r,i})K_1(\gamma_{i+1} r_i)I_0(\gamma_i r_i)} \quad (\text{B.5})$$

$$T^{i+1,i}(\kappa) = \frac{(1/r_i \mu_{r,i+1})}{(\gamma_{i+1}/\mu_{r,i+1})K_0(\gamma_{i+1} r_i)I_1(\gamma_i r_i) + (\gamma_i/\mu_{r,i})K_1(\gamma_{i+1} r_i)I_0(\gamma_i r_i)} \quad (\text{B.6})$$

For the coil inside a tube, the only modification is to replace the Γ of borehole by that of tube. The reflection coefficient can be obtained by

$$\Gamma(\kappa) = \Gamma^{3,4}(\kappa) + \frac{T^{4,3}(\kappa)\Gamma^{4,5}(\kappa)T^{3,4}(\kappa)}{1 - \Gamma^{4,3}(\kappa)\Gamma^{4,5}(\kappa)} \quad (\text{B.7})$$

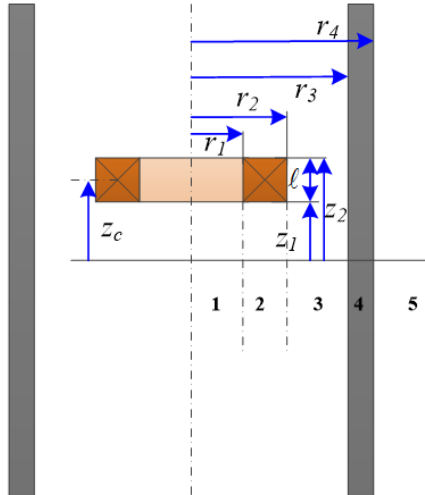


Figure B.2: A eddy current coil located inside coaxial with Tube, the number 1,2,3,4,5 indicates different region

The coil impedance changes outside a conductive tube whose axis is co-axis with that of tube, Fig. B.3, is determined by

$$\Delta Z = -8i\omega\mu_0 v^2 \int_0^\infty \sin^2\left(\frac{\kappa\ell}{2}\right) \frac{1}{\kappa^6} \psi_K^2(\kappa r_3, \kappa r_4) \Gamma(\kappa) d\kappa \quad (\text{B.8})$$

where Γ is the reflection coefficient of a source outside the tube, which can be calculated by

$$\Gamma(\kappa) = \Gamma^{3,2}(\kappa) + \frac{T^{2,3}(\kappa)\Gamma^{2,1}(\kappa)T^{3,2}(\kappa)}{1 - \Gamma^{2,1}(\kappa)\Gamma^{2,3}(\kappa)} \quad (\text{B.9})$$

Similarly, the impedance change of coil circulating a conductive rod can be obtained by replace the reflection coefficient by that of rod with source outside.

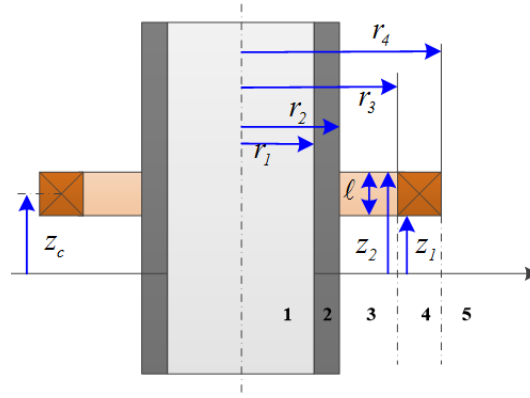


Figure B.3: A eddy current coil located outside coaxial with Tube, the number 1,2,3,4,5 indicates different region

APPENDIX C. USEFUL MATHEMATICAL FORMULATIONS

C.1 Fourier and Bessel Transforms

- Fourier Transform

$$f(t) = \frac{1}{2\pi} \int_{-\infty}^{\infty} g(\omega) e^{-i\omega t} d\omega \quad (\text{C.1})$$

$$g(\omega) = \int_{-\infty}^{\infty} f(t) e^{i\omega t} dt \quad (\text{C.2})$$

which are usually used for time domain

$$f(x) = \frac{1}{2\pi} \int_{-\infty}^{\infty} g(h) e^{ihx} dh \quad (\text{C.3})$$

$$g(h) = \int_{-\infty}^{\infty} f(x) e^{-ihx} dx \quad (\text{C.4})$$

which are usually used for space domain

- Hankel Transform

$$F_v(\kappa) = \int_0^{\infty} f(\rho) J_v(\kappa\rho) \rho d\rho \quad (\text{C.5})$$

$$f(\rho) = \int_0^{\infty} F_v(\kappa) J_v(\kappa\rho) \kappa d\kappa \quad (\text{C.6})$$

where v is assumed to be a positive real constant not necessarily integer.

C.2 Identities

Some useful identities of vector analysis and dyadic analysis frequently encountered in this thesis will be listed in the following sections. The dyadic analysis is an extension of vector analysis to a higher level. More comprehensive details about dyadic analysis can be found in Tai's book [96].

C.2.1 Differential Operators

$$1. \nabla(f\mathbf{A}) = \mathbf{A}\nabla f + f\nabla\mathbf{A}$$

$$2. \nabla^2 f = \nabla \cdot (\nabla f)$$

In Spherical Coordinate System

$$1. \mathcal{I} = \hat{r}\hat{r} + \hat{\theta}\hat{\theta} + \hat{\phi}\hat{\phi} = \hat{x}\hat{x} + \hat{y}\hat{y} + \hat{z}\hat{z}$$

$$2. \nabla\hat{r} = \frac{1}{r}(\hat{\theta}\hat{\theta} + \hat{\phi}\hat{\phi})$$

$$3. \nabla\hat{\theta} = -\hat{r}\frac{1}{r} + \hat{\phi}\frac{1}{r}\cot\theta$$

$$4. \nabla\hat{\phi} = -\hat{\phi}\frac{1}{r} - \hat{\theta}\frac{1}{r}\cot\theta$$

$$5. \nabla r = \hat{r}$$

$$6. \nabla\frac{1}{r} = -\frac{\hat{r}}{r^2}$$

$$7. \nabla\nabla\frac{1}{r} = -\nabla\frac{\hat{r}}{r^2} = -(\hat{r}\nabla\frac{1}{r^2} + \frac{1}{r^2}\nabla\hat{r}) = 3\hat{r}\frac{1}{r^3} - \mathcal{I}\frac{1}{r^3}$$

In Cylindrical Coordinate System

$$1. \nabla f = \hat{\rho}\frac{\partial f}{\partial\rho} + \hat{\phi}\frac{\partial f}{\rho\partial\phi} + \hat{z}\frac{\partial f}{\partial z}$$

$$2. \nabla \cdot \mathbf{A} = \frac{1}{\rho}\frac{\partial}{\partial\rho}(\rho A_\rho) + \frac{\partial A_\phi}{\rho\partial\phi} + \frac{\partial A_z}{\partial z}$$

$$3. \nabla \times \mathbf{A} = \hat{\rho}\left(\frac{1}{\rho}\frac{\partial A_z}{\partial\phi} - \frac{\partial A_\phi}{\partial z}\right) + \hat{\phi}\left(\frac{\partial A_\rho}{\partial z} - \frac{\partial A_z}{\partial\rho}\right) + \hat{z}\frac{1}{\rho}\left(\frac{\partial(\rho A_\phi)}{\partial\rho} - \frac{\partial A_\rho}{\partial\phi}\right)$$

$$4. \nabla^2 \mathbf{A} = \hat{\rho}\left(\frac{\partial^2 A_\rho}{\partial\rho^2} + \frac{1}{\rho}\frac{\partial A_\rho}{\partial\rho} - \frac{A_\rho}{\rho^2} + \frac{1}{\rho^2}\frac{\partial^2 A_\rho}{\partial\phi^2} - \frac{2}{\rho^2}\frac{\partial A_\phi}{\partial\phi} + \frac{\partial^2 A_\rho}{\partial z^2}\right) \\ + \hat{\phi}\left(\frac{\partial^2 A_\phi}{\partial\rho^2} + \frac{1}{\rho}\frac{\partial A_\phi}{\partial\rho} - \frac{A_\phi}{\rho^2} + \frac{1}{\rho^2}\frac{\partial^2 A_\phi}{\partial\phi^2} + \frac{2}{\rho^2}\frac{\partial A_\rho}{\partial\phi} + \frac{\partial^2 A_\phi}{\partial z^2}\right) \\ + \hat{z}\left(\frac{\partial^2 A_z}{\partial\rho^2} + \frac{1}{\rho}\frac{\partial A_z}{\partial\rho} + \frac{1}{\rho^2}\frac{\partial^2 A_z}{\partial\phi^2} + \frac{\partial^2 A_z}{\partial z^2}\right)$$

$$5. \nabla^2 \psi = \frac{\partial^2 \psi}{\partial\rho^2} + \frac{1}{\rho}\frac{\partial\psi}{\partial\rho} + \frac{1}{\rho^2}\frac{\partial^2 \psi}{\partial\phi^2} + \frac{\partial^2 \psi}{\partial z^2}$$

$$6. \nabla\hat{\rho} = \frac{1}{r}\hat{\phi}\hat{\phi}$$

$$7. \nabla\hat{\phi} = -\frac{1}{r}\hat{\phi}\hat{r}$$

$$8. \nabla\hat{z} = 0$$

$$9. \nabla f = \hat{\rho}\frac{\partial f}{\partial\rho} + \hat{\phi}\frac{1}{\rho}\frac{\partial f}{\partial\phi} + \hat{z}\frac{\partial f}{\partial z}$$

C.2.2 Integral Identities

$$\int_{z_G-\Delta z/2}^{z_G+\Delta z/2} e^{\gamma_{ij}z'} dz' = \frac{2e^{\gamma_{ij}z_G}}{\gamma_{ij}} \sinh\left(\gamma_{ij} \frac{\Delta z}{2}\right) \quad (C.7)$$

$$\int_{z_G-\Delta z/2}^{z_G+\Delta z/2} e^{-\gamma_{ij}z'} dz' = \frac{2e^{-\gamma_{ij}z_G}}{\gamma_{ij}} \sinh\left(\gamma_{ij} \frac{\Delta z}{2}\right) \quad (C.8)$$

$$\int_{x_G-\Delta x/2}^{x_G+\Delta x/2} \sin(u_i x') dx' = \frac{2}{u_i} \sin(u_i x_G) \sin\left(u_i \frac{\Delta x}{2}\right) = \Delta x \sin(u_i x_G) \operatorname{sinc}\left(u_i \frac{\Delta x}{2\pi}\right) \quad (C.9)$$

$$\int_{x_G-\Delta x/2}^{x_G+\Delta x/2} \cos(u_i x') dx' = \frac{2}{u_i} \cos(u_i x_G) \sin\left(u_i \frac{\Delta x}{2}\right) = \Delta x \cos(u_i x_G) \operatorname{sinc}\left(u_i \frac{\Delta x}{2\pi}\right) \quad (C.10)$$

C.3 Bessel Function

Here we defining

$$\Lambda_m(x) = \frac{xI'_m(x)}{I_m(x)}, M_m(x) = \frac{xK'_m(x)}{K_m(x)} \quad (C.11)$$

We can easily get

$$\Lambda_m(x) - M_m(x) = \frac{x(I'_m K_m - I_m K'_m)}{I_m K_m} = \frac{1}{I_m K_m} \quad (C.12)$$

$$\Lambda_m(x) = \frac{xI'_m(x)}{I_m(x)} = m + \frac{xI_{m+1}(x)}{I_m(x)} \quad (C.13)$$

$$M_m(x) = \frac{xK'_m(x)}{K_m(x)} = m - \frac{xK_{m+1}(x)}{K_m(x)} \quad (C.14)$$

$$\psi_I(r_1, r_2) = \int_{r_1}^{r_2} I_1(x) x dx \quad (C.15)$$

$$\psi_K(r_1, r_2) = \int_{r_1}^{r_2} K_1(x) x dx \quad (C.16)$$

$$\chi(s_1, s_2) = \int_{s_1}^{s_2} J_1(x) x dx \quad (C.17)$$

$$I'_m(z) = I_{m-1}(z) - \frac{m}{z} I_m(z) \quad (C.18)$$

$$I'_m(z) = I_{m+1}(z) + \frac{m}{z} I_m(z) \quad (C.19)$$

$$I'_m(z) = \frac{I_{m+1}(z) + I_{m-1}(z)}{2} \quad (C.20)$$

$$K'_m(z) = -K_{m-1}(z) - \frac{m}{z}K_m(z) \quad (\text{C.21})$$

$$K'_m(z) = -K_{m+1}(z) + \frac{m}{z}K_m(z) \quad (\text{C.22})$$

$$K'_m(z) = -\frac{K_{m+1}(z) + K_{m-1}(z)}{2} \quad (\text{C.23})$$

Note that both $I'_m(z)$ and $K'_m(z)$ are even functions with respect to order m .

$$\int zJ_0(kz)dz = \frac{z}{k}J_1(kz) \quad (\text{C.24})$$

$$\int J_1(z)dz = -J_0(z) \quad (\text{C.25})$$

$$\int_a^b zJ_0(kz)dz = \frac{b}{k}J_1(kb) - \frac{a}{k}J_1(ka) \quad (\text{C.26})$$

page 222 [102]

$$J'_0(z) = -J_1(z) \quad (\text{C.27})$$

$$J'_v(z) = J_{v-1}(z) - (v/z)J_v(z) \quad (\text{C.28})$$

$$J'_v(z) = -J_{v+1}(z) + (v/z)J_v(z) \quad (\text{C.29})$$

BIBLIOGRAPHY

- [1] Satish S Udpa and Patrick O Moore. Nondestructive testing handbook, volume 5-. *Electromagnetic Testing, ASNT*, 2004.
- [2] John D Kraus and Ronald J Marhefka. *Antenna for all applications*. Upper Saddle River, NJ: McGraw Hill, 2002.
- [3] Nicola Bowler. Four-point potential drop measurements for materials characterization. *Measurement Science and Technology*, 22(1):012001, 2010.
- [4] Alfred J Bahr. *Microwave nondestructive testing methods*, volume 1. CRC Press, 1982.
- [5] Yiming Deng and Xin Liu. Electromagnetic imaging methods for nondestructive evaluation applications. *Sensors*, 11(12):11774–11808, 2011.
- [6] Satish S Udpa and Lalita Udpa. Eddy current nondestructive evaluation. *Wiley encyclopedia of electrical and electronics engineering*, 1999.
- [7] D McA McKirdy, A Cochran, GB Donaldson, and A McNab. Forward and inverse processing in electromagnetic nde using squids. In *Rev. Prog. Q.*, pages 347–354. Springer, 1996.
- [8] A Sophian, GY Tian, D Taylor, and J Rudlin. Electromagnetic and eddy current ndt: a review. *Insight-wigston then northampton*, 43(5):302–306, 2001.
- [9] CV Dodd and WE Deeds. Analytical solutions to eddy-current probe-coil problems. *J. Appl. Phys.*, 39(6):2829–2838, 1968.
- [10] JR Bowler. Review of eddy current inversion with application to nondestructive evaluation. *Int. J. Appl. Electromag. and Mechanics*, 8(1):3–16, 1997.

- [11] BA Auld and JC Moulder. Review of advances in quantitative eddy current nondestructive evaluation. *J. Nondestruct. Eval*, 18(1):3–36, 1999.
- [12] William H Hannum, Gerald E Marsh, and George S Stanford. Smarter use of nuclear waste. *Sci. Amer.*, 293(6):84–91, 2005.
- [13] W Sharatchandra Singh, B Purnachandra Rao, S Thirunavukkarasu, S Mahadevan, CK Mukhopadhyay, and T Jayakumar. Development of magnetic flux leakage technique for examination of steam generator tubes of prototype fast breeder reactor. *Ann. Nucl. Eneq.*, 83:57–64, 2015.
- [14] J R Bowler, T P Theodoulidis, and N Poulakis. Eddy current probe signals due to a crack at a right-angled corner. *IEEE Trans. Mag.*, 48(12):4735–4746, Dec 2012.
- [15] TP Theodoulidis and JR Bowler. Eddy current coil interaction with a right-angled conductive wedge. In *Proceedings of the Royal Society of London A: Mathematical, Physical and Engineering Sciences*, volume 461, pages 3123–3139. The Royal Society, 2005.
- [16] JR Bowler and N Harfield. Thin-skin eddy-current interaction with semielliptical and epicyclic cracks. *IEEE Trans. Mag.*, 36(1):281–291, 2000.
- [17] Nicola Harfield and John R Bowler. Theory of thin-skin eddy-current interaction with surface cracks. *J. Appl. Phys.*, 82(9):4590–4603, 1997.
- [18] Konstantinos Pipis, Anastassios Skarlatos, Theodoros Theodoulidis, and Dominique Leselieur. Ect-signal calculation of cracks near fastener holes using an integral equation formalism with dedicated greens kernel. *IEEE Trans. Mag.*, 52(4):1–8, 2016.
- [19] J R Bowler, T P Theodoulidis, H Xie, and Y Ji. Evaluation of eddy current probe signals due to cracks in fastener holes. *IEEE Trans. Mag.*, 48(3):1159–1170, Mar 2012.
- [20] John R Bowler and Theodoros Theodoulidis. Boundary element calculation of eddy currents in cylindrical structures containing cracks. *IEEE Trans. Mag.*, 45(3):1012–1015, 2009.

- [21] Anastassios Skarlatos, Grégoire Pichenot, Dominique Lesselier, Marc Lambert, and Bernard Duchene. Electromagnetic modeling of a damaged ferromagnetic metal tube by a volume integral equation formulation. *IEEE Trans. Mag.*, 44(5):623–632, 2008.
- [22] JR Bowler, SA Jenkins, LD Sabbagh, and HA Sabbagh. Eddy-current probe impedance due to a volumetric flaw. *J. Appl. Phys.*, 70(3):1107–1114, 1991.
- [23] Daniel Ioan and Mihai Rebican. Numerical model for eddy-current testing of ferromagnetic steel parts. *IEEE Trans. Mag.*, 38(2):629–632, 2002.
- [24] Theodoros Theodoulidis and John R Bowler. Impedance of a coil at an arbitrary position and orientation inside a conductive borehole or tube. *IEEE Trans. Mag.*, 51(4):1–6, 2015.
- [25] Anastassios Skarlatos and Theodoros Theodoulidis. Calculation of the eddy-current flow around a cylindrical through-hole in a finite-thickness plate. *IEEE Trans. Mag.*, 51(9):1–7, 2015.
- [26] Theodoros Theodoulidis and Anastassios Skarlatos. Eddy current interaction of an arbitrarily positioned probe coil with a conductive cylinder. *IEEE Trans. Mag.*, 48(8):2392–2394, 2012.
- [27] SK Burke, RJ Ditchburn, and TP Theodoulidis. Impedance of a curved circular spiral coil around a conductive cylinder. *NDT & E International*, 64:1–6, 2014.
- [28] JW Luquire, WE Deeds, and CV Dodd. Alternating current distribution between planar conductors. *J. Appl. Phys.*, 41(10):3983–3991, 1970.
- [29] SK Burke. Eddy-current inspection of cracks in a multilayer conductor. *J. Appl. Phys.*, 67(1):465–476, 1990.
- [30] CV Dodd, CC Cheng, and WE Deeds. Induction coils coaxial with an arbitrary number of cylindrical conductors. *J. Appl. Phys.*, 45(2):638–647, 1974.
- [31] SK Burke. Impedance of a horizontal coil above a conducting half-space. *J. Phys. D: Appl. Phys.*, 19(7):1159, 1986.

- [32] TP Theodoulidis. Analytical modeling of wobble in eddy current tube testing with bobbin coils. *J. Res. Nondestruct. Eval*, 14(2):111–126, 2002.
- [33] SK Burke and TP Theodoulidis. Impedance of a horizontal coil in a borehole: a model for eddy-current bolthole probes. *J. Phys. D: Appl. Phys.*, 37(3):485, 2004.
- [34] Theodoros Theodoulidis. Analytical model for tilted coils in eddy-current nondestructive inspection. *IEEE Trans. Mag.*, 41(9):2447–2454, 2005.
- [35] Theodoros P Theodoulidis and Epameinondas E Kriezis. *Eddy current canonical problems (with applications to nondestructive evaluation)*. Tech Science Press, 2006.
- [36] Theodoros Theodoulidis and Epameinondas Kriezis. Series expansions in eddy current nondestructive evaluation models. *J. Mater. Process. Technol.*, 161(1):343–347, 2005.
- [37] John R Bowler and Theodoros P Theodoulidis. Eddy currents induced in a conducting rod of finite length by a coaxial encircling coil. *J. Phys. D: Appl. Phys.*, 38(16):2861, 2005.
- [38] Haiyan Sun, John R Bowler, and Theodoros P Theodoulidis. Eddy currents induced in a finite length layered rod by a coaxial coil. *IEEE Trans. Mag.*, 41(9):2455–2461, 2005.
- [39] SK Burke, JR Bowler, and TP Theodoulidis. An experimental and theoretical study of eddy-current end effects in finite rods and finite length holes. In *Rev. Prog. Q.*, volume 820, pages 361–368. AIP Publishing, 2006.
- [40] Theodoros P Theodoulidis and John R Bowler. Impedance of an induction coil at the opening of a borehole in a conductor. *J. Appl. Phys.*, 103(2):024905, 2008.
- [41] Theodoros Theodoulidis and John R Bowler. Interaction of an eddy-current coil with a right-angled conductive wedge. *IEEE Trans. Mag.*, 46(4):1034–1042, 2010.
- [42] CP Trampel and JR Bowler. Eddy-current coil interaction with a perfectly conducting wedge of arbitrary angle. *Res. Nondestruct. Eval*, 25(3):186–202, 2014.

- [43] A Mor and S Gavril. On the operation of the rectangular eddy current probe coil at an arbitrary inclination over a thin conductor sheet. *J. Franklin Inst.*
- [44] Theodoros P Theodoulidis and Epameinondas E Kriezis. Impedance evaluation of rectangular coils for eddy current testing of planar media. *NDT & E International*, 35(6):407–414, 2002.
- [45] TP Theodoulidis, SM Panas, and EE Kriezis. Eddy current detection of crack orientation using elliptical excitation. *IEE Proceedings-Science, Measurement and Technology*, 141(1):41–47, 1994.
- [46] Xiao Chun-Yan and Zhang Jun. Analytical solutions of transient pulsed eddy current problem due to elliptical electromagnetic concentrative coils. *Chinese physics B*, 19(12):120302, 2010.
- [47] SK Burke, RJ Ditchburn, and TP Theodoulidis. Impedance of curved rectangular spiral coils around a conductive cylinder. *J. Appl. Phys.*, 104(1):014912, 2008.
- [48] Theodoros P Theodoulidis. Model of ferrite-cored probes for eddy current nondestructive evaluation. *J. Appl. Phys.*, 93(5):3071–3078, 2003.
- [49] Yi Lu, John R Bowler, and Theodoros P Theodoulidis. An analytical model of a ferrite-cored inductor used as an eddy current probe. *J. Appl. Phys.*, 111(10):103907, 2012.
- [50] Hr Sabbagh. A model of eddy-current probes with ferrite cores. *IEEE Trans. Mag.*, 23(3):1888–1904, 1987.
- [51] Andrzej Krawczyk and John A Tegopoulos. *Numerical modelling of eddy currents*. Clarendon Press, 1993.
- [52] O Biro and K Preis. Finite element analysis of 3-d eddy currents. *IEEE Trans. Mag.*, 26(2):418–423, 1990.
- [53] A Bossavit and J-C Vérité. A mixed fem-biem method to solve 3-d eddy-current problems. *IEEE Trans. Mag.*, 18(2):431–435, 1982.

- [54] R Spal and AH Kahn. Eddy currents in a conducting cylinder with a crack. *J. Appl. Phys.*, 50(10):6135–6138, 1979.
- [55] Theodoros P Theodoulidis and John R Bowler. The truncated region eigenfunction expansion method for the solution of boundary value problems in eddy current nondestructive evaluation. In *AIP Conference Proceedings*, volume 760, page 403. IOP INSTITUTE OF PHYSICS PUBLISHING LTD, 2005.
- [56] John Bowler and Nicola Harfield. High frequency eddy-current interaction with cracks. *Electromagnetic Nondestructive Evaluation (II)*, 2:9, 1998.
- [57] John R Bowler, L David Sabbagh, and Harold A Sabbagh. A theoretical and computational model of eddy-current probes incorporating volume integral and conjugate gradient methods. *IEEE Trans. Mag.*, 25(3):2650–2664, 1989.
- [58] Marek Augustyniak and Zbigniew Usarek. Finite element method applied in electromagnetic ndte: A review. *J. Nondestruct. Eval*, 35(3):1–15, 2016.
- [59] T Kincaid and M Chari. The application of finite element method analysis to eddy current nondestructive evaluation. *IEEE Trans. Mag.*, 15(6):1956–1960, 1979.
- [60] Nathan Ida and William Lord. A finite element model for three-dimensional eddy current ndt phenomena. *IEEE Trans. Mag.*, 21(6):2635–2643, 1985.
- [61] L Udpa and W Lord. Impedance and mesh structure considerations in the finite element analysis of eddy current ndt probe phenomena. *IEEE Trans. Mag.*, 21(6):2269–2272, 1985.
- [62] Joachim Fetzer, Stefan Kurz, and Günther Lehner. The coupling of boundary elements and finite elements for nondestructive testing applications. *IEEE Trans. Mag.*, 33(1):677–681, 1997.
- [63] Takayoshi Nakata, N Takahashi, and K Fujiwara. Efficient solving techniques of matrix equations for finite element analysis of eddy currents. *IEEE Trans. Mag.*, 24(1):170–173, 1988.

- [64] Roger F Harrington and Jan L Harrington. *Field computation by moment methods*. Oxford University Press, 1996.
- [65] John R Bowler and Tao Wu. Eddy current tube inspection using a rotary probe. In *42ND ANNUAL Rev. Prog. Q.: Incorporating the 6th European-American Workshop on Reliability of NDE*, volume 1706, page 090009. AIP Publishing, 2016.
- [66] W Rucker and K Richter. Calculation of two-dimensional eddy current problems with the boundary element method. *IEEE Trans. Mag.*, 19(6):2429–2432, 1983.
- [67] RE Beissner. Boundary element model of eddy current flaw detection in three dimensions. *J. Appl. Phys.*, 60(1):352–356, 1986.
- [68] John R Bowler. Eddy-current interaction with an ideal crack. i. the forward problem. *J. Appl. Phys.*, 75(12):8128–8137, 1994.
- [69] Kazuhisa Ishibashi. Eddy current analysis by boundary element method utilizing impedance boundary condition. *IEEE Trans. Mag.*, 31(3):1500–1503, 1995.
- [70] Ming Yang, Jiming Song, Zhigang Chen, and Norio Nakagawa. A fast multipole boundary integral equation method for two-dimensional diffusion problems. In *Rev. Prog. Q.*, volume 894, pages 294–301. AIP Publishing, 2007.
- [71] JR Bowler, LD Sabbagh, and HA Sabbagh. Eddy-current probe impedance due to a surface slot in a conductor. *IEEE Trans. Mag.*, 26(2):889–892, 1990.
- [72] Daniel Dos Reis, Marc Lambert, and Dominique Lesselier. Eddy-current evaluation of three-dimensional defects in a metal plate. *Inverse problems*, 18(6):1857, 2002.
- [73] P Weidelt. Electromagnetic induction in three-dimensional structures. *J. Geophys.*, 41(85):109, 1975.
- [74] W Scott Dunbar. The volume integral method of eddy current modeling. *J. Nondestruct. Eval.*, 5(1):9–14, 1985.

- [75] W Scott Dunbar. The volume integral method of eddy-current modeling: Verification. *J. Nondestruct. Eval*, 7(1-2):43–54, 1988.
- [76] David M McKirdy. Recent improvements to the application of the volume integral method of eddy current modeling. *J. NDE*, 8(1):45–52, 1989.
- [77] Kazuhisa Ishibashi. Nonlinear eddy current analysis by volume integral equation method. *IEEE Trans. Mag.*, 23(5):3038–3040, 1987.
- [78] Patrick Dular, Gerard Meunier, Francis Piriou, Christophe Reboud, Denis Prémel, Dominique Lesselier, and Bernard Bisiaux. New discretisation scheme based on splines for volume integral method: application to eddy current testing of tubes. *COMPEL-The international journal for computation and mathematics in electrical and electronic engineering*, 27(1):288–297, 2008.
- [79] John R Bowler. Eddy current calculations using half-space greens functions. *J. Appl. Phys.*, 61(3):833–839, 1987.
- [80] John R Bowler. Time domain half-space dyadic greens functions for eddy-current calculations. *J. Appl. Phys.*, 86(11):6494–6500, 1999.
- [81] Stephen A Jenkins and John R Bowler. Numerical evaluation of singular matrix elements in three dimensions [maxwell equations]. *IEEE Trans. Mag.*, 27(6):4438–4444, 1991.
- [82] John R Bowler and Fangwei Fu. Time-domain dyadic green’s function for an electric source in a conductive plate. *IEEE Trans. Mag.*, 42(11):3661–3668, 2006.
- [83] Nicola Bowler. Analytical solution for the electric field in a half space conductor due to alternating current injected at the surface. *J. Appl. Phys.*, 95(1):344–348, 2004.
- [84] Stephan E Barlow. Alternative electrostatic greens function for a long tube. *J. Appl. Phys.*, 94(9):6221–6222, 2003.
- [85] Lingling Xing. Rapid calculation of eddy current field green’s function using the matrix pencil method. *NDT & E International*, 42(2):85–91, 2009.

- [86] Houda Zaidi, Laurent Santandrea, Guillaume Krebs, Yann Le Bihan, and Edouard Demaldent. Fem technique for modeling eddy-current testing of ferromagnetic media with small skin depth. *IEEE Trans. Mag.*, 50(2):129–132, 2014.
- [87] N Harfield and John R Bowler. Prediction of eddy-current probe impedance due to surface cracks in ferromagnetic steels. In *Rev. Prog. Q.*, pages 241–248. Springer, 1997.
- [88] Nicola Harfield and John R Bowler. Theory of eddy-current interaction with surface crack in ferromagnetic steels. *Electromag. Nondestruct. Eval.*, pages 59–66, 1997.
- [89] Constantine A Balanis. *Advanced Engineering Electromagnetics*, volume 20. Wiley New York, 1989.
- [90] Weng Cho Chew. *Waves and fields in inhomogeneous media*, volume 522. IEEE press New York, 1995.
- [91] Tao Wu, Wei Hong, and Jixin Chen. A high-rejection substrate integrated waveguide filter for q-linkpan applications. In *Microwave Workshop Series on Millimeter Wave Wireless Technology and Applications (IMWS), 2012 IEEE MTT-S International*, pages 1–4. IEEE, 2012.
- [92] Jian-Ming Jin. *Theory and computation of electromagnetic fields*. John Wiley & Sons, 2011.
- [93] Weng Chew, Mei-Song Tong, et al. *Integral Equation Methods for Electromagnetic and Elastic Waves*. Morgan & Claypool Publishers, 2008.
- [94] Leopold B Felsen and Nathan Marcuvitz. *Radiation and Scattering of Waves*, volume 31. John Wiley & Sons, 1994.
- [95] Julius Adams Stratton. *Electromagnetic theory*, volume 33. John Wiley & Sons, 2007.
- [96] Chen-To Tai. *Dyadic Green Functions in Electromagnetic Theory*, volume 272. IEEE press New York, 1994.
- [97] Jean G Van Bladel. *Electromagnetic fields*, volume 19. John Wiley & Sons, 2007.

- [98] LE Sun and WC Chew. A novel formulation of the volume integral equation for electromagnetic scattering. *Wave Random Complex*, 19(1):162–180, 2009.
- [99] Theodoros Theodoulidis, Nikolaos Poulakis, and Athanasios Dragogias. Rapid computation of eddy current signals from narrow cracks. *NDT & E International*, 43(1):13–19, 2010.
- [100] NC Haywood and JR Bowler. Eddy-current imaging of buried cracks, by inverting field data. *IEEE Trans. Mag.*, 28(2):1336–1339, 1992.
- [101] Aria Abubakar and Peter M van den Berg. Iterative forward and inverse algorithms based on domain integral equations for three-dimensional electric and magnetic objects. *J. Comput. Phys.*, 195(1):236–262, 2004.
- [102] Frank WJ Olver. *NIST handbook of mathematical functions*. Cambridge University Press, 2010.
- [103] David M Pozar. *Microwave engineering*. John Wiley & Sons, 2009.
- [104] John R Bowler, Theodoros P Theodoulidis, Hui Xie, and Yuan Ji. Evaluation of eddy-current probe signals due to cracks in fastener holes. *IEEE Trans. Mag.*, 48(3):1159–1170, 2012.
- [105] A Yaghjian. Electric dyadic green’s functions in the source region. *Proc. IEEE*, 68(2):248–263, 1980.
- [106] Shung-Wu Lee, Johannes Boersma, Chak-Lam Law, and Georges A Deschamps. Singularity in green’s function and its numerical evaluation. *IEEE Trans. Antennas. Propag.*, 28(3):311–317, 1980.
- [107] Alan Jeffrey and Daniel Zwillinger. *Table of Integrals, Series, and Products*. Academic Press, 2007.
- [108] Nicola Bowler and Yongqiang Huang. Electrical conductivity measurement of metal plates using broadband eddy-current and four-point methods. *Measurement Science and Technology*, 16(11):2193, 2005.

- [109] John R Bowler and Nicola Bowler. Theory of four-point alternating current potential drop measurements on conductive plates. In *Proceedings of the Royal Society of London A: Mathematical, Physical and Engineering Sciences*, volume 463, pages 817–836. The Royal Society, 2007.
- [110] Alan P Berens and PW Hovey. Statistical methods for estimating crack detection probabilities. In *Probabilistic Fracture Mechanics and Fatigue Methods: Applications for Structural Design and Maintenance*. ASTM International, 1983.
- [111] Tao Wu and John R Bowler. Limitations of eddy current testing in a fast reactor environment. In *42nd Annual Review of Progress in Quantitative Nondestructive Evaluation*, volume 1706, page 170007. AIP Publishing, 2016.
- [112] Grzegorz Tytko and Leszek Dziczkowski. E-cored coil with a circular air gap inside the core column used in eddy current testing. *IEEE Trans. Mag.*, 51(9):1–4, 2015.
- [113] Sergey Sergeyeovich Vinogradov, Paul Denis Smith, and Elena Dmitrievna Vinogradova. *Canonical problems in scattering and potential theory part II: Acoustic and electromagnetic diffraction by canonical structures*. CRC Press, 2002.
- [114] Andrew Gray, George Ballard Mathews, and Ernst Meissel. *A treatise on Bessel functions and their applications to physics*. Macmillan and Company, 1895.
- [115] George Neville Watson. *A treatise on the theory of Bessel functions*. Cambridge university press, 1995.
- [116] HJ Tsaknakis and EE Kriezis. Field distribution due to a circular current loop placed in an arbitrary position above a conducting plate. *IEEE Trans. Geosci. Remote Sens.*, (6):834–840, 1985.
- [117] Theodoros Theodoulidis, Nikolaos Poulakis, and Athanasios Dragogias. Rapid computation of eddy current signals from narrow cracks. *NDT & E International*, 43(1):13–19, 2010.